SYNTHETIC TURBULENCE BASED ON THE MULTI-SCALE TURNOVER LAGRANGIAN MAP

SUKAINA AL-BAIRMANI

SUBMITTED FOR THE DEGREE OF DOCTOR OF PHILOSOPHY

School of Mathematics and Statistics

November 2017

Supervisor: Dr. Yi Li

University of Sheffield, United Kingdom

Abstract

Synthetic turbulence refers to stochastic fields having characteristics of real hydro-dynamic turbulent flows, which has been useful in the modelling and simulation of turbulence, and for further understanding fundamental properties of turbulent motion. Synthetic turbulence aims to construct the field variables (such as velocity distributions) by simpler processes to reproduce characteristic features of turbulent fluctuations with a reduced computational cost in comparison with a formal numerical solution of the Navier-Stokes equations. A new approach of synthetic turbulence has been recently proposed, which showed that realistic synthetic isotropic turbulent fields could be generated using the Multi-scale turnover Lagrangian map (MTLM).

The initial focus of this thesis is on studying the MTLM synthetic fields using the filtering approach. This approach, which has not been pursued so far, sheds new light on the potential applications of the synthetic fields in large eddy simulations and subgrid-scale (SGS) modelling. Our investigation includes SGS stresses, and SGS dissipations and related statistics, SGS scalar variance, and its relations with other quantities (such as the filtered molecular scalar dissipation). It is well-known that, even if a synthetic field had reproduced faithfully the multi-fractal statistics, it may not be able to produce the energy flux across the energy spectrum. Therefore, from the LES and/or SGS modelling perspective, many questions remain unclear, such as the PDF of the SGS dissipation, the amount of back-scattering, among others. They are addressed in this work. It demonstrates that using the MTLM is able to build a synthetic SGS model with a number of good features which many current SGS models (including those for the scalar flux) do not have. We also show that it has advantages in representing the filtered molecular scalar dissipation. In addition, we generalize the formulation of MTLM to include the effects of a mean scalar gradient on the scalar field. Our numerical tests provide the necessary proof that the effects of the mean gradient can be captured by MTLM. Furthermore, we investigate the effects of the input spectra on the statistics of the MTLM fields. We study the effects of the shape of the spectra by using truncated spectra and a model spectra (the Kovasznay spectra) as the input. The additional case, and the additional quantities we examine, have shedded light on how to apply the MTLM technique in simulations, as well as the robustness of the technique.

The Constrained MTLM is a new technique generalizing the MTLM procedure to generate anisotropic synthetic turbulence in order to model inhomogeneous turbulence by using the adjoint formulation. Li and Rosales [107] derived the optimality system corresponding to the MTLM map and applied this method to synthesize two Kolmogorov flows. In this thesis, we derive a new optimality system to generate anisotropic synthetic turbulence according to the CMTLM approach in order to include the effects of solid wall boundaries, which were not taken into account in the last study. We consider the difference introduced by the solid wall, under the impermeable boundary conditions, where the normal components velocity field are zero, while the tangent components may be non-zero. To accomplish this task, we have modified the CMTLM procedure to generate a reflectionally symmetric synthetic field which serves as a model of the velocity field in a fully developed channel flow. That the MTLM procedure preserves the reflectional symmetries is proved, the adjoint optimality system with reflectional symmetry are derived.

We aim to obtain accurate turbulent statistics, and compare our results with computed and experimental results.

CMTLM procedure formulates MTLM procedure as an optimization problem with the initial Gaussian random field as the control and some known velocity field as the target. Thus, with the purpose to quantify the contributions of the adjoint operator in the modelling process, the effects of the control variable on the cost function gradient and the corresponding adjoint field is examined. Contours of the mean of the gradients of the cost functions and adjoint fields for three cases with data taken from synthetics CMTLM Kolmogorov flows and from CMTLM synthetics velocity field generated with DNS data as the target are computed.

Finally, in order to define a new SGS model to simulate interactions between different length scales in turbulence, we will combine DNS data with Constrained MTLM method. Three data sets are truncated from DNS data with different degrees of resolution, filtered with the cutoff filter with large filter scale, which are then used as target fields to synthesize three CMTLM fields. The CMTLM fields are merged with these target fields. Data from the merged fields are used to predict the SGS quantities, and are compared with exact SGS quantities which have been computed from DNS field. In addition, the statistical geometry between the SGS and filtered quantities for real and predicted data are also investigated.

Contents

List of Figures

Chapter 1

Introduction

1.1 Turbulence

Fluid turbulence is a typical phenomenon in nonlinear classical physics. Beginning perhaps with Reynolds' work, statistical approach has been used to capture the complex and multiscale nature of turbulent velocity fluctuations. Unsteady chaotic motion of each eddy is unpredictable, which is an important aspect of turbulence. This property is in contrast to the smooth, laminar state, which is observable when the length scale of the flow is sufficiently small. The fluid turbulent velocity field varies essentially and irregularly in space and time simultaneously; it is a time-dependent random vector field which may be denoted by $u(x,t)$ where x refers to the position and t refers to the time [145]. Reynolds [151] first established a non-dimensional number, to characterise the transition between two flow regimes, which is given by

$$Re = \frac{UL}{\nu}, \tag{1.1}$$

where U indicates the characteristic velocity and L refers to the length scale of the flow field, respectively, and ν refers to the kinematic viscosity of the fluid. A turbulent regime exists when the Reynolds number is above a critical value so that small perturbations that happen in the flow are amplified and developed to multiscale coherent structures. Below this value, small perturbations are damped by the viscous stress and the flow remains laminar [104]. These coherent structures in turbulence are generally correlated with rotating motions of the fluid flow, which are referred to as eddies or vortices.

A more complete picture could be given by considering Richardson's concept of energy cascade, which suggests that turbulence might be represented by a formation of eddies of various sizes. The existence of these eddies is usually connected with regions of shear. The width of the shear layer determines their characteristic size. The large scale eddies ultimately turn unstable and split into smaller eddies. In other words, the large scale coherent eddies are unsteadily split-up, conceding their energy to a slightly smaller coherent eddies. These smaller eddies are subject to a similar split-up operation transporting their energy to yet smaller eddies. This process carries on until the local Reynolds number is small enough at which the molecular viscosity dissipates the kinetic energy effectively [154]. This picture is important because it locates the dissipation at the end of the sequence of processes. Consequently, at high Reynolds numbers the rate of dissipation ϵ is controlled by large scales, and is given by

$$\epsilon \sim \frac{u_0^3}{\ell_0}, \qquad (1.2)$$

regardless of molecular viscosity ν, in which the ℓ_0 refers to the characteristic velocity and lengthscale, respectively, of the largest eddies. ℓ_0 is comparable with the flow scale L.

1.2 Modelling and Simulation of Turbulence

In this section, we provide a summary of the leading modelling methods utilized in the numerical simulation of turbulence. Direct Numerical Simulation (DNS), Reynolds-averaged Navier-Stokes (RANS), Large-Eddy Simulation (LES), and hybrid RANS-LES techniques are compared in terms of their governing equations, computational mechanisms used, modelling assumptions, computational cost and current applications. In order to illustrate how simulation and modelling can complement each other in supplying a good description of the physical systems that have been simulated.

1.2.1 Governing Equations

The *Navier-Stokes equations* (NSEs) describe the movement of fluids, which govern an incompressible flows, with density and dynamic viscosity being constant; in other words, the flow of *constant-property Newtonion fluids*. For comprehensive review, one can refer to the texts of Batchelor [11], Panton [135], and Tritton [190]. The *mass-conservation* equation is defined as

$$\frac{d\rho}{dt} + \rho \frac{\partial u_i}{\partial x_i} = 0. \qquad (1.3)$$

where ρ refers to the density of the fluid, and u_i represents the velocity components. The operator $\frac{d}{dt}$ in the first term represents the material time derivative which has the form:

$$\frac{d}{dt} = \frac{\partial}{\partial t} + \mathbf{u} \cdot \nabla. \qquad (1.4)$$

The flow is presume to be incompressible (i.e., ρ in the flow is regardless of x and of t), thus the velocity field becomes *solenoidal* or *divergence-free*

$$\frac{\partial u_i}{\partial x_i} = 0. \qquad (1.5)$$

The momentum equation, depending on Newton's second law, reads

$$\frac{du_i}{dt} = -\rho^{-1} \frac{\partial p}{\partial x_i} + \nu \frac{\partial^2 u_i}{\partial x_j \partial x_j}. \qquad (1.6)$$

where $\nu \equiv \frac{\mu}{\rho}$ and p is the *pressure*. Precisely, the *Navier-Stokes equations* Eq. 1.6 and the *solenoidal* condition Eq. 1.5 govern the flow of *constant-property Newtonion fluids*.

The passive scalar equation for incompressible flow is

$$\frac{\partial \theta}{\partial t} + \frac{\partial}{\partial x_i}(u_i \theta) = \kappa \frac{\partial^2 \theta}{\partial x_i \partial x_i}. \tag{1.7}$$

where θ indicates the passive scalar and κ refers to diffusion coefficient.

The mathematical description of the fluids motion like air or water is of central interest both in academics and in industry. However, the Navier-Stokes equations are analytically unsolvable in most situations. For this reason, the flow is subject to numerical simulation methods aiming to understand the conduct of the flow in a particular situation. However, the direct numerical simulation (DNS) of the above Navier-Stokes equations, Eqs. 1.5 and 1.6, was computationally quite costly due to the turbulent behaviours of the flow, since eddies a wide spectrum of length scales and time scales need to be captured. Solving all these scales needs a very fine mesh resolution and that needs too demanding computations for most cases. Consequently, modelling the NSEs has been used as an alternative, which attempts to minimize the complication of the system to be simulated. In such ways, in a sensible amount of time computers are capable to solve the equations.

The Reynolds Averaged Navier-Stokes (RANS), Large-Eddy Simulation (LES), and Hybrid RANS-LES are the prime modelling techniques utilized in the numerical simulation of turbulence. In RANS, only the mean motion is considered in the governing equations and models are implemented in order to describe turbulence. In the large eddy simulation (LES), a filtering procedure is used to decompose the velocity and scalar turbulent fields into the large scales, and the subgrid-scale (SGS). The large scales are resolved directly, whereas the effects of the subgrid-scales (SGS) are modelled (see Refs. [103], [125], [142] and [116] for reviews)

RANS models tend to do well for a thin boundary layer. However, its empirical modelling assumptions limit its reliability in new complex cases. Finely resolved LES supplies quite precise predictions in comparison with RANS models for complex three-dimensional non-equilibrium flows away from walls. In fact, RANS has been used a log-law approximation in order to mimic wall flows, this log-law approximation is invalid for non-equilibrium flows with acceleration, separation or rotation [201]. In addition, a potential restriction of RANS is that it just produces an averaged sight of the flow. Furthermore, in the industry RANS models has inexpensive computational cost due to homogeneity in the mean flow which reduces resolution requirements. On the other hand, LES simulation of wall-bounded flows at high Reynolds numbers would be prohibitively costly.

For sake of LES with minimum computational requirements and to modify the achievement and the application range of RANS models simultaneously. Hybrid RANS-LES methods are proposed with the target to address the gap between them via the combination of RANS and LES strategies in one approach. For more details about the reconciliation between the RANS and LES representations of turbulence, where these two representations overlap at the interface, see the Semi-Deterministic Model (SDM) of Kourta and Minh [122], the Two-Layer wall function approach of Balaras et al. [8], the Detached Eddy Simulation (DES) of Spalart et al. [172], Very-Large Eddy Simulation (VLES) of Speziale [176], the Limited-Numerical Scales (LNS) of Batten et al. [12], the Partially Integrated Transport Model (PITM) of Chaouat and Schiestel [20], the Two-Velocities hybrid method of Uribe et al. [192] among others.

1.2.2 Direct Numerical Simulation (DNS)

The NSEs result in a complex behaviour of turbulence. Nonetheless, analytical solutions for these equations do not exist. But, numerical solutions of NSEs can provide a full characterization of turbulent motion. Those solutions are named as direct numerical simulations (DNS). DNS represents a research tool that simulates the NSEs, such that it precisely and entirely resolves all ranges of length and time scales for turbulence, with suitable initial and boundary conditions to an examined flow via a numerical grid which is applied in the absence of any modelling assumption.

A precise reproduction of turbulence evolution over a wide range of length and time scales demands numerical solutions in the direct simulation of turbulence. The scope of these scales that should be precisely simulated in the calculation is determined by physics. For example, the smallest length in homogeneous turbulence is the Kolmogorov length scale $\eta \equiv (\nu^3/\epsilon)^{1/4}$. It was shown by Yeung and Pope [208] that the valid resolution of the smallest scales requires $\kappa_{max}\eta \geq 1.5$, and the comparable grid spacing in physical space is $\frac{\Delta_x}{\eta} \approx 2.1$. The solution domain should have the size of the same order of the largest eddies. Since turbulence is three-dimensional, the required number of grid points to resolve this cube corresponds to $Re^{9/4}$ for homogeneous turbulence. The requisited number of grid points to discretize wall turbulence is in proportion to Re_τ^3, since smallest structures are characterized by the *viscous length scale* $\delta_\nu = \frac{\nu}{u_\tau}$ within a near wall layer, in which u_τ refers to *friction velocity*, whereas the geometrical length scale δ determines the size of large eddies of the flow. δ represents the channel half-height or boundary layer thickness and $Re_\tau \equiv \frac{u_\tau \delta}{\nu} = \frac{\delta}{\delta_\nu}$ is the *friction Reynolds number*.

The error in Direct Numerical Simulation (DNS) results from the utilized numerical method. In fact, aliasing is the more critical source of error. Kim et al. [87] demonstrated how aliasing error can cause turbulence decay in the computation of turbulent flows. Further, numerical instability can ensue from aliasing error as found by Zang [210], Kravchenko and Moin [2], and Blaisdell et al [15]. In DNS, a wide range of time scales are handled by using time advancement algorithms with a small time step. Time accuracy in DNS requires small time step Δt. The courant number condition restricts the time step Δt; the solution should advanced over just a portion of the grid spacing Δx within Δt. The Fourier representation of functions means the representation of such functions in terms of Fourier modes (e.g. finite number of basis functions), which implies that the artificial periodic boundary conditions must be imposed on the solution over statistically homogeneous directions. This approach works very well for incompressible flow [87].

In spite of DNS contributions in supplying dependable databases to confirm the hypothesises which are applied in turbulent models [100], providing knowledge which is intractable via experiments [3], and in examining suggested control strategies [34], from a computer power requirement point of view, the actual complex engineering applications are unavailable by DNS in the remote future.

1.2.3 Large-Eddy Simulation (LES)

In LES approach, at large energy-containing scales the detailed space and time reliance of the flow are simulated, while the impacts of transferring the momentum and energy to the small scales must be modelled. For review see Lesieur and Metais [103] and Moin [125]. It is obvious that the LES approach is introduced based on two related justifications. First, in terms of computational cost, just the large-scale of motions are resolved. A large majority of modes are in the dissipative range in a fully resolved DNS for instance. Consequently, the resolution requirements in the dissipation range are reduced in LES. From a modelling point of view, second justification stems from the Kolmogorov hypothesis which proposes that the large scales are anisotropic and influenced by the boundary conditions generating the turbulence, while, in the inertial and dissipative range the small scales display a quasi-universal behaviour with weak control by the large scales. Hence, it can be parametrized by the rate of energy transfer inside the cascade [145].

The contributions of LES to turbulence research over the past 40 years have been spectacular, for instance, in modelling the unresolved processes, precise numerical techniques on structured and unstructured grids, detailed comparison of LES calculations with DNS and empirical data in canonical flows [146]. Numerous developments have been made starting with early works of Smagorinsky [169], Lilly [109], Deardorff [39], Schumann [163], among others. Precise results have been gained about mass, momentum and energy transport issues in shear-free boundary layers at high Reynolds numbers since these quantities and the rate-controlling procedures are decided by the resolved large scales [146]. On the other hand, in wall-bounded turbulent flows the LES predictions can be expected to have a first-order reliance on those rate-controlling models [21].

In LES, the turbulent field decomposes to large (resolved) and small (unresolved) scales fields of turbulence, which are explicitly calculated and modelled, respectively, by filtering the equations of motion. The small scales are coarse grained via a filtering process, so that degrees of freedom in the system are minimized. In fact, the numerical modelling of turbulence needs a large number of degrees of freedom to resolve up to the subgrid scales which holds the molecular dissipation for the turbulent energy. Modelling the small scales/ subgrid scales (SGS), in the case of very large Reynolds numbers, commonly depend on the proposition that an inertial subrange of scales exists in which the energy is transported locally from scale to scale in wavenumber space, and regardless of the viscous dissipation. Consequently, LES simulates the large energy containing motions. Meanwhile the dissipative motions are modelled.

The spatial low-pass filtering operation with Δ as a characteristic width is given as

$$\widetilde{f}(\mathbf{x}) = \int G_\Delta(\mathbf{x} - \mathbf{y}) f(\mathbf{y}) d\mathbf{y}, \tag{1.8}$$

where G_Δ is a filter kernel at a length scale Δ. Then in LES $\mathbf{u}$, θ and p are decomposed to the large and small scale variables

$$\mathbf{u} = \widetilde{\mathbf{u}} + \mathbf{u}', \quad \theta = \widetilde{\theta} + \theta', \tag{1.9}$$

and

$$p = p + p'. \tag{1.10}$$

16

where the tilde indicates the filtered (or large-scale/ resolved) part and the prime indicates the residual (or subgrid-scale/ unresolved, SGS) part of the flow field variables. Applying this filter to Eqs. 1.5, 1.6 and 1.7 results in new sets of equations named as filtered NSEs or momentum equations, and scalar transport equations which describe the evolution of the large scales motions:

$$\partial_t \widetilde{u}_i + \widetilde{u}_j \partial_j \widetilde{u}_i = -\partial_i \widetilde{p} + \nu \partial_{jj}^2 \widetilde{u}_i - \partial_j \tau_{ij}, \tag{1.11}$$

$$\partial_t \widetilde{\theta} + \widetilde{u}_i \partial_i \widetilde{\theta} = \kappa \partial_{ii}^2 \widetilde{\theta} - \partial_i \tau_i^\theta, \tag{1.12}$$

$$\partial_i \widetilde{u}_i = 0. \tag{1.13}$$

Filtering results in unclosed terms which are unable to get from filtered NSEs, and thus modelling as a function of resolved quantities is needed. These unclosed terms are the unresolved momentum and scalar fluxes terms, named *subgrid-scale* (SGS) stress, or *residual* stress τ_{ij} and the *subgrid-scale* scalar flux τ_i^θ. These quantities are defined by

$$\tau_{ij} = \widetilde{u_i u_j} - \widetilde{u}_i \widetilde{u}_j, \tag{1.14}$$

$$\tau_i^\theta = \widetilde{u_i \theta} - \widetilde{u}_i \widetilde{\theta}. \tag{1.15}$$

See, e.g. Piomelli et al. [140] and Meneveau & Katz [116] for recent reviews of LES.

These terms reflect the influence of the SGS scales on the dynamic of the resolved ones, which indicates the correlations of SGS motions. The effects of SGS stress model on the resolved scales could be studied by looking into the transport equation for the resolved energy $\widetilde{\vartheta}^2 = \widetilde{u}_i \widetilde{u}_i$,

$$\partial_t \widetilde{\vartheta}^2 + \partial_j \widetilde{\vartheta}^2 \widetilde{u}_j = \partial_j \left(-2\widetilde{p}\widetilde{u}_j - 2\widetilde{u}_i \tau_{ij} + \nu \partial_j \widetilde{\vartheta}^2 \right) - 2\nu \partial_j \widetilde{u}_j \partial_j \widetilde{u}_j + 2\tau_{ij} \widetilde{S}_{ij}, \tag{1.16}$$

in which $\widetilde{S}_{ij}$ is the resolved strain-rate tensor

$$\widetilde{S}_{ij} = 1/2(\partial_j \widetilde{u}_i + \partial_i \widetilde{u}_j). \tag{1.17}$$

The $\tau_{ij}\widetilde{S}_{ij}$ term in Eq. 1.16 represents the cascade (flux) of kinetic energy from resolved towards unresolved motions. When it is negative, forward cascade is implied, whereas if it is positive, energy releases to the resolved ones (backscattering). The term is known as the SGS dissipation rate. Meneveau and Katz [116] showed that the most significant statistical feature of τ_{ij} and τ_i^θ is their influence on the mean kinetic energy and scalar-variance budgets of the large scale motions, in which their main impact is via the kinetic energy and scalar-variance dissipations that grows from interactions between large and small motions. The SGS dissipation is of major importance for it can be employed to investigate the hypothesis of specific LES models. The predicted subgrid scale dissipation and the empirically measured value are used to evaluate the existing model coefficients (see O'Neil and Meneveau [132], Kang and Meneveau [79] for reviews).

In LES of turbulence, the subgrid-scale models that are generally applied are classified into three sets: first, the eddy viscosity models or eddy diffusivity models, second, the similarity models, and, third, the eddy viscosity/ diffusivity model combined with similarity model expressions which are referred to as mixed models. In LES for turbulence, the parametrization in subgrid-scale models must be in terms of the resolved variables, for instance, in terms of large-scale velocity gradient tensor, the filtered vorticity vector $\widetilde{\omega}_i$ ($\widetilde{\omega}_i = \varepsilon_{ijk}\partial \tilde{u}_k/\partial x_j$), and the filtered strain-rate tensor $\widetilde{S}_{ij}$. Eq. 1.14 shows that, we may define

$$k_r = \frac{1}{2}\tau_{ii}, \tag{1.18}$$

where k_r is the *SGS kinetic energy*, and define

$$\tau_{ij}^r = \tau_{ij} - \frac{2}{3}k_r\delta_{ij}, \tag{1.19}$$

as the *anisotropic SGS-stress tensor*. Smagorinsky [169] achieved closure by modelling τ_{ij}^r, in which the eddy viscosity coefficient model is utilized. According to eddy-viscosity model the deviatoric part of the SGS stress tensor is proportional to the rate of strain tensor $\widetilde{S}_{ij}$ by establishing a turbulent viscosity of the SGS motions, ν_r, which works as a proportionality coefficient,

$$\tau_{ij} - \frac{1}{3}\tau_{kk}\delta_{ij} = -2\nu_r\widetilde{S}_{ij}. \tag{1.20}$$

Turbulent viscosity ν_r is modelled as

$$\nu_r = (C_S\Delta)^2|\widetilde{S}|. \tag{1.21}$$

where C_S is the Smagorinsky constant, and $|\widetilde{S}|$ is the characteristic filtered rate of strain, which could be written as

$$|\widetilde{S}| = (2\widetilde{S}_{ij}\widetilde{S}_{ij})^{1/2}. \tag{1.22}$$

Here, Δ is the characteristic SGS length scale (LES mesh size). The SGS stress and filtered rate of strain are related through the linear eddy-viscosity model based on the assumption that they are completely aligned. However, Tao, Katz and Meneveau [185] showed that the eigenvectors for SGS stress tensors and the strain-rate cannot be parallel to each other, where an assessment of the alignment was done via holographic particle image velocimetry used to quantify the three-dimensional velocity distributions. In addition, Clark, Ferziger and Reynolds [30] have shown that the correlation coefficient between the exact and the modelled SGS stress tensor τ_{ij} using the Smagorinsky model in general is low, being approximately 0.2. C_S values that have been used are in the range $0.1 - 0.2$. For instance $C_S \approx 0.18$ has been derived in Lilly [109] as a hypothetical value of the Smagorinsky constant for the case of freely decaying isotropic turbulent flow. Because $\nu_r > 0$, all eddy-viscosity models including Smagorinsky model [169] have yielded unconditionally dissipative models. Consequently, they fail to account for backscattering of energy from SGS scales to resolved scales which is locally seen in the Kolmogorov cascade. That results in imprecise prediction of the turbulent evolution (see Piomelli [140] for review).

A more intricate issue with assuming C_S to be constant in laminar and wall-bounded flows is that the SGS viscosity predominates the molecular viscosity, i.e., the eddy viscosity does not disappear, so the model always dissipates small fluctuations. The necessary asymptotic near-wall decay of $\nu_r \propto y^{+3}$ is not reproduced with a constant value of C_S in the case of wall-bounded flows, where $y^+ = \frac{u_\tau y}{\nu}$ refers to the distance to the wall in wall units. This problem was circumvented by using the damping function to reduce Smagorinsky constant value as it is closer to the wall [193]. For the purpose of employing an established constant in the Smagorinsky model, in the dynamic model introduced by Germano et al. [58], the SGS stresses are assessed at two filter scales. The filter width and the grid size in the LES filter are equivalent, while the width of test filter is twice of the first filter width. Both SGS stresses tensors at the two scales are represented using same model. As such, the Smagorinsky constant is adaptively computed as the simulation advances in time. Dynamic models reproduce the behaviour in which C_S tends towards zero as it is close to the wall. Also it addressed the backscattering in the Kolmogorov cascade by allowing negative values of C_S, although it causes more unstable simulations. Averaging and limiters have been proposed so the Smagorinsky constant do not vary too unpredictably (see e.g. Piomelli and Liu [141] and Meneveau et al. [115] for reviews).

On employing the large-scale velocities, $\widetilde{u}_i$, the SGS primitive velocities are directly modelled in the scale-similarity model of Bardina [10], such that modelled SGS stress tensor reads

$$\tau_{ij} \simeq \widetilde{\widetilde{u}_i \widetilde{u}_j} - \widetilde{\widetilde{u}}_i \widetilde{\widetilde{u}}_j. \tag{1.23}$$

This model showed a very large correlation with the real SGS stress τ_{ij} compared with the SGS eddy viscosity model (see e.g. Clark et al. [30] and Piomelli [142]). The Smagorinsky model has a low correlation coefficient (with a value being approximately 0.2) when DNS data were used in order to assess its accuracy [30]. However, the SGS eddy viscosity model has a much better agreement when the correlation of the SGS production term $P = -\tau_{ij}\widetilde{S}_{ij}$ was calculated with correlation coefficient being 0.6, as it was confirmed by Clark et al. [30]; Liu, Meneveau and Katz [111]; Piomelli [142] and others.

In the nonlinear model the Taylor's expansion was used such that the scale-similarity SGS stress tensor in Eq. 1.23 becomes

$$\tau_{ij} \simeq \frac{\Delta^2}{12} \partial_k \widetilde{u}_i \partial_k \widetilde{u}_j. \tag{1.24}$$

This model gives an excellent prediction of the SGS stresses compared with the Smagorinsky model (see Clark et al. [30] and Liu et al. [111] for reviews). Preferential alignment between the stress eigenvectors of the nonlinear model in the same orientation as those for measured ones has been reported by Tao et al. [186].

The subgrid-scale flux τ_i^θ is modelled by investing an the eddy diffusivity approach (see Moin et al. [124] and Pierce et al. [139]) as follows:

$$\tau_i^\theta = -\Delta^2 C_S^2 Sc_{sgs}^{-1} |\widetilde{S}| \partial_i \widetilde{\theta}. \tag{1.25}$$

Here, C_S is the Smagorinsky constant which can be specified a priori or obtained dynamically by Germano identity, and $C_S^2 Sc_{sgs}^{-1}$ refers to the lumped coefficient that involves C_S with the SGS Schmidt number Sc_{sgs} (see Germano [58], Lilly [110] and [179] for reviews). Improved results were obtained with dynamic determination of C_S in comparison with using constant values of

C_S. Chumakov [27] displayed that the main fault in this model is supposing that the SGS scalar flux aligns well with the gradient of the resolved scalar based on the molecular analogy. However, dynamic determination of C_S does not remove such fault. Corrsin et al. [31] criticized this assumption, among others.

The scale-similarity model for Bardina et al. [9] reads

$$\tau_i^\theta \approx -C_{SS}L_i^\theta, \quad L_i^\theta = \widehat{\widetilde{u_i}\widetilde{\theta}} - \hat{\widetilde{u}}_i\hat{\widetilde{\theta}}, \tag{1.26}$$

which shows a much better prediction, where L_i^θ is the Leonard term and it is acquired via a test filter, in which the LES base-filtered flow subject to such filter with a characteristic length $\hat{\Delta} > \Delta$. C_{SS} is the scaling constant provided by the user. The Clark model has been carried out as the first term in the Taylor series expansion for τ_i^θ as follows:

$$\tau_i^\theta \approx C_C\Delta^2\partial_j\widetilde{u}_i\partial_j\widetilde{\theta}. \tag{1.27}$$

In a priori tests it has a perfect prediction [30]. Leonard [102] proved that it blows up in computations. This could be attributed to the fact that it produces efficient negative diffusion. The blow-up issue is addressed by adding eddy viscosity term Eq. 1.25 to the model which results in a mixed model [68]

$$\tau_i^\theta \approx C_C\Delta^2\partial_j\widetilde{u}_i\partial_j\widetilde{\theta} - (C_S\Delta)^2|\widetilde{S}|\partial_i\widetilde{\theta}. \tag{1.28}$$

where the value of C_C is assumed to be 1/12, and C_S is determined via Germano identity. The dynamic structure (DS) model has been derived by Chumakov [22] and Rutland [26] as follows:

$$\tau_i^\theta \approx \frac{\phi}{\Phi}L_i^\theta, \tag{1.29}$$

where $\phi = \widetilde{\theta\theta} - \widetilde{\theta}\widetilde{\theta}$ represents the SGS scalar variance, $\Phi = \widehat{\widetilde{\theta}\widetilde{\theta}} - \hat{\widetilde{\theta}}\hat{\widetilde{\theta}}$, and L_i^θ is the Leonard term. The model might be considered as a scale-similarity model accompanied by special scaling coefficient or it be could derived from dynamic technique by means of Germano identity.

For further details about additional formulations to the SGS stress model see e.g. the scale similarity model by Bardina et al. [9], the mixed scale model by Sagaut [159], the approximate deconvolution model by Stolz and Adams [180], and models including the resolution of a transport equation for the SGS energy by Schumann [163] or Yoshizawa [209] among others. Note that the dynamic technique of Germano et al. [58] has been connected with some of such models to calculate the constants engaged in them. Improvement in measuring methods with increasing in the computational power has encouraged a priori testing to the SGS models. Especially, the promise of SGS models is often based on the model capability to match the topological aspects of the modelled quantities, for instance, the eigenvalue configuration [26], alignment trends in terms of resolved flow structures like vorticity, scalar gradient, and principal strain directions. For some of the insights into the scale and geometry relationships in the filtered turbulence see e.g. Tsinober et al. [191], Vincent and Meneguzzi [197], Lund & Rogers, and Tao et al. [184] & [185] among others. The relevant data to explore and to demonstrate the misalignment of principal axes to the SGS stresses τ_{ij} and the strain rate tensor $\widetilde{S_{ij}}$ have been reviewed by Horiuti [70] via using DNS, and through experimental data by Tao et al. [186] and by Kang and Meneveau [81].

1.2.4   Reynolds Averaged Navier-Stokes (RANS)

Reynolds [152] first derived the govern equation of the mean velocity field $\bar{\mathbf{u}}$, in which the full velocity $\mathbf{u}$ was decomposed according to Reynolds decomposition into its fluctuating and mean components $\mathbf{u} = \mathbf{u}' + \bar{\mathbf{u}}$, where $\mathbf{u}'$ indicates fluctuating component and $\bar{\mathbf{u}}$ indicates the mean/averaged component. Labourasse and Sagaut [97] defined the RANS averaging operator by

$$\bar{\mathbf{u}} = \frac{1}{N} \sum_{j \in \Omega} \mathbf{u}_{(\mathbf{j})}. \tag{1.30}$$

The operator is a ensemble average on a samples set Ω, which is named as Reynolds averaging, in which N represents the samples number in the set Ω and $\mathbf{u}_{(\mathbf{j})}$ refers to realization j of the sample [72]. The exact solution $\mathbf{u}$ of the NSEs has been subjected to such an averaging operator in order to simulate only averaged quantities with the aim to minimize the complication of the system to be simulated. In RANS, the dominant equations on the evolution of the averaged quantities $\bar{\mathbf{u}}$ and $\bar{p}$, are resulted from applying the RANS separation operator to the NSEs 1.5 and 1.6, so the mean momentum equation or Reynolds equations reads

$$\partial_t \bar{u}_i + \bar{u}_j \partial_j \bar{u}_i = -\partial_i \bar{p} + \nu \partial_{jj}^2 \bar{u}_i - \partial_j \overline{u'_i u'_j} = -\partial_i \bar{p} + \nu \partial_{jj}^2 \bar{u}_i + \partial_j \tau_{ij}, \tag{1.31}$$

$$\partial_i \bar{u}_i = 0, \tag{1.32}$$

where $\tau_{ij} = -\overline{u'_i u'_j} = -(\overline{u_i u_j} - \bar{u}_i \bar{u}_j)$. It is the *Reynolds stresses* tensor in the RANS approach, in which the impact of the fluctuating velocities is represented. Such a set of unclosed equations are unable to solve except if the Reynolds stresses $\overline{u'_i u'_j}$ could be modelled. In turbulent-viscosity models, the anisotropic part of the Reynolds stresses is often assumed to be proportional to the mean rate of strain tensor $\bar{S}_{ij}$ via a simple eddy/turbulent viscosity ν_t

$$\overline{u'_i u'_j} - \frac{1}{3} \overline{u'_k u'_k} \delta_{ij} = -2\nu_t \bar{S}_{ij}. \tag{1.33}$$

The specification of turbulent viscosity ν_t solves the closure problem in Eq. 1.31. This means the length and time turbulent scales for the turbulent mixing operation must be calculated. The eddy viscosity models include one equation models, where usually the turbulent kinetic energy is solved (see Prandtl's one-equation model [61], Baldwin-Barth model [203], and Spalart-Allmaras model [33] for reviews), and two equation models, where the turbulent kinetic energy k is the most often transported variables, whereas the second transported variable could be the turbulent dissipation, ϵ, or the specific turbulence dissipation rate, ω based on the type of two-equation model. The k-ϵ and the k-ω models have commonly applied in industrial frameworks and in engineering issues (see Refs. [18], [202], and [44] among other). In general, the supposition that the Reynolds stresses are locally specified by the mean rate of strain tensor has been proved invalid [145]. In fact, turbulent structures are generated by the history of straining they experience, among others. Therefore the Reynolds stress has also been modelled [99] by solving modelled transport equations. As there is no need to use the eddy viscosity, in Eq. 1.33, therefore the empiricism that are present in eddy viscosity models is not present (see e.g. Refs. [204], [47], [120], [119] and [147] for reviews).

Note that usually, the goal of RANS models is to simulate the flow outside the viscous sublayer in which the viscous impacts are negligible in comparison with inertial impacts. So it coupled with the *wall function* technique to simulate wall-bounded flows, where a log-law approximation is used to predict the velocity within a near-wall region with the assumption that the flow is at equilibrium. Practically, for non-equilibrium flows with acceleration, separation or rotation, the log-law approximation is invalid [201]. Thus, the existing high-Reynolds number models are modified to consider the near-wall impacts in a better way; low-Reynolds number versions of such modes have been derived. For instance, the Launder and Sharma model [98], where the Van Driest damping function [193] has been used in order to solve the equations down to the wall via an adaptation of the original model of Jones and Launder [75]. In 1991 Durbin obtained the Elliptic relaxation models [43], in order to take into account the wall impacts via modelling the non-local influences caused by walls.

RANS and LES models must have a grid spacing comparable to the integral length scale in order to get isotropic small scales ([5] and [153]), which means they have identical resolution requirements theoretically. Practically, RANS has a cheapest computation cost. Consequently, these models have been shown to be very successful in industry. However, the empirical principle of the RANS models results in inaccurate models to predict a real new complex flows, while a finely resolved LES could supply very correct predictions for complex three-dimensional non-equilibrium flows apart from walls. For a review of RANS engineering applications and its future contribution in CFD techniques see e.g. [136] and [66], respectively.

1.2.5   Hybrid RANS-LES

Hybrid RANS-LES is a more recent alternative strategy incorporated RANS and LES. The justification for Hybrid RANS-LES arise from the earlier outlined limitations, which were firstly an excessively high cost of LES for simulated wall-bounded flows at large Reynolds numbers, while the thin attached boundary layer flows is well simulated by RANS models. Secondly, in contrast to RANS empirical modelling hypotheses which restraint its precision in complex cases, the preferable scheme for complex non-equilibrium flows away from walls is LES models. The main aim of Hybrid RANS-LES is to build a bridge over the gap between them by decreasing computational cost of LES models and increasing the accuracy and applicability range of RANS models at the same time.

A big body of Hybrid RANS-LES techniques have been introduced since 1990s. Over the past two decades, in tracing the Hybrid RANS-LES methods progression, the complication of reconciling the RANS and the LES representations of turbulence has been confirmed by the continuous efforts (see e.g. Semi-Deterministic Model (SDM) of Kourta and Minh [122], the Two-Layer wall function approach of Balaras et al. [8], the Detached Eddy Simulation (DES) of Spalart et al. [172], the Partially Integrated Transport Model (PITM) of Chaouat and Schiestel [20] or the Two-Velocities hybrid method of Uribe et al. [192] for reviews among many others). The DES of Spalart et al. [172] has proven to be the easiest method to be used and execute. It is the most common model used among CFD users. This method is centred on the strategies that RANS and LES have to use a single grid, and that one solves the same group of equations on the full flow. The model was actually proposed for separated flows where the quick formation of turbulent eddies is due to intense instabilities. However, the enhancement of the formation of turbulent eddies needs a robust instability. In the thick boundary layers or comparatively low Reynolds number flows this factor is unavailable in comparison with the separated flows. This in turn generates a *grey area* around the interface between the RANS and the LES modes, where there is a low assistance from the RANS model to the Reynolds stresses and large eddies

are not either produced [130]. The conversion of the modelled turbulent kinetic energy of the RANS area into resolvable fluctuations for the LES area via using synthetic turbulence has been used to deal with this challenge (see Refs. [143], [36] and [85] for reviews)

In addition, synthetic turbulence could be used to handle the problem that arises from using the grid refinement to enhance LES mode within boundary layer in order, for example, to predict separation in the DES and the hybrid techniques [173]. It minimizes the empirical effects in the RANS area. The reduction of the grey area among the RANS and the LES modes requires generation of LES content prior reaching the separation, and after, as brief a growth length as possible. In the forcing technique of Keating et al. (2006) [85] an upstream RANS simulation and a downstream LES are coupled in order to supply a precise interface conditions for the hybrid simulation of turbulent boundary layer flows. It was found that the valid flow statistics are retrieved using synthetic turbulence [85].

1.3   Generation of Inflow Boundary Conditions

The specification of immediate turbulent inlet boundary conditions (BCs) is of great significance in a spatially developing flows simulation since the flow behaviour inside the domain is affected by the inflow data. Consistent inflow data at the inlet with the chosen turbulence model to be simulated are required. Generally, it is easy to force an analytical or empirical mean velocities and turbulent variables profiles in RANS simulations. However, the inflow should be turbulence in LES and DNS, so its design is not easy, which is in general restricted by available statistical information like the mean velocity or turbulent kinetic energy profile and the mean mass flow rate. In fact, a genuine inlet condition to the primary simulation should be prepared via the simulation of the upstream flow coming in the calculation range. But infinite extension for upstream calculation is unavailable. Consequently, it can not be applied to generate inflow conditions. For the sake of reducing the computational cost of LES and DNS of spatially evolving flows, and to minimize the impact of the approximate conditions on the flow within the domain, artificial inflow conditions should be as precise as possible. Accordingly, the transition region length should be as short as possible. In addition, for different flows under consideration, the inlet boundary conditions have different impacts on the downstream flow. Li et al. [106] mentioned that for free shear flows the role of inlet boundary conditions in downstream of the inlet is small in comparison with the inviscid instability that intensifies exponentially the small perturbations, in contrast to attached flows where the prescription of precise inflow conditions is required to quickly approach a turbulent situation in the downstream flow. The generation of the inflow boundary conditions for the DNS and LES has been done via a considerable variety of methods which would fall into two main groups: precursor simulation approaches where at the inlet some shape of turbulence are prior calculated and inserted to the domain, synthesis approaches where at the inlet some shape of random fluctuation is produced and incorporated with the mean flow. In addition controlling the evolution of the flow towards a pre-specified condition via combination of precursor simulation, synthesis and forcing methods has been examined by Keating et al. [84] and Tabor et al. [182].

1.3.1 Recycling Methods

One approach to obtain an appropriate inlet condition is to determine inflow data from a precursor simulation or rescaling of a database produced from it. For example, periodic boundary conditions in the mean flow direction could be used in the precursor simulation of a fully developed turbulence at the inlet of the master simulation like ducts, channels or pipes flows. Consequently, the flow is recycled at the outflow plane, and at the inlet it is reinserted, which allows the simulation to produce its inflow data. In a plane at a specific streamwise position of the precursor simulation, velocity fluctuations are extracted and specified as the inlet condition of the primary simulation in every time step.

Inflow conditions for LES of a backward-facing step and for LES of a plane diffuser are generated by such technique (see respectively Arnal [50] and Kaltenbach et al. [77]). Lund et al. [112] generated inlet conditions for a zero pressure gradient spatially developing boundary layer by using a more adaptable method where the velocity signal at the inlet plane is evaluated via using the velocity in a plane placed in the rescaling station. Planes of velocity data from this simulation are saved used and then used in the primary LES as inflow data. This developed version has been used to produce inlet data for a hydrofoil upstream of the trailing edge and for turbulent flow over a backward-facing step by Wang and Moin [198] and by Aider and Danet [1], respectively. The original technique of Lund et al. [112] has been extended to compressible turbulence by Sagaut et al. [161], where they added the rescaling and recycling of the pressure and temperature fluctuations to the process in the original method. However, high sensitivity in the initialization of the flow field in the Lunds technique was found by Ferrante and Elghobashi [48] in their DNS of spatially developing turbulent boundary layers. A more robust version was proposed by them via synthetic turbulence using a specified energy spectrum with the shear stress profile in order to initialize flow field.

To decrease the storage and the calculation expense from prior running of the precursor simulation ahead of primary simulation, Li et al. [106] suggested a different strategy. They simulated the spatially evolving turbulent mixing layer, which resulted from the crossing of a low- and high-speed boundary layer on the edge of a splitter plate. In their procedure, the boundary layer simulation was used to extract just a time series of instantaneous velocity planes with period roughly equivalent to the integral time scale of the flow which are stored on disk. Such strategy is used as an alternative of the precursor boundary layer simulations along with the mixing layer simulation. However, using this procedure for wall-bounded flows where destabilizing impacts are weak might need a lengthy transition zone in order to lower the periodicity included by the inflow [106]. Schluter et al. [164] proposed another technique to generate inflow data from a precursor simulation for LES or DNS, in which periodic boundary conditions or the recycling and rescaling method of Lund et al. [112] was used to create a database including instantaneous planes of velocity from a precursor LES. Then the database was used to extract the turbulent velocity fluctuations which are rescaled to have the desired statistics. Each database is particular for one geometry so it is not general, which represents the main obstacle in the methods depending on rescaling of databases.

1.3.2 Synthetic Turbulence

The need for suitable inlet data in order to use DNS or LES models has been discussed in the preceding section. This section highlights the usage of synthetic turbulence to produce inflow boundary conditions. Synthetic turbulence uses a stochastic procedure to synthesize inflow conditions, where a random velocity signal matched to turbulence is constructed.

1.3.2.1 Algebraic methods

In algebraic methods, synthetic fluctuations were obtained from a sets of random numbers. Transformation are applied to the numbers in order to match the desired statistics. Following the most simple style to generate synthetic fluctuations using this strategy, the inflow signal may be written in the form

$$u_i = U_i + r_i \sqrt{\frac{2}{3}k}, \tag{1.34}$$

where r_i is a random number, different for every velocity component at every point and at every time step, given by a normal distribution $\mathcal{N}(\mu = 1, \sigma^2 = 0)$. r_i is rescaled therefore the fluctuations possess turbulent kinetic energy k correctly. It is then gathered with a mean velocity profile $\mathbf{U}$. As a result, the target mean velocity and kinetic energy profiles are reproduced. However, it should be noted that the two-point and two-time correlations are equal to zero, also a cross-correlations among the velocity components are zero as well. When the Reynolds stress tensor exists, a signal would be reconstructed via the Cholesky decomposition a_{ij} of the Reynolds stress tensor R_{ij} [112], and we have

$$u_i = U_i + r_j a_{ij}, \tag{1.35}$$

which reproduces the desired cross-correlations although the two-point and two-time correlations are still unavailable [72]. The absence of large-scale predominance in the inflow data that are produced by the random technique is another drawback. In fact, more drawbacks were reported while using the above random procedures to generate the inlet conditions (see e.g. Refs. [112], [89], [60], [164] and [1]). More sophisticated methods have been proposed including Digital-filtering methods, Proper orthogonal decomposition methods (POD), and Synthetic Eddy Methods (SEM). We give a brief review below.

A very dynamic technique to create such turbulence is desired. A digital-filter-based production of pseudo turbulent inflow conditions is presented in Klein et al. (2003) [89] based on the fact that the shapes of correlation functions of typical turbulent shear flows are somewhat similar to the decaying exponentials. The specified integral length scales and Reynolds-stress-tensor are reached by an artificially produced turbulent inflows, in which the specified first and second order (one point) statistic and the autocorrelation functions are captured via inverse Fourier Transform. Klein et al. [89] have been used a digital filtering technique to address the last mentioned drawback. Supposing that the one dimension velocity signal $u'(i)$ at the point i is determined through a digital linear non-recursive filter

$$u'(i) = \sum_{j=-N}^{N} b_j r(i+j), \tag{1.36}$$

where b_j represents the filter coefficients, $r(i+j)$ is the random number created at point $(i+j)$ according to the a normal distribution $\mathcal{N}(\mu = 1, \sigma^2 = 0)$ and N is linked to the support of the filter. Consequently, the two-point correlation among points i and $(i+k)$ is given by

$$\langle u'(i)u'(i+k) \rangle = \sum_{j=-N+k}^{N} b_j b_{j-k}. \tag{1.37}$$

Choosing the filter coefficients b_j in accordance to the last equation would ensure the fluctuations produce precisely the required two-point correlations. In addition, due to a lack of the data of two-point autocorrelation tensor, Klein et al. [89] supposed that the Gaussian form of the filter coefficients relied on the lengthscale L, one single parameter. Thus the filter coefficients b_j would be analytically calculated without inverting Eq. 1.37. Such procedure allowed them to examine the impact of the length and time scales on the evolution of a plane jet and the primary break-up of a liquid jet. The digital filtering method of Klein et al. [89] with a periodically repeating construction have been used in [194] in order to produce inlet conditions for a channel flow. Due to that the different length-scales in the filtering process are allowed, the best agreement between reference LES and periodic boundary conditions was found.

Klein et al. [89] proposed a new method to examine the effects of the inflow conditions and the turbulence inside the nozzle on jet breakup, using the fact that the correlation function has a Gaussian shape for last-stage homogeneous turbulence. A two-dimensional slices of data organized at the axial direction with proper spatial correlations are achieved using a three-dimensional digital filter. In addition, it maintains the temporal correlations. Further, there is an equivalent between solving suitable diffusion equation for a set of three-dimensional random data by the procedure and applying a Gaussian function based filter for the same random data [86]. A digital filter depending on an arbitrary correlation function has been structured by di Mare et al. [113], in which such correlation function might take a Gaussian or an exponential forms, or even a forms obtained from experiments or precursor numerical simulation. An array of equations of the unknown filter and correlation coefficients are solved in this method. However, some drawbacks are outlined in [113]. The equations are conflicting; the solution is not unique and the guarantee that the equations could be solved for each correlation coefficient is unavailable. In order to handle these issues, locally defined spatio-temperal correlation functions are produced to satisfy the equations in a least squares, i.e., to minimize the residual.

The influence of using spatially various turbulence scales in the generation of inflow data is investigated by Veloudis et al. [195] using three-dimensional digital filter method. According to the mean and turbulent flow profiles, applying spatially varying scales results in better prediction for a channel flow, where the turbulence scale profile is divided into several regions in which they are constant. An inflow technique based on a particular inner- and outer-layer turbulence with related phase data is improved by Sandham et al. [162]. However, it could be applied only for high-resolution LES for the reason that it focuses on modelling the strips in the inner layer. The original Klein' s method [89] has been modified by Xie and Castro [206] in order to handle issues like Reynolds number dependence, among others. The modified version of Xie and Castro is more effective because it used an exponential correlation function to correlate the velocity on the two-dimensional inlet plane at current and previous time steps. In addition, correlation scales in all three directions are modelled. It should be noted that very important quantities like length scale, spectra, mean velocity and Reynolds stresses are estimated more or less satisfactorily in all digital filter depend techniques produce an artificial turbulence, so further progresses are needed.

The proper orthogonal decomposition method (POD) has also been used to generate inflow conditions, such as [The flow downstream of a half cylinder in terms of passive control [32], in-cylinder engine flow [42], the generation inlet conditions for channel flow [74], and turbulent jet in cross flow [121] among many others].

Another development is the construction of a synthetic velocity signal as a sum a limited number of eddies with random intensities and locations. The method is called Synthetic Eddy Method (SEM). In other words, the stochastic velocity signal is constructed depending on the decomposition of a turbulent flow field into stochastic coherent structures. The SEM technique was instituted to generate synthetic velocity fluctuations in such a way [71], that the mean velocity U_i, the Reynolds stress tensor R_{ij}, and the length scales σ_i are defined and computed as input data to the method. Next it should define a box that includes synthetic eddies as $B = [(-\sigma_i, \sigma_i), i = 1, 2, 3]$, σ_i represents the length scale in the ith direction. Then velocity signal generated by N eddies can be written as:

$$u_i'(\mathbf{x}) = \frac{1}{\sqrt{N}} \sum_{h=1}^{N} a_{ij} \varepsilon_j^h f_{\sigma(\mathbf{x})}(\mathbf{x} - \mathbf{x}^h). \tag{1.38}$$

where $\mathbf{x}^h$ and ε_j^h indicate the random position and a randomly produced intensity for each eddy in which $\varepsilon_j^h \in \{-1, 1\}$, respectively. The Cholesky decomposition of the Reynolds stress tensor is represented by a_{ij}. $\mathbf{x}$ refers to the location in the mesh and $\mathbf{x}^h$ refers to location of the eddy h, respectively. The velocity distribution of the eddy situated at $\mathbf{x}^h$ is given by the shape function $f_{\sigma(\mathbf{x})}(\mathbf{x} - \mathbf{x}^h)$

$$f_{\sigma(\mathbf{x})}(\mathbf{x} - \mathbf{x}^h) = \frac{\sqrt[3]{V_B}}{\sigma_{x_1}\sigma_{x_2}\sigma_{x_3}} \prod_{i=1}^{3} f(\frac{x_i - x_i^h}{\sigma_{x_i}}), \tag{1.39}$$

where V_B represents the volume of the box B [72]. Assuming that eddies are convected over the box with a reference velocity scale U_0, and the mean flow is caused by the advection of turbulence past a fixed point in accordance to the Taylor's frozen turbulence assumption, the new position for the eddy reads

$$x_i^h(t + dt) = x_i^h(t) + U_0 dt. \tag{1.40}$$

Note that, when the eddy comes to the end of the box $(x_i > \sigma)$, with a new random intensity the eddy at $x_i = -\sigma$ is regenerated at a random location in the two other direction. Sergent (2002) [167] suggested creation of ghost vortices at the boundaries in the specified region for applying periodic boundary conditions with the aim to correct the non-periodicity of the SEM signal, which could result from errors between the calculated and theoretical spectra. However, Keating et al. [84] mentioned that the periodic inflow data in the spanwise direction result in evolved turbulence without variation at the channel downstream of the inlet. On the other hand, the technique could be less transferable and difficult to implement if it is subject to a particular handling at the boundaries.

1.3.2.2 Spectral methods

The decomposition of the turbulent velocity signal in to Fourier modes in order to generate a synthetic flow field has been first used by Kraichnan [94] in order to examine the diffusion of a passive scalar, where the homogeneous and isotropic synthetic velocity field with three dimensions has been employed to initialize the flow domain. It is a well known fact that each periodic function,f, has a period of $2L$ could be written in terms of Fourier series as follows:

$$f(x) = \frac{a_0}{2} + \sum_{n=1}^{\infty}(a_n \cos(k_n x) + b_n \sin(k_n x)), \tag{1.41}$$

x refers to the spatial coordinate, and k_n refer to wavenumber which is defined as

$$k_n = \frac{n\pi}{L}. \tag{1.42}$$

The Fourier coefficients are defined by

$$a_n = \frac{1}{L}\int_{-L}^{L} f(x)\cos(k_n x)dx, \tag{1.43}$$

$$b_n = \frac{1}{L}\int_{-L}^{L} f(x)\sin(k_n x)dx. \tag{1.44}$$

Generation a synthetic turbulence with using Fourier decomposition has been modified by Batten et al. [12], in which the input parameters, mean velocity, Reynolds stress tensor, and dissipation rate have been used to specify the velocity signal. The fluctuations has been written as:

$$u_k'(x_j, t) = a_{ki}\sqrt{\frac{2}{N}}\sum_{n=1}^{N}[\alpha_i^n \cos(\hat{\gamma}_j^n \hat{x}_j + \omega^n \hat{t}) + \beta_i^n \sin(\hat{\gamma}_j^n \hat{x}_j + \omega^n \hat{t})], \tag{1.45}$$

a_{ki} represents the the Cholesky decomposition of the Reynold stress tensor, which works to guarantee turbulence anisotropy [112]. The full number of modes is referred to by N; α_i^n and β_i^n are amplitudes, the modified wave numbers is γ_j^n, the frequency is ω^n, and the spectral coordinates $\hat{x}_j$ and $\hat{t}$ are defined as:

$$\hat{x}_j = \frac{2\pi x_j}{L_t}, \quad \hat{t} = \frac{2\pi t}{\tau_t}, \tag{1.46}$$

where $L_t = \frac{k^{3/2}}{\epsilon}$ and $\tau_t = \frac{k}{\epsilon}$ represent the local turbulent length and time scales, respectively. k refers to the turbulent kinetic energy, and ϵ is the dissipation rate. The correlation in space and time is ensured via translation of the spatial and temporal variables. The frequency ω^n is taken from a Normal distribution $N(\mu, \sigma^2) = N(1, 1)$, while the wavenumbers $\hat{\gamma}_j^n$ is generated from the $N(\mu, \sigma^2) = N(0, 1/2)$. α_i^n and β_i^n amplitudes are calculated as:

$$\alpha_i^n = \varepsilon_{ijk}\eta_j^n \hat{\gamma}_k^n, \quad \beta_i^n = \varepsilon_{ijk}\xi_j^n \hat{\gamma}_k^n, \tag{1.47}$$

where ε_{ijk} represents the cross product named as Levi-Civita tensor, and the η_j^n and ξ_j^n values are obtained from $N(\mu, \sigma^2) = N(1, 1)$. In addition, the modified wavenumbers $\hat{\gamma}_j^n$ is given by

$$\hat{\gamma}_j^n = \gamma_j^n \frac{V_t}{C_n}, \tag{1.48}$$

here $V_t = \frac{L_t}{\tau_t}$ is referred to the turbulent velocity scale also C_n coefficient is calculated as:

$$C_n = \sqrt{\frac{3}{2} R_{lm} \frac{\gamma_l^n \gamma_m^n}{\gamma_k^n \gamma_k^n}} \tag{1.49}$$

where R_{lm} refer to the Reynolds stress tensor. Note that, the Cholesky decomposition of the Reynolds stress tensor, a_{ki}, is locally calculated in all cells because the Reynolds stress tensor is locally calculated in all cells. At all modes the variables are calculated, and at all modes at each time step the synthesised turbulent velocities are calculated.

In 1997, Le et al. [100] generalized the spectral method which has been suggested by Lee et al. (1992) [101] to generate the velocity fluctuations in which the reconstructed fluctuations capture the prescribed Reynolds stress tensor by rescaling the velocity fluctuations in accordance to Eq. 1.35. An inlet condition has been produced via this technique for a turbulent boundary layer upstream of a backward facing step. This synthetic procedure is also employed to determine inlet data to the LES domain, in which the precursor simulation uses to achieve the desired Reynolds shear stress profiles via a recycling technique of Lund et al. [112]. It was found that the friction coefficient has a best convergence in comparison with the case when synthetic turbulence was specified at the inlet without forcing.

The main issue with this method is that the inlet mesh is not homogeneous, so it is not possible to use a fast Fourier transform in the wall normal-direction, which results in a three-dimensional inverse Fourier transform with a high cost calculation in comparison with an initial suggestion of Lee et al. (1992) [101]. Nevertheless, it gives a considerably better results than those resulted from the random technique by Lund et al. [112], since the right statistics of the boundary layer can be recuperated via just 12 boundary layer thickness downstream of the inlet.

Furthermore, it must be mentioned that the structure and dynamics of turbulence rely on the phases of the Fourier modes in the Fourier representation. Consequently, Le et al. [100] needed an extended transition region in order to retrieve turbulence statistics because of the absence of structural information of the random phases. More advanced methods have been explored using phase randomization or amplitude randomization with the aim to minimize the length of this transition region, where the Fourier decomposition is calculated by precursor simulation (see Refs. [128], [65] and [29] for reviews). Despite that the signal is produced with correct turbulence statistics via phase randomization in the above mentioned methods, flow turbulent structures were badly regenerated. To decrease the transition length, the Taylor's hypothesis has been used by Na and Moin [128] in order to convect a frozen DNS field within the inlet plane of their simulation. In such way, amplitude factors of the Fourier coefficients were subjected to amplitude randomization, whereas their phase angles have been kept the same. Next to only three boundary layer thicknesses, right levels of friction coefficient are recovered. Same results have been found with similar approaches used by Chung and Sung [29] to generate inlet conditions for LES. Note that the computation of Fourier decomposition of the flow demands a precursor simulation in these approaches. If such simulation is unavailable such phase randomization or amplitude randomization ideas could be used to modify generation of synthetic turbulence methods [100] via new models which able to correlate phase angles between Fourier modes (see e.g. Le et al. [100], Sandham et al. [162], Terracol [188], Eggers and Grossmann [46] and Fung et al. [53] for reviews).

In a general industrial framework, Smirnov et al. [170] improved the technique of Le et al. [100] to synthesize a non-homogeneous turbulence. This method demands an explicit diagonalization of the Reynolds stress tensor R_{ij} instead of Cholesky decomposition in Eq. 1.35. Depending on local turbulent time and length scales, various spectra at various positions over the flow have been employed to calculate the Fourier coefficients with Fourier decomposition. In addition, a restricted number of modes have been taken randomly from the normal distribution. In 2004, Smirnov's formulation [170] has been adjusted by Batten et al. [12], in which it could explicitly define the velocity signal in terms of input parameters like a mean velocity U_i, Reynolds stress tensor R_{ij} and dissipation rate ϵ. Ultimately, the fluctuations are reconstructed in accordance to Eq. 1.35. Results show a reduced computational cost because a restricted number of modes have to be simulated. Also a non-homogeneous turbulence might be obtained via rescaling the spatial coordinate with local length scale and an interim coordinate with time scale.

1.3.2.3 Mixed methods

Most techniques designed for production of synthetic turbulence are already reviewed in terms of their performed processes in Fourier space or in physical space. In fact, some methods have performed operations in both spaces at the same time. These methods are termed as mixed methods. In this method, the isotropic turbulent fluctuations are produced at each time step following the same way in the premier method of Kraichnan [94], also does not based on the formerly produced signals. In this case, it was shown by Davidson [38] that the technique depending on the Fourier decomposition and digital filters to produce inlet conditions for LES and DNS can accomplished the Fourier transform using just two dimensions without randomization of the phase angles in order to breach the cyclicity of the signal as in the method of Le et al. [100].

However, similar to the method in [100], the synthesized turbulent field is homogeneous. Since correlations generated in the non-homogeneous directions could be destroyed via scaling of the fluctuations, so this scaling is not implemented. Consequently, the fluctuations are multiplied by a blending function thus the fluctuations adjacent to the wall also in the free stream are minimized. The hybrid RANS-LES method of Davidson and Billson [35] has been used with this method to generate inlet conditions for a diffuser flow and the flow over a curved wall in a square duct [38], and for a flow over a three-dimensional hill.

An additional mixed configuration has been proposed in order to mimic physical loadings regarding to an earthquakes, atmospheric turbulence or ocean waves. Glaze and Frankel (2003) [60] have used a spectral representation method which is depending on weighted amplitude wave (WAWS) where it is efficient to imitate a non-homogeneous, multidimensional, multivariate stochastic fields. They produced the inlet boundary conditions for the case of fully turbulent jet. Also spatial decay of isotropic turbulence was simulated using the same method by Kondo et al. (1997) [92]. For the reason to calculate the signal at all grid point, the summation through all inlet mesh nodes and simulated frequencies are included. The WAWS method has an identical computational cost in comparison with the digital filtering method of Klein et al. (2003) [89]. Furthermore, it uses a filtering process in physical space while in the frequency domain it uses a Fourier decomposition so it is addressed as a mixed method.

In 2006 [156], Rosales and Meneveau introduced a simple method to generate synthetic vector fields as representatives for turbulent velocity fields, the multiscale minimal Lagrangian map (MMLM) method applies the minimal Lagrangian map to deform an initial Gaussian field produced using random-phase Fourier modes. Fluid parcels moves with their constant velocity, in which the inter-parcel interactions are disregard, over a series of low-pass filtered fields for some scale-dependent time-interval. It is found that the non-Gaussian synthetic field displays a set of turbulence-like statistics and realistic geometric features, including skewnesses of velocity derivatives and longitudinal velocity increments at different scales, stretched exponential tails in the PDFs of the longitudinal and transverse velocity increments, the vortex stretching and the predominant self-amplification of the strain rate, and the alignment of the vorticity and the intermediate strain-rate eigenvector. From the point of view of inflow boundary conditions generation, the MMLM approach can be applied to produce a precomputed data base from which sequential planes are taken to supply the inlet velocities. Even though it might still require an adjustment zone, the zone is expected to be shorter than those requested by techniques employing synthetic turbulence in the absence of right phase information [156].

In a recently proposed Multiscale Turnover Lagrangian Map (MTLM) method [157], an initial random field is converted into a synthetic field after a series of simple mappings, with moderate computational cost. The procedure is based on the multiscale minimal Lagrangian map [156], in which the advection Lagrangian map time scale is considered but with the appropriate Kolmogorov inertial-range turnover time scale instead of the sweeping time scale used in the MMLM approach in order to produce anomalous exponents scaling properties. The resultant non-Gaussian synthetic field from the modified MTLM method captured realistic anomalous scaling exponents features like the intermittency and multifractal nature of the energy dissipation. Also it has proven that the derived pressure field from the MTLM velocity field has quite realistic features.

A new method, the constrained multi-scale turnover Lagrangian map (CMTLM) approach, was previously introduced by Li and Rosales [107]. They attempted to generalize the MTLM method to anisotropic turbulence, which is more relevant to practical applications. CMTLM procedure formulates the problem as an optimization problem using the adjoint formulation, in which the initial random field is taken as the control variable, and the additional features presented in inhomogeneous turbulence are taken as a target function to be matched by the synthetic fields. Two Kolmogorov flows were synthesized using the constrained MTLM approach, where, by Kolmogorov flows, we mean turbulent flows generated by constant large scale sinusoidal forces in a periodic box.

In comparison with the DNS data, the results show that mean flow statistics like the Reynolds stress distribution and mean turbulent kinetic energy balance are closely reproduced. Furthermore, distributions of mean SGS energy dissipation, and the alignment among the SGS stress tensor and the filtered strain rate tensor display the ability of the CMTLM method to reproduce the impacts s of inhomogeneity on small scale structures. In LES or in RANS equations, modelling the SGS stress or Reynolds stress is a main task. Such turbulent stress (Reynolds stress) tends to evolve towards a rod-like axisymmetric configuration as in the SGS stress, and it tends to be universal as well. These observations have been proven by Li (2015) [108]. In this work the CMTLM method has been used in order to generate realistic initial turbulent fields with any specified anisotropic Reynolds stress tensor to investigate the decaying process from initial turbulent fields with the aim to prove the universality.

1.3.3 Forcing Techniques

A recent progress has been using control methods to speed up evolution towards equilibrium turbulence, because a transition area downstream of the inlet is present from approximate inlet conditions before the equilibrium. In the control method of Spille and Kaltenbach [177], capturing a desired profile for the Reynolds shear stress via amplifying the wall-normal velocity fluctuations for a some number of control planes downstream of the inlet is an aim of the method. In this controlled-forcing approach, the momentum governing equation for RANS and LES of an incompressible reads

$$\partial_t \bar{u}_i + \bar{u}_j \partial_j \bar{u}_i = -\partial_i \bar{p} + \nu \partial_{jj}^2 \bar{u}_i - \partial_j \overline{u'_i u'_j} + f_i = -\partial_i \bar{p} + \nu \partial_{jj}^2 \bar{u}_i + \partial_j \tau_{ij} + f_i. \tag{1.50}$$

where the body force f_i dominate the flow at the wall-normal direction in the control zone. This term is appended to the wall-normal momentum equation in order to amplify the velocity fluctuations v' in this direction, so the production term in the shear-stress budget is enhanced. In fact, its aim is to enhance or damp local flow states like bursts and sweeps which contribute to the Reynolds shear stress $\langle u'v' \rangle$. The forcing amplitude is specified by a controller depending on the error in the Reynolds shear-stress as follows:

$$e(y,t) = \langle u'v' \rangle^*(x_o, y) - \langle u'v' \rangle^{z,t}(x_o, y, t), \tag{1.51}$$

where $\langle u'v' \rangle^*(x_o, y)$ refers to the target Reynolds shear stress at the control plane $x = x_o$, also $\langle u'v' \rangle^{z,t}(x_o, y, t)$ refers to the current Reynolds shear stress which is averaged over the spanwise direction and time. The force magnitude is given by

$$f(x_o, y, z, t) = r(y,t)[u(x_o, y, z, t) - \langle u \rangle^{z,t}(x_o, y)], \tag{1.52}$$

where f is connected to the error via

$$r(y,t) = \alpha e(y,t) + \beta \int_0^t e(y, t')dt'. \tag{1.53}$$

in which the integral part of the controller works to reduce the force response to very acute variation which might leads to unstable system. The constants α and β have been chosen to minimize the error quickly, without leading to unsteadiness (see Res. [177], [84] and [85] for reviews).

The matching of the target profile of Reynolds shear stress is done in forcing method by enhancing the wall-normal velocity fluctuations in a number of control planes downstream of the inlet [177]. The friction coefficient has a best convergence in comparison with the synthetic turbulence is specified at the inlet without forcing in the synthetic technique of Le et al. [100], where a precursor simulation was used to obtain target Reynolds shear stress profiles based on recycling procedure [112]. In a plane channel flow case, Keating et al. [84] utilized the forcing method of Spille and Kaltenbach [177] together with the inlet conditions produced from a technique of Batten et al. [12]. The shear stress profiles are somewhat quicker recapture when continuous forcing with two and four control planes are used. A precise interface conditions are achieved to couple between an upstream RANS and a downstream LES simulations in the hybrid simulation of turbulent boundary layer flows in zero, favourable and adverse pressure gradients. The RANS simulation is used to extract the desired shear stress profiles, so there is no need to use precursor

simulation. However, in comparison with the recycling method of Lund et al. [112], results for adverse pressure gradient case show some differences. The RANS solution and the LES inlet location affected the technique's precision significantly.

1.4   The Motivation, Objectives and the Outline of the Thesis

Synthetic turbulence has been helpful in supplying an appropriate structure for numerical experiments, different techniques have been modelled different features of turbulence in order to understand its mechanisms, for examples, modelling small-scale intermittency , SGS dissipation and interscale interactions and temporal correlation properties (see e. g. Refs. [76], [4], [165], [166], [53] and [54] for reviews). In addition, LES applications for more complex flows demads more advanced techniques of prescribing the turbulent features of the flow at inlet boundaries, the generation initial and inlet boundary conditions for numerical simulations has been done via synthetic turbulence. The generation of an artificial inflow velocity profiles that must catch the fundamental aspects of the flow is useful in the cases with non-periodic boundary conditions due to flow geometry or when subsidiary simulation is unavailable. One advantage of synthetic turbulence generation methods is that it handled both a lack of generality and a heavy computational cost in the same time, which is in contrary to other methods. However only simple estimation of real turbulence has been represented via synthesized turbulence so far. The mechanism demonstrated above still do not reproduced any higher order statistics, for instance, the dissipation rate and the pressure-strain terms in the Reynolds stresses budget. Actually, it built on the implicit hypothesis that the creation of low order statistics like turbulent kinetic energy, mean velocity, Reynolds stresses also the two-point and two-time correlations might leads to good approximations of the turbulent flow including higher order statistics.

When current synthetic turbulence models are used as inlet conditions [[105, 16, 170, 12, 37, 101, 100, 78, 89, 113, 88]], a significant transition region within the the computational domain is needed. Therefore further refinement is needed. Realistic synthetic isotropic turbulent fields have been generated using novel methods based on MMLM and MTLM maps [156] and [157]. Multi-scaling characteristics of small scale turbulence, characteristics regarding to small-scale geometrical structures, and pressure statistics are accurately reproduced. In time evolving problems, more realistic time evolution is found when non-Gaussian fields are employed as initial conditions in DNS and LES. For stationary problems, the initial adjustment period would be remarkably shortened [156]. MTLM synthetic scalar field has high-order statistics consistent with the ones noted in real hydrodynamic turbulence. It is found that the MTLM procedure can produce the anomalous scaling for several type of structure functions of real turbulence. The spatial structure and the kinetic energy of the scalar field are quite realistic, also the dissipation fields for the scalar variance have several quite realistic features, as well as the geometric statistics [158]. In addition, investigation about the pressure field related with the velocity field have been done [25]. As a consequence, this thesis has focused on investigating the properties of the synthetic field generated by MTLM and constrained MTLM.

The overarching good of this thesis is to investigate the applications of MTLM and CMTLM in more realistic flows. Specifically, we consider the MTLM and/or CMTLM models for scalar fields with a linear mean profile, velocity in channel flows, and SGS motions, which are discussed in chapter 2, chapter 3, and chapter 5, respectively. In the process, we recognize that a better understanding of the MTLM and CMTLM maps is required, which leads to the investigation summarized in chapter 4.

The thesis is organized as follows:

In chapter 2, our target is to study the MTLM synthetic velocity and scalar fields using the filtering approach. This approach, which has not been pursued so far, provides insights on the potential applications of the synthetic fields in large eddy simulations and subgrid-scale (SGS) modelling. The MTLM method is first generalized to model scalar fields produced by an imposed linear mean profile. We then calculate the subgrid-scale stress, SGS scalar flux, SGS scalar variance, as well as related quantities from the synthetic fields. Comparison has been done with DNS data. In addition, the sensitivity of the synthetic fields on the input spectra is assessed by using truncated spectra or model spectra as the input.

Li and Rosales [107] produced a novel technique to generate anisotropic synthetic turbulence, which is generalized from the MTLM procedure to model inhomogeneous turbulence and called CMTLM. Li and Rosales formulate the problem as an optimization problem. In this procedure the aim is to adjust the random input to the map so that the output contains the large scale anisotropic structure. It was applied to synthesize two Kolmogorov flows in which nontrivial mean flow statistics and local anisotropy in small scales are produced via persistent large scale structures. Comparing CMTLM synthetic fields with DNS data shows that the mean flow statistics like Reynolds stress distribution and mean turbulent kinetic energy balance are closely reproduced. Furthermore, the influences of inhomogeneity on small scale structures are also reproduced by the CMTLM synthetic fields.

The next step to generalize this method is to include the effects of the solid wall boundaries. In chapter 3, our aim is to derive a new optimality system in order to generate anisotropic synthetic turbulence by using the CMTLM approach to include such effects. We will consider the difference introduced by the solid wall, imposing the impermeable boundary condition where the normal components velocity field are zero, while the tangent components may be non-zero. Our purpose is to find the optimal control variable which minimizes the difference between the target function and the synthetic field where the desirable features presented in anisotropic turbulence field are taken as a target function. To accomplish this task, we will modify the CMTLM procedure. Then in accordance to the modified CMTLM procedure we will generate a reflectionally symmetric synthetic field in which that the symmetric field is a model of the velocity field in a fully developed channel flow. We prove that each operator of the MTLM procedure preserves the reflectional symmetries, derived the adjoint optimality system with reflectional symmetry. We finally consider the mean statistics of the CMTLM synthetic fields in comparison with the computed and experimental results data.

As the CMTLM method has been proposed only very recently, there are still many questions about the inner mechanism of the method. Therefore, in chapter 4, we take a step back, and look into some of the basic properties of CMTLM applied to simple flow field. Specifically, we aim to study the gradients of cost function and the adjoint field of the Constrained MTLM procedure which have not be fully examined in preceding works. We want to quantify the relative importance of the adjoint operator and to investigate the influences of the control variable on the cost function gradient. In other words, our goal is to find out how imposing a different cost function could affect the results, particularly with target from DNS data. So we consider again the CMTLM synthesized Kolmogorov flows that have been investigated in Li and Rosales [107], then we consider an arbitrary cost function and the corresponding synthetic fields. We compute contours of the mean gradients of the cost functions and the adjoint fields for the above three cases, as well as other statistical properties. The analysis sheds light on the how the CMTLM method works, and provides useful information for the further improvements of the method.

In chapter 5, we explore a new SGS modelling approach via incorporation between the LES of turbulence and the CMTLM method. As a first step to do that, we investigate a priori the viability of using CMTLM synthetic fields as SGS Models. To do so, we merge between the DNS data and CMTLM field. The SGS quantities are predicted using these merged fields, then compared with real SGS quantities computed from DNS field. A number of characteristics regarding the statistical geometry between the SGS and filtered quantities for real and predicted data are studied.

In chapter 6, conclusions, perspectives, and recommendations for future work are summarized.

In the appendix A, we reported the details of the transformation property of the MTLM procedure and the derivation of the adjoint system with reflectional symmetry of the CMTLM procedure. In addition, we review the pseudo-code for the numerical implementation of the CMTLM map in the appendix B.

Chapter 2

Subgrid-Scale Stresses and Scalar Fluxes Constructed by the Multi-Scale Turnover Lagrangian Map

2.1 Introduction

The transport and mixing of passive scalars by turbulent flows is a phenomenon of both practical and fundamental interests due to its wide applications[168, 199, 40]. The subject has attracted continuous interests; to name a few, we note recent efforts that have led to new insights into its scaling properties [63], its role in cloud formation [13], and its modelling. [150] One approach to understand and model the mechanisms of turbulent mixing is to use synthetic turbulence models.[53, 76, 88, 207, 196, 46, 69, 95, 23, 57, 51] Synthetic turbulence refers to stochastic fields that have characteristics of real hydrodynamic turbulent flows. This methodology aims to construct the field variables (such as velocity and scalar fields) by simpler processes, while reproducing the remarkable characteristics of turbulent fields. Synthetic fields can be generated with little computational cost. Yet, various synthetic models, with different levels of sophistication, have found a wide range of applications.

Many models have been proposed with the applications in large eddy simulations (LES) in mind. In LES, artificial field data are usually needed to initialize the calculation and/or provide the inflow boundary condition. Synthetic turbulence is one of the main methods used to meet this need[71, 73, 88, 207, 183, 84, 96]. These models have found wide applications in conjunction with LES. Nevertheless, the main aim of these methods has been matching the mean velocity profiles, the second order moments and the integral length scales. No significant effort has been devoted to modelling the nonlinear interactions in real turbulence in an efficient way, even though the latter has been identified as an important factor to make further improvement [84]. In one of the most popular methods, the synthetic eddy method (SEM), the synthetic field is composed of localized velocity fluctuations (the eddies). Arguably, the nonlinear interaction could be captured to some extent, since the eddies are allowed to evolve over a short time. Nevertheless, no systematic research has been reported on this aspect of the method, and results shown in [71] suggest that key nonlinear features of real turbulence are missing in SEM fields. Finally, it is worth noting that, apart from the above applications, synthetic models have also been used directly as a subgrid-scale (SGS) model in some simulations (see, e.g., [49]and [166] and references therein).

Other synthetic models have been proposed as a vehicle to study the fundamental mechanisms of real turbulence. For instance, particle dispersion has been studied by means of kinematic simulations [53, 133, 129], and multi-fractal models [76, 196, 46, 14, 137, 24] have been proposed to understand some aspects of real turbulence, in particular small scale intermittency. However, going beyond Gaussian models, it has proven no easy task to synthetic three-dimensional (3D) velocity fields with realistic statistical and structural characteristics of turbulence. A new procedure based on the multi-scale turnover Lagrangian map (MTLM) is proposed in [156] and [157]. The MTLM procedure builds a velocity field by distorting an initially random field via a non-linear map over a hierarchy of spatial scales. Results show that the procedure allows both the statistical and the structural properties of the velocity field as well as the pressure field in real turbulence are faithfully reproduced [157, 156, 25].

The MTLM procedure has been generalized to turbulent mixing[158] in the convective-inertial regime[187, 145, 199], in which the fluid particles carry a passive scalar. The mapping thus also distorts the scalar field recursively in a multi-scale fashion. Results show that the MTLM procedure allows the synthetic velocity field to establish the coherence among the particles transporting the scalar, leading to correct level of decorrelation over separation [158]. Numerical results show that the synthetic scalar fields have stronger intermittency in the dissipative and inertial ranges than its advecting velocity field, as is observed in real turbulent fields. Quantita-

tive agreement was found for high-order statistics, the scaling exponents for structure functions, and the characteristics of the dissipation fields. Finally, the spatial structure of the scalar field are also close to experimental results. As a result, the statistical geometry at dissipative scales that results from the conjunction of velocity and scalar gradients behaves in agreement with a real scalar turbulence[158].

The MTLM method has been used to investigate the closure for the pressure Hessian in the Lagrangian models for the velocity gradient [25], to synthesizing magnetic fields [181], and to study particle clustering [131]. Applications to inhomogeneous turbulence have also been explored[107, 108]. What is missing is the perspective of subgrid-scale (SGS) modelling. Such a perspective is crucial given the potential applications of the MTLM fields in LES, either as SGS models or initial/boundary conditions, in particular in the LES of, e.g., particle dispersion in atmospheric boundary layer, particulate flows and combustion. Thus, we present in this paper an *a priori* analysis of the filtered synthetic MTLM velocity and scalar fields, and the corresponding SGS stresses and SGS scalar fluxes. Specifically, we have three objectives. Firstly, to model a more realistic scalar field, we generalize the MTLM to the mixing of a passive scalar with a linear mean profile, following the suggestion in [158]. Secondly, we examine the statistics related to the SGS stresses, the SGS scalar flux, and related quantities. We aim to find out if the synthetic fields are able to capture the SGS energy and scalar dissipation correctly, and if they are able to capture the geometrical statistics of the SGS motions. We also examine if the synthetic scalar field captures the effects of the mean scalar profile, as documented in DNS studies by, e. g., [149]. Thirdly, we note that the MTLM procedure requires the energy spectrum (and, for MTLM with scalar advection, the scalar spectrum) as part of the input. A question is how the synthetic fields depend on the input spectra. We thus also perform analysis of MTLM fields obtained using modified spectra. The results of the above three objectives provide useful insights to the ability and robustness of the MTLM fields to model the SGS stress and flux, and other SGS processes.

In Section 2.2, we explain briefly the advection of a passive scalar by turbulent velocity fields. The proposed MTLM procedure is described in detail in Section 2.4. Section 2.6 reviews the key concepts in LES and SGS modelling. In Section 2.7, we consider the statistics of the filtered MTLM scalar and velocity fields, and those of the SGS stresses and fluxes, where the geometric alignment statistics of real and modelled stress tensors are also examined. The effects of modified spectra are also presented in Section 2.7. Conclusions are summarized in Section 2.8.

2.2   The advection of a passive scalar

The mixing of a passive scalar Θ is governed by the linear advection-diffusion equation

$$\partial_t\Theta + (\mathbf{u}\cdot\nabla)\Theta = \kappa\nabla^2\Theta + S(\mathbf{x},t). \tag{2.1}$$

In the above equation, the passive scalar Θ is mixed by a turbulent velocity field $\mathbf{u}(\mathbf{x},t)$, in the presence of a constant molecular diffusivity κ, and a source term $S(\mathbf{x},t)$. Θ could represent, e.g., the temperature perturbation in a flow field where the buoyancy force can be neglected.

The velocity field $\mathbf{u}$ is governed by the forced Navier-Stokes (NS) equation

$$\partial_t\mathbf{u} + \mathbf{u}\cdot\nabla\mathbf{u} = -\nabla p + \nu\nabla^2\mathbf{u} + \mathbf{f}, \tag{2.2}$$

and the continuity equation

$$\nabla\cdot\mathbf{u} = 0. \tag{2.3}$$

In Eq. 2.2, p is the pressure field, ν is the kinematic viscosity, and $\mathbf{f}$ is the external forcing term. $\rho = 1$ has been assumed.

The scalar field is advected by the velocity field, which squeezes and stretches the former. As a consequence, the characteristic length scale of a parcel of the scalar decreases and a scalar variance cascade is generated, accompanying the turbulent kinetic energy cascade. In the inertial range of homogeneous turbulence, the energy spectrum $E(k)$ is, according to the Kolmogorov phenomenology,

$$E(k) = C_K \langle \epsilon \rangle^{2/3} k^{-5/3}, \tag{2.4}$$

where $k \equiv |\mathbf{k}|$ is the magnitude of the wavenumber $\mathbf{k}$, and C_K is the Kolmogorov constant. The scalar cascade at a particular length scale is governed by the relevant straining time scale of the velocity field. Depending on the Schmidt number $Sc = \nu/\kappa$, three regimes can be identified [187, 145]. We consider only the case where $Sc \sim 1$. In this so-called inertial-convective regime, the dominant straining time scale for the scalar field is the local eddy turnover time scale, and the spectrum of scalar variance $E_\theta(k)$ is given by

$$E_\theta(k) = C_{OC} \langle \epsilon \rangle^{-1/3} \langle \epsilon_\theta \rangle k^{-5/3}, \tag{2.5}$$

where $\langle \epsilon_\theta \rangle = \kappa \langle |\nabla \theta|^2 \rangle$ is the mean dissipation of scalar variance, and C_{OC} is the Obukhov-Corrsin constant.

Scalar fluctuations have to be maintained by a source $S(\mathbf{x}, t)$. In this paper we consider fluctuations generated by a linear mean variation with respect to space. Thus, we may write

$$\Theta(\mathbf{x}, t) = \mathbf{G} \cdot \mathbf{x} + \theta(\mathbf{x}, t), \tag{2.6}$$

where $\theta(\mathbf{x}, t)$ is the scalar fluctuation, and $\mathbf{G}$ indicates the imposed uniform mean scalar gradient. As a result, the equation for θ is given by

$$\partial_t \theta + (\mathbf{u} \cdot \nabla)\theta = \kappa \nabla^2 \theta - \mathbf{G} \cdot \mathbf{u}(\mathbf{x}, t). \tag{2.7}$$

2.3 The MTLM map for the velocity field

Before we consider the MTLM map for a scalar field driven by a linear mean profile, we briefly summarize the MLTM map that was proposed in [156] and [157], which has been applied to synthesize turbulent velocity fields.

The MTLM map is motivated by the fact that the non-linear advection term in the NS equation captures the key physical mechanism by which the non-Gaussian statistics in real turbulence is generated. In the MTLM map, the effects of this term is modelled as an advection map. The advection map is then applied to a Gaussian field in a multi-scale fashion to model the multi-scale interactions in real turbulence.

Mathematically, the advection map is the solution of the Riemann equation

$$\partial_t \mathbf{u} + (\mathbf{u} \cdot \nabla)\mathbf{u} = 0, \tag{2.8}$$

which describes the evolution of non-interacting fluid particles. Eq. 2.8 is an approximation for high Re flows of rarefied gases [156]. The solution of the equation can be written as

$$\mathbf{u}(\mathbf{X}(t), t) = \mathbf{u}(\mathbf{y}), \tag{2.9}$$

where $\mathbf{X}(t)$ is the position of a fluid particle whose initial location is at point $\mathbf{y}$. Eq. 2.8 shows that $\mathbf{X}(t)$ is given by

$$\mathbf{X}(t) = \mathbf{y} + t\mathbf{u}(\mathbf{y}), \tag{2.10}$$

in which $\mathbf{u}(\mathbf{y})$ represents the initial velocity field. In deriving Eq. 2.10, we have used the fact that, according to Eq. 2.8, the velocity of a Lagrangian fluid particle is constant along the particle's path.

It is observed in [107] that the above solution can be written as an integral operator applied to the initial velocity field $\mathbf{u}(\mathbf{y})$. We will call it the advection operator or the advection map, and denote it by $\mathcal{A}^u$:

$$\mathbf{u}_t(\mathbf{x}) = \mathcal{A}^u \mathbf{u} = \int W(\mathbf{x} - \mathbf{y} - t\mathbf{u}(\mathbf{y}))\mathbf{u}(\mathbf{y})d^3\mathbf{y}, \tag{2.11}$$

where we use $\mathbf{u}_t(\mathbf{x})$ to denote the velocity at location $\mathbf{x}$ and time t, and $W(\mathbf{x})$ is a weighting function. In MTLM, time t is chosen as a parameter of the operator.

The solution given by Eqs. 2.9 and 2.10 can be recovered from Eq. 2.11 when $W(\mathbf{x}) = \delta(\mathbf{x})$, where the latter represents the Dirac-δ function. In our numerical implementation, $W(\mathbf{x}) = C/|\mathbf{x}|$ is used to approximate the Dirac-δ function, where C is a normalization factor.

As mentioned earlier, the advection operator is applied recursively to the initial velocity field. To explain the idea in details, we introduce several other operators, in a way similar to [107]. Note, however, that some of the notations used here are different. A filtering operator $\mathcal{G}$ will be used to separate the large scales of a velocity field from the small scales. $\mathcal{G}$ is defined as follows: for an arbitrary velocity field $\mathbf{u}(\mathbf{x})$, we have

$$\mathcal{G}\mathbf{u}(\mathbf{x}) = \int G(\mathbf{x} - \mathbf{y})\mathbf{u}(\mathbf{y})d^3\mathbf{y}, \tag{2.12}$$

where G represents the cut-off filter with a given filter scale. To remove the divergence of a vector field, we apply the projection operator $\mathcal{P}$. In the Fourier space, $\mathcal{P}$ is defined by

$$\mathcal{P}\hat{\mathbf{u}}(\mathbf{k}) = [I - \hat{\mathbf{k}} \otimes \hat{\mathbf{k}}]\hat{\mathbf{u}}(\mathbf{k}) \tag{2.13}$$

where $\hat{\mathbf{u}}(\mathbf{k})$ is the Fourier transform of an arbitrary velocity field $\mathbf{u}(\mathbf{x})$, $\mathbf{k}$ is the wavenumber and $\hat{\mathbf{k}} = \mathbf{k}/|\mathbf{k}|$. Finally, we also use the rescaling operator $\mathcal{R}$, defined by

$$\mathcal{R}^u \hat{\mathbf{u}}(\mathbf{k}) = \left(\frac{E_p^u(k)}{E^u(k)}\right)^{1/2} \hat{\mathbf{u}}(\mathbf{k}), \tag{2.14}$$

in which $E^u(k)$ is the energy spectrum of $\hat{\mathbf{u}}(\mathbf{k})$, and $E_p^u(k)$ is a prescribed energy spectrum. The output of $\mathcal{R}^u$ is a velocity field with energy spectrum given by $E_p^u(k)$, while the Fourier modes of the velocity field have the same phases as those of the input velocity field.

We are now ready to give a brief summary of the MTLM map. We will adopt the explanation in [107] with notations modified slightly for the problems we are considering here. First of all, the input to the map includes a random divergence-free velocity field $\mathbf{u}(\mathbf{x})$, the prescribed energy spectrum $E_p^u(k)$, and a hierarchy of M chosen length scales $\ell_n = 2^{-n}L$ ($n = 1, 2, ..., M$) where L is a reference length at the order of the integral length scale and M is determined by the number of grids in the simulation. The MTLM map has M iterations, corresponding to length scales ℓ_n ($n = 1, 2, ..., M$), respectively. Each iteration takes the velocity field generated from the previous iteration as the input, and generate a new velocity field.

The outcome of the iterations is an isotropic synthetic velocity field with $E_p^u(k)$ as its energy spectrum, which we denote as $\mathbf{u}_e$. Let $\mathbf{u}_{10}$, $\mathbf{u}_{20}$, ..., and $\mathbf{u}_{M0}$ be the input to the ith iteration, where $i = 1, 2, ..., M$, respectively, where $\mathbf{u}_{10} \equiv \mathbf{u}$. Obviously $\mathbf{u}_{n0}$ is also the output of the $(n-1)$th iteration. In each iteration, the advection operator, the projection operator and the rescaling operator are applied successively to the input velocity field. Let us consider the nth iteration, where the input is $\mathbf{u}_{n0}$. The operators are applied in the following order:

1. $\mathbf{u}_{n0}$ is low-pass filtered; the resulted velocity field is denoted as $\mathbf{u}_{n1} \equiv \mathcal{G}_n\mathbf{u}_{n0}$, where $\mathcal{G}_n$ represents the filtering operation with length scale ℓ_n. Meanwhile, the high wavenumber components of $\mathbf{u}_{n0}$ are kept unchanged.

2. Let $\mathcal{A}_n^u$ represent the advection operator associated with ℓ_n. $\mathcal{A}_n^u$ and the projection operator $\mathcal{P}$ are then applied to $\mathbf{u}_{n1}$ m_n times. Let the resulted velocity field be $\mathbf{u}_{n2}$, i.e. $\mathbf{u}_{n2} \equiv (\mathcal{P}\mathcal{A}_n^u)^{m_n}\mathbf{u}_{n1}$. The advection time t_n and m_n are specified below.

3. $\mathbf{u}_{n2}$ is rescaled, giving $\mathbf{u}_{n3} = \mathcal{R}_n^u\mathbf{u}_{n2}$, where $\mathcal{R}_n^u$ denotes the rescaling operator associated with $\mathbf{u}_{n2}$.

4. $\mathbf{u}_{n3}$ is then merged with the high wavenumber components of $\mathbf{u}_{n0}$ to generate the final velocity field of this iteration. As the resulted velocity field is also the initial field for the next iteration, i.e., $\mathbf{u}_{(n+1)0}$, we have

$$\mathbf{u}_{(n+1)0} = \mathbf{u}_{n3} + \mathcal{G}_n^c\mathbf{u}_{n0} = [\mathcal{R}_n^u(\mathcal{P}\mathcal{A}_n^u)^{m_n}\mathcal{G}_n + \mathcal{G}_n^c]\mathbf{u}_{n0},$$

where $\mathcal{G}_n^c = 1 - \mathcal{G}_n$.

Repeating the above procedure for each n for $n = 1, 2, ..., M$, we obtain the final velocity field $\mathbf{u}_e$. Mathematically, we have

$$\mathbf{u}_e = \mathcal{M}^u\mathbf{u} \tag{2.15}$$

where

$$\mathcal{M}^u = \prod_{n=1}^{M} [\mathcal{R}_n^u(\mathcal{P}\mathcal{A}_n^u)^{m_n}\mathcal{G}_n + \mathcal{G}_n^c]\mathcal{P} \tag{2.16}$$

is the MTLM map for the synthetic velocity field. The product in the right hand side of the above equation is ordered such that from left to right n decreases from M to 1.

The advection time scale t_n for operator $\mathcal{A}_n^u$ is chosen as follows:

$$t_n = \ell_n/u_n' \tag{2.17}$$

with u_n' being the root-mean-square velocity of the filtered velocity field. u_n' can be calculated from $E_p^u(k)$ as follows:

$$u_n' = \left(\frac{2}{3}\int_0^{k_{c,n}} E_p^u(k)dk\right)^{1/2}, \tag{2.18}$$

where $k_{c,n} \equiv \pi/\ell_n$ is the cut-off wavenumber corresponding to ℓ_n. t_n is the time scale needed for a fluid particle to travel over the local length scale ℓ_n, and it is only over this time period that the interactions of the particles can be reasonably neglected, as implied in the advection maps.

On the other hand, energy cascade in turbulence takes place over the eddy-turnover time scale. In order to capture the effects of energy cascade, it is necessary to iterate the advection maps so that the total advection time is at the order of the eddy-turnover time scale. Intuitively speaking, doing so is would ensure eddies are broken down sufficiently.

Let $\langle \epsilon \rangle$ be the energy dissipation rate corresponding to the prescribed energy spectrum, then the eddy turnover time scale τ_n at scale ℓ_n is given by

$$\tau_n = \frac{\ell_n^{2/3}}{\langle \epsilon \rangle^{1/3}}. \tag{2.19}$$

Thus, the advection map is iterated m_n times, where $m_n = \tau_n/t_n$. A consequence of this, however, is that the interaction between fluid particles can no longer be completely ignored. The MTLM model thus applies the projection operator $\mathcal{P}$ after each application of $\mathcal{A}_n^u$. The purpose is to recover incompressibility, which captures the first and most important effect of the interaction between fluid particles.

With the parameters t_n and m_n chosen as above, the definition of the MTLM map is complete. The map has been implemented numerically in [157]. It is evident that the numerical implementation of the operators $\mathcal{G}_n$, $\mathcal{P}$ and $\mathcal{R}_n^u$ is straightforward. A few comments are made here regarding the choice of M and the implementation of the advection operator $\mathcal{A}_n^u$, among others. To simplify the numerical implementation, the geometrical domain is chosen as $[0, 2\pi]^3$, which is discretized into N^3 grid points. M and L are chosen in such a way that the smallest scale ℓ_M is the same as the grid size $2\pi/N$. We take $N = 128$ as an example. In this case, we have chosen $L = \pi/2$ and $M = 5$, so that $\ell_n = 2^{-(n+1)}\pi$, i.e., $\ell_1 = \pi/4$, $\ell_2 = \pi/8$, ..., $\ell_M = \pi/64$. As a consequence, the filtered velocity fields at the nth iteration (i.e., $\mathbf{u}_{n0}$, $\mathbf{u}_{n1}$, $\mathbf{u}_{n2}$ and $\mathbf{u}_{n3}$) can be represented on a set of $(2^{n+2})^3$ grid points with grid size ℓ_n. In the Fourier space, the cut-off wavenumber corresponding to ℓ_n is $k_{c,n} = 2^{n+1}$, and the filtered velocity fields simply correspond to the Fourier modes of the full velocity fields with wavenumbers $-2^{n+1} \leq k_i \leq 2^{n+1}$ ($i = 1, 2, 3$). The integration in the advection operator $\mathcal{A}_n^u$, on the discrete grid points, becomes a weighted interpolation, which can be calculated easily. For more details, see [156].

2.4 The multi-scale turnover Lagrangian map for advected scalar with linear mean profile

For the scalar field, if we focus on the fluctuations over a length scale which is much larger than the Kolmogorov length scale (such as in high Re flows), the effects of molecular diffusion is negligible. The advection-diffusion equation thus becomes:

$$\partial_t \theta + (\mathbf{u} \cdot \nabla)\theta = -\mathbf{G} \cdot \mathbf{u}(\mathbf{x}, t). \tag{2.20}$$

The equation can be formally integrated by using Lagrangian coordinates, which gives

$$\theta(\mathbf{X}(t), t) = \theta(\mathbf{x}, 0) - \mathbf{G} \cdot \int_0^t \mathbf{u}(\mathbf{X}(t'), t')dt'. \tag{2.21}$$

With the approximation to the velocity field given by Eq. 2.9, the solution for θ becomes

$$\theta(\mathbf{X}(t), t) = \theta(\mathbf{y}) - t\mathbf{G} \cdot \mathbf{u}(\mathbf{y}), \tag{2.22}$$

In other words, $\mathbf{u}$ has been frozen at its value at $t = 0$. The solution can be represented by an integral operator $\mathcal{A}^s$ as follows:

$$\theta_t(\mathbf{x}) = \mathcal{A}^s\theta = \int W(\mathbf{x} - \mathbf{y} - t\mathbf{u}(\mathbf{y}))$$
$$(\theta(\mathbf{y}) - t\mathbf{G} \cdot \mathbf{u}(\mathbf{y}))d^3\mathbf{y}, \tag{2.23}$$

where we have used $\theta_t(\mathbf{x})$ to represent the scalar fluctuation field at $\mathbf{x}$ and time t. The operator $\mathcal{A}^s$ is the advection operator for the scalar field. Its expression is a new contribution of this article.

As a first step in the application of the MTLM to the fluctuation scalar field θ, the fluctuation scalar field θ is decomposed into low-pass and high-pass filtered parts for each length scale ℓ_n as follows:

$$\mathcal{G}_n\theta(\mathbf{x}) = \int G(\mathbf{x} - \mathbf{y})\theta(\mathbf{y})d^3\mathbf{y}, \tag{2.24}$$

Then the low-pass filtered scalar field, $\mathcal{G}_n\theta$, subject to the advection operators $\mathcal{A}^s$, while the high-pass filtered scalar field is saved unchanged. Note that the applying of the MTLM procedure to the fluctuation scalar θ do not demand any projection in Fourier space. Consequently, the advection operator applied to low-pass filtered scalar field at scale ℓ_n is $(\mathcal{A}_n^s)^{m_n}$.

As a last step, to maintain the prescribed scalar variance spectra $E_p^s(k)$, the resulted scalar fields is rescaled using rescaling operator $\mathcal{R}_n^s$ as follows:

$$\mathcal{R}_n^s\hat{\theta}(\mathbf{k}) = \left(\frac{E_p^s(k)}{E^s(k)}\right)^{1/2}\hat{\theta}(\mathbf{k}), \tag{2.25}$$

where $E^s(k)$ is the scalar variance spectra of the synthetic scalar field at $k = |\mathbf{k}|$. As mentioned before for the velocity case, the above operators have been applied to the low-pass filtered fields $\mathcal{G}_n\theta$. The resulted scalar fields is then merged with the high wavenumber components to form the full field, which is then filtered with $\mathcal{G}_{n+1}$ at the next length scale ℓ_{n+1} and subject to similar operations again. The procedure starts from $n = 1$ and is iterated until $n = M$. After M iterations, The final scalar field is given by

$$\theta_e = \mathcal{M}^s\theta, \tag{2.26}$$

with

$$\mathcal{M}^s = \prod_{n=1}^{M}[\mathcal{R}_n^s(\mathcal{A}_n^s)^{m_n}\mathcal{G}_n + \mathcal{G}_n^c]. \tag{2.27}$$

$\mathcal{M}^s$ is the MTLM map for the scalar fields.

We use the MTLM method to generate samples of the synthetic field on a periodic cubic domain $[0, 2\pi]^3$ which, in most cases, is discretized with 256^3 grid points. The 3D energy and scalar variance spectra, $E_p^u(k)$ and $E_p^s(k)$, are taken from DNS data, and are used as the input parameters. The spectra are shown in Fig. 2.1. Note that, due to the limit of resolution, no clearly visible inertial range is observed. Fifty synthetic fields are generated and in most cases the statistics presented are averaged over these 50 fields; some are calculated with a subset of the samples. The number of iteration levels M is chosen as 6. For more discussion of how to choose M see [158].

In what follows, we will use the Gaussian filter[145]. Unless stated otherwise, the filter scale Δ is always chosen as $\Delta = 8\delta_x$, which gives approximately $\Delta \approx 9\eta$. We have checked that the results for $\Delta = 16\delta_x \approx 18\eta$ are qualitatively the same, although occasionally we also plot the results for $\Delta = 16\delta_x$ as a comparison. The two filter scales are indicated in Fig. 2.1 by the vertical lines.
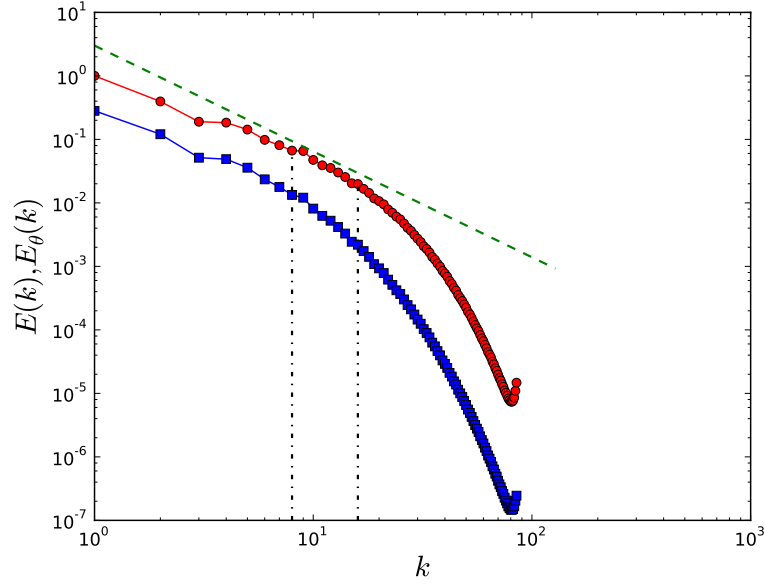
Figure 2.1: Spectra for the DNS fields. Blue squares: the energy spectra $E^p(k)$. Red circles: the scalar variance spectra $E^p_\theta(k)$. Green dashed line: the Kolmogorov $-5/3$ spectrum. The two vertical dash-dotted lines indicate filter scales $\Delta = 8\delta_x$ and $\Delta = 16\delta_x$.

2.5   The DNS data and their Parameters

We will compare the statistics calculated from the MTLM fields with those calculated from DNS. To obtain the DNS dataset, the incompressible Navier-Stokes equation (Eq. 2.2) along with the advection-diffusion equations (Eq. 2.7) are solved by a pseudo-spectral method. The computation box is a $[0, 2\pi]^3$ cubic box with periodic boundary conditions for the velocity and for the fluctuating part of the scalar θ in three directions. The spatial resolution is 256^3. Full dealiasing is achieved through truncation according to the 2/3 rule. Energy is injected into the velocity field at a constant rate $\langle \epsilon \rangle = 0.1$ by the forcing term, which is non-zero only for Fourier modes with wavenumber $|k| \leq 2$. Statistical stationary of scalar fluctuations is achieved by the mean gradient through the source term $-\mathbf{G} \cdot \mathbf{u}$ where $\mathbf{G} = -\mathbf{e}_y$ has been chosen. In other words, the mean scalar gradient is in the negative y-direction.

Our study has been limited to the inertial-convective regime ($Sc = 1$). The viscosity is $\nu = 0.003$, which is the same as the diffusivity κ. Therefore, we have $k_{\max}\eta \approx 2.9$ where η is the Kolmogorov length scale. The simulation is thus very well resolved. Computation shows that $u_{\mathrm{rms}} = 0.7$ in the steady state, hence the Taylor Reynolds number $Re_\lambda \approx 109$.

2.6 Analysis of subgrid-scale processes

In LES, the relevant field variables are decomposed into large- and small-scale components. This decomposition is achieved by applying spatial filtering to the field variables. Then the large scales of the flow are explicitly computed from the filtered NS equation, while the effect of the unresolved, or subgrid scales (SGS) is modelled [145, 117, 160] . Applying the filtering procedure to the NS equation leads to the filtered NS equation

$$\partial_t \widetilde{u}_i + \widetilde{u}_j \partial_j \widetilde{u}_i = -\partial_i \widetilde{p} + \nu \nabla^2 \widetilde{u}_i - \partial_j \tau_{ij} + \widetilde{f}_i, \tag{2.28}$$

with

$$\nabla \cdot \widetilde{\mathbf{u}} = 0. \tag{2.29}$$

In the above equation, tilde denotes low-pass filtering, and $\widetilde{u}_i$ is the ith component of the filtered velocity vector, defined as

$$\widetilde{u}_i(\mathbf{x}) = \int G_\Delta(\mathbf{x} - \mathbf{y}) u_i(\mathbf{y}) d\mathbf{y}. \tag{2.30}$$

with G_Δ being the filter with length scale Δ.

The effect of the subgrid scales on the resolved scales is contained in the SGS stress tensor $\tau_{ij} \equiv \widetilde{u_i u_j} - \widetilde{u}_i \widetilde{u}_j$. τ_{ij} represents the effects of the small scales, and has to be modelled. Many models have been proposed, which have been reviewed in, e.g., [117], [160], and [145]. Usually τ_{ij} is calculated explicitly as a function of certain resolved variables, such as the resolved vorticity vector $\widetilde{\omega}_i = \varepsilon_{ijk} \partial_j \widetilde{u}_k$, the resolved strain-rate tensor $\widetilde{S}_{ij} = (\partial_i \widetilde{u}_j + \partial_j \widetilde{u}_i)/2$, or the test-filtered resolved velocity field as in the so-called dynamical models. Some of the parameters may have to be found from additional transport equations. This methodology includes the eddy-viscosity-type models, similarity models, among others, with or without using the dynamic procedure. In another approach, the SGS velocity field is reconstructed by explicit estimation or approximate de-convolution (see, e.g., [41] and more recently [19]). From this reconstructed velocity field, one may calculate the approximate τ_{ij}, although its expression is not derived explicitly. The MTLM method potentially provides a new method to reconstruct the SGS velocity and scalar fields. In either case, it is important to examine the relations between the resolved quantities and the SGS stress, in order to either develop or validate the SGS models.

The SGS energy dissipation is defined as

$$\Pi \equiv -\tau_{ij} \widetilde{S}_{ij}. \tag{2.31}$$

The SGS energy dissipation describes the rate of kinetic energy being transferred from the resolved to the SGS motions, and is the most important parameter that characterizes the effects of τ_{ij} [140, 145, 117, 160]. The behavior of Π is correlated with the relative alignment between the eigenframes of SGS stress tensor τ_{ij} and filtered strain-rate tensor $\widetilde{S}_{ij}$. To see this more clearly, we denote the eigenvalues of $-\tau_{ij}$, in decreasing order, as $\alpha_{-\tau} \geq \beta_{-\tau} \geq \gamma_{-\tau}$, and the corresponding eigenvectors $\boldsymbol{\alpha}_{-\tau}$, $\boldsymbol{\beta}_{-\tau}$, and $\boldsymbol{\gamma}_{-\tau}$.

The eigenvalues of $\widetilde{S}_{ij}$ are denoted by $\alpha_s \geq \beta_s \geq \gamma_s$, which are referred to as the extensive, intermediate and contracting eigenvalues, respectively. The corresponding eigenvectors are denoted by $\boldsymbol{\alpha}_s$, $\boldsymbol{\beta}_s$ and $\boldsymbol{\gamma}_s$, With these definitions, the SGS kinetic energy dissipation can be written as

$$
\begin{aligned}
\Pi =& \alpha_{-\tau}\alpha_s(\boldsymbol{\alpha}_{-\tau},\boldsymbol{\alpha}_s)^2 + \alpha_{-\tau}\beta_s(\boldsymbol{\alpha}_{-\tau},\boldsymbol{\beta}_s)^2 \\
&+ \alpha_{-\tau}\gamma_s(\boldsymbol{\alpha}_{-\tau},\boldsymbol{\gamma}_s)^2 + \beta_{-\tau}\alpha_s(\boldsymbol{\beta}_{-\tau},\boldsymbol{\alpha}_s)^2 \\
&+ \beta_{-\tau}\beta_s(\boldsymbol{\beta}_{-\tau},\boldsymbol{\beta}_s)^2 + \beta_{-\tau}\gamma_s(\boldsymbol{\beta}_{-\tau},\boldsymbol{\gamma}_s)^2 \\
&+ \gamma_{-\tau}\alpha_s(\boldsymbol{\gamma}_{-\tau},\boldsymbol{\alpha}_s)^2 + \gamma_{-\tau}\beta_s(\boldsymbol{\gamma}_{-\tau},\boldsymbol{\beta}_s)^2 \\
&+ \gamma_{-\tau}\gamma_s(\boldsymbol{\gamma}_{-\tau},\boldsymbol{\gamma}_s)^2,
\end{aligned}
\tag{2.32}
$$

where $(\boldsymbol{\alpha}_{-\tau},\boldsymbol{\alpha}_s)$ is the cosine of the angle between the vectors $\boldsymbol{\alpha}_{-\tau}$ and $\boldsymbol{\alpha}_s$, and similarly for others. The expression shows that the relative alignment between the eigenvectors is an important factor controlling the magnitude of Π.

For the passive scalar, we may also write down the filtered scalar transport equation

$$
\partial_t\widetilde{\theta} + \widetilde{u}_i\partial_i\widetilde{\theta} = \kappa\nabla^2\widetilde{\theta} - \partial_i\tau_i^{\theta} - \mathbf{G}\cdot\widetilde{\mathbf{u}},
\tag{2.33}
$$

where $\widetilde{\theta}$ is the filtered fluctuation of passive scalar θ defined in a way similar to $\widetilde{u}_i$. The SGS scalar flux, τ_i^{θ}, is defined as

$$
\tau_i^{\theta} = \widetilde{u_i\theta} - \widetilde{u}_i\widetilde{\theta}
\tag{2.34}
$$

Π^{θ} will be used to denote the SGS scalar variance dissipation that characterizes the effects of τ_i^{θ}. The definition of Π^{θ} is

$$
\Pi^{\theta} = -\tau_i^{\theta}\partial_i\widetilde{\theta}.
\tag{2.35}
$$

Similar to the SGS energy dissipation Π, Π^{θ} plays a central role in the SGS modelling of the SGS flux vector τ_i^{θ}. Its definition also shows the importance of the relative orientation between τ_i^{θ} and the gradient of the filtered scalar fluctuation.

In many applications, the SGS stresses τ_{ij} and the SGS fluxes τ_i^{θ} are the only quantities needed to be modelled. However, in some other applications, notably the LES of turbulent reactive flows [138, 144], it is also necessary to model the SGS scalar variance Z_v defined as

$$
Z_v \equiv \widetilde{\theta\theta} - \widetilde{\theta}\,\widetilde{\theta},
\tag{2.36}
$$

and the filtered (molecular) scalar dissipation

$$
\widetilde{\epsilon}_{\theta} \equiv 2\kappa[\widetilde{\partial_i\theta\partial_i\theta} - \partial_i\widetilde{\theta}\partial_i\widetilde{\theta}\,].
\tag{2.37}
$$

These two quantities are important because they are the key parameters needed to model the chemical reaction rates of the species in a turbulent reactive flow, and the latter are crucial for the LES of such flows (for recent discussions, see, e.g., [6], [7], [90] and [56]). We will examine the statistics of Z_v in what follows. On the other hand, the statistics of $\widetilde{\epsilon}_{\theta}$ can be inferred from those of $\partial_i\theta$, thus will not be discussed in details.

The quantities listed above (τ_{ij}, τ_i^θ, Π, Π_θ, Z_v and related quantities) provide a comprehensive description of the SGS processes, and their interactions with the resolved ones. Once an MTLM field has been constructed, these quantities can all be calculated. We will calculate the statistics of these quantities and examine the results against DNS data. In doing so, we show that the synthetic MTLM fields capture the inter-scale interactions with good accuracy, hence potentially can be useful in SGS modelling.

2.7 Results and analysis

2.7.1 Anisotropic scalar statistics due to the mean scalar gradient
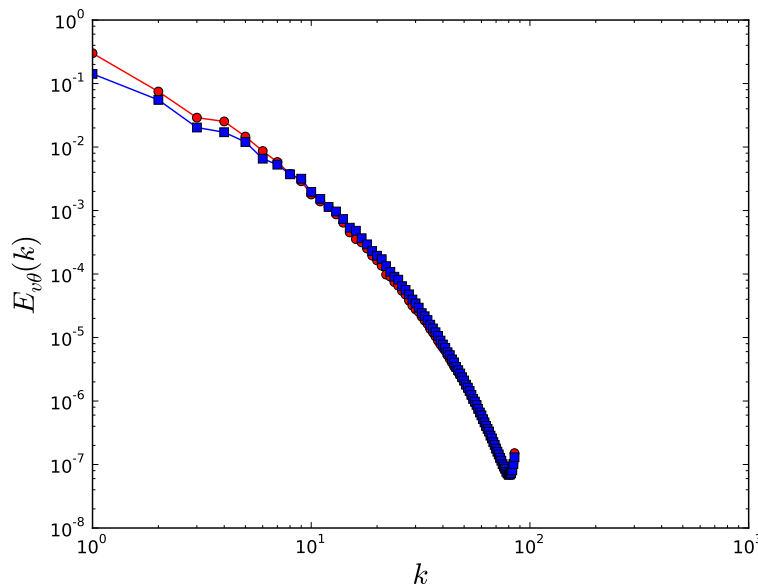
Figure 2.2: The co-spectra between θ and v-velocity component. Blue squares: MTLM fields. Red circles: DNS fields.

We first present some basic scalar statistics with emphasis on the anisotropic statistics due to the mean gradient. The co-spectra between the scalar θ and the v-velocity component are presented in Fig. 2.2. The spectrum from MTLM fields under-predicts the DNS result slightly at the low wavenumber end. The agreement nevertheless is very good. We note that the co-spectrum for the synthetic field is not part of the input to the MTLM procedure; it is generated by the non-linear mapping embedded in procedure, although undoubtedly, it depends crucially on the input energy and scalar spectra.

The PDF distributions of scalar gradients $\partial_i\theta$ in the synthetic MTLM fields are shown in Figs. 2.4 and 2.3. Due to statistical symmetry, the PDFs for $\partial\theta/\partial x$ and $\partial\theta/\partial z$ are expected to be the same. Fig. 2.4 shows indeed that the two PDFs are close to each other. There are some discrepancies at the ends of the tails, which may be attributed to statistical fluctuations. For all PDFs in these two figures, strong deviation from a Gaussian distribution is observed, displaying the characteristic flaring tails seen in scalar turbulence [200, 189, 127, 178]. The PDF for $\partial\theta/\partial y$ (Fig. 2.3) has a strong negative skewness, which means that it is skewed in the direction of the
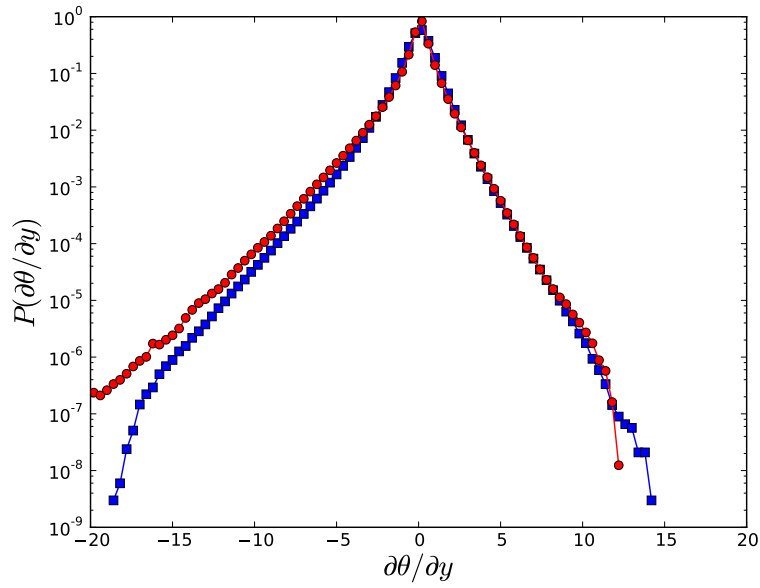
Figure 2.3: PDFs for $\partial\theta/\partial y$. Blue squares: MTLM fields. Red circles: DNS fields.

mean scalar gradient (the negative y-direction). Overall, the MTLM fields underestimate the PDFs for large fluctuations to some extent. However, all results are close to those obtained from DNS fields, as is shown by these figures (see also [149]).
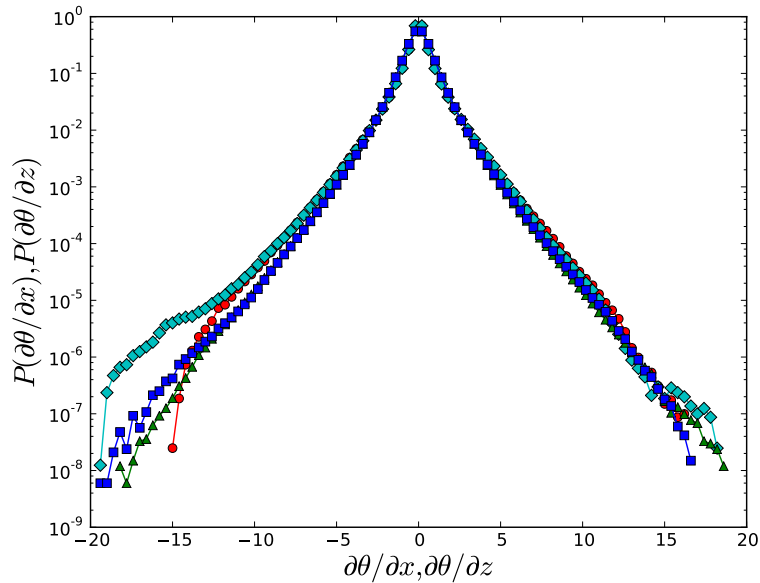
Figure 2.4: PDFs for scalar gradients. Blue squares: $\partial\theta/\partial x$ from MTLM fields. Red circles: $\partial\theta/\partial x$ from DNS fields. Green triangles: $\partial\theta/\partial z$ from MTLM fields. Cyan diamonds: $\partial\theta/\partial z$ from DNS.

The skewness is an indication of small scale anisotropy due to the negative mean gradient. It has been correlated to the observation that the cliffs in the scalar distribution sit on the edges of the vortices in the velocity field [69, 149]. We may also understand it qualitatively from the equation for $g_y \equiv \partial\theta/\partial y$, which is

$$\partial_t g_y + \mathbf{u} \cdot \nabla g_y = -(\partial_y \mathbf{u}) \cdot \nabla\theta + \kappa\nabla^2 g_y + \partial_y v \qquad (2.38)$$

where v is the y component of the velocity field, and we have used the fact that the mean scalar gradient $\mathbf{G} = -\mathbf{e}_y$. The last term on the right hand side represents the direct contribution from the mean scalar gradient. Note that $\partial_y v$ is the longitudinal gradient of v. It is well-known that, in real turbulence, the longitudinal gradient of the velocity has a negative skewness. The same has been observed in MTLM velocity fields too [156]. As such, the last term on the right hand side of Eq. (2.38) is more likely to be negative, which tends to reduce g_y. This term thus provides a driving mechanism for the negative skewness in the PDF of g_y that is absent from other components of the gradient. Fig. 2.3 shows that the same mechanism is captured by the MTLM procedure, although results for the MTLM fields appear to somewhat underestimate the probabilities for large fluctuations.
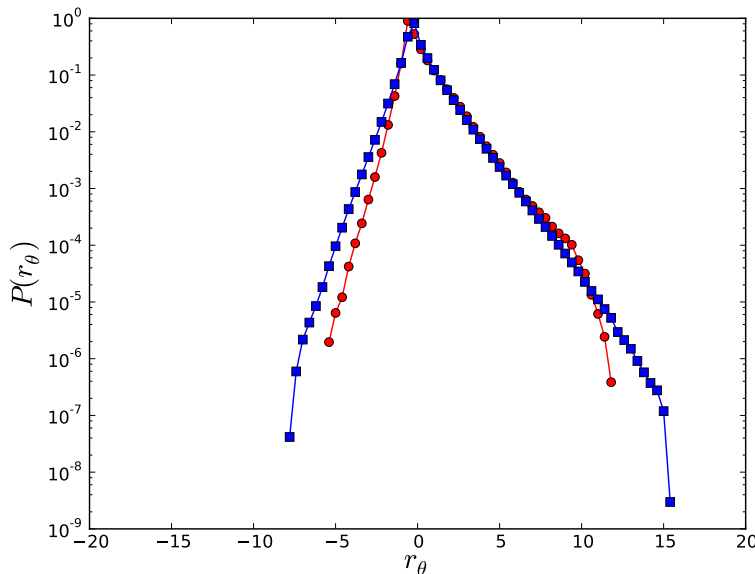
Figure 2.5: The PDFs of the normalized fluctuating flux r_θ. Blue squares: MTLM fields. Red circles: DNS fields.

The source term in the equation of θ is $-\mathbf{G} \cdot \mathbf{u} = v$, according to Eq. 2.33. By writing down the equation for $\langle\theta^2\rangle$ (not shown), we can see that, to provide a positive source for the scalar fluctuations, a positive correlation must exist between v and scalar θ. The PDFs of the normalized product $r_\theta \equiv v\theta$, from both DNS and MTLM fields, are presented in Fig. 2.5. As expected, both PDFs displays a positive skewness. The positive skewness is consistent with the co-spectrum shown in Fig. 2.2, both indicating a positive correlation between v and θ. A physical explanation for the positive correlation is given in Ref. [62] using a Lagrangian closure. Intuitively, positive fluctuation of θ at a point is generated when a parcel of fluid carrying a larger value of the scalar moves to the point. Given that the mean gradient of the scalar is in the negative y direction, this parcel is more likely to come from the negative y direction. Thus, on average, this parcel will have a positive v on its path to this point. Given the positive spatial

correlation of v, it is also more likely that v is positive at the given point. Thus we observe positive v together with positive θ, hence positive correlation between the two. Fig. 2.5 shows that the mechanism is captured very well by the MTLM fields.

2.7.2 SGS energy dissipation, scalar variance dissipation and scalar variance
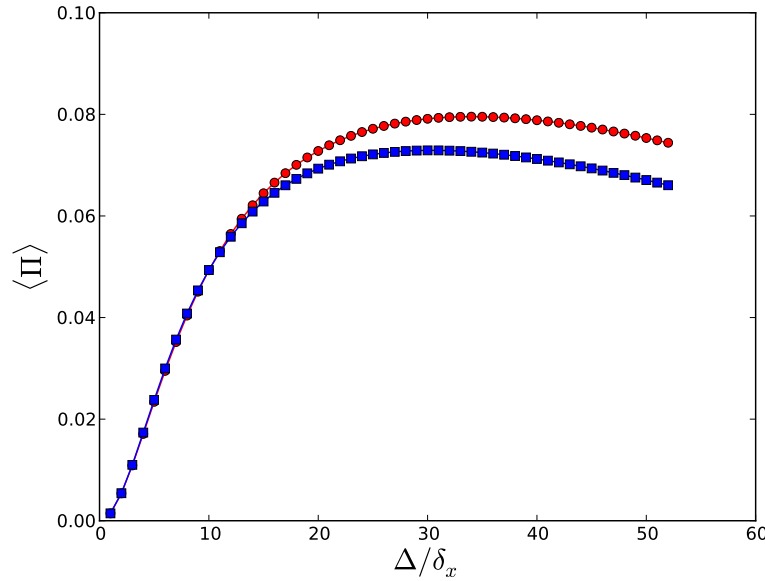
Figure 2.6: Mean SGS energy dissipation rate $\langle \Pi \rangle$ as a function of filter scale Δ (δ_x is the grid size of the simulation): Blue squares: MTLM fields. Red circles: DNS fields.

The mean SGS energy dissipation rate $\langle \Pi \rangle$ as a function of the filter scale Δ is shown in Fig. 2.6, while the mean SGS scalar variance dissipation rate $\langle \Pi^\theta \rangle$ is shown in Fig. 2.7. For the scalar dissipation, the agreement between MTLM results and DNS results is rather good with some small over-prediction (at about 3%). For the velocity fields, the MTLM results underestimate the DNS values by a small amount, which measures at about 10% at the largest filter scales. The fact that the prediction for SGS scalar dissipation is better may be explained by the following observation. The synthesized velocity field is missing both viscous diffusion and the nonlocal effect of the pressure. The synthesized scalar field, on the other hand, is missing only the diffusion effect. Though these effects are partially compensated for by imposing the energy and scalar spectra, the approximation to the velocity fields is still stronger.
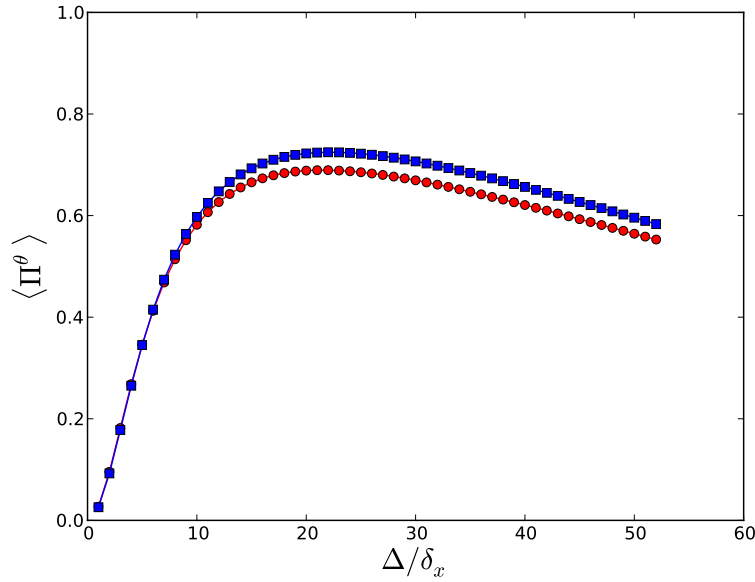
Figure 2.7: Mean SGS scalar variance dissipation rate $\langle \Pi^\theta \rangle$ as a function of filter scale Δ (δ_x is the grid size): Blue squares: MTLM fields. Red circles: DNS fields.
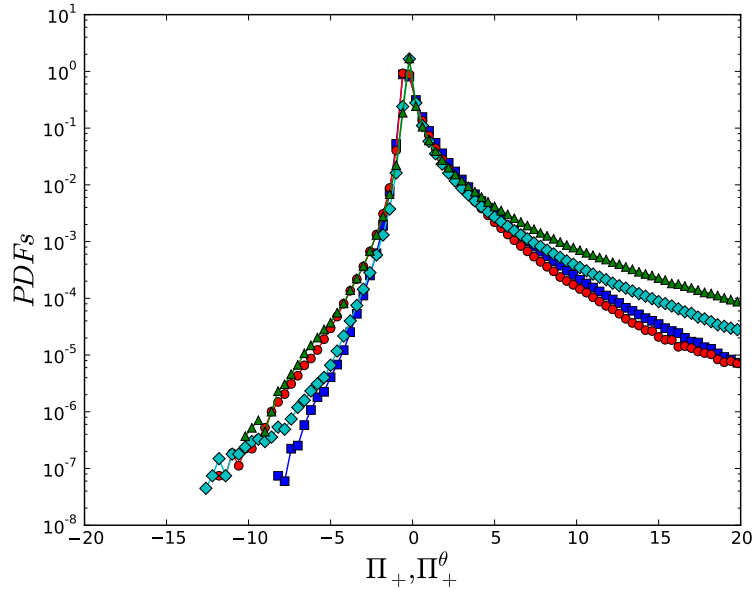
Figure 2.8: The PDFs of the normalized SGS energy dissipation $\Pi_+ = (\Pi - \langle \Pi \rangle)/\sigma_\Pi$ and the normalized SGS scalar variance dissipation $\Pi_+^\theta = (\Pi^\theta - \langle \Pi^\theta \rangle)/\sigma_{\Pi^\theta}$. Blue squares: PDF of Π_+ for MTLM fields. Red circles: PDF of Π_+ for DNS fields. Cyan diamonds: PDF of Π_+^θ for MTLM fields. Green triangles: PDF of Π_+^θ for DNS fields.

The PDFs for both the SGS energy and SGS scalar variance dissipations are shown in Fig. 2.8. We use $\Pi_+ = (\Pi - \langle \Pi \rangle)/\sigma_\Pi$ to represent the normalized SGS energy dissipation, where $\langle \Pi \rangle$ is the mean and σ_Π is the r.m.s. of Π. A similar notation Π_+^θ denotes the normalized SGS scalar

dissipation. The PDFs from MTLM fields are shown with blue squares and cyan diamonds, whereas DNS fields are shown with red circles and green triangles. The strong positive skewness observed in the curves indicates the dominance of forward energy and scalar variance cascade. A significant probability for negative fluctuations is also observed (flaring up left tail), which indicates a backscattering from small scales to large ones. The PDF of Π_+^θ has a slightly wider positive tail than that of Π_+ from the same data set (either MTLM or DNS). The MTLM fields capture all these behaviours. Quantitatively, the positive tail for Π_+ agrees rather well with DNS result, though the negative tail is somewhat underestimated for both the scalar variance and energy dissipations.
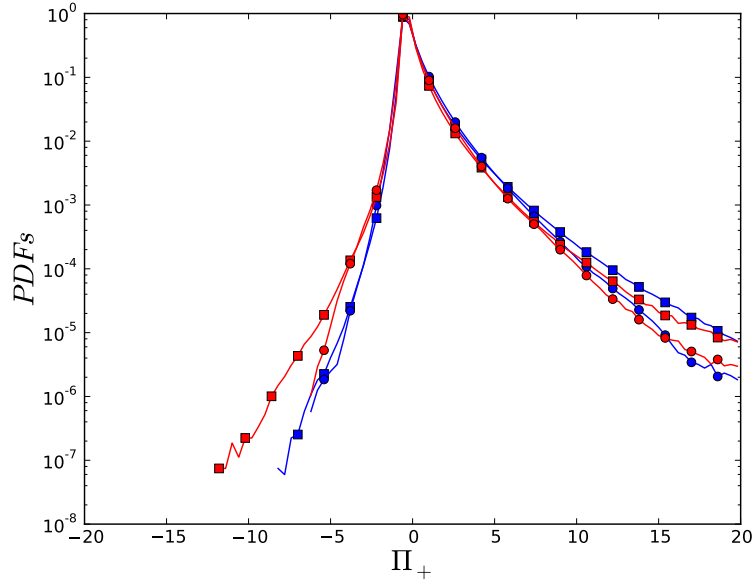
Figure 2.9: The PDFs of the normalized SGS energy dissipation $\Pi_+ = (\Pi - \langle\Pi\rangle)/\sigma_\Pi$. Blue squares: PDF of Π_+ for MTLM fields with filter scale $\Delta = 8\delta_x$. Blue circles: PDF of Π_+ for MTLM fields with filter scale $\Delta = 16\delta_x$. Red squares: PDF of Π_+ for DNS fields with filter scale $\Delta = 8\delta_x$. Red circles: PDF of Π_+ for DNS fields with filter scale $\Delta = 16\delta_x$.

Fig. 2.9 presents the PDFs for the normalized SGS energy dissipation Π_+, where these PDFs are evaluated using the Gaussian filter [145] with with two different filter scales $\Delta = 8\delta_x$ and $\Delta = 16\delta_x$, which are referenced in Fig. 2.1. The PDFs from MTLM fields are displayed with blue squares and circles at $\Delta = 8\delta_x$ and $\Delta = 16\delta_x$ respectively, while the The PDFs from DNS fields are displayed with red squares and circles at $\Delta = 8\delta_x$ and $\Delta = 16\delta_x$ respectively.

As analysis of these PDFs, it can be seen that the larger the filter scale is, the more wider the tail is, the positive tails for MTLM and DNS results agrees rather well with those have same filter scale than with those have same data set, although the negative tails for MTLM results is slightly underestimated for both filter scales. Moreover, those PDFs show some differences between two filter scales for same data set at large fluctuations.
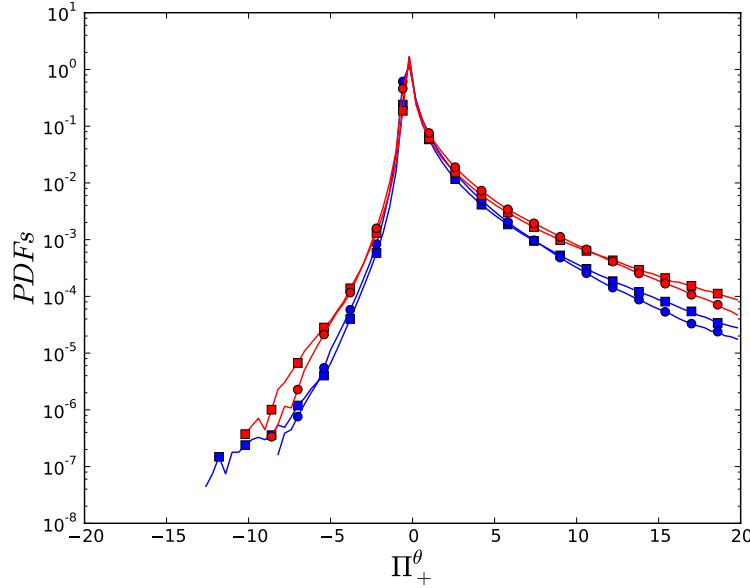
Figure 2.10: The PDFs of the normalized SGS scalar variance dissipation $\Pi_+^\theta = (\Pi^\theta - \langle \Pi^\theta \rangle)/\sigma_{\Pi^\theta}$. Blue squares: PDF of Π_+^θ for MTLM fields with filter scale $\Delta = 8\delta_x$. Blue circles: PDF of Π_+^θ for MTLM fields with filter scale $\Delta = 16\delta_x$. Red squares: PDF of Π_+^θ for DNS fields with filter scale $\Delta = 8\delta_x$. Red circles: PDF of Π_+^θ for DNS fields with filter scale $\Delta = 16\delta_x$.

The PDFs for the normalized SGS scalar variance dissipation Π_+^θ for MTLM and DNS data set with $\Delta = 8\delta_x$ and $\Delta = 16\delta_x$ filter scales are shown in Fig. 2.10. As argued recently, the PDFs behaviour is similar to that in Fig. 2.9 except that in this case the PDFs for MTLM data set at two different filter scales are agreed rather well with each other than with those for the DNS data set. Also the PDFs for MTLM data set at two different filter scales are both underestimated.

To quantify the backscattering, we calculate separately the mean of the negative SGS dissipation (denoted by $\Pi^{<0}$) and the mean of positive SGS dissipation (denoted by $\Pi^{>0}$), and look into their relative magnitudes, given by ratio

$$\frac{\langle |\Pi^{<0}| \rangle}{\langle |\Pi^{<0}| \rangle + \langle |\Pi^{>0}| \rangle}. \tag{2.39}$$

We calculate the ratio for both velocity and scalar fields from both MTLM and DNS data. Fig. 2.11, shows a plot of the ratio as a function of Δ. One can observe from the figure that MTLM fields indeed generate significant backscattering, as in DNS fields. For the velocity fields, the ratio tends to 0.20 for both MTLM and DNS fields when Δ increases, although for smaller Δ MTLM results somewhat underestimate the value. For the scalar fields, the ratio tends to around 0.18 for MTLM fields and 0.17 for DNS fields, i.e., it is overestimate slightly in the MTLM fields.
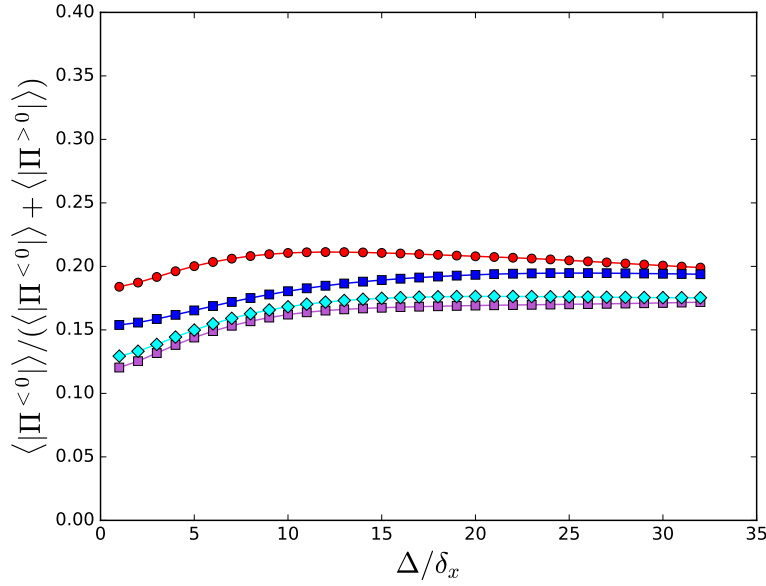
Figure 2.11: The proportion of backscattering defined by $\langle|\Pi^{<0}|\rangle/\langle|\Pi^{<0}|\rangle + \langle|\Pi^{>0}|\rangle$ as a function of filter scale Δ (δ_x is the grid size). Blue squares and red circles: SGS energy dissipation for MTLM and DNS fields, respectively. Cyan diamonds and medium-orchid squares: SGS scalar variance dissipation for MTLM and DNS fields, respectively.
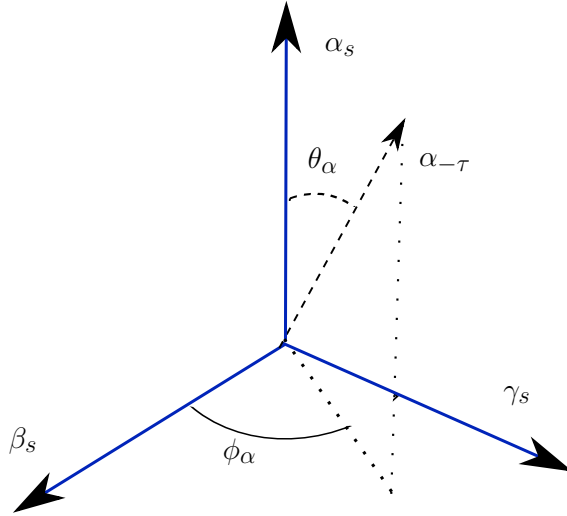
Figure 2.12: Definitions of θ_α and ϕ_α for the two-dimensional joint PDF characterizing the alignment of the vector $\boldsymbol{\alpha}_{-\tau}$ with the eigenvectors of tensor $\widetilde{S}_{ij}$.

The above results regarding the SGS energy dissipation rates can be complemented by the statistics of the alignment between the eigenvectors of the tensors, as is indicated by Eq. 2.32. We will present the results in terms of the orientations of the eigenvectors of the SGS stress tensor $-\tau_{ij}$ in the eigenframe of the filtered strain rate tensor $\widetilde{S}_{ij}$. To describe the orientation

54
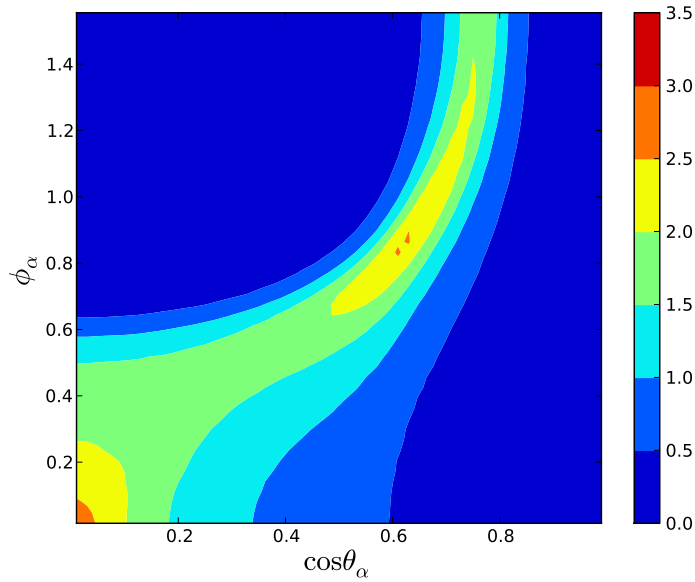
Figure 2.13: Joint PDF of $(\cos\theta_\alpha, \phi_\alpha)$ from DNS fields.

of the eigenvector $\boldsymbol{\alpha}_{-\tau}$ in the eigenframe of $\widetilde{S}_{ij}$, we need two angles ϕ_α and θ_α[185, 186, 70], as can be seen in Fig. 2.12. Note that three dimensional joint PDFs of the three angles describing the relative orientation of the two eigenframes have also been used (see, e.g.,[185]). The 3D joint PDFs have the advantage of providing a direct picture of the relative orientation of the frames. Nevertheless, quantitative details are sometimes obscured by the 2D projection of a 3D distribution. We thus choose to use 2D joint PDFs in what follows.
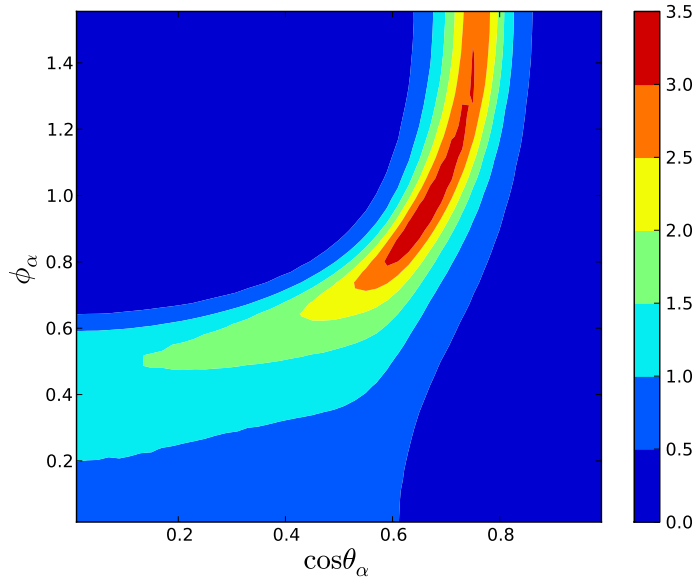
Figure 2.14: Joint PDF of $(\cos\theta_\alpha, \phi_\alpha)$ for MTLM fields.
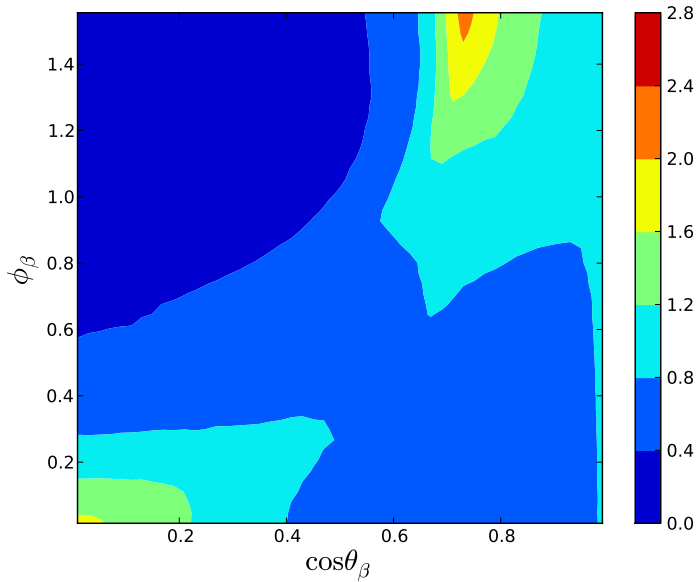
Figure 2.15: Joint PDF of $(\cos\theta_\beta, \phi_\beta)$ for DNS fields.

To observe the preferential alignment configurations between $\boldsymbol{\alpha}_{-\tau}$ and the eigenframe of $\widetilde{S}_{ij}$, Fig. 2.13 shows the two-dimensional joint PDF of $\cos\theta_\alpha$ and ϕ_α for DNS fields. It displays a bi-modal distribution with two peaks at $(\theta_\alpha, \phi_\alpha) = (90°, 0°)$ and $(50°, 48°)$, with approximate peak value 2.5 at both. As a comparison, the MTLM result, given in Fig. 2.14, shows only one peak at approximately $(50°, 48°)$, which locates at about the same location of the peak in DNS result. The peak value for the MTLM result is stronger than the one for DNS, reaching about 3.5, as is illustrated by Fig 2.14. This discrepancy is most likely due to the fact that MTLM fields produce insufficient vortex tubes[157].

We now consider the orientation of the eigenvector $\boldsymbol{\beta}_{-\tau}$ in the eigenframe of $\widetilde{S}_{ij}$, which is characterised by angles θ_β and ϕ_β. The two angles are defined in the same way as those shown in Fig. 2.12. Two peaks at $(\theta_\beta, \phi_\beta) = (90°, 0°)$ and $(45°, 90°)$ are seen in Fig. 2.15 for the DNS fields, with peak values 1.6 and 2.0, respectively. The joint PDF for the MTLM fields shows two peaks at about the same locations (see Fig. 2.16). However, the peak values are approximately 2.4 and 1.6, i.e., the strengths of the two peaks are reversed.
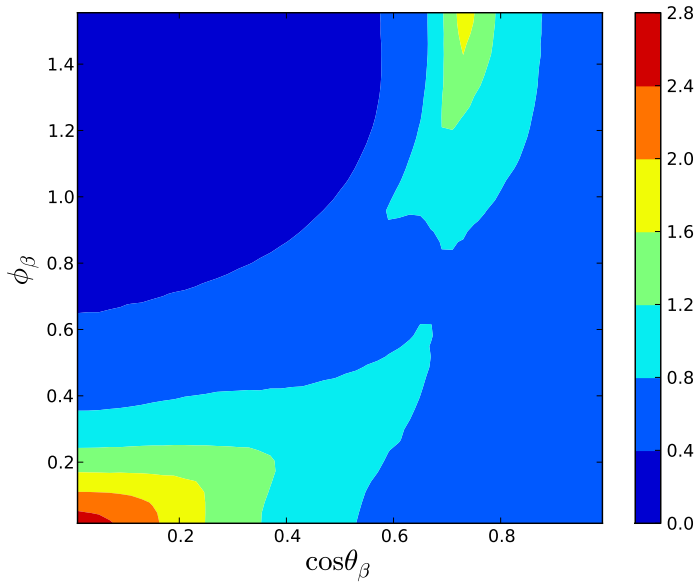
Figure 2.16: Joint PDF of $(\cos\theta_\beta, \phi_\beta)$ for MTLM fields.
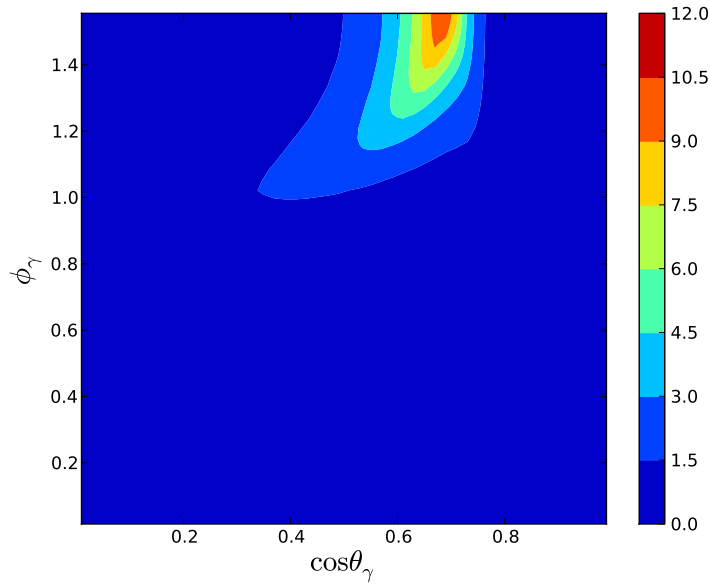
Figure 2.17: joint PDFs of $(\cos\theta_\gamma, \phi_\gamma)$ for 256^3 DNS fields.

Finally, we briefly summarize the results about the joint PDFs of the orientation of the eigenvector $\boldsymbol{\gamma}_{-\tau}$ for the DNS and MTLM fields which are shown in Figs 2.17 and 2.18, respectively. The main observation is that, for both DNS and MTLM fields, the peaks of the joint PDFs are found at the same location $\phi_\gamma \approx 90°$ and $\theta_\gamma \approx 42°$, with peak values 9.0 and 10.5 respectively. Angles θ_γ and ϕ_γ are defined again in the same way as before.
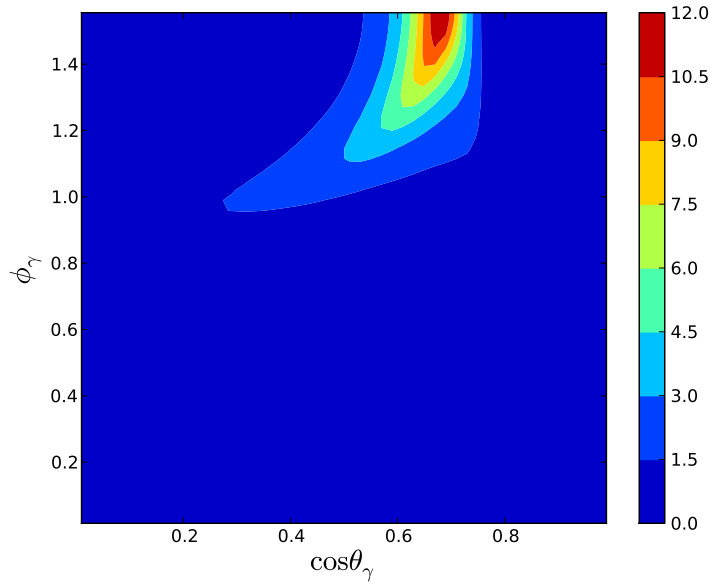
Figure 2.18: joint PDFs of $(\cos\theta_\gamma, \phi_\gamma)$ for 256^3 MTLM fields.
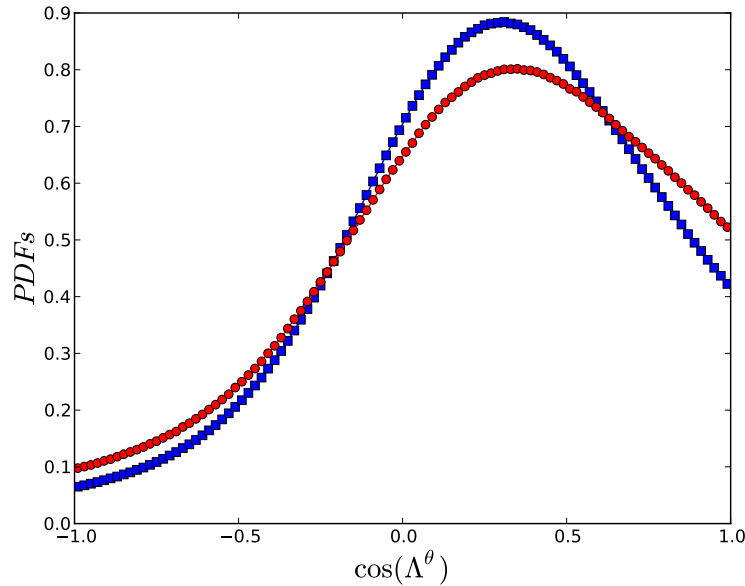
Figure 2.19: PDFs of the cosine of the angle between τ_i^θ and $\partial_i\widetilde{\theta}$, Λ^θ. Blue squares: MTLM fields. Red circles: DNS fields.

Similar analysis can be conducted for the scalar SGS dissipation. The PDFs of the cosine of the angle between the SGS scalar flux vector τ_i^θ and the gradient of the filtered scalar $\partial_i\widetilde{\theta}$ are shown in Fig. 2.19, where we have used Λ^θ to denote the angle. The PDFs for both MTLM and DNS data display the same preferred alignment at $\cos\Lambda^\theta \approx 0.3$, corresponding roughly to $\Lambda^\theta = 72°$. Thus the SGS scalar flux vector does not align perfectly with the resolved scalar gradient, in contradiction with what is implied in an eddy diffusivity model. On the other hand, the peak

value of the PDF from MTLM fields is somewhat higher than the DNS value.

To briefly summarize, the above results for the relative orientation of the eigenvectors calculated from the MTLM fields bear close resemblance to those from DNS fields. Some discrepancies exist in terms of the alignment results, which are consistent with previously known features of the MTLM fields. Nevertheless, the discrepancy has only small effects on the SGS dissipation rates. These results reveal the ability of the MTLM procedure to reproduce SGS dissipations and the geometrical structures of the SGS stress and scalar flux.
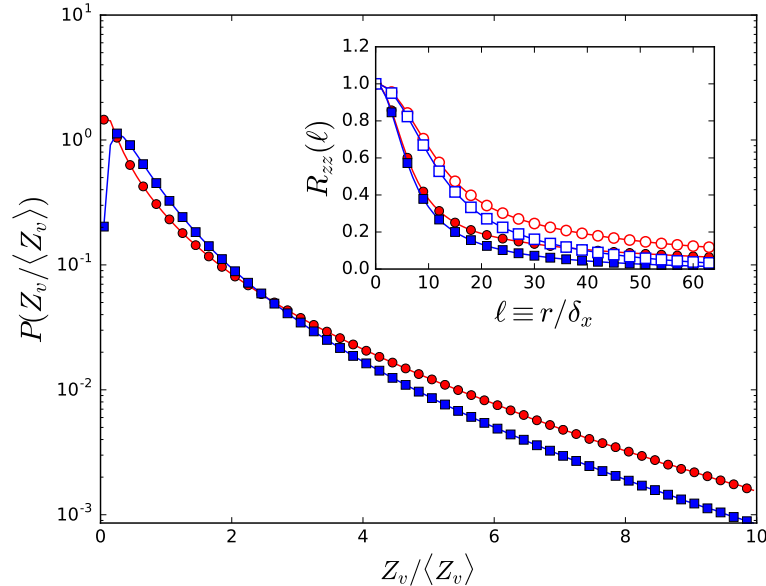
Figure 2.20: PDFs of $Z_v/\langle Z_v \rangle$ for $\Delta = 8\delta_x$. Blue squares: MTLM fields. Red circles: DNS fields. The inset is the two-point correlation coefficient for Z_v. Blue squares: MTLM. Red circles: DNS. Filled and empty symbols are for $\Delta = 8\delta_x$ and $16\delta_x$, respectively.

We now present results related to Z_v. Note that the mean of Z_v is determined by the scalar spectrum. Therefore by design, the mean of Z_v for the MTLM fields is the same as that of the DNS fields. However, it is interesting to examine statistics beyond the mean. Fig. 2.20 compares the PDFs for Z_v calculated from the MTLM fields (blue squares) and DNS data (red circles). It shows that the MTLM fields underestimate the probability of large values. This mild discrepancy seems to be consistent with some of the results show previously where MTLM fields have also been found to under-estimate large fluctuations to some degree. The MTLM fields also show a low probability for Z_v very close to zero, whereas in the DNS fields, the most probable value is $Z_v = 0$. The inset shows the correlation coefficient for Z_v, defined as

$$R_{zz}(r) = \frac{\langle (Z_v(\mathbf{x}) - \langle Z_v \rangle)(Z_v(\mathbf{x} + r\mathbf{e}) - \langle Z_v \rangle) \rangle}{\langle (Z_v(\mathbf{x}) - \langle Z_v \rangle)^2 \rangle}, \tag{2.40}$$

plotted against the displacement r normalized by δ_x, where in the definition $\mathbf{e}$ is a fixed given direction. Results for both $\Delta = 8\delta_x$ and $16\delta_x$ are shown. It is expected that the correlation is stronger for larger filter scales. The correlation for MTLM fields decays somewhat quicker than that for the DNS fields, i.e., the MTLM fields somewhat underestimate the long range correlations in the scalar fields.
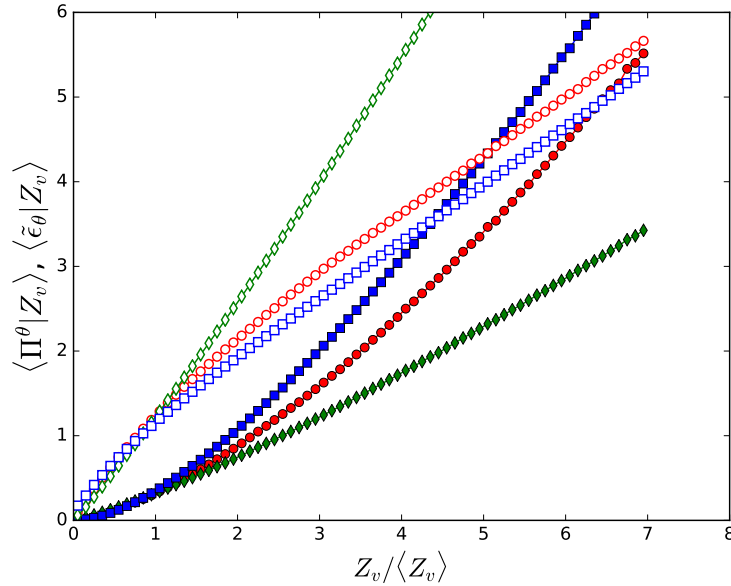
Figure 2.21: Conditional averages for $\Delta = 8\delta_x$. Filled symbols: $\langle \Pi^\theta | Z_v \rangle$. Empty symbols: $\langle \widetilde{\epsilon}_\theta | Z_v \rangle$. Blue squares: MTLM fields. Red circles: DNS fields. Green diamonds: reference models (see text).

The evolution of Z_v is dominantly controlled by the SGS scalar dissipation Π^θ and the filtered (molecular) scalar dissipation $\widetilde{\epsilon}_\theta$, which provide the source and the sink terms for Z_v, respectively. To predict the PDF of Z_v correctly, the conditional averages $\langle \Pi^\theta | Z_v \rangle$ and $\langle \widetilde{\epsilon}_\theta | Z_v \rangle$ need to be correctly parametrized. The conditional averages are shown in Fig. 2.21. To put the results from the MTLM fields in context, the results from two other models are also presented. For $\langle \Pi^\theta | Z_v \rangle$, an eddy-diffusivity-type model

$$\tau_i^\theta = c_\tau \Delta^2 |\widetilde{\mathbf{S}}| \partial_i \widetilde{\theta} \tag{2.41}$$

is used as a reference, where $|\widetilde{\mathbf{S}}| \equiv (2\widetilde{S}_{ij}\widetilde{S}_{ij})^{1/2}$ is the modulus of $\widetilde{S}_{ij}$. The result from this model is shown with solid green diamonds. In SGS modelling, the coefficient c_τ is usually calculated from the dynamic procedure. Here, we choose c_τ empirically, so that the model result matches the DNS result (shown with red circles) at $Z_v/\langle Z_v \rangle = 1$. This simple choice is sufficient to show that the model does not provide consistent prediction for $\langle \Pi^\theta | Z_v \rangle$, because it underestimates the latter, and the discrepancy increases with Z_v. Meanwhile, the result from MTLM fields over-estimates $\langle \Pi^\theta | Z_v \rangle$ by a rather significant amount, although, at large Z_v, the discrepancy is smaller than that of the reference model.

For $\langle \widetilde{\epsilon}_\theta | Z_v \rangle$, we choose

$$\widetilde{\epsilon}_\theta = c_\epsilon \frac{Z_v}{\tau_\epsilon} \tag{2.42}$$

as the reference model, where the time scale τ_ϵ is taken as $|\widetilde{\mathbf{S}}|^{-1}$ (see, e.g., [144] and [7]). c_ϵ is chosen in the same way as c_τ above. In this case, the MTLM result (empty blue squares) follows quite closely with the DNS result, whereas the result from the reference model (empty green diamonds) is off by large amount.

2.7.3 Geometrical statistics of SGS stresses and fluxess

In this subsection, we examine how the geometrical statistics related to the SGS stresses and fluxes are captured by the synthetic MTLM fields. Overall, we find that the MTLM fields reproduce the alignment statistics accurately, including $\tau_i^\theta - \widetilde{\omega}_i$, $\tau_i^\theta - \widetilde{S}_{ij}$, $\tau_i^\theta - \tau_{ij}$, $\widetilde{\omega}_i - \tau_{ij}$, and $\widetilde{\omega}_i - \widetilde{S}_{ij}$ alignment. In what follows, we present only the first three results as an illustration. The PDFs of the cosine of the angle Λ^θ between SGS scalar flux vector τ_i^θ and the filtered vorticity vector $\widetilde{\omega}_i$ is given in Fig. 2.22. The PDFs have a sharp peaks at zero, which means that the SGS scalar flux vector tends to be perpendicular to the filtered vorticity. The MTLM results show a good quantitative agreement with the DNS results.
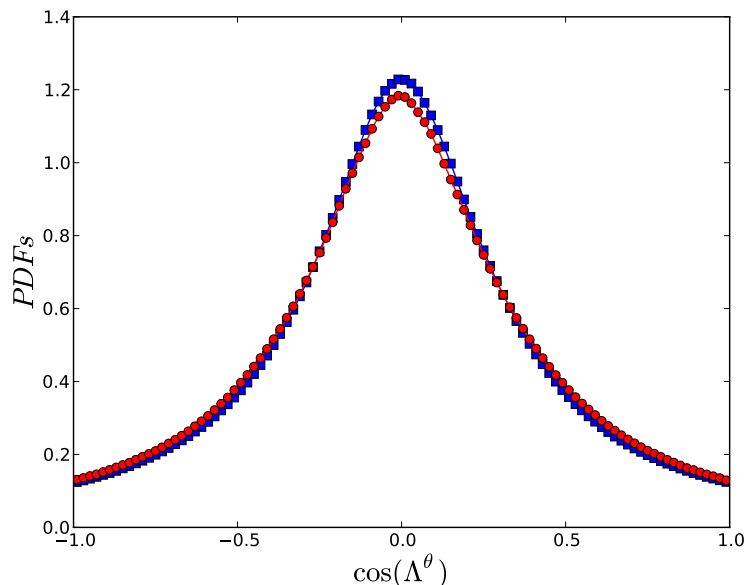
Figure 2.22: PDFs of the cosine of the angle between τ_i^θ and $\widetilde{\omega}_i$, Λ^θ. Blue squares: MTLM fields. Red circles: DNS fields.

Fig. 2.23 shows the PDFs of the cosines of the angles between the SGS scalar flux τ_i^θ and the three eigenvectors $\boldsymbol{\alpha}_s$, $\boldsymbol{\beta}_s$ and $\boldsymbol{\gamma}_s$ of the filtered strain-rate tensor $\widetilde{S}_{ij}$, denoted by Λ_α, Λ_β and Λ_γ, respectively. Both DNS and MTLM results are plotted. The comparison shows that the results of MTLM fields are nearly the same as the DNS results. It is observed that τ_i^θ tends to make a 53° angle with $\boldsymbol{\alpha}_s$, and a 37° angle with $\boldsymbol{\gamma}_s$, whereas τ_i^θ tends to be perpendicular to $\boldsymbol{\beta}_s$.
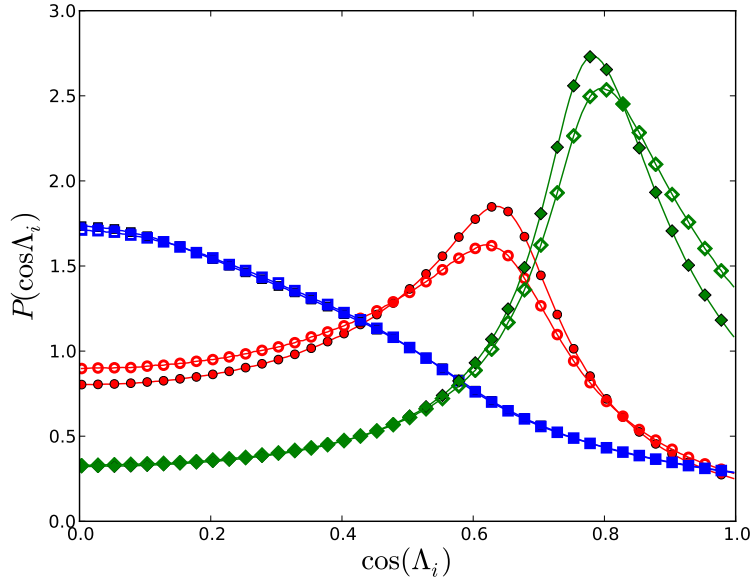
Figure 2.23: PDFs of the cosine of the angles between τ_i^θ and the eigenvectors of $\widetilde{S}_{ij}$ from DNS fields (empty symbols) and MTLM fields (filled symbols). Red circles: $P(\cos\Lambda_\alpha)$. Blue squares: $P(\cos\Lambda_\beta)$. Green squares: $P(\cos\Lambda_\gamma)$.
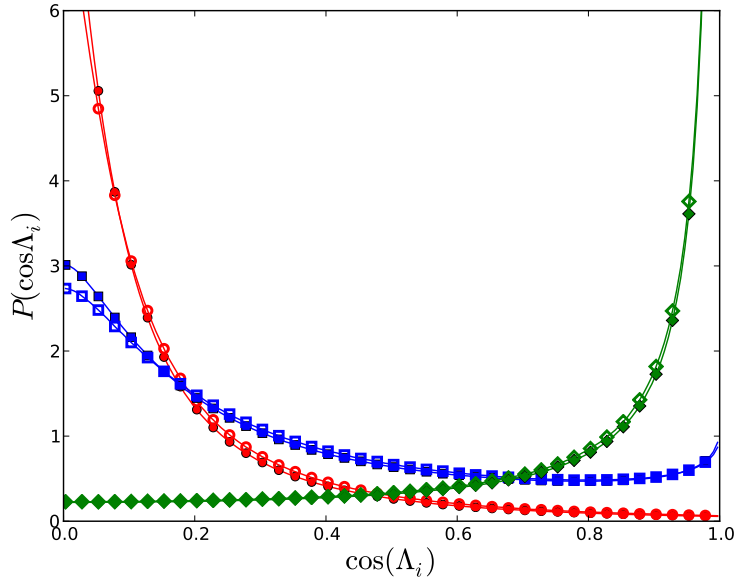
Figure 2.24: PDFs of the cosine of the angles between τ_i^θ and the eigenvectors of $-\tau_{ij}$ for DNS fields (empty symbols) and MTLM fields (filled symbols). Red circles: $P(\cos\Lambda_\alpha)$. Blue squares: $P(\cos\Lambda_\beta)$. Green squares: $P(\cos\Lambda_\gamma)$.

The preferential alignment between the SGS scalar flux vector τ_i^θ and the eigenvectors of the SGS stress tensor τ_{ij} is presented in Fig. 2.24. Note that, for simplicity, we have used same notation for the angles as in previous figure. Here, the PDFs from MTLM fields nearly overlap

with those from DNS fields, except that the peaks are slightly underestimated by MTLM (the peaks have been truncated hence are not shown in the figures). τ_i^θ tends to align with $\boldsymbol{\gamma}_{-\tau}$ with very high probability. On the other hand, τ_i^θ tends to be perpendicular to both $\boldsymbol{\alpha}_{-\tau}$ and $\boldsymbol{\beta}_{-\tau}$, but with a higher probability for the former.

The high peak probabilities suggest a near deterministic alignment. This trend has been observed previously, and has motivated a strategy to model τ_i^θ in terms of τ_{ij} [28].
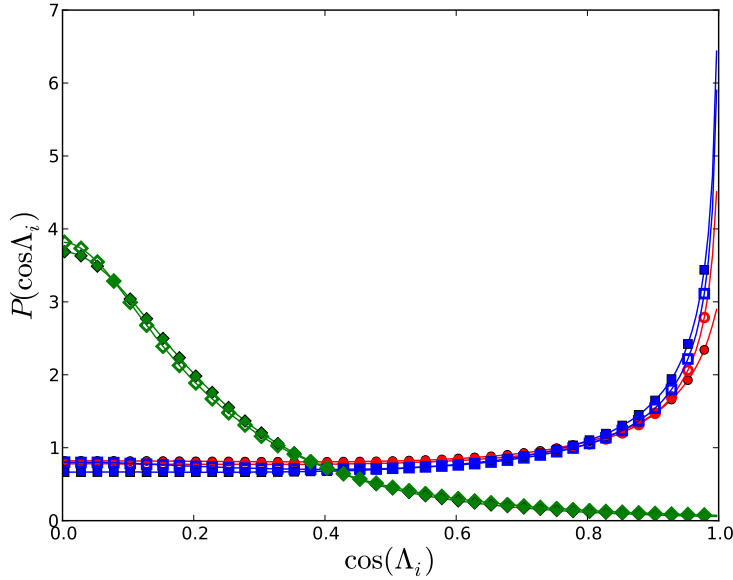
Figure 2.25: PDFs of the cosine of the angles between $\widetilde{\omega}_i$ and the eigenvectors of $-\tau_{ij}$ for DNS fields (empty symbols) and MTLM fields (filled symbols). Red circles: $P(\cos \Lambda_\alpha)$. Blue squares: $P(\cos \Lambda_\beta)$. Green squares: $P(\cos \Lambda_\gamma)$.

Fig. 2.25 shows the distributions of the PDFs for the cosines of the angles between the filtered vorticity vector $\tilde{\omega}_i$ and the eigenvectors of τ_{ij} tensor. The angles are again denoted by Λ_α, Λ_β and Λ_γ. These distributions display a good agreement between DNS and MTLM results, also it is consistent with the previous studies [70]. It shows that, $\tilde{\omega}_i$ tends to be aligned with an extensive and intermediate eigendirections $\boldsymbol{\alpha}_{-\tau}$ and $\boldsymbol{\beta}_{-\tau}$, respectively. While, $\tilde{\omega}_i$ tends to be perpendicular to a contracting eigendirection $\boldsymbol{\gamma}_{-\tau}$.

2.7.4 Effects of input energy and scalar spectra

In previous subsections, we have used the energy and scalar spectra from the 256^3 DNS data set as the input for the MTLM procedure. When MTLM is applied in a more practical setting, the input spectra may have to be estimated, hence contain errors. It is thus important to understand the effects of the input spectra. To achieve this, we now examine the MTLM fields with input spectra modified in two different ways. In one case, we consider MTLM fields generated from only parts of the spectra from the 256^3 DNS data shown in Fig. 2.1. Specifically, we generate MTLM fields with 64^3 grid points using the spectra in Fig. 2.1 in the range $k \in [1, 32]$ as the input, as well as MTLM fields with 128^3 grid points using the spectra in the range $k \in [1, 64]$ as the input.
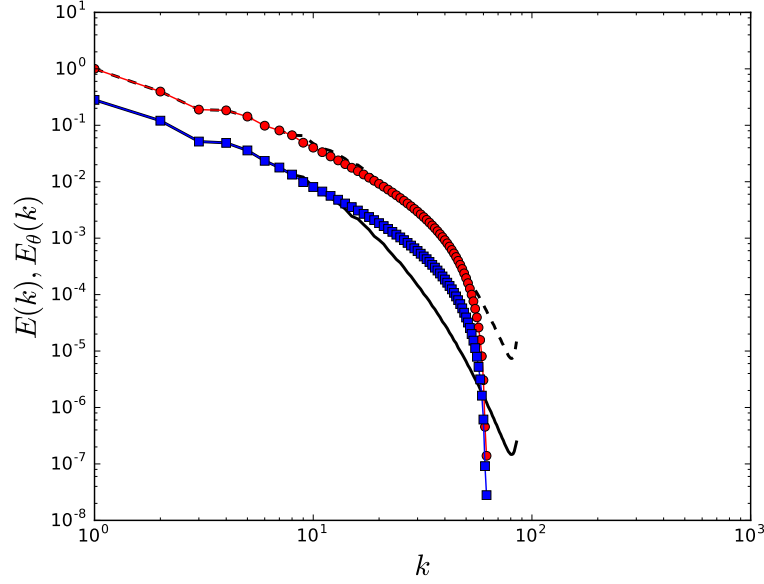
Figure 2.26: The Kovasznay energy (blue squares) and scalar variance (red circles) spectra. The lines are the DNS spectra. Solid line: energy spectrum. Dashed line: scalar variance spectrum.

These fields are missing most of the dissipation range due to the truncations. In another case, we consider an analytical spectrum with a model for the dissipation range as the input. For the velocity field, we use the Kovasznay spectrum [93], whose expression can be written as [134]:

$$E(k) = C_k \langle \epsilon \rangle^{2/3} k^{-5/3} \left(1 - \frac{C_k}{2} \nu \langle \epsilon \rangle^{-1/3} k^{4/3} \right)^2. \tag{2.43}$$

In other words, the spectrum is the Kolmogorov spectrum corrected for viscous dissipation by the factor in the parentheses. For scalar, we assume the spectrum is given by Eq. 2.5 multiplied by the correction factor in Eq. 2.43. In order to ensure this case is comparable with previous results, an empirical modification is applied. Namely, we use Eq. 2.43 (and the scalar equivalence) for $k \geq 8$ only. The spectrum for $k \leq 8$ is still taken from DNS data. The dissipation rates in the Kovasznay spectra are chosen in such a way that the two segments joins smoothly. The spectra constructed this way are plotted in Fig. 2.26.

We use the model spectra to generate 256^3 MTLM fields. The Kovasznay spectrum is reasonably realistic but still deviates significantly from the observed turbulent energy spectrum. Therefore it is a relevant yet stringent test. To help with exposition, we summarize all the data sets used in this subsection in Table 2.1, along with their names.

Dataset	Description
M64	64^3 MTLM fields with truncated DNS spectra as input
M128	128^3 MTLM fields with truncated DNS spectra as input
M256	256^3 MTLM fields with full DNS spectra as input
MKov	256^3 MTLM fields with Kovasznay spectra as input
DNS	256^3 DNS fields

Table 2.1:   Datasets and descriptions.

We show in Fig. 2.27 the co-spectra between the scalar θ and the y-velocity component. It can be seen that the agreement between the three resolutions is very good, all agreeing closely with the DNS result. The spectra of M64 and M128 are slightly lower than that of M256, but overall the effects of truncation is very small. Since the M64 and M128 fields, with 64^3 and 128^3 grid points, are obtained with few iterations than the M256 fields, this shows that number of iterations is not essential for the development of the proper correlation between the scalar field and the advecting velocity. Such correlation must come basically from the strong coupling between the scalar and velocity mappings, rather than from the mimicked cascade process. This is corroborated by the result from MKov data. Here the co-spectrum at the high wavenumber end displays similar features as the Kovasznay energy and scalar spectra, where it bulges upward before dropping off sharply.
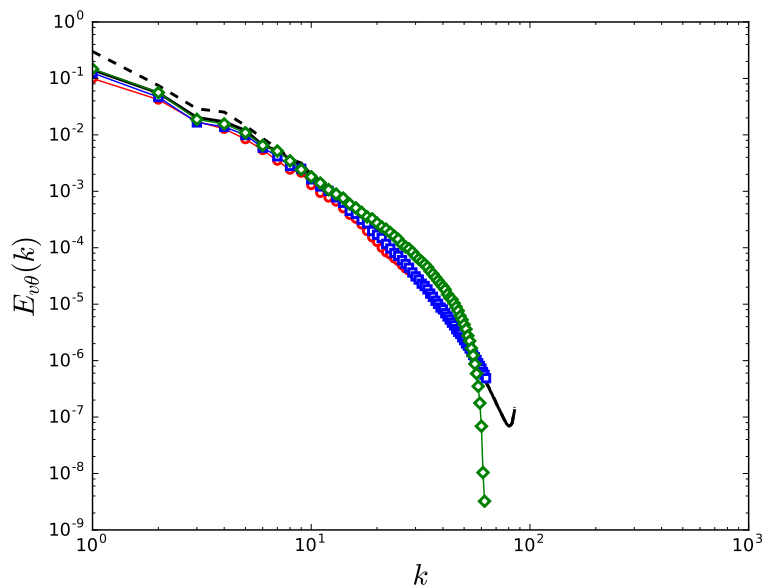
Figure 2.27: The co-spectra between θ and y-velocity component. Black solid line: 256^3 MTLM fields. Black dashed line: 256^3 DNS. Red circles: 64^4 MTLM fields. Blue squares: 128^3 MTLM fields. Green diamonds: from Kovasznay spectra.
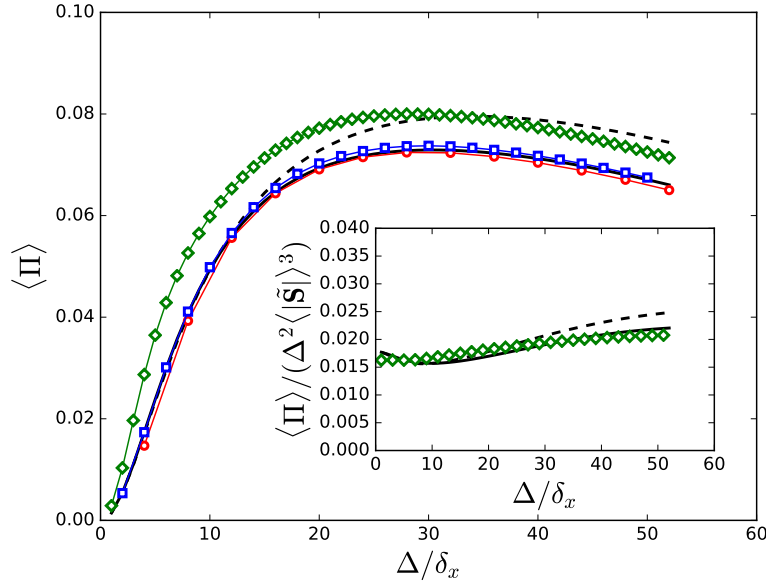
Figure 2.28: The averaged SGS energy dissipation as a function of filter scale Δ. Symbols and colors are the same as in Fig. 2.27. The inset shows $\langle \Pi \rangle$ normalized by $\Delta^2 \langle |\widetilde{\mathbf{S}}| \rangle^3$.
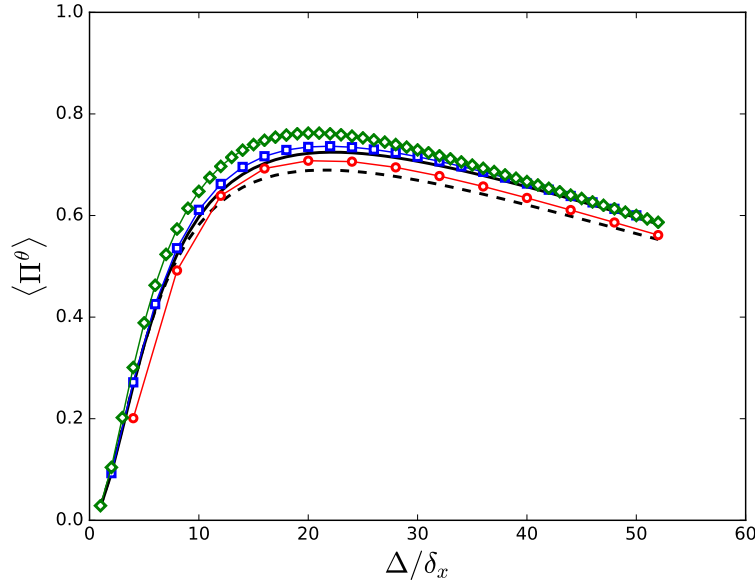
Figure 2.29: Same as Fig. 2.28 but for the SGS scalar variance dissipation.

The mean SGS energy dissipation as a function of the filter scales is shown in Fig. 2.28. The truncation has little effects on energy dissipation $\langle \Pi \rangle$, since the results for M64, M128 and M256 all collapse on the same curve. On the other hand, the result from MKov fields deviates significantly from the one from M256, and the difference is observed over all Δ values. To understand the significance of this observation, the inset plots $\langle \Pi \rangle$ from MKov, M256 and DNS, normalized by $\Delta^2 \langle |\widetilde{\mathbf{S}}| \rangle^3$. Now the results for MKov and M256 become very close to each other. Therefore, the deviation in $\langle \Pi \rangle$ comes mainly from the difference between the Kovasznay

spectrum and the DNS spectrum, hence can be removed by suitable normalization. Since the normalization factor can be calculated from the energy spectrum, the remain question is how to find a good approximation for the spectrum. Though it is in no way easy, this question is a standard one with much previous research can be drawn upon. Therefore the observation from this figure is encouraging.

Fig. 2.29 shows that truncation has stronger effects on scalar SGS dissipation $\langle \Pi^\theta \rangle$. In particular, the M64 fields produce slightly smaller values. The result from MKov fields is close to the M256 results, with slight over-estimation for approximately $10 \leq \Delta/\delta_x \leq 30$. This observation is not surprising, since the scalar Kovasznay spectrum is not very much different from the DNS scalar spectrum (cf. Fig. 2.26).
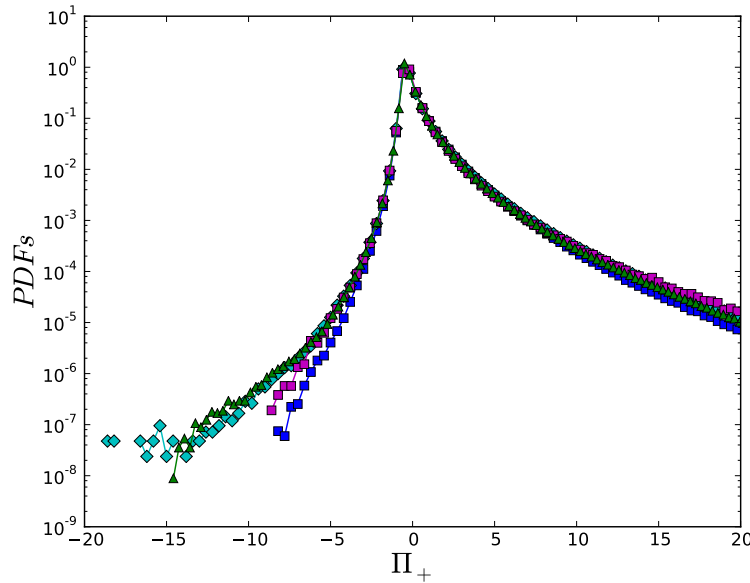
Figure 2.30: The PDFs of the normalized SGS energy dissipation: $\Pi_+ = (\Pi - \langle \Pi \rangle)/\sigma_\Pi$. Blue squares: 256^3 MTLM fields. Cyan diamonds: 128^3 MTLM fields. Medium-orchid squares: 64^3 MTLM fields. Green triangles: from the Kovasznay spectra.

The PDFs of the normalized SGS energy dissipation Π_+ are given in Fig. 2.30. These results show that the strong positive skewness remains mostly unchanged by the change in input energy spectrum. The PDF from MKov fields agrees particular well with the PDF from M64. Some differences can be discerned for the probabilities of large negative fluctuations; they seem to decrease with increasing resolutions.

Note that the difference between M256 data and M64 (or M128) is that, in the latter, the small scales in the dissipation range are decimated or absent. Thus the above observation is consistent with the notion that the scales much smaller than the filter scale can be modelled by an eddy-viscosity-type model, since their overall effects are dissipative and reducing backscattering. Nevertheless, we caution against drawing definite conclusions because statistical fluctuations are relatively large at the tails of the PDFs. In any case, the effects are rather small. The PDFs for the normalized SGS scalar variance dissipation, Π_+^θ, show again little difference for the different data sets, therefore the figure has been omitted.
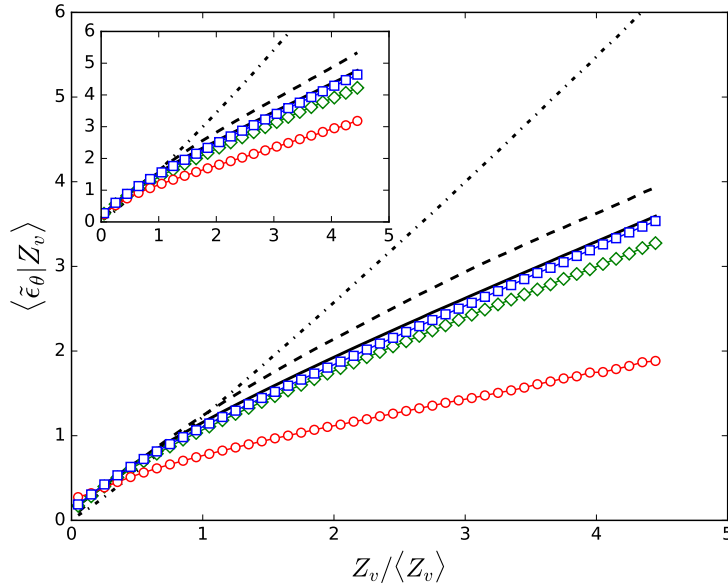
Figure 2.31: Conditional average $\langle \widetilde{\epsilon}_\theta | Z_v \rangle$ with $\Delta = 8\delta_x$ (main figure) and $16\delta_x$ (inset). Red circles: 64^3 MTLM fields. Blue squares: 128^3 MTLM fields. Green diamonds: from Kovasznay spectra. Solid line: 256^3 MTLM fields with DNS spectra. Dashed line: DNS result. Dash-dotted line: reference model (Eq. 2.42) calculated from DNS data.

The results for conditional average $\langle \widetilde{\epsilon}_\theta | Z_v \rangle$ is shown in Fig. 2.31. Since the dominant contribution to $\widetilde{\epsilon}_\theta$ comes from dissipation range, one would expect the changes in the input spectra have stronger effect. Indeed, the result from M64 shows significant deviation from the M256 and DNS results. The result from M128 stays close to that of M256, arguably because the truncation is less severe and part of the dissipation range is retained. The result from MKov is not much changed from that of M256 either. The inset shows the same results with $\Delta = 16\delta_x$. Same trends are observed, but MTLM fields results are closer to the DNS results in relative terms. The results shown in this figure suggest that a reasonably accurate model spectrum can provide good approximation to $\langle \widetilde{\epsilon}_\theta | Z_v \rangle$.

Finally, we note that we have also looked into the geometrical statistics for these new datasets as in previous subsections. The general observation is that all data sets reproduce the preferred alignment configurations in DNS, although the probabilities for the preferred configurations become weaker when the resolution is decreased (from 256^3 to 64^3). We present only Figs. 2.32 and 2.33 to illustrate the above observation. Fig. 2.32 shows the PDFs of $\cos \Lambda_\alpha = (\boldsymbol{\alpha}_{-\tau}, \tau_i^\theta)$ from M256, M128 and M64 fields. All three PDFs show the same preferred alignment at $\cos \Lambda_\alpha = 0$, the two vectors being perpendicular to each other. The PDFs of $\cos \Lambda_\alpha = (\boldsymbol{\alpha}_{-\tau}, \widetilde{\omega}_i)$ from same data sets are showen in Fig. 2.33. The same can be said about the preferred alignment for three PDFs, but with peak values at $\cos \Lambda_\alpha = 1$, which means that the $\widetilde{\omega}_i$ vector tends to align with the eigenvector $\boldsymbol{\alpha}_{-\tau}$. However, the peak probability decreases with the resolution, as we mention above.
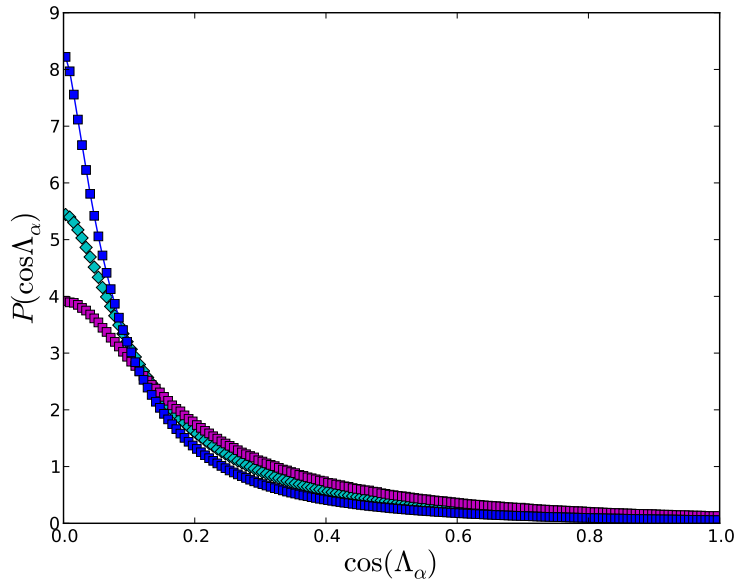
Figure 2.32: PDFs of the cosine of the angles between τ_i^θ and the eigenvector of $\boldsymbol{\alpha}_{-\tau}$. Blue squares: 256^3 MTLM fields. Cyan diamonds: 128^3 MTLM fields. Medium-orchid squares: 64^3 MTLM fields.
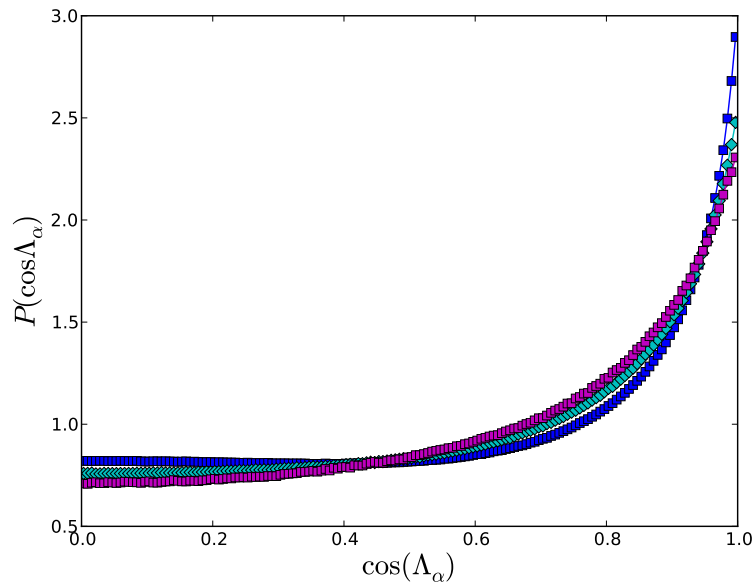
Figure 2.33: PDFs of the cosine of the angles between $\widetilde{\omega}_i$ and eigenvector $\boldsymbol{\alpha}_{-\tau}$. Blue squares: 256^3 MTLM fields. Cyan diamonds: 128^3 MTLM fields. Medium-orchid squares: 64^3 MTLM fields.

2.8 Conclusions

In this chapter, the multi-scale turnover Lagrangian map is generalized to synthesize passive scalar fields driven by a uniform mean scalar gradient. The synthetic velocity and scalar fields are then investigated from the perspective of SGS modelling. We calculate the statistics related to the SGS stress, the SGS scalar flux, and the SGS scalar variance obtained by filtering the synthetic MTLM fields. We also look into how the synthetic fields are affected by the input spectra.

Comparisons with DNS data show that the resultant non-Gaussian MTLM fields display many properties commonly observed in DNS data, including the skewed and intermittent probability density distributions for the SGS dissipation rates, the preferential alignment between different objects, the scalar-velocity correlations, and the skewness of the scalar gradient in the direction of mean gradient. The results obtained from fields with different spectra as the input demonstrate the robustness of the MTLM procedure. Most of the statistics are unchanged by the spectra. Some statistics, such as the mean SGS energy dissipation, depend rather strongly on the energy spectrum. However, the dependence may be parametrized in a simple way.

We show that the linear mean scalar profile can be modelled by the MTLM procedure easily with little additional computation cost. It shows that the MTLM can be generalized to include other linear effects without difficulties. This study complements previous discussions (see [156], [157], and [158] for discussions on other properties) on this technique, and provides solid basis for its applications in LES and SGS modelling. Future research will focus on technical challenges such as, among others, the modelling of inhomogeneous flows, where no complete information regarding the spectra is available. In such cases, one may have to estimate the spectra from the resolved the scales, and make use of the physics of the flows. How to implement such as scheme is a topic of our on-going research.

Chapter 3

Synthesizing Turbulence Using a Constrained Multi-Scale Turnover Lagrangian Map

.

3.1 Introduction

Synthetic turbulence models are based on a combination of Fourier modes, [105, 16, 170, 12, 37] which are rescaled to comply with a target spectrum. Then, according to a given Reynolds stress distribution the turbulent fluctuations are rescaled at each point in order to produce the required anisotropic turbulent Reynolds stress [145]. Most of the rescaling techniques that have been proposed [170, 101, 100, 78, 89, 113] are based on certain matrix decomposition (such as the Cholesky decomposition) of the Reynolds stress tensor. A digital-filter-based generation of turbulent inflow conditions for large eddy simulations is presented as a very efficient method of generation a small-scale urban canopy flows [88]. As is mentioned, the synthetic fields can be used to combine between the weather scale flows and the street scale computations to provide the dynamic large-scale inlet boundary conditions. The generation of the three-dimensional, vector valued, divergence-free functions that reproduces the non-Gaussian statistics, intermittency, and non-trivial skewness remains, however, a challenge. As a consequence, there is a serious need for improvement in the computation of turbulence.

Rosales and Meneveau [157] proposed MTLM to generate non-Gaussian synthetic field. In previous chapter MTLM has been reviewed. A new method, the constrained multi-scale turnover Lagrangian map (CMTLM) approach has been introduced by Li and Rosales [107]. They attempted to generalize the MTLM method to anisotropic turbulence, which is more relevant to practical applications. CMTLM procedure formulates the problem as an optimization problem using the adjoint formulation, in which the initial random field is taken as the control variable, and the additional features presented in inhomogeneous turbulence are taken as a target function to be matched by the synthetic fields. In Li [108] the CMTLM method has been used in order to generate realistic initial turbulent fields with any specified anisotropic Reynolds stress tensor to investigate the decaying process from initial turbulent fields with the aim to prove the universality.

In general, optimization and control problems are made up of the following ingredients [64]:

1. State variables: In the fluid mechanics setting , the sate variable could be one or more of the velocity vector, velocity potential, pressure, density, temperature and internal energy—in short, the mechanical and dynamical variable that describe the flow.

2. Control variables or design parameters: The control or design variables could be the heat flux or temperature at a wall, an inflow mass, or parameters that determine the shape of the boundary— in short, one or more of the data specified that serve to determine the state variables.

3. An objective, or cost, or performance functional: There are many possibilities for a objective functional, it may measure, e.g., how close the velocity field is to a given field, or the size of the drag or lift, or temperature variations, etc.

4. Constraints that candidate state and control variables are required to satisfy: The constraints are of two types, the main constraints are the governing flow equations, e.g., the Navier Stokes , or Euler, or potential flow equation. In addition, one can encounter sides such as minimum lift, or minimum volume, or maximum power requirements.

The optimization problem is then to find the state and control variables that minimize(or maximize, as the case may be) the objective functional subject to the requirement that the constraints are satisfied. The solution of the optimal control and optimization problems can be approaches by one-shot, or adjoint, or co-state, or Lagrangian multiplier methods through introduce the Lagrange multiplier or adjoint variable or co-state variable [107].

In this work, we derive a new optimality system generalizing the CMTLM technique in order to model anisotropic turbulence on the solid wall. We modify CMTLM procedure to formulate the problem as an optimization problem using the adjoint formulation where the control variable is constrained to generate anisotropic synthetic turbulence with the impermeable boundary conditions. Practically, synthesizing the turbulent channel flow according to the modified CMTLM approach to implement the effects of the solid walls. Our purpose is to find the optimal control variable which minimizes the difference between the target function and the synthetic field where the desirable features presented in anisotropic turbulence field are taken as a target function.

As we consider a fully developed channel flow as an example. We now briefly review some basics. Shapes of mean velocity profiles and the frictions laws describe the shear stress exerted by the fluid on the wall are the most important features in this flow. In examining fully developed channel flow, we have looked into the flow among a rectangular channel of height $h = 2\delta$, $y = 0$ and $y = 2\delta$ refer to the bottom and top walls, respectively, whereas $y = \delta$ refers to the mid-plane. In the axial direction $(x = x_1)$, a mean flow is prevalent, while at the cross-stream direction $(y = x_2)$ the mean velocity is essentially changed. The flow is statistically independent of z. $(U, V, W) = (U_1, U_2, U_3)$ refers to velocities in the three coordinate directions, and their fluctuations are represented by $(u, v, w) = (u_1, u_2, u_3)$.

The flow is statistically one-dimensional because statistics are regardless of x_3, also it is statistically unchanged under reflections of the x_2 coordinate axis. Consequently, these two conditions result in

$$\frac{\partial f}{\partial x_3} = 0$$

$$f(V_1, V_2, V_3; x_1, x_2, x_3, t) = f(V_1, -V_2, V_3; x_1, -x_2, x_3, t).$$

where $f(V; x, t)$ represents the PDF of velocity. Then the second equation means $\langle W \rangle = -\langle W \rangle$ at $x_3 = 0$, in other words, the mean of the span-wise velocity $\langle W \rangle = 0$, $\langle u_1 u_3 \rangle = 0$ and $\langle u_2 u_3 \rangle = 0$. Also the turbulent channel flow is statistically symmetric about the plane $x_2 = 0$, which implies that $\langle U_2 \rangle$ and $\langle u_1 u_2 \rangle$ are odd functions of x_2, whereas $\langle U_1 \rangle$ and the normal stresses are even functions.

The near-wall turbulent behaviours at a large scope are universal. The idea that all wall turbulence at high Reynolds numbers are described by a thin region close to the wall $(y/\delta \ll 1)$, in which δ represents the characteristic flow width is firstly preposed by Prandtl (1925)[148]. This region is called the an *inner layer* and the viscous scales specifies the mean velocity profile via the viscosity ν.

The total shear stress $\tau(y)$ is

$$\tau = \rho\nu\frac{d\langle U \rangle}{dy} - \rho\langle uv \rangle. \tag{3.1}$$

where $\rho\nu\frac{d\langle U\rangle}{dy}$ and $\rho\langle uv\rangle$ represents the viscous stress and the Reynolds stress respectively. At the wall Reynolds stresses are zero. As a consequence, viscosity ν is completely responsible for producing the wall shear stress τ_w. In other words,

$$\tau_w \equiv \rho\nu \left(\frac{d\langle U\rangle}{dy}\right)_{y=0}. \tag{3.2}$$

Evidently, these parameters play a crucial roles adjacent to the wall. Consequently, some *viscous scales* can be defined from dimensional analysis:

$$u_\tau \equiv \sqrt{\frac{\tau_w}{\rho}}, \tag{3.3}$$

$$\delta_\nu = \frac{\nu}{u_\tau}. \tag{3.4}$$

u_τ and δ_ν are the *friction velocity* and *viscous length scales*, respectively. The viscous length scale δ_ν is the suitable lengthscale at a viscous wall region, whereas δ is the suitable lengthscale at a outer layer region. We define

$$Re_\tau \equiv \frac{u_\tau \delta}{\nu} = \frac{\delta}{\delta_\nu}. \tag{3.5}$$

where Re_τ is the *friction Reynolds number*.

The *viscous scales* are used as *wall units* to non-dimensionalize y and u:

$$y^+ \equiv \frac{y}{\delta_\nu} = \frac{u_\tau y}{\nu}, \tag{3.6}$$

$$u^+ \equiv \frac{\langle U\rangle}{u_\tau}. \tag{3.7}$$

where y represents the distance from the wall. There is a very thin region closed the wall with $y^+ < 5$, termed *viscous sublayer*, where the inertial effects and the Reynolds shear stress can be ignored. In this region, the mean velocity profile has a universal shape given by the linear relation of the wall law $U^+ = y^+$. On the other hand, in *outer layer* region where $y^+ > 50$, the effect of molecular viscosity on shear stress is trivial and the size of the large eddies are measured by the characteristic geometrical length scale δ. This region does not have a universal velocity profile and it varies for various flows, in opposition to the universal wall law $U^+ = y^+$.

Supposing that a local equilibrium within production and dissipation of energy processes at an overlap area between *viscous sublayer* and *outer layer* regions which is for $y/\delta \ll 1$ and $y^+ \gg 1$, von Karman (1930) [82] derived the logarithmic wall law for a mean velocity profile

$$u^+ = \frac{1}{K}\log y^+ + A, \tag{3.8}$$

with $K \approx 0.4$ is called the von Karman constant with $A \approx 5.2$. Experiments [145] demonstrated that the log-law is standing for $y^+ > 30$ and $y/\delta < 0.3$.

This chapter is organized as follow. In Section 3.2 , we illustrate briefly the MTLM procedure. The optimality system of the modified CMTLM with reflectionally symmetric is derived in

Section 3.3. Section 3.4 shows the solution of the optimality system with the adjoint of the discretized advection operator. In Section 3.5, we look into the computational domain and numerical requirements. Statistical analysis of the CMTLM synthetic fields are given in Section 3.6. Conclusions are outlined in Section 3.7.

3.2 The MTLM procedure

As explained in the second chapter Sec. 2.4, after the MTLM procedure, the final field $\mathbf{u}_e$ is given by

$$\mathbf{u}_e = \mathcal{M}\boldsymbol{\varphi}, \tag{3.9}$$

where

$$\mathcal{M} = \prod_{n=1}^{M} [\mathcal{R}_n (\mathcal{P}\mathcal{A}_n)^{m_n} \mathcal{G}_n + \mathcal{G}_n^c]\mathcal{P}, \tag{3.10}$$

where $\mathcal{R}_n$ is the notation we will use here for rescaling operator in the nth iteration. In general,

$$\mathcal{R}\hat{\mathbf{u}}(\mathbf{k}) = \left(\frac{E_p(k)}{E(k)}\right)^{1/2} \hat{\mathbf{u}}(\mathbf{k}). \tag{3.11}$$

The rescaling operator is applied in order to impose the prescribed energy spectrum $E_p(k)$. Therefore, the amplitudes of the Fourier modes $\hat{\mathbf{u}}(\mathbf{k})$ are scaled proportional to $\sqrt{E(k)}$ in order to match the desired spectrum, in which $E(k)$ is the energy spectrum of $\hat{\mathbf{u}}(\mathbf{k})$ at $k = |\mathbf{k}|$, and $E_p(k)$ is a prescribed kinetic energy spectrum. $\mathcal{A}$, $\mathcal{G}$ and $\mathcal{P}$ are defined in the same way as previously in Sec. 2.4. Note that, we have changed the input to the map $\mathbf{u}(\mathbf{x})$ to $\boldsymbol{\varphi}(\mathbf{x})$ to make it consistent with the notation used in [107], however, we have also used $\mathbf{u}(\mathbf{x})$ in some notations for more clarifications.

3.3 The optimality system of the modified CMTLM with reflectionally symmetric controls

We now explain how to synthesize the turbulent channel flow with a prescribed energy spectrum $E_p(k)$ using the modified CMTLM procedure. We assume that velocity field $\mathbf{w}(\mathbf{x})$ is known, and our aim is to model some of its features with a modified CMTLM synthetic velocity field. Then the optimization problem is to find the controls $\boldsymbol{\varphi}$, state $\mathbf{u}_e$, and co-state $\boldsymbol{\xi}$ variable that minimize J over all possible $\boldsymbol{\varphi}(\mathbf{x})$ subject to the constraint equation. The solution of the optimal control and optimization problems can capture by Lagrangian multiplier methods through introducing the adjoint variable $\boldsymbol{\xi}$ [107].

In the CMTLM procedure, the Lagrangian functional is defined as

$$\mathcal{L}(\boldsymbol{\varphi}, \mathbf{u}_e, \boldsymbol{\xi}) = J(\mathbf{u}_e) + \int \boldsymbol{\xi}.(\mathbf{u}_e - \mathcal{M}\boldsymbol{\varphi})d^3\mathbf{x}, \tag{3.12}$$

where the cost function

$$J(\mathbf{u}_e) = \frac{1}{2}\|\mathcal{F}[\mathbf{u}_e(\mathbf{x}) - \mathbf{w}(\mathbf{x})]\|^2, \tag{3.13}$$

where $\mathcal{F}$ is the filtering operator that extracts some particular features of the velocity field. We suppose that velocity field $\mathbf{w}(\mathbf{x})$ is known.

The constraint equation is defined as

$$f(\mathbf{u}_e, \boldsymbol{\varphi}) = \mathbf{u}_e - \mathcal{M}\boldsymbol{\varphi} = 0. \tag{3.14}$$

The first order necessary conditions that yield an optimality system from which optimal states and design parameters may be determined to be

$$\lim_{\epsilon \to 0} \left(\frac{\mathcal{L}(\boldsymbol{\xi} + \epsilon\widetilde{\boldsymbol{\xi}}) - \mathcal{L}(\boldsymbol{\xi})}{\epsilon} \right) = 0 \Rightarrow state - equation, \text{ for arbitrary } \widetilde{\boldsymbol{\xi}}.$$

$$\lim_{\epsilon \to 0} \left(\frac{\mathcal{L}(\mathbf{u}_e + \epsilon\widetilde{\mathbf{u}_e}) - \mathcal{L}(\mathbf{u}_e)}{\epsilon} \right) = 0 \Rightarrow adjoint - equation, \text{ for arbitrary } \widetilde{\mathbf{u}_e}.$$

$$\lim_{\epsilon \to 0} \left(\frac{\mathcal{L}(\psi + \epsilon\widetilde{\psi}) - \mathcal{L}(\psi)}{\epsilon} \right) = 0 \Rightarrow optimality - condition, \text{ for arbitrary } \widetilde{\psi}.$$

Given the many desirable properties of the modified CMTLM synthetic fields, our goal is to use this procedure in order to model anisotropic turbulence near the wall. We want to consider impermeable boundary conditions, i.e., $\mathbf{u}_n = 0$ where the normal components of velocity field are zero but tangent components may be non-zero. The aim is to model $\mathbf{w}(\mathbf{x})$ with a modified CMTLM synthetic velocity field and take into account the effects of the impermeable boundary conditions.

We assume that $x_2 = 0$ is where the solid wall is. Thus we need to force $u_{e2} = 0$ at $x_2 = 0$. Our idea is in some way to make sure u_{e2} is an odd function with respect to x_2. To achieve this we limit the initial velocity field $\boldsymbol{\varphi}$ to ones that have the following properties: φ_1 is an even function of x_2, φ_2 is an odd function of x_2 and φ_3 is an even function of x_2. To enforce these properties we let

$$\boldsymbol{\varphi}(\mathbf{x}) = \frac{1}{2}[\psi(\mathbf{x}) + H\psi(H\mathbf{x})], \tag{3.15}$$

where H is defined as

$$H = \begin{pmatrix} 1 & 0 & 0 \\ 0 & -1 & 0 \\ 0 & 0 & 1 \end{pmatrix},$$

and

$$H\mathbf{x} = \begin{pmatrix} x_1 \\ -x_2 \\ x_3 \end{pmatrix} = \mathbf{x}^*.$$

Then for arbitrary ψ, $\boldsymbol{\varphi}$ is guaranteed to have the above reflectional symmetries. We will thus use ψ as the control to find the optimal solution. Note that this way is simpler then imposing these symmetries directly on $\mathbf{u}_e$. However, we do need to show $\mathbf{u}_e$ has the same symmetries. It means we need to prove that the MTLM procedure conserves the symmetries, which is done in Appendix A.

With ψ introduced, we have a new map, which is

$$\mathbf{u}_e = \mathcal{M}\left[\frac{1}{2}[\psi(\mathbf{x}) + H\psi(H\mathbf{x})]\right]. \tag{3.16}$$

Therefore, the next step is to derive the optimality system for this new map. The details are given in the Appendix A, we only summarize the results below.

The optimal solution for ψ can be found as part of the solution of the coupled optimality system, which includes the constraint Eq. 3.16, the adjoint equation and the optimality condition [107]. Setting the first variation of $\mathcal{L}$ with respect to the Lagrange multiplier $\boldsymbol{\xi}$ equal to zero, following the standard technique [64], would recover the state equation $\mathbf{u}_e = \mathcal{M}\boldsymbol{\varphi}$, where

$$\boldsymbol{\varphi}(\mathbf{x}) = \frac{1}{2}[\psi(\mathbf{x}) + H\psi(H\mathbf{x})]. \tag{3.17}$$

The adjoint equation is given through that the functional derivative of $\mathcal{L}$ with respect to the state variable $\mathbf{u}_e$ equal to zero, which is resulting in

$$\boldsymbol{\xi}(\mathbf{x}) = -\mathcal{F}[\mathbf{u}_e(\mathbf{x}) - \mathbf{w}(\mathbf{x})], \tag{3.18}$$

when $\mathcal{F}$ is a cut-off filter operator.

The optimality condition is achieved by setting the first variation of the $\mathcal{L}$ with respect to the control variable ψ equal to zero, which is equivalent to the condition

$$\lim_{\epsilon \to 0} \left(\frac{\mathcal{L}(\psi + \epsilon\widetilde{\psi}) - \mathcal{L}(\psi)}{\epsilon} \right) = -\int \frac{1}{2}[(\mathcal{M}^+\boldsymbol{\xi})(\mathbf{x}) + H(\mathcal{M}^+\boldsymbol{\xi})(H\mathbf{x})].\widetilde{\psi}(\mathbf{x})d^3\mathbf{x} = 0$$

$$= \langle \widetilde{\psi}(\mathbf{x}), \frac{-1}{2}[(\mathcal{M}^+\boldsymbol{\xi})(\mathbf{x}) + H(\mathcal{M}^+\boldsymbol{\xi})(H\mathbf{x})\rangle. \tag{3.19}$$

Thus, the Gateaux derivative of $\mathcal{L}$ with respect to ψ is

$$\frac{\delta\mathcal{L}}{\delta\psi}|_{\mathbf{u}_e,\boldsymbol{\xi}} = \frac{-1}{2}\{(\mathcal{M}^+\boldsymbol{\xi})(\mathbf{x}) + H(\mathcal{M}^+\boldsymbol{\xi})(H\mathbf{x})\}. \tag{3.20}$$

Since the adjoint equation and the state equation are solved exactly [107], we have

$$\frac{\mathcal{D}J}{\mathcal{D}\psi} = \frac{\delta\mathcal{L}}{\delta\psi}|_{\mathbf{u}_e,\boldsymbol{\xi}} = \frac{-1}{2}\{(\mathcal{M}^+\boldsymbol{\xi})(\mathbf{x}) + H(\mathcal{M}^+\boldsymbol{\xi})(H\mathbf{x})\}. \tag{3.21}$$

It can be calculated from the $\boldsymbol{\xi}$ and the operator $\mathcal{M}^+$. The optimality condition becomes

$$\{(\mathcal{M}^+\boldsymbol{\xi})(\mathbf{x}) + H(\mathcal{M}^+\boldsymbol{\xi})(H\mathbf{x})\} = 0, \tag{3.22}$$

where formally $\mathcal{M}^+$ is the adjoint operator of the tangent operator of $\mathcal{M}$ defined as

$$\mathcal{M}^+ = \mathcal{P}\prod_{n=1}^{M}(\mathcal{B}_n + \mathcal{G}_n^c) = \mathcal{P}\sum_{i=1}^{M}\mathcal{G}_{i-1}^c\prod_{n=i}^{M}\mathcal{B}_n. \tag{3.23}$$

where the operators in the products are ordered such that n increases from left to right. $\mathcal{G}_0^c$ denotes the identity operator, and $\mathcal{B}_n$ is defined by

$$\mathcal{B}_n = \mathcal{G}_n\mathcal{D}_n^{A+}\mathcal{D}_n^{R+}. \tag{3.24}$$

Where $\mathcal{D}_n^{R+}$ and $\mathcal{D}_n^{A+}$ are the adjoint of the the tangent operators of the of $\mathcal{R}_n$ and the composite $(\mathcal{P}\mathcal{A}_n)^{mn}$, respectively. Following same ideas presented in [107], we now give the expressions of the above adjoint operators for clarification. Starting with $\mathcal{R}_u$, to find the $\mathcal{D}_u^{R+}$, we use the definition of $\mathcal{R}$, Eq. 3.11, when it is acting on a generic velocity field $\mathbf{u}$. The operation of $\mathcal{D}_u^{R+}$ on a test function $\boldsymbol{\eta}(\mathbf{x})$ is given by

$$\mathcal{D}_u^{R+}\hat{\boldsymbol{\eta}}(\mathbf{k}) = \mathcal{R}_u\hat{\boldsymbol{\eta}}(\mathbf{k}) - \frac{E_p(k)^{1/2}}{E(k)^{3/2}}\zeta_{u\eta}(k)\hat{\mathbf{u}}(\mathbf{k}), \tag{3.25}$$

where $\hat{\boldsymbol{\eta}}$ is the Fourier transform of $\boldsymbol{\eta}$ and $\zeta_{u\eta}(k)$ is the co-spectrum between $\mathbf{u}$ and $\boldsymbol{\eta}$, defined as

$$\zeta_{u\eta}(k)\hat{\mathbf{u}}(\mathbf{k}) = \frac{1}{2}\oint_{\mathcal{S}_k}\hat{\boldsymbol{\eta}}^*.\hat{\mathbf{u}}d\mathcal{S}. \tag{3.26}$$

The integration is conducted over the surface $\mathcal{S}_k = \{\mathbf{k} : |\mathbf{k}| = k\}$ in the Fourier space, and the asterisk refers to the complex conjugate. The next step is to illustrate $\mathcal{D}_n^{A+}$, in which it may write

$$\mathcal{D}_n^{A+} = \mathcal{D}_{n0}^{A+}\mathcal{D}_{n1}^{A+}...\mathcal{D}_{n(m_n-1)}^{A+}, \tag{3.27}$$

Therefore, we need to find $\mathcal{D}_{ni}^{A+}$ in order to find $\mathcal{D}_n^{A+}$. We consider $\mathcal{D}_u^{A+}$, namely the adjoint of $\mathcal{PA}$ when it is applied to a generic velocity field $\mathbf{u}$. By use of test function $\boldsymbol{\eta}(\boldsymbol{x})$, the expression for $\mathcal{D}_u^{A+}$ acting on this function is given as follows:

$$\mathcal{D}_u^{A+}\boldsymbol{\eta}(\boldsymbol{x}) = \int d\mathbf{y}W(\mathbf{y} - \mathbf{x} - \mathbf{u}(\mathbf{y})t)\mathcal{P}\boldsymbol{\eta}(\boldsymbol{y})$$
$$+ \int d\mathbf{y}W(\mathbf{y} - \mathbf{x} - \mathbf{u}(\mathbf{y})t)[\nabla_y P\boldsymbol{\eta}(\boldsymbol{y})].\mathbf{u}(\mathbf{y})t, \tag{3.28}$$

where $W(.)$ is the weight function and t is the advection time parameter for the advection operator $\mathcal{A}$. ∇_y denotes the gradient operator with respect to $\mathbf{y}$. Note that $\mathcal{D}_u^{A+}$ is the same as $\mathcal{D}_{ni}^{A+}$ with $\mathbf{v}_{ni}$ replaced by $\mathbf{u}$, in which $\mathbf{v}_{ni}$ can be formed as:

$$\mathbf{v}_{ni} = (\mathcal{PA}_n)^i\mathbf{u}_{n1}, \tag{3.29}$$

for $i = 0, 1, ..., m_n-1$, where $\mathbf{v}_{n0} \equiv \mathbf{u}_{n1}$ and $(\mathcal{PA}_n)^{m_n}\mathbf{u}_{n1} = \mathbf{u}_{n2}$ Thus, $\mathbf{v}_{ni}$ for $i = 0, 1, ..., m_n-1$, and $\mathbf{u}_{n2}$ are found and stored during the solution of the state equation Eq. 3.16 in order to evaluate $\mathcal{M}^+\boldsymbol{\xi}$.

Equations 3.16, 3.18 and 3.22 are the optimality system for the optimization problem, which provides an optimal initial field $\boldsymbol{\psi}(\mathbf{x})$, so that the modified CMTLM procedure produces the synthetic field that matches the desired features in the target flow field and at the same time satisfies the impermeable boundary conditions.

3.4 Solution of the optimality system with the adjoint of the discretized advection operator

In the CMTLM technique, Li and Rosales [107] have solved the optimization problem using numerical implementation. So to find $\boldsymbol{\psi}$ that minimize the difference between $\boldsymbol{u}_e$ and $\mathbf{w}$, we will solve the state equation which is given by Eq. 3.16, adjoint equation given by Eq. 3.18, and the gradient of the cost function which is given by Eq. 3.21 using the iteration procedure as follows:

1. The state equation Eq. 3.16 can be solved by applying the MTLM procedure on $\boldsymbol{\psi}^i$ which is resulting in $\boldsymbol{u}_e^i$, and saved the intermediate velocity field.

2. Obtaining the cost function $J^i \equiv J(\boldsymbol{u}_e^i)$. Exit if $J^i < e$, otherwise continue to the next step.

3. The adjoint variable can be calculated $\boldsymbol{\xi}^i$ from the adjoint equation Eq. 3.18.

4. Using the $\boldsymbol{\xi}^i$ and the velocity field saved in the first step to evaluate the gradient of the cost function J^i with respect to the control $\boldsymbol{\psi}^i$, to perform steepest descent iterations. The gradient is given by

$$\frac{\mathcal{D}J^i}{\mathcal{D}\boldsymbol{\psi}^i} = \frac{-1}{2}\{(\mathcal{M}^+\boldsymbol{\xi^i})(\mathbf{x}) + H(\mathcal{M}^+\boldsymbol{\xi^i})(H\mathbf{x})\}. \tag{3.30}$$

5. Update the approximate solution i.e., the control $\boldsymbol{\psi}^i$ depending on steepest descent method with back tracking [108].

$$\boldsymbol{\psi}^i - \lambda\frac{\mathcal{D}J^i}{\mathcal{D}\boldsymbol{\psi}^i} \rightarrow \boldsymbol{\psi}^i, \tag{3.31}$$

where λ is the stepsize. It increased by a fraction if the cost function is successfully reduced during the current iteration. Otherwise , we reduce λ and retry the iteration. In this algorithm, starting with that $\boldsymbol{\psi}^0$, as the initial guess for $\boldsymbol{\psi}$ and a tolerance e, we repeat the above steps for i= 0, 1, 2, . . . :

As is illustrated in Ref. [107], $\frac{\mathcal{D}J^i}{\mathcal{D}\boldsymbol{\psi}^i}$ is computed in accordance to Eq. 3.30 depending on the set of nested operations for the adjoint operator $\mathcal{M}^+$ in Eq. 3.23, which can be written as

$$\mathcal{P}\{\{[...]\mathcal{B}_{M-2} + \mathcal{G}_{M-2}^c\}\mathcal{B}_{M-1} + \mathcal{G}_{M-1}^c\}\mathcal{B}_M, \tag{3.32}$$

In other words, operators in the products have been ordered such that from right to left n decrease from M to 1. Consequently, in the wavenumber space at length scale ℓ_{M-1} the evaluated $\mathcal{B}_M\boldsymbol{\xi}^i$ subject to the filter $\mathcal{G}_{M-1}$ in order to decompose it into low wavenumber components $\mathcal{B}_{M-1}\mathcal{B}_M\boldsymbol{\xi}^i$ and high wavenumber components $\mathcal{B}_M\boldsymbol{\xi}^{i^c}$. Then at length scale ℓ_{M-2}, $\mathcal{B}_{M-1}\mathcal{B}_M\boldsymbol{\xi}^i$ subject to filter $\mathcal{G}_{M-2}$ in order to decompose it into $\mathcal{B}_{M-2}\mathcal{B}_{M-1}\mathcal{B}_M\boldsymbol{\xi}^i$ and $\mathcal{B}_{M-1}\mathcal{B}_M\boldsymbol{\xi}^{i^c}$, while $\mathcal{B}_{M-1}\mathcal{B}_M\boldsymbol{\xi}^{i^c}$ are kept unchanged. This procedure will repeat until $\mathcal{B}_1\mathcal{B}_2...\mathcal{B}_M\boldsymbol{\xi}^i$ is merged with all high wavenumber components which are kept unchanged. Note that in the numerical implementation of the MTLM map, the operations are applied recursively over a set of finer and finer grids defined by the length scales, whereas CMTLM procedure is started from the finest grid and iterates on coarser and coarser ones.

Due to the nature of numerical methods, the continuous versions of the adjoint equation and gradient of the cost function are discretization when they are solved numerically. Li and Rosales [107] used a "differentiate-then-discretize" method in the numerical implementation. The numerical implementations of the CMTLM map are given in more details in the Appendix A.

3.5 Computational domain and numerical requirements

Our computation is carried out over a cubic domain of size $[0, 2\pi]^3$, discretized in a regular mesh of a $N_M^3 = 128$ nodes, with periodic boundary conditions in all three X, Y and Z directions. The prescribed energy spectrum is given by [80], [156].

$$E(k) = C_k \varepsilon^{2/3} k^{-5/3} \left[\frac{kl}{((kl)^{\alpha_2} + \alpha_1)^{1/\alpha_2}} \right]^{5/3+\alpha_3} \times \exp(-\alpha_4 k\eta)$$

with a value $C_k = 1.613$ for the Kolmogorov constant, and the parameters $\alpha_1 = 0.39$, $\alpha_2 = 1.2$, $\alpha_3 = 4.0$, $\alpha_4 = 2.1$. The imposed mean energy dissipation rate $\varepsilon = 0.1$, $\nu = 0.0018$ and the imposed r.m.s. velocity is $u_{rms} = 0.2\pi$ and it is prescribed such that these combinations of parameters results in a Reynolds number of $Re_\lambda \approx 140$ for the 128^3 mesh. We let tolerance $e = 2\%$. The number of grids points is 128^3, so we have grid size $\delta x = \pi/64$. Hence, for a given parameters δx is about three times the Kolmogorov length scale $\eta = (\nu^3/\varepsilon)$. The results shown were obtained with $M = 5$ scale levels, on grids of $4^3, 8^3, 16^3, 32^3$, and 64^3 nodes.

The modified CMTLM optimality system are solved iteratively through the implementation of modified CMTLM procedure in a modified code, 500 of the realizations synthetic velocity fields are generated. All solutions are found to within 2% tolerance in less than 10 iterations. Given that the fully developed channel flow fields are homogeneous in the streamwise and spanwise directions, so that the statistical values presented here have, unless otherwise stated, been time averaged over all the realizations and also averaged over x and z planes.

As we explained above, the effects of the wall are modelled by imposing reflection symmetry around the mid-plane of the periodic box $Y = \pi$, where Y is the distance to the bottom of the box. Due to periodicity of the domain, the plane at $Y = 3\pi$ is also a symmetric plane. As a result, the velocity fields between $Y = \pi$ and $Y = 3\pi$ is the model for the velocity field in the channel. The field is symmetric with respect to $Y = 2\pi$. Therefore, in what follows, we show the results from $Y = \pi$ to 2π only, which corresponds to $y = 0$ to π as y is the distance to the wall.

3.6 Statistical Analysis of the CMTLM Synthetic Fields

3.6.1 Mean velocities

The profiles of the turbulent mean velocities fluctuations $\langle v_x \rangle$, $\langle v_y \rangle$ and $\langle v_z \rangle$ are shown in Fig. 3.1, where $\langle \cdot \rangle$ denotes the average which is taken over different realizations and the x and z directions, and $\langle v_x \rangle$, $\langle v_y \rangle$ and $\langle v_z \rangle$ are functions of y.

The general character of the $\langle v_x \rangle$ velocity curve is quite similar to that from the DNS of Kim et al. (1987) [87]. It is evident that, the viscous stress is dominated at the wall. For example, the viscous contribution to the total shear stress accordingly to [145], drops from 92% at the wall ($y = 0$) to 42% at $y \approx 0.6$, and to less than 2% by ($y \approx 2.0$). However, the negative velocity indicates that there is a background flow adjusted to the wall, which means more works are needed to get more an accurate results.
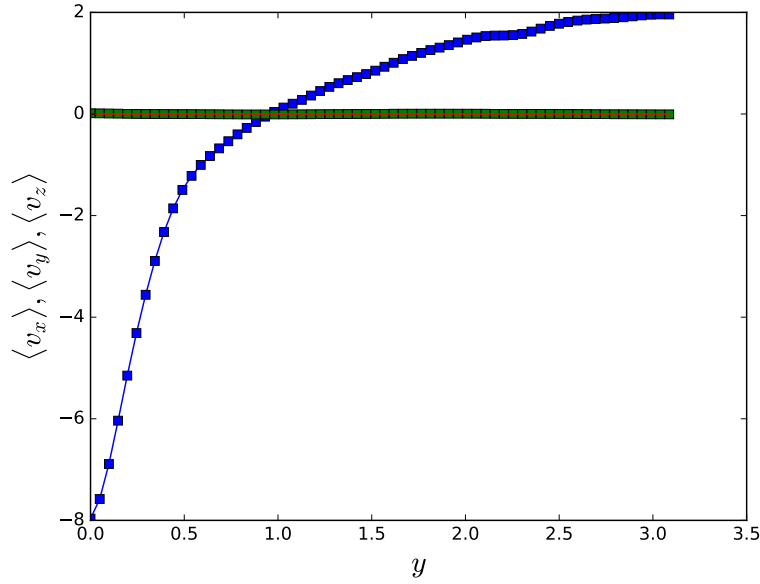
Figure 3.1: The mean velocity profiles. Blue squares: the averaged streamwise velocity, $\langle v_x \rangle$. Red line: the averaged wall-normal velocity, $\langle v_y \rangle$. Green squares: the averaged spanwise velocity, $\langle v_z \rangle$.
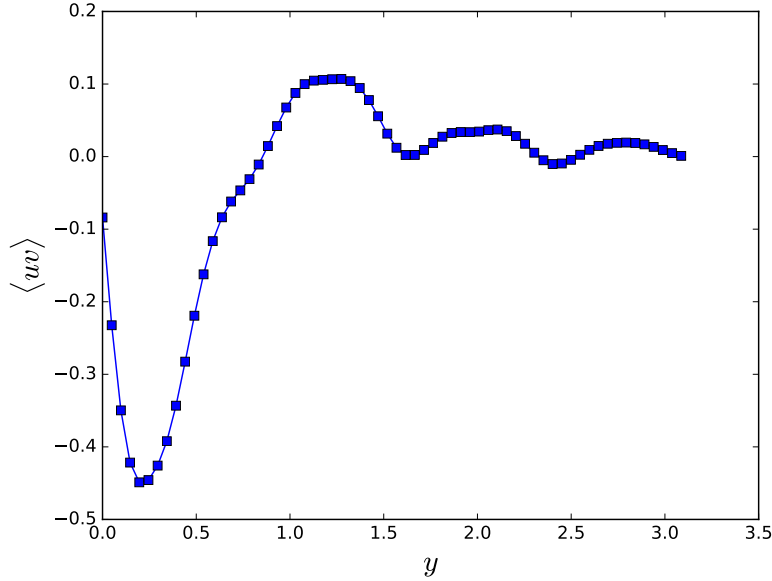
Figure 3.2: Cross correlation

3.6.2 Turbulence intensities and shear stresses

We look now at the result of cross correlation between u and v velocity components which is plotted against y, and averaged over all realizations and over x and z directions as shown in Fig. 3.2. It is evident that close to the wall $y = 0$, the viscous stress $\rho \nu \frac{d \langle U \rangle}{dy}$ dominates at the wall since $\langle uv \rangle$ close to zero. The negative value of the cross correlation for y in the range $[0, 1]$ is an

indication of the Reynolds shear stress is negligible compared with the viscous stress, and their contribution to total shear stress Eq. 3.1 in this region is zero. However, the two correlation behaviour has been a subject of some disagreement for $y \geq 0.25$, in which the profile should be a straight line when the flow reaches an equilibrium state [87].

Turbulence intensities for the three velocities fluctuations components u_{rms},v_{rms} and w_{rms} are presented in Fig. 3.3, where $u_{rms} = \sqrt{\langle u^2 \rangle}$ and $u = v_x - \langle v_x \rangle$ is the fluctuation of the x-component of the velocity. $\langle u^2 \rangle$, $\langle v^2 \rangle$ and $\langle w^2 \rangle$ are averaged over different realizations and the x and z directions and as functions of y, where $v = v_y - \langle v_y \rangle$ and $w = v_z - \langle v_z \rangle$ are the y and z-components of the velocity field. We may qualitatively compared with those at Reynolds number of 3300 from DNS data of Kim et al. (1986) [87]. The general shape of the profiles is in good agreement, in which the level of the normal component of intensity is the lowest. Also the location of maximum streamwise fluctuation is at $y \approx 0.3$, which corresponds to the location of the maximum production. Note that the maximum u_{rms} is about 1.35, where the streamwise turbulence intensity at $y = 0$ is as high as about 1.12, mainly due to the non-zero turbulence production there. There is a considerable discrepancy in turbulence intensity in the near-wall region, which possible could be ascribed to Reynolds number effects. It can be seen that there are considerable overlap between u_{rms} and w_{rms}, in which u_{rms} reaches the distinct minimum value of about 1.12, whereas w_{rms} has the distinct maximum at this region. Note, however, u_{rms} and w_{rms} are constant close to the wall. Although the normal component v_{rms} in our simulation is increasing towards a maximum in the wall-region, for obtaining accurate quantitative data for channel flow, it should decrease to zero at the wall, this is an overprediction. A similar discrepancy is noticeable for turbulence intensity for the experimental data of Hanratty el al. (1977)[67], and for DNS of Kim et al. (1986)[87].
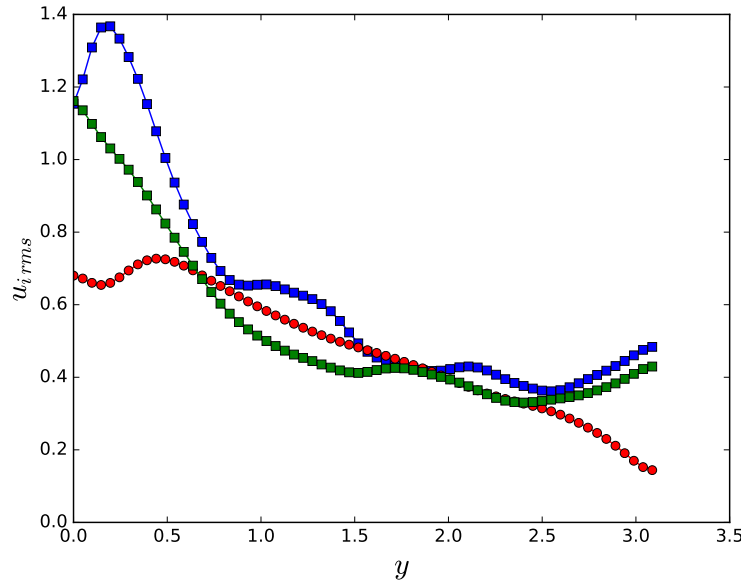
Figure 3.3: Root-mean-square velocity fluctuations. Blue squares: u_{rms}. Red circles: v_{rms}. Green squares: w_{rms}.

3.7 Conclusions

The objectives of this chapter is to provide a background about the Constrained MTLM technique, modify the CMTLM procedure to include the effects of solid wall boundaries, and synthesize the turbulent channel flow according to the modified CMTLM approach. The modified CMTLM procedure outlined in this chapter generates a reflectionally symmetric synthetic field. The symmetric field is a model of the velocity field in a fully developed channel flow. We prove that each operator of the MTLM procedure preserves the reflectional symmetries, derived the new adjoint optimality system with reflectional symmetry depending on the new map of the modified CMTLM procedure. We finally consider the mean statistics of the modified CMTLM synthetic fields in comparison with the computed and experimental results.

Our work has presented a new method for generating anisotropic synthetic turbulence with the impermeable boundary conditions and taking into account the technical difference for the turbulence on the solid wall. We set the mean channel flow profile as the target field for the modified CMTLM fields. The mean velocity generated by the modified CMTLM procedure reproduces the target field we have specified. Qualitative agreement was found in some detail for mean velocity profiles, turbulence intensities and cross correlation, in comparisons with experimental and DNS data. The fully developed channel flow is an ideal environment for testing the modelling of the anisotropic turbulence. However, further work is needed to obtain more reliable results.

Chapter 4

The Cost Function and the Adjoint Field of the Constrained Multiscale Turnover Lagrangian Map (CMTLM) method

4.1 Introduction

In this section, we study the relative importance of the $\mathcal{M}^+$ operator in the CMTLM procedure, and quantify the effects of control variable φ on a cost function gradient evolution. In accordance to Eqs. 4.6, 4.7 and 4.9, we restrict our investigations to study the structure and the behaviour of the gradient of cost function with respect to the control variable, $\frac{\mathcal{D}J}{\mathcal{D}\varphi}$, and those of the adjoint field $\boldsymbol{\xi}(\mathbf{x})$, which are built up by CMTLM procedure. In particular, we investigate the effects of imposing a different cost function , and how it affects the results, especially, when the target field is taken from DNS data. Equipped with this knowledge, we could modify CMTLM and make it more flexible to synthesize more complex turbulent flows. To do so, we look into the CMTLM synthesized two Kolmogorov flows, which have been reported in Li and Rosales [107], and we also consider an arbitrary cost function J as follows:

$$J(\mathbf{u}_e) = \mathbf{u}_e(\mathbf{x}) \cdot \mathbf{w}(\mathbf{x}), \tag{4.1}$$

in order to produce an arbitrary adjoint field $\boldsymbol{\xi}$, defined as

$$\boldsymbol{\xi}(\mathbf{x}) = -\mathbf{w}(\mathbf{x}). \tag{4.2}$$

Then, we use this arbitrary cost function and their adjoint field to analyse the CMTLM procedure. The target flow field $\mathbf{w}(\mathbf{x})$ is taken from DNS which is reported in Sec. 2.5.

The two Kolmogorov flows are synthesized using the Constrained MTLM procedure [107]. Using the adjoint formulation, Li and Rosales formulated the problem as an optimization problem. The initial random field was taken as the control variable, and it is adjusted using an adjoint-based optimization technique. Minimization of the difference between the target field and the synthetic field by an appropriate optimal control variable is the goal.

The Constrained MTLM method is a generalization of the MTLM method [156]. This method requires a known velocity field $\mathbf{w}(\mathbf{x})$ in order to formulate the problem. The aim is to model some aspects of this known velocity field via CMTLM method. To do so, we adjust the initial random Gaussian field $\varphi(\mathbf{x})$ hence adjust the non-Gaussian final field $\mathbf{u}_e$. At the optimum, $\mathbf{u}_e$ matches the desirable features of $\mathbf{w}(\mathbf{x})$.

We quickly summarize the notations. Introducing a generic cost function enables us to find such an initial field by means of an optimization procedure:

$$J(\mathbf{u}_e) = \frac{1}{2}\|\mathcal{F}[\mathbf{u}_e(\mathbf{x}) - \mathbf{w}(\mathbf{x})]\|^2, \tag{4.3}$$

where $\mathcal{F}$ is a filtering operator that extracts some specific features of a velocity field. Usually, $\mathcal{F}$ is a cut-off filter with a large filter scale to ensure that the optimization procedure will only improved the large scale structures of $\mathbf{u}_e$. The purpose of this technique is to minimize J over all possible $\varphi(\mathbf{x})$, subject to the constraint or the state equation:

$$\mathbf{u}_e = \mathcal{M}\varphi. \tag{4.4}$$

where

$$\mathcal{M} = \prod_{n=1}^{M}[\mathcal{R}_n(\mathcal{P}\mathcal{A}_n)^{m_n}\mathcal{G}_n + \mathcal{G}_n^c]\mathcal{P}. \tag{4.5}$$

In terms of optimal flow terminologies, $\boldsymbol{\varphi}$ is the control variable, $\mathbf{u}_e$ is the state variable [64].

An important step for finding the optimal solution for $\boldsymbol{\varphi}$ is introducing the Lagrangian of the system $\mathcal{L}(\boldsymbol{\varphi}, \mathbf{u}_e, \boldsymbol{\xi})$ in accordance to Eq. 3.12, where $\boldsymbol{\xi}$ is a Lagrangian multiplier or the adjoint variable. Then depending on the the standard technique [64], adjoint equation was obtained by following the condition that functional derivative of $\mathcal{L}$ with respect to the state variable $\mathbf{u}_e$ equals zero, so that the generic adjoint equation reads

$$\boldsymbol{\xi}(\mathbf{x}) = -\mathcal{F}[\mathbf{u}_e(\mathbf{x}) - \mathbf{w}(\mathbf{x})], \qquad (4.6)$$

Next, using Eqs. 4.4 and 4.6 with the optimality condition that the partial functional derivative of $\mathcal{L}$ with respect to the control variable $\boldsymbol{\varphi}$ is zero at the optimum resulting in

$$\frac{\delta \mathcal{L}}{\delta \boldsymbol{\varphi}} \Big|_{\mathbf{u}_e, \boldsymbol{\xi}} = \mathcal{M}^+ \boldsymbol{\xi}, \qquad (4.7)$$

where $\mathcal{M}^+$ is the adjoint of the tangent operator of $\mathcal{M}$, which is defined as

$$\mathcal{M}^+ = \mathcal{P} \prod_{n=1}^{M} (\mathcal{B}_n + \mathcal{G}_n^c) = \mathcal{P} \sum_{i=1}^{M} \mathcal{G}_{i-1}^c \prod_{n=i}^{M} \mathcal{B}_n, \qquad (4.8)$$

The adjoint equation and the state equation have been solved exactly [64]. Hence, the gradient of the cost function is given by [107]

$$\frac{\mathcal{D}J}{\mathcal{D}\boldsymbol{\varphi}} = \frac{\delta \mathcal{L}}{\delta \boldsymbol{\varphi}} \Big|_{\mathbf{u}_e, \boldsymbol{\xi}}. \qquad (4.9)$$

According to above results the optimality condition becomes

$$\mathcal{M}^+ \boldsymbol{\xi} = 0. \qquad (4.10)$$

The optimal synthetic field $\mathbf{u}_e$ is the solution of the optimality system which consists of the constraint Eq.4.4, the adjoint equation Eq.4.6, and the optimality condition Eq.4.10 [64]. In Li and Rosales [107], both flows exhibit anisotropic large scale circulations structures which leads to non-trivial mean flow statistics and local anisotropy in small scales. It is found that the anisotropic distribution in subgrid-scale dissipation and alignment between the subgrid-scale stress and the filtered strain rate tensor are revealed how well they reproduce anisotropic inhomogeneity effects.

Section 4.2 presents results from the first Kolmogorov flow, i.e., the analysis of contours of the mean of the gradients of the cost function and the adjoint field. In Section 4.3, the results of the gradients of the cost function with its adjoint field for the second Kolmogorov flow are analyzed. We consider the DNS data as the target field to synthesize turbulent flow field via CMTLM method in Section 4.4. In addition, the dependence of an arbitrary cost function gradient upon the control variable are illustrated via the mean statistics of the such cost function and adjoint fields. Section 4.5 summarizes the conclusions and perspectives.

4.2 The first Kolmogorov flow

The first Kolmogorov flow was produced by choosing

$$\mathbf{w}(\mathbf{x}) = A[\sin k_f y, \sin k_f x, 0], \tag{4.11}$$

where A is the forcing amplitude, chosen to match the desired spectrum $E_p(k)$. Kolmogorov flow is a three-dimensional turbulent flow driven by a deterministic sinusoidal forcing in a periodic box $[0, 2\pi]^3$, which usually contains continuous anisotropic large scale circulations. We choose $k_f = 1$ and define the set of wavenumbers: $\Omega = \{(1,0,0), (0,1,0), (-1,0,0), (0,-1,0)\}$, so that $\mathbf{w}$ is non-zero only on the set Ω [17].

The adjoint variable in terms of Fourier modes reads

$$\hat{\boldsymbol{\xi}}(\mathbf{k}) = -[\hat{\mathbf{u}}_e(\mathbf{k}) - \hat{\mathbf{w}}(\mathbf{k})], \tag{4.12}$$

for $\mathbf{k} \in \Omega$, and $\hat{\boldsymbol{\xi}}(\mathbf{k}) = 0$ otherwise. Only the difference between $\mathbf{u}_e(\mathbf{x})$ and $\mathbf{w}(\mathbf{x})$ over Ω is measured by the cost function. In other words, the operator $\mathcal{F}$ is defined to be 1 on Ω, and 0 otherwise.

The data were generated by using the energy spectrum $E_p(k)$ from the DNS of stationary turbulence flow (with 256^3 grid points), in a periodic box of size $L = 2\pi$, at a Taylor micro-scale Reynolds number $Re_\lambda \approx 140$ with the mean dissipation rate of $\epsilon = 0.1$. And the viscosity was selected according to $\nu = [\eta^4 \epsilon]^{1/3} = 0.0015$.

The CMTLM velocity fields are synthesized using the CMTLM procedure. The results shown were obtained with $M = 6$ decomposition scale levels, on grids of 8^3, 16^3, 32^3, 64^3, 128^3, 256^3 nodes, with grid size $\delta_x = \pi/128$ and tolerance $e = 3\%$ (see Ref. [107]).

4.2.1 Results and analysis

With substitution from Eq. 4.11, Eq. 4.3 becomes

$$J(\mathbf{u}^e) = \frac{1}{2}\|\mathcal{F}[u_x^e(\mathbf{x}) - w_x(\mathbf{x})]\|_2^2 + \frac{1}{2}\|\mathcal{F}[u_y^e(\mathbf{x}) - w_y(\mathbf{x})]\|_2^2. \tag{4.13}$$

Using this cost function with the corresponding adjoint variable fields Eq.4.12

$$\xi_x(\mathbf{x}) = -[u_x^e(\mathbf{x}) - w_x(\mathbf{x})], \tag{4.14}$$

and

$$\xi_y(\mathbf{x}) = -[u_y^e(\mathbf{x}) - w_y(\mathbf{x})]. \tag{4.15}$$

The initial Gaussian random velocity field $\boldsymbol{\varphi}$ to the CMTLM procedure is homogeneous in the z-direction. The gradient components of cost function $\frac{\mathcal{D}J}{\mathcal{D}\varphi_x}$, $\frac{\mathcal{D}J}{\mathcal{D}\varphi_y}$ and $\frac{\mathcal{D}J}{\mathcal{D}\varphi_z}$ are computed at the first iteration so we could see the effects of the adjoint operator $\mathcal{M}^+$.
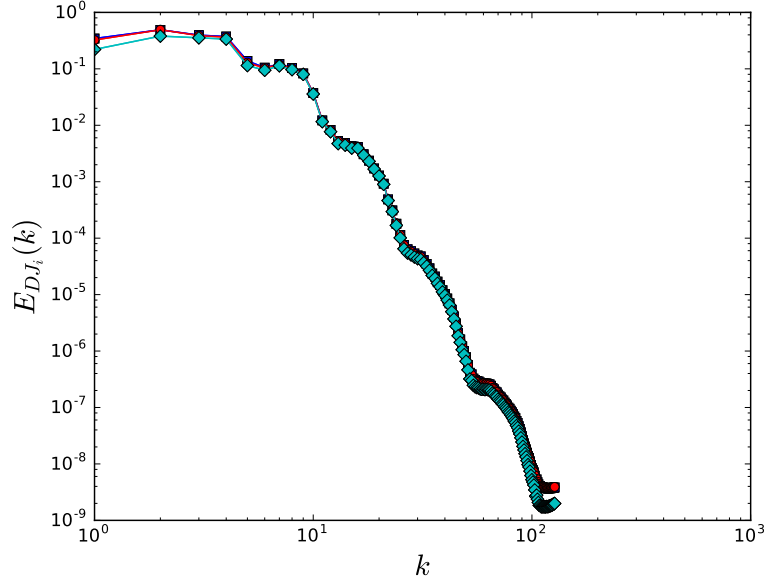
Figure 4.1: Spectra for 256^3 gradient of the cost function fields. Blue squares: the energy spectra for $\frac{\mathcal{D}J}{\mathcal{D}\varphi_x}$. Red circles: the energy spectra for $\frac{\mathcal{D}J}{\mathcal{D}\varphi_y}$. Cyan diamonds: the energy spectra for $\frac{\mathcal{D}J}{\mathcal{D}\varphi_z}$.

Fig. 4.1 shows the 3D energy spectra for the gradient of the cost function components with respect to control variable φ in x,y and z-directions $\frac{\mathcal{D}J}{\mathcal{D}\varphi_x}$, $\frac{\mathcal{D}J}{\mathcal{D}\varphi_y}$ and $\frac{\mathcal{D}J}{\mathcal{D}\varphi_z}$. We generated about 99 realizations for each component, then each energy spectral component is averaged over all these realizations. All spectral components almost agree with each others at the high wavenumber end. It showed an expected differences between them at the low wavenumber end, where the third component is the smallest one.

Note that the target field $\mathbf{w}$ is scaled by $k_f = 1$, and is non-zero only on a set of four wavenumbers: $\Omega = \{(1,0,0),(0,1,0),(-1,0,0),(0,-1,0)\}$. Thus, the cost function J depends only on $\mathbf{u}_e$ at $\|\mathbf{k}\| = 1$, which means that the cost function J just depending on the Fourier modes of the control φ at the lowest wavenumber end. However, Fig. 4.1 shows that even at high wavenumber k, $\frac{\mathcal{D}J}{\mathcal{D}\varphi} \neq 0$, which indicates that the high wavenumber Fourier modes of φ could still effect the cost J in the first range. This behaviour is justified by the nonlinearity of CMTLM procedure in which the state variable $\mathbf{u}_e$ is depending on all Fourier modes of φ as it appears from Eq. 4.4.

We now look closer into the mean values for those gradient components, in which the data are averaged in the spanwise direction at each realization, and then over all 99 realizations. Fig. 4.2, shows a contour of the mean of the gradient for the cost function $\frac{\mathcal{D}J}{\mathcal{D}\varphi_x}$, with respect to the control variable φ in the x-direction. It can be seen that the very large stretching structures mimic the target flow field. The peak value of the gradient occurs at upper half of the mean flow field which varies with y-direction and it elongates with x-direction. This can be interpreted as that increasing x-component of the control variable φ_x in that range would increase J. In contrast, increasing x-component of the control variable φ_x in the lower half of the flow field would decrease J.

Figure 4.2: Mean of the gradient for the cost function fields $\frac{\mathcal{D}J}{\mathcal{D}\varphi_x}$, with respect to the control variable $\boldsymbol{\varphi}$ on the x-direction.

Figure 4.3: Mean of the gradient for the cost function fields $\frac{\mathcal{D}J}{\mathcal{D}\varphi_y}$, with respect to the control variable $\boldsymbol{\varphi}$ on the y-direction.

As is shown in Fig. 4.3, the mean of y-component for gradient of the cost function $\frac{\mathcal{D}J}{\mathcal{D}\varphi}_y$ displays same behaviour as in Fig. 4.2. The only difference is that the anisotropic large scale structures expand along y-direction and varies with x-direction, which is compatible with y-target field component $w_y = \sin x$. There is a peak value of the gradient at the right half of the mean flow field, whereas the lower values are found at the left half of the mean flow field. Such anisotropic

large scale structures show the dependence of u_y^e and J on φ_y as discussed above.

Figure 4.4: Mean of the gradient for the cost function fields $\frac{\mathcal{D}J}{\mathcal{D}\varphi_z}$, with respect to the control variable φ on the z-direction.

Figure 4.5: Mean of the x-component of the adjoint field $\xi_x(\mathbf{x})$.
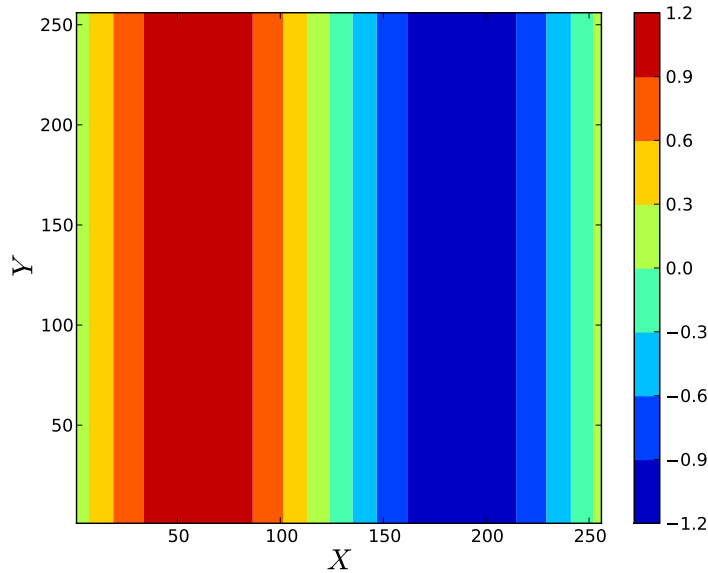
Figure 4.6: Mean of the y-component of the adjoint field $\xi_y(\mathbf{x})$.

The z-component of the mean of the gradient of the cost function $\frac{\mathcal{D}J}{\mathcal{D}\varphi}_z$ is shown in Fig. 4.4. Despite a few number of very lower values, the contours show clearly that the gradient tends to take a larger values in centre of the mean flow field, whereas lower values are observed on the boundaries. This is consistent with the imposed target flow field Eq. 4.11 since the flow field is statistically isotropic following from the homogeneity of the target vector field in the z-direction.

In what follows, in order to study the adjoint field we compute the mean of the ξ_x and ξ_y components of the adjoint field, which are saved at the first iteration and averaged over the homogeneous direction of the flow field for just one realization. The contour of the mean for ξ_x-component of the adjoint field is plotted in Fig. 4.5, which is given by Eq. 4.14. It displays a uniform distribution which is due to calculate it just for non-zero Fourier modes of u_x^e and w_x on the set $\Omega = \{(0,1,0),(0,-1,0)\}$, varies with respect to y-direction within values range $(-1,+1)$. Fig. 4.6 shows the contour of the mean for ξ_y-component of the adjoint field Eq. 4.15, at which the uniform distribution displays the difference between u_y^e and w_y over $\Omega = \{(1,0,0),(-1,0,0)\}$, and such difference elongates with y-direction and varies with x-direction.

4.3 The second Kolmogorov flow

The second Kolmogorov flow corresponds to a flow simulated by Borue and Orszag [17]. In this case a anisotropic three-dimensional large-scale flow fields are generated with large-scale constant force $f_y = F\cos(k_f x)$, where $F = 0.16$ with $k_f = 1$ in the wavenumber space. The resolution is 128^3 grid points in a periodic box of size $L = 2\pi$. Consequently, the synthetic velocity fields were generated using the CMTLM procedure on a periodic cubic domain $[0, 2\pi]^3$, discretized with 128^3 grid points [107].

The mean velocity profile is resulted from DNS of Borue and Orszag [17], which is taken as a target field for the CMTLM procedure, defined as follows:

$$\mathbf{w}(\mathbf{x}) = A[0, \cos(k_f x), 0], \tag{4.16}$$

where $A = 0.4$ with $k_f = 1$. $\mathcal{F} = 1$ on $\Omega = \{(1, 0, 0)\}$ and 0 otherwise. Using tolerance $e = 10\%$, we synthesize about 100 CMTLM fields. The mean statistics are averaged over z-direction in each realization and then over all realizations.

4.3.1 Results and analysis

The cost function equation in accordance to Eqs. 4.3 and 4.16, could be written as

$$J(\mathbf{u}^e) = \frac{1}{2} \|\mathcal{F}[u_y^e(\mathbf{x}) - w_y(\mathbf{x})]\|_2^2. \tag{4.17}$$

The adjoint field just reads

$$\xi_y(\mathbf{x}) = -[u_y^e(\mathbf{x}) - w_y(\mathbf{x})]. \tag{4.18}$$

The distributions of 3D energy spectra for the gradient of the cost function components with respect to control variable $\boldsymbol{\varphi}$ in x,y and z-directions $\frac{\mathcal{D}J}{\mathcal{D}\varphi_x}$, $\frac{\mathcal{D}J}{\mathcal{D}\varphi_y}$ and $\frac{\mathcal{D}J}{\mathcal{D}\varphi_z}$ are shown in Fig. 4.7. All energy spectral components are averaged over 99 realizations. $\frac{\mathcal{D}J}{\mathcal{D}\varphi_y}$ has the maximum energy spectra which is consistent with Eq. 4.17. The results for $\frac{\mathcal{D}J}{\mathcal{D}\varphi_x}$ and $\frac{\mathcal{D}J}{\mathcal{D}\varphi_z}$ show the dependence of the cost J on the high wavenumber Fourier modes of $\boldsymbol{\varphi}$ in the first range, which agrees with observations in Fig. 4.1.
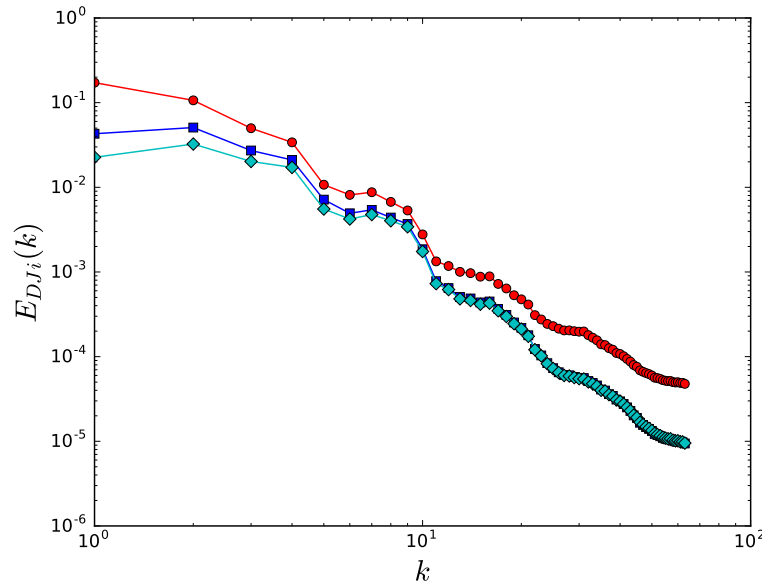
Figure 4.7: Spectra for 128^3 gradient of the cost function fields. Blue squares: the energy spectra for $\frac{\mathcal{D}J}{\mathcal{D}\varphi_x}$. Red circles: the energy spectra for $\frac{\mathcal{D}J}{\mathcal{D}\varphi_y}$. Cyan diamonds: the energy spectra for $\frac{\mathcal{D}J}{\mathcal{D}\varphi_z}$.
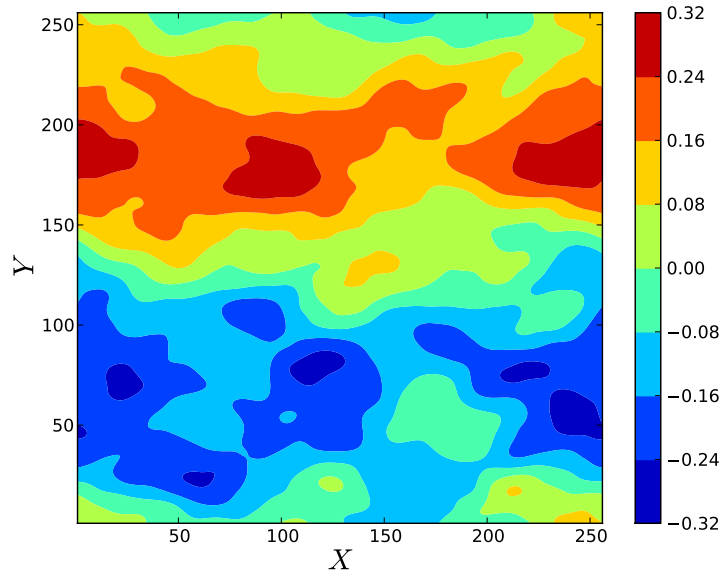
Figure 4.8: Mean of the gradient for the cost function fields $\frac{\mathcal{D}J}{\mathcal{D}\varphi_x}$, with respect to the control variable $\boldsymbol{\varphi}$ on the x-direction.
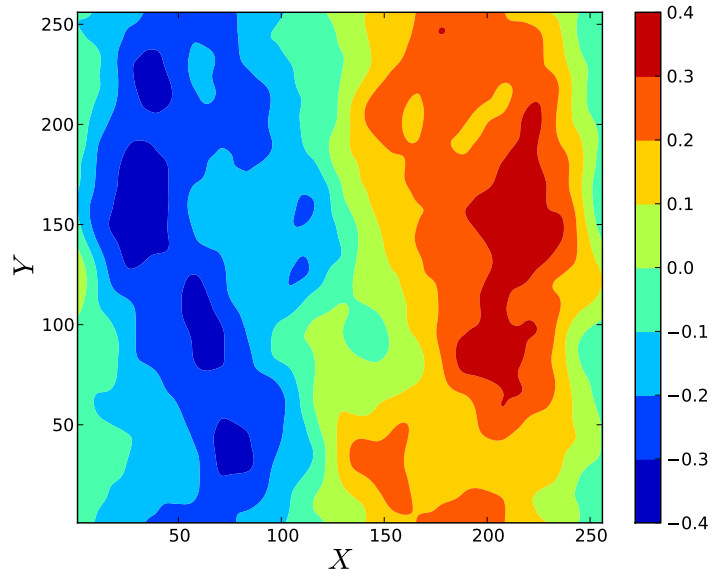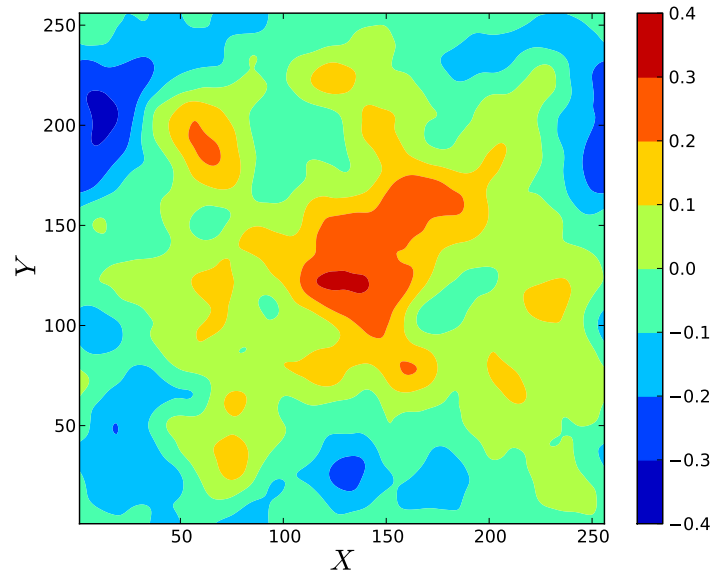

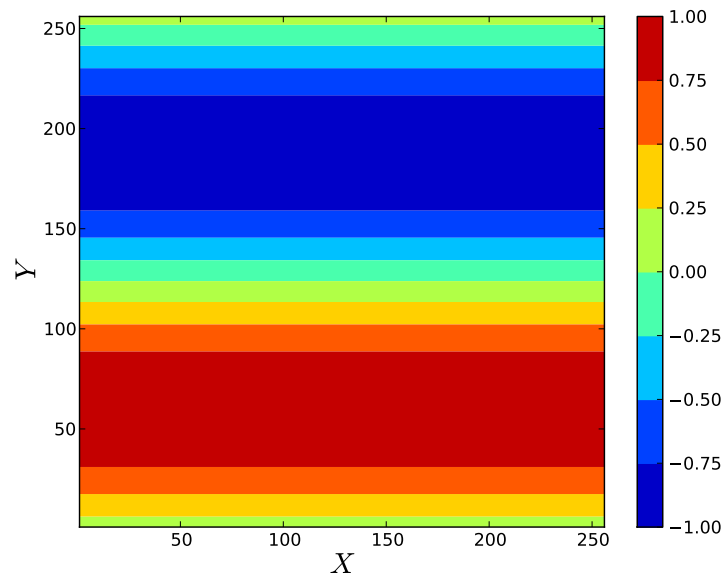Figure 4.9: Mean of the gradient for the cost function fields $\frac{\mathcal{D}J}{\mathcal{D}\varphi_y}$, with respect to the control variable $\boldsymbol{\varphi}$ on the y-direction.

The contour of the mean value of the x-component for $\frac{\mathcal{D}J}{\mathcal{D}\boldsymbol{\varphi}}$ is sketched in Fig. 4.8. We remark that the peak and lower values of anisotropic large-scale flow fields are extended along the x-direction and it varies with y-direction which mimics the target flow field Eq. 4.16, with high probability to increase J by an increasing u_y^e via increases φ_x at the high values area in the mean flow field. In the low values area of the mean field, an increasing φ_x could leads to decrease J.

On the other hand, in Fig. 4.10 of the z-component for $\frac{\mathcal{D}J}{\mathcal{D}\boldsymbol{\varphi}}$, large elongated structures are almost aligned in the y-direction, which shows the influence of the z-component of the control φ_z on the evolution of the gradient of the cost function J.
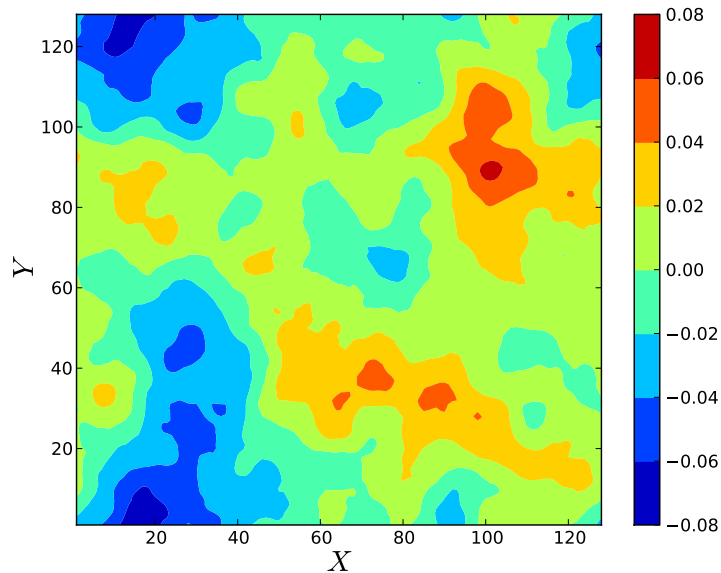
Figure 4.10: Mean of the gradient for the cost function fields $\frac{\mathcal{D}J}{\mathcal{D}\varphi_z}$, with respect to the control variable $\boldsymbol{\varphi}$ on the z-direction.
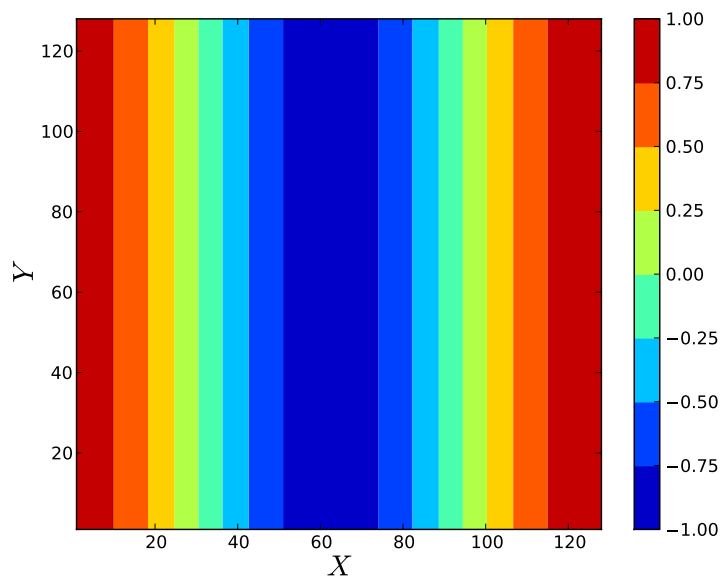
Figure 4.11: Mean of the y-component of the adjoint field $\xi_y(\mathbf{x})$

Eq. 4.2 expresses the adjoint field in Fourier space with limited number of non-zero components. However, we have only non-zero y-component of the adjoint field Eq. 4.15 for the second Kolmogorov flow. The overall behaviour of ξ_y is on the whole quite similar to the y-components of $\frac{\mathcal{D}J}{\mathcal{D}\varphi}$, as can be seen from Figs. 4.9 and 4.11. They show a uniform distribution, with one difference, which is the reversed peak and lower values locations. The peak values are located on the lift and right boundaries, and the lower values are located at the middle of the mean field for ξ_y, while it is reversed for the y-components of $\frac{\mathcal{D}J}{\mathcal{D}\varphi}$. In addition, in both cases different levels of contours are found in the x-direction which extend in y-direction, but with bigger range $(-1, +1)$ for $\xi_y(\mathbf{x})$.

4.4 Using DNS data as the target

In the Kolmogorov flows a specific cost function has been used, in which it measured the difference between the state variable $\mathbf{u_e}$ and the target field $\mathbf{w}$ over a limited set Ω. In this case we introduce another cost function in order to get more general results. The cost function and their adjoint field have been given in Eqs. 4.1 and 4.2:

$$J(\mathbf{u}^e) = u_x^e(\mathbf{x}) \cdot w_x(\mathbf{x}) + u_y^e(\mathbf{x}) \cdot w_y(\mathbf{x}) + u_z^e(\mathbf{x}) \cdot w_z(\mathbf{x}), \tag{4.19}$$

with

$$\xi_x(\mathbf{x}) = -w_x(\mathbf{x}), \tag{4.20}$$

$$\xi_y(\mathbf{x}) = -w_y(\mathbf{x}), \tag{4.21}$$

and

$$\xi_z(\mathbf{x}) = -w_z(\mathbf{x}). \tag{4.22}$$

These equations now are employed to synthesize CMTLM velocity field using DNS data for $\mathbf{w}$, in order to study the adjoint operator properties $\mathcal{M}^+$. We recalculate the mean statistics for the above equations following the same way as in Sec. 4.2.1.

4.4.1 Results and analysis

The results for the 3D energy spectra for the gradient of the cost function components with respect to control variable $\boldsymbol{\varphi}$ in x, y, and z-directions $\frac{\mathcal{D}J}{\mathcal{D}\varphi_x}$, $\frac{\mathcal{D}J}{\mathcal{D}\varphi_y}$ and $\frac{\mathcal{D}J}{\mathcal{D}\varphi_z}$ are plotted in Fig. 4.12. It is averaged over 99 realizations. It displays same behaviour as in Fig. 2.1 for the first Kolmogorov flow except that it has lower values at the anisotropic low wavenumber end, and the x-component agrees with z-component rather than with y-component. Overall it confirms again the nonlinearity of CMTLM procedure.
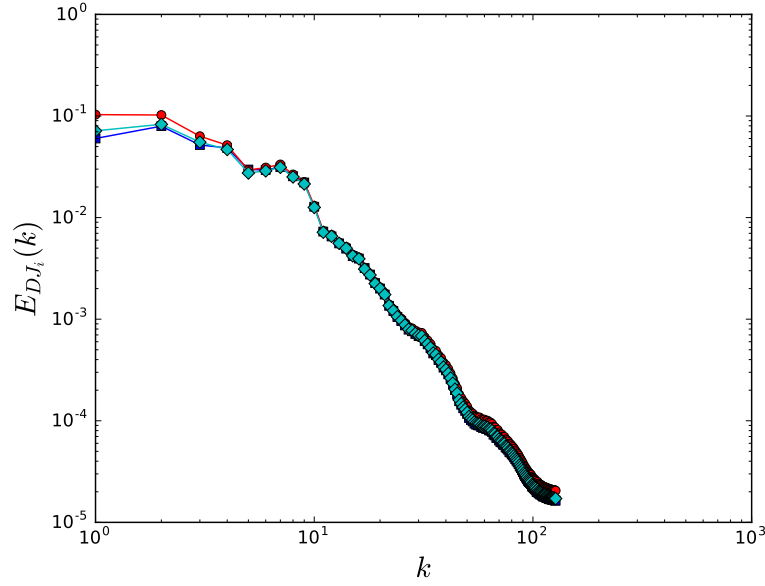
Figure 4.12: Spectra for 256^3 gradient of the cost function fields. Blue squares: the energy spectra for $\frac{\mathcal{D}J}{\mathcal{D}\varphi_x}$. Red circles: the energy spectra for $\frac{\mathcal{D}J}{\mathcal{D}\varphi_y}$. Cyan diamonds: the energy spectra for $\frac{\mathcal{D}J}{\mathcal{D}\varphi_z}$.
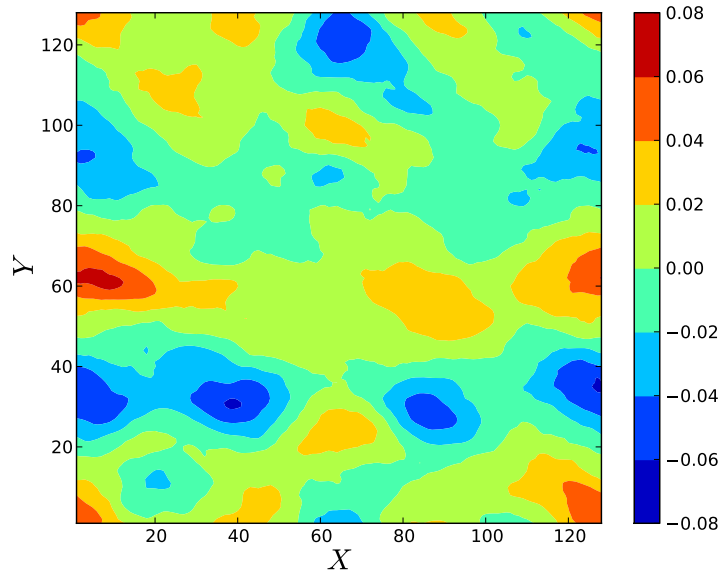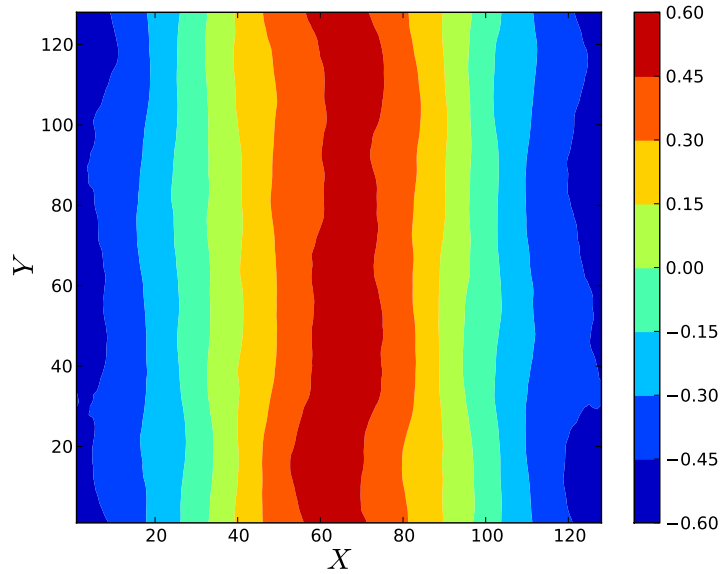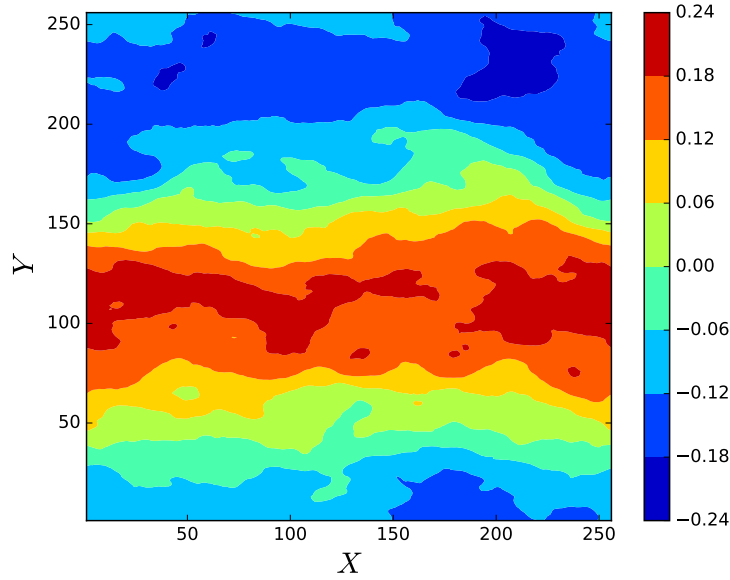

Figure 4.13: Mean of the gradient for the cost function fields $\frac{\mathcal{D}J}{\mathcal{D}\varphi_x}$, with respect to the control variable φ on the x-direction.

Figs. 4.13, 4.14 and 4.15 presented the contours of the mean of $\frac{\mathcal{D}J}{\mathcal{D}\varphi_x}$, $\frac{\mathcal{D}J}{\mathcal{D}\varphi_y}$ and $\frac{\mathcal{D}J}{\mathcal{D}\varphi_z}$, respectively. Despite that the contours for $\frac{\mathcal{D}J}{\mathcal{D}\varphi_x}$, $\frac{\mathcal{D}J}{\mathcal{D}\varphi_y}$ show that the gradient tends to take larger values in the medial of mean flow field, the mean gradient distributions show a close correlation with those in Figs. 4.2, 4.3 and 4.4. In addition, the same can be said about the dependence of the cost

96
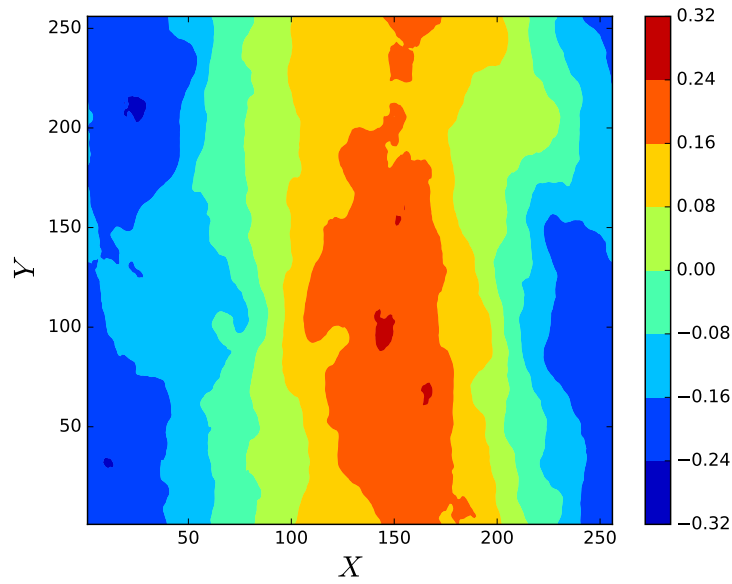
Figure 4.14: Mean of the gradient for the cost function fields $\frac{\mathcal{D}J}{\mathcal{D}\varphi_y}$, with respect to the control variable $\boldsymbol{\varphi}$ on the y-direction.
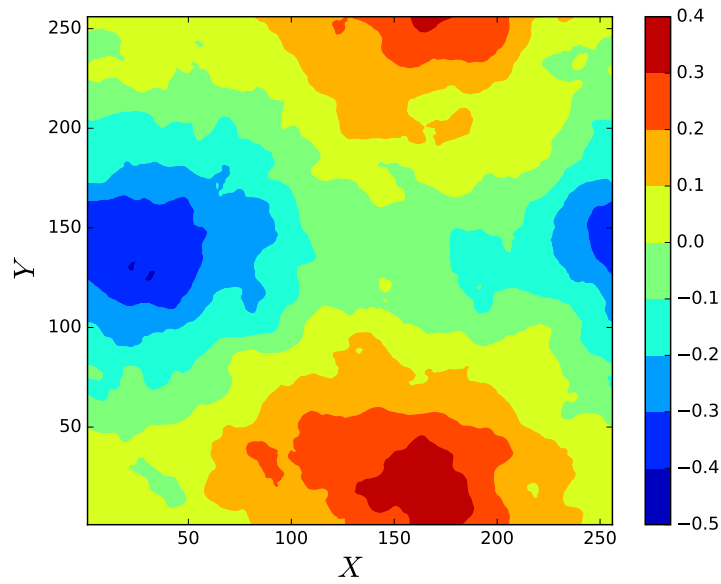
Figure 4.15: Mean of the gradient for the cost function fields $\frac{\mathcal{D}J}{\mathcal{D}\varphi_z}$, with respect to the control variable $\boldsymbol{\varphi}$ on the z-direction.

function J on the control variable $\boldsymbol{\varphi}$ via the the state variable $\mathbf{u}_e$.
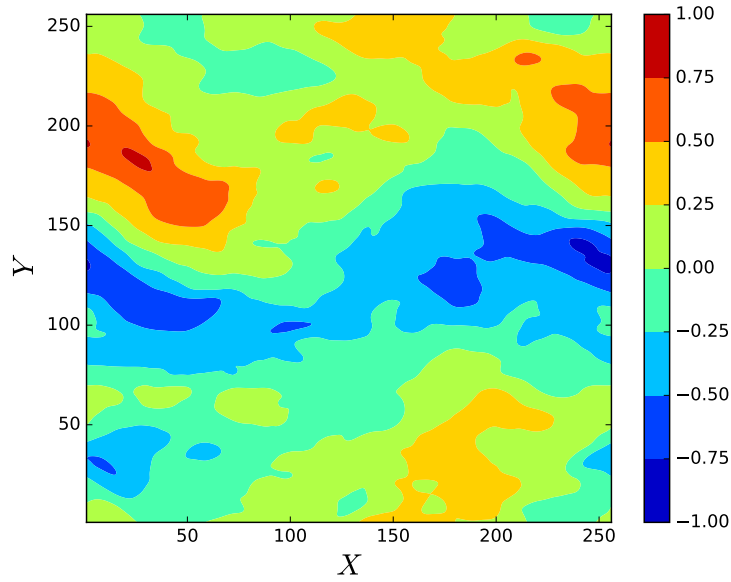
Figure 4.16: Mean of the x-component of the adjoint field $\xi_x(\mathbf{x})$.

Contours of the mean of ξ_x, ξ_y, and ξ_z-components of the adjoint fields as expressed in Eqs. 4.20, 4.21 and 4.22 are shown in Figs. 4.16, 4.17 and 4.18, respectively. As previously observed in Figs. 4.5 and 4.6 for first Kolmogorov flow, and for second Kolmogorov flow Figs. 4.9 and 4.11, it also present the same behaviour for the gradient of the cost function but with opposed peaks locations as can be seen from Figs. 4.13, 4.14 and 4.15.
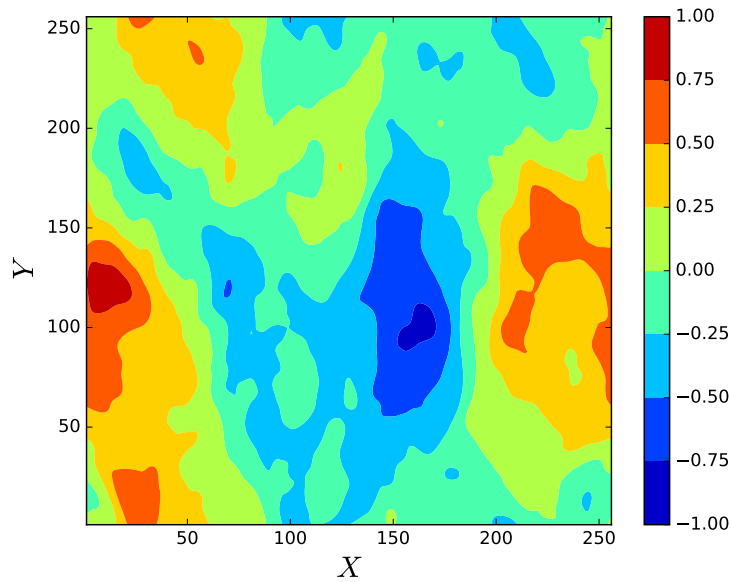
Figure 4.17: Mean of the y-component of the adjoint field $\xi_y(\mathbf{x})$.
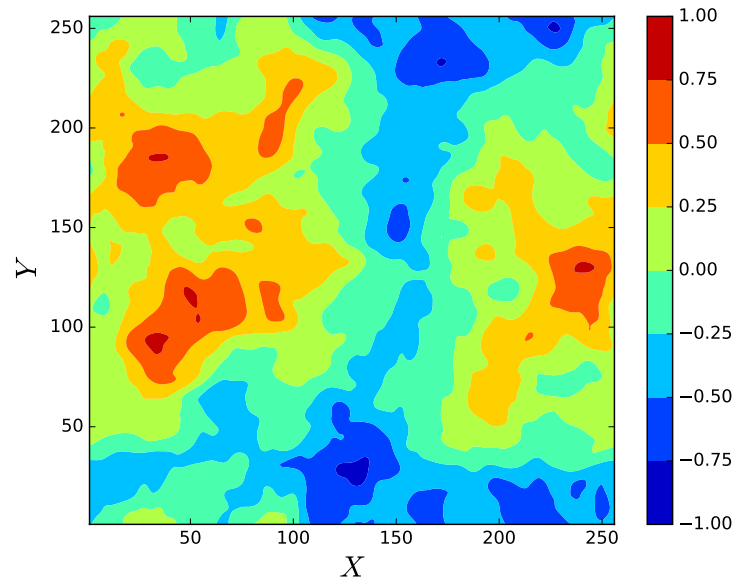
Figure 4.18: Mean of the z-component of the adjoint field $\xi_z(\mathbf{x})$.

4.5   Conclusions

The Constrained Multiscale Turnover Lagrangian Map method [107] has been used to produce anisotropic synthetic turbulence, where it generalized the MTLM method [156] In previous works, the adjoint fields and the gradients of the cost function have not be thoroughly investigated. Consequently, one is curious about the effects that could occur by using different cost functions. Therefore, we quantify in this chapter how the cost function gradient depends upon the control variable φ, thus highlight the contributions of the adjoint operator $\mathcal{M}^+$ in the modelling process. This study focuses on the cost function gradient and adjoint calculated from two CMTLM Kolmogorov flows. Also we use the CMTLM procedure to synthesize a flow with a target taken from DNS data, a new cost function and corresponding adjoint field. From 3D spectra of the gradient of the cost function fields, we can see the nonlinearity of CMTLM procedure through spectral behaviour on the anisotropic low wavenumber end, which shows contributions of all Fourier modes of the control variable φ to the state variable $\mathbf{u}_e$.

The contours of the mean of the gradient of J, with respect to the control variable $\boldsymbol{\varphi}$, for the Kolmogorov flows, are quite correlated to the target flow field $\mathbf{w}$. In addition, the z-component of the mean of the gradient for all cases emphasized the homogeneity of the target flow field in z-direction.

We conclude that the target field has considerable impacts on the adjoint field and the gradient of the cost function, which has been demonstrated by the above results. More insights can be obtained by considering other statistics, which include the correlation between the flow structures in the target fields and the adjoint field or the gradient of the cost function, and related conditional statistics. These analyses are topics for future investigations.

Chapter 5

The Constrained Multiscale Turnover Lagrangian Map Synthetic Fields as Sub-gridscale Models

5.1 Introduction

Turbulence has a wide range of length and time scales, which requires enormous computer resources. The complication and strong sensitivity to initial conditions of turbulent flow fields makes it hard to be simulated. Consequently, turbulence models are used in order to minimize the level of characterization of the flow field. In LES, the models are called SGS models.

A SGS model supplies an evaluation of the unresolved velocity and temperature fields, which are captured in the SGS stress tensor and heat flux. There are several models used in LES as SGS models, for instance, the eddy viscosity models, the similarity models , mixed models and dynamic models (see e.g. [103] , [55] , [58] and [59] for a review). In spite of the major advances in SGS modelling, model performance for various flows and for higher Reynolds numbers still requires further work.

We seek for a new SGS model to simulate turbulence interaction via a combination of LES and CMTLM method. As a first step to do that, we will merge a DNS field and a CMTLM field, then assess its achievement in modelling the interactions between large and small scales. We examine geometrical alignment aspects of the filtered vorticity vector, filtered strain-rate and the SGS stresses tensors, compared with relevance results of DNS data.

Section 5.2 reviews the truncation of the 256^3 DNS data into three truncated DNS data sets with 128^3, 64^3 and 32^3 grid resolutions, then these truncated DNS data sets are filtered with cutoff wavenumber filter with large filter scale $\Delta = 32\delta_x$ to obtain the target field. CMTLM data sets with 128^3, 64^3 and 32^3 grid resolutions are generated using CMTLM approach with those DNS data sets as target. We describe the combination between the truncated DNS and the CMTLM synthetics fields at cutoff wavenumber $k_c = \pi/4$. The merged fields are called TDNS-CMT fields. The properties of the SGS energy dissipation in the merged fields are examined in comparison with DNS fields in Section 5.2 as well. The geometric alignment statistics of real (DNS) and modelled (TDNS-CMT fields) SGS energy stress tensor are investigated in Section 5.3. We present our conclusions in Section 5.4.

5.2 TDNS-CMT merged velocity field structure and relevance importance statistics

We demonstrate in this section how to merge between the DNS data and CMTLM field, that is, how to build up a new merged velocity field from the truncated DNS and the CMTLM data in order to investigate the ability of the CMTLM method to reconstruct the turbulent fluctuations for LES. In this case, we will explicitly reconstruct the turbulent velocity fluctuations. We conduct three a priori tests, examining the ability of the TDNS-CMT fields to reproduce the alignments of the SGS stress eigenvectors with the filtered vorticity and filtered strain-rate eigenvectors in filtered DNS data, and the statistics of the SGS energy dissipation.

5.2.1 The filtered DNS data sets description

In the actual formation of the new TDNS-CMT merged field, the DNS parameters are summarized in Sec. 2.5 (Eq. 2.2). Three different truncated DNS velocity fields are extracted from 256^3 DNS velocity field. These fields have 128^3, 64^3 and 32^3 grid points, respectively. We will indicate these three truncated DNS fields by 128^3 TDNS, 64^3 TDNS and 32^3 TDNS fields. Then these three truncated DNS fields are spatially filtered via a cut-off filter with a large filter scale $\Delta = 32\delta x$ and these filtered truncated DNS fields are used as the target fields in the generation of the CMTLM synthetic fields, and as part of the construction of the new TDNS-CMT merged velocity fields.
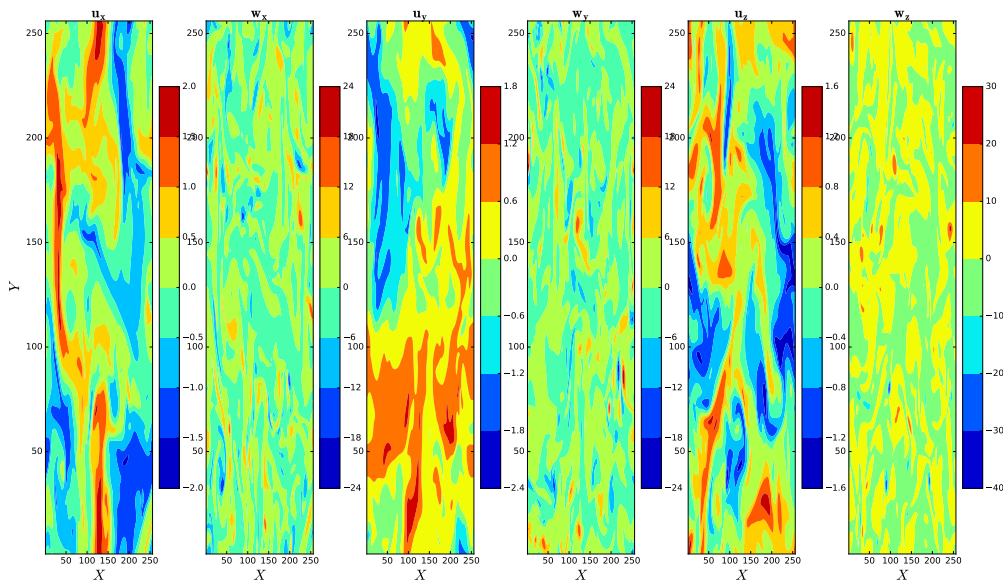
Figure 5.1: The contours of the x, y and z velocity and vorticity components for 256^3 DNS field on a two dimensional cut.

To illustrate the structure of the 256^3 DNS fields, Fig 5.1 shows the contours of the three components of the velocity and vorticity fields on a two dimensional cut of the DNS fields. Overall velocities distributions show an anisotropic large scale structure, straining and rotation almost dominate in the middle of the square and centres of the counter rotating velocities

on the left and bottom boundaries for u_x and u_y, respectively. It is observed that the large scale circulation where the straining is the strongest [107](i.e., where the strain-rate magnitude becomes maximum) is elongated along the elongation directions of the gradient. The contours of the three components of vorticity ω_x, ω_y and ω_z follow closely what one would find from the vorticity definition $\nabla \times \mathbf{u}$, and the distributions of vorticity components display a close correlation with the distributions of relevance velocity components shown in same figure.

Fig. 5.2 displays the prescribed energy spectra $E_p(k)$ used in CMTLM which are taken from the 128^3, 64^3 and 32^3 truncated DNS fields, respectively.
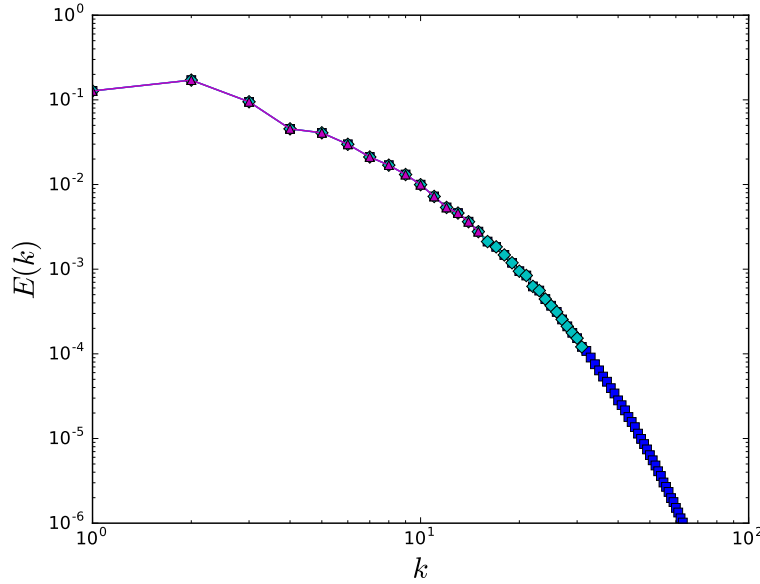
Figure 5.2: The energy spectra for a truncated DNS velocity fields. Blue squares: 128^3 truncated DNS field. Cyan diamonds: 64^3 truncated DNS field. Medium-orchid triangles: 32^3 truncated DNS field.

5.2.2 CMTLM data sets description

We will construct the TDNS-CMT merged velocity fields from the above outlined filtered DNS fields with those calculated from CMTLM method. To obtain the CMTLM data sets, we use the CMTLM method to generate 10 realizations of the synthetic fields in periodic box $[0, 2\pi]^3$, with grid points $N^3 = 128^3$, $N^3 = 64^3$, and $N^3 = 32^3$ with tolerance $e = 2\%$ for all grid sizes. Thus the corresponding grid size are $\delta x = \pi/64$, $\delta x = \pi/32$, and $\delta x = \pi/16$, respectively. The 3D input energy spectra $E_p(k)$ for these cases are taken from the previously described 128^3, 64^3 and 32^3 truncated DNS data sets. The spectra are shown in Fig 5.2. The number of iteration levels M is given as 6, 5, and 4 for 128^3, 64^3, and 32^3 grid points, respectively.

5.2.3 TDNS-CMT data sets description and their SGS energy dissipation

The TDNS-CMT merged velocity field can be constructed by applying a cut-off wavemunber filter with a large filter scale $\Delta = 32\delta_x$ in the wavenumber space to the DNS velocity fields generated in Sec. 5.2.1 as a first step, in which we employ a cutoff filter at wavenumber $k_c = 4$. Then, the DNS velocity field truncated at the wavenumber $|\mathbf{k}| \leq k_c$ would be merged with the high wavenumber components of 128^3, 64^3 and 32^3 CMTLM velocity fields at the wavenumber $|\mathbf{k}| > k_c$, respectively. We will indicate the cases Case A, with 128^3 grid size, Case B, with 64^3 grid size, and Case C, with 32^3 grid size, respectively.
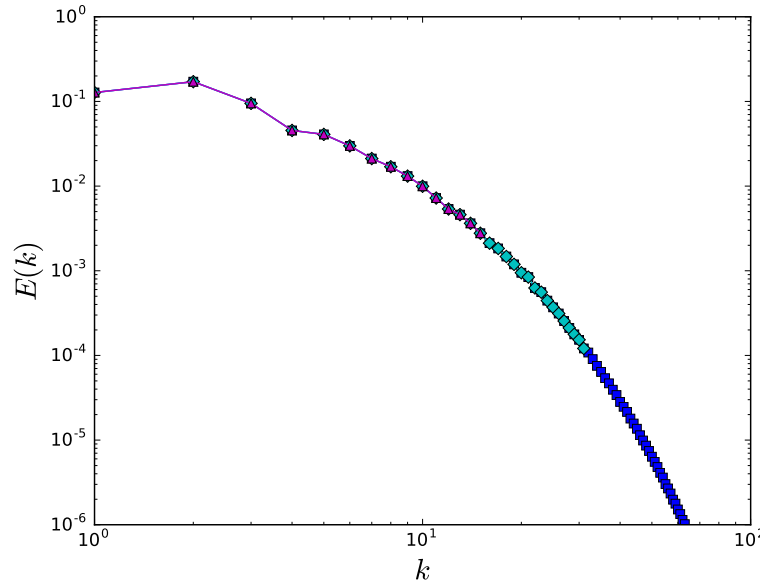
Figure 5.3: The energy spectra for a TDNS-CMT merged velocity field. Blue squares: 128^3 TDNS-CMT field. Cyan diamonds: 64^3 TDNS-CMT field. Medium-orchid triangles: 32^3 TDNS-CMT field.

Fig. 5.3 shows energy spectra through 128^3, 64^3 and 32^3 grid sizes for the TDNS-CMT merged velocity fields. It is seen from the figure the expected behaviours at the low wavenumber parts of the spectra due to filtered DNS data sets contributions in TDNS-CMT velocity fields. We produced 10 realizations of the merged DNS-CMT velocity fields.
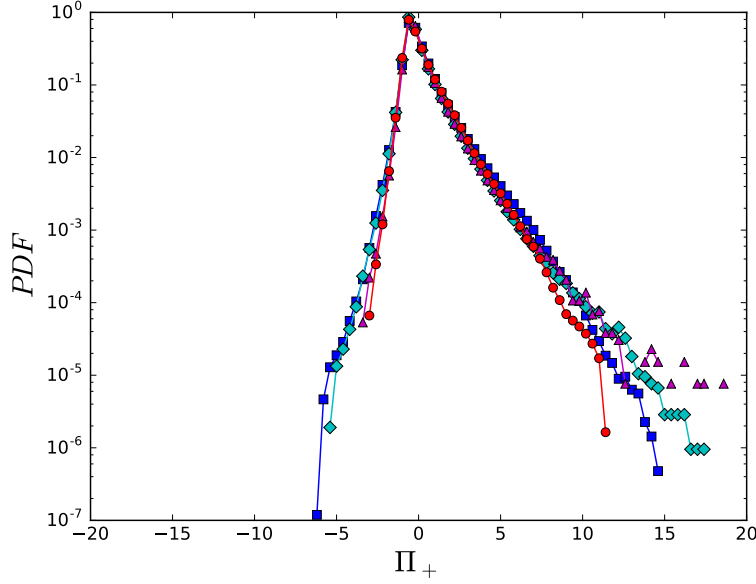
Figure 5.4: The PDFs of the normalized SGS energy dissipation using the Gaussian filter with filter scale $\Delta = \pi/4$: $\Pi_+ = (\Pi - \langle\Pi\rangle)/\sigma_\Pi$. Blue squares: 128^3 TDNS-CMT merged velocity field. Cyan diamonds: 64^3 TDNS-CMT merged velocity field. Medium-orchid triangles: 32^3 TDNS-CMT merged velocity field. Red circles: 256^3 DNS velocity field.

The PDFs of the normalized SGS energy dissipation $\Pi_+ = (\Pi - \langle\Pi\rangle)/\sigma_\Pi$ among different grid sizes for 128^3, 64^3 and 32^3 TDNS-CMT merged velocity fields and for 256^3 DNS field are shown in Fig. 5.4. These PDFs are obtained via using the Gaussian filter[145] with filter scale Δ. In all three cases the filter scale Δ is chosen as $\Delta = 32\delta x$ in accordance to 256^3 grid resolution, which yields $\Delta \approx 100\eta$. Therefore, for the low resolution 128^3, 64^3 and 32^3 results, the filter scales are taken as 16 times, 8 times, and 4 times of the respective grid sizes. Therefore, that the present filter scales keep the same as the one applied in the analysis of the 256^3 data. The PDFs are averaged over all 10 realizations of the TDNS-CMT fields in each case.

We note that the PDFs show a modest positive skewness with a weak probability for negative fluctuations, especially for 64^3 which indicates a weak backscattering from small to large scales. Also these PDFs agree well with each other except some differences specially at large positive tails, and between the PDFs of 32^3 TDNS-CMT fields and DNS data, and the PDFs between 128^3 and 64^3 TDNS-CMT fields at negative fluctuations tails. Comparing with 256^3 DNS, we observe that the TDNS-CMT field have very good quantitative agreement, except that TDNS-CMT results have a somewhat longer tails than the 256^3 DNS ones.

The PDFs of Π_+ in Fig 5.5 are computed for the same data sets, i.e., the 256^3 DNS field and Case A, Case B and Case C that have been used in Fig. 5.4, but it is computed with filter scale $\Delta = 16\delta x$ ($k_c = 8, \delta_x = 2\pi/256$). As expected, it displayed a stronger positive skewness (wider tails) in comparison with ones for the larger filter scale. However, it also display weak negative fluctuations but with longer tails. In addition, it also shows a better agreement with the PDF of 256^3 DNS field.

106
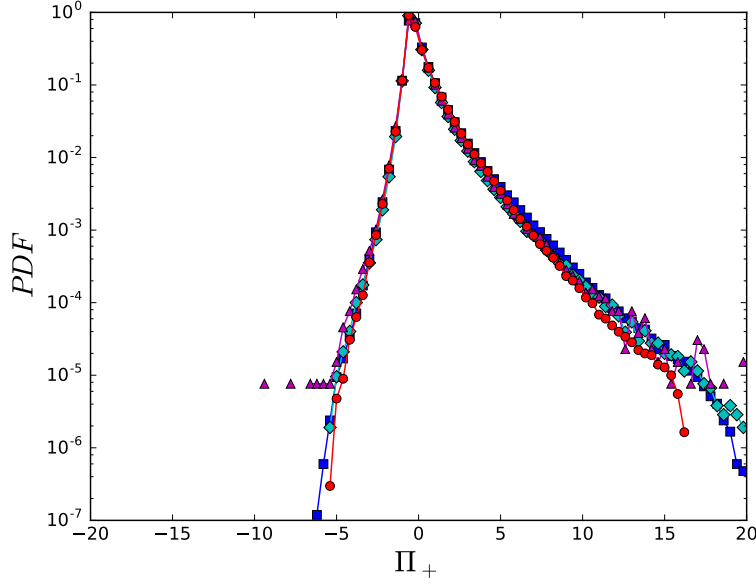
Figure 5.5: The PDFs of the normalized SGS energy dissipation using the Gaussian filter with filter scale $\Delta = \pi/8$: $\Pi_+ = (\Pi - \langle\Pi\rangle)/\sigma_\Pi$. Blue squares: 128^3 TDNS-CMT merged velocity field. Cyan diamonds: 64^3 TDNS-CMT merged velocity field. Medium-orchid triangles: 32^3 TDNS-CMT merged velocity field. Red circles: 256^3 DNS velocity field.

5.3 The Geometrical alignment statistics for TDNS-CMT merged velocity fields

From a statistical geometry point of view, we will look at the SGS stress tensor $-\tau_{ij}$ alignment trends with respect to the filtered flow structures like vorticity and principal strain directions. In this task we use 2D joint PDFs to describe the orientations of the eigenvectors of the SGS stress tensor $-\tau_{ij}$ in the eigenframe of the filtered strain rate tensor $\tilde{S}_{ij}$. This basis assigned by eigenvectors of filtered strain-rate tensor $\widetilde{S}_{ij}$ is shown in Fig. 2.12.

The alignment of $\alpha_{-\tau}$ gives one peak at approximately $(\theta_\alpha, \phi_\alpha) = (50°, 43°)$ with peak value 1.5, as can be seen from Fig. 5.6 (a) for the alignment trends between the eigenvector $\alpha_{-\tau}$ and the eigenframes of $\widetilde{S}_{ij}$ for the 256^3 DNS data. For comparison, the two-dimensional joint PDFs of $\cos\theta_\alpha$ and ϕ_α for 128^3 (Case A), 64^3 (Case B) and 32^3 (Case C) TDNS-CMT merged velocity fields, given in Fig. 5.6 (b), (c) and (d), respectively, display as well one peak at approximately $(50°, 43°)$, which is the same as the ones for DNS result, but with higher peak values for Case B and Case C.

In Fig. 5.7, we introduced the orientation of the eigenvector $\beta_{-\tau}$ in the eigenframe of $\widetilde{S}_{ij}$ using the same method. At angles $(\theta_\beta, \phi_\beta) = (90°, 0°)$, there is one peak in the joint PDFs for 256^3 DNS data and for cases A, B and C, with peak values 1.2, 1.5, 1.7 and 1.5, as shown in Fig. 5.7 (a), (b), (c) and (d), respectively.
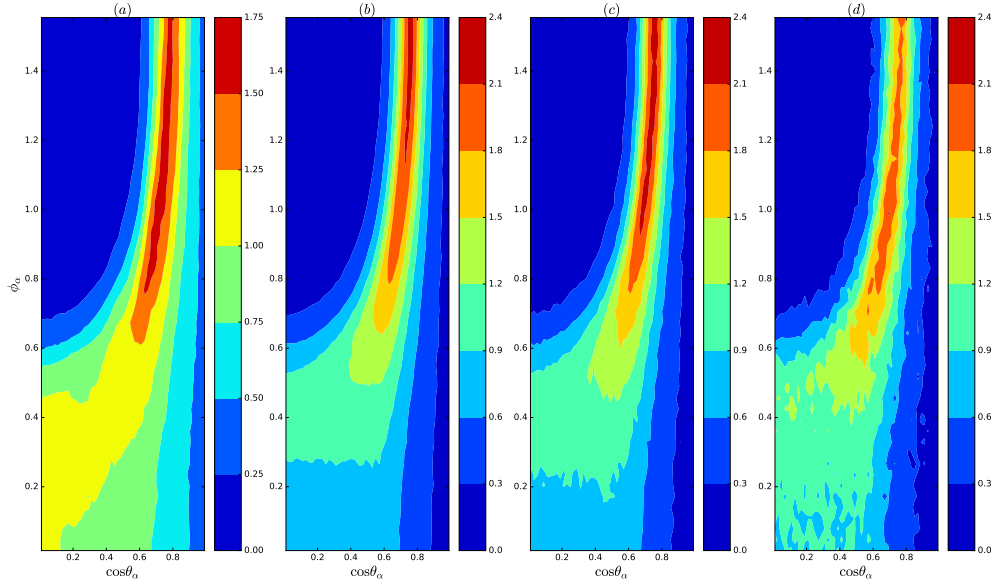
Figure 5.6: Joint PDFs of $(\cos\theta_\alpha, \phi_\alpha)$. (a): 256^3 DNS velocity field. (b): 128^3 TDNS-CMT merged velocity field. (c): 64^3 TDNS-CMT merged velocity field. (d): 32^3 TDNS-CMT merged velocity field.
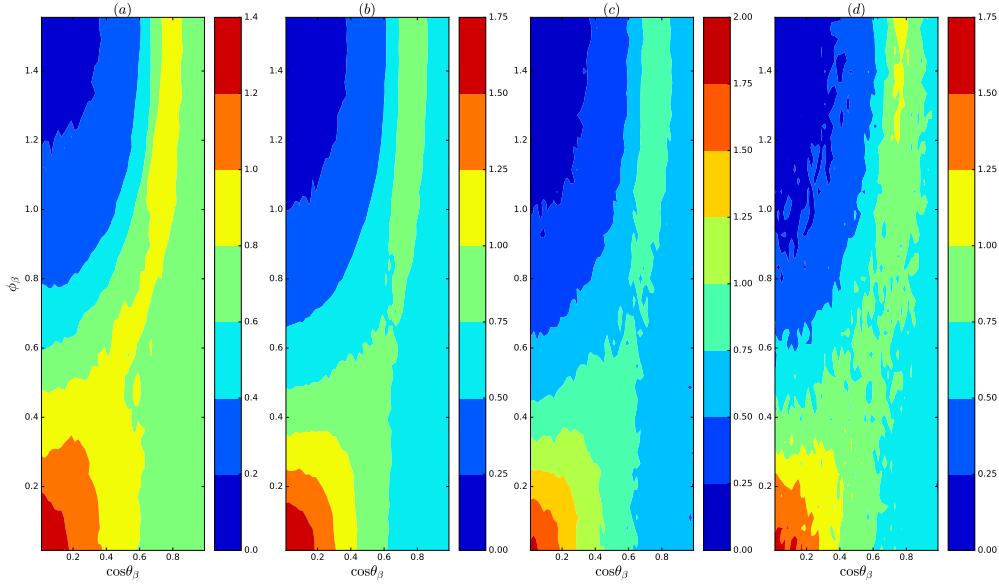
Figure 5.7: Joint PDFs of $(\cos\theta_\beta, \phi_\beta)$. (a): 256^3 DNS velocity field. (b): 128^3 TDNS-CMT merged velocity field. (c): 64^3 TDNS-CMT merged velocity field. (d): 32^3 TDNS-CMT merged velocity field.

The joint PDFs of the orientation for the eigenvector $\gamma_{-\tau}$ is shown in Fig. 5.8. $\theta\gamma$ and $\phi\gamma$ are defined using Fig. 2.12 as well.
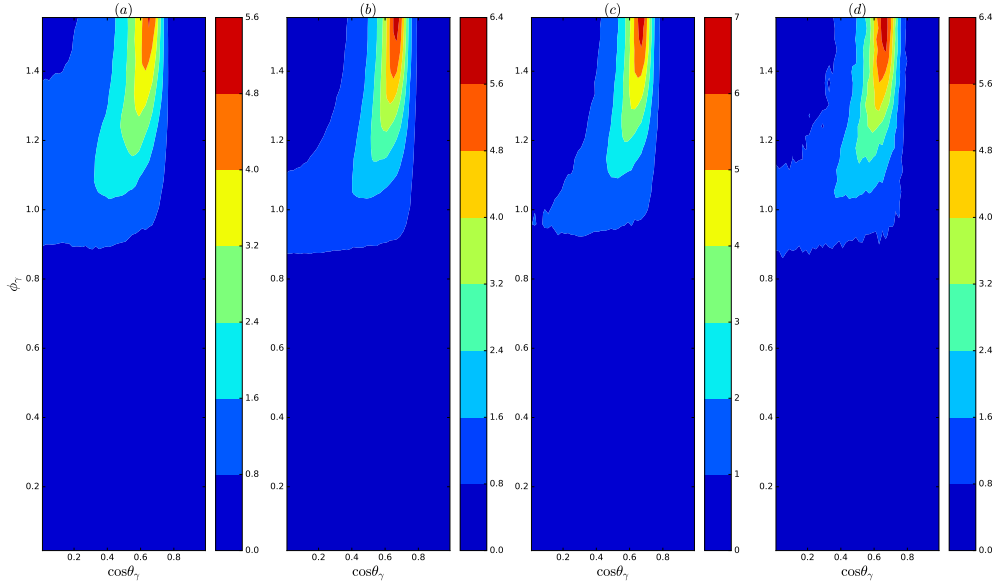
Figure 5.8: Joint PDFs of $(\cos\theta_\gamma, \phi_\gamma)$. (a): 256^3 DNS velocity field. (b): 128^3 TDNS-CMT merged velocity field. (c): 64^3 TDNS-CMT merged velocity field. (d): 32^3 TDNS-CMT merged velocity field.

Peak values for DNS data and for cases A, B, and C as well are approximately located at $\phi_\gamma \approx 90°$ and $\theta_\gamma \approx 44°$, with peak values 4.8, 5.6, 6.0 and 5.6, as given in Fig. 5.8 (a), (b), (c), and (d), respectively. Overall, the agreement between DNS and merged fields is very good. Also we note that statistical fluctuations increase with decreasing resolution in all cases.

The PDFs of $\cos(\Lambda_\alpha)$, $\cos(\Lambda_\beta)$ and $\cos(\Lambda_\gamma)$ of the geometrical alignment trends between the filtered vorticity vector $\tilde{\omega}_i$ and the SGS stress $-\tau_{ij}$ tensor for 256^3 DNS field is given in Fig. 5.9, and for cases A, B, and C are given in Figs. 5.10- 5.12, respectively. The blue, cyan and medium orchid curves represent the PDFs of the cosines of the angles Λ_α, Λ_β and Λ_γ, respectively. Note that, we utilized same notations for the angles in Sec. 2.7.3.
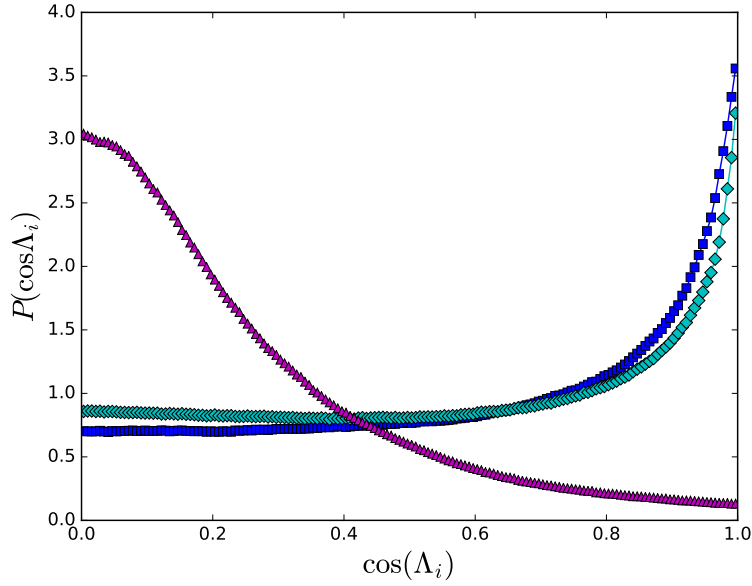
Figure 5.9: PDFs of the cosine of the angles between $\tilde{\omega}_i$ and the eigenvectors of $-\tau_{ij}$. Blue squares: $P(\cos \Lambda_\alpha)$. Cyan diamonds: $P(\cos \Lambda_\beta)$. Medium-orchid triangles: $P(\cos \Lambda_\gamma)$ for 256^3 DNS velocity field.
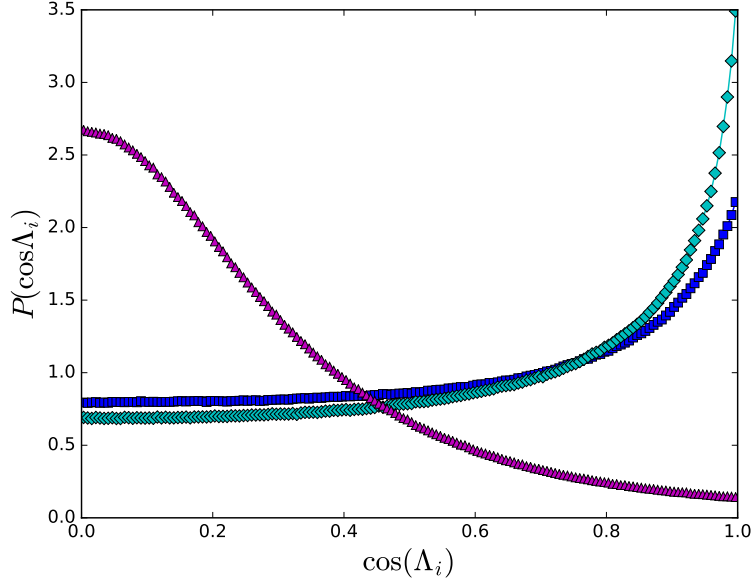
Figure 5.10: PDFs of the cosine of the angles between $\tilde{\omega}_i$ and the eigenvectors of $-\tau_{ij}$. Blue squares: $P(\cos \Lambda_\alpha)$. Cyan diamonds: $P(\cos \Lambda_\beta)$. Medium-orchid triangles: $P(\cos \Lambda_\gamma)$ for 128^3 TDNS-CMT merged velocity field.

As analysis of the current trends, we remark that the direction of $\tilde{\omega}_i$ tends to align with the directions of the most extensive and intermediate eigenvectors $\alpha_{-\tau}$ and $\beta_{-\tau}$ of SGS stress $-\tau_{ij}$. The PDF of $\cos(\Lambda_\gamma)$ shows $\tilde{\omega}_i$ tends to be perpendicular with the direction of the contracting eigenvector $\gamma_{-\tau}$. These results are found to be consistent with the observation of Horiuti [70]. In

general, all merged data sets reproduce the preferred alignment configurations in DNS, in spite of showing higher probability for $\cos \Lambda_\beta = (\beta_{-\tau}, \tilde{\omega}_i)$ than for $\cos \Lambda_\alpha = (\alpha_{-\tau}, \tilde{\omega}_i)$ in all cases.
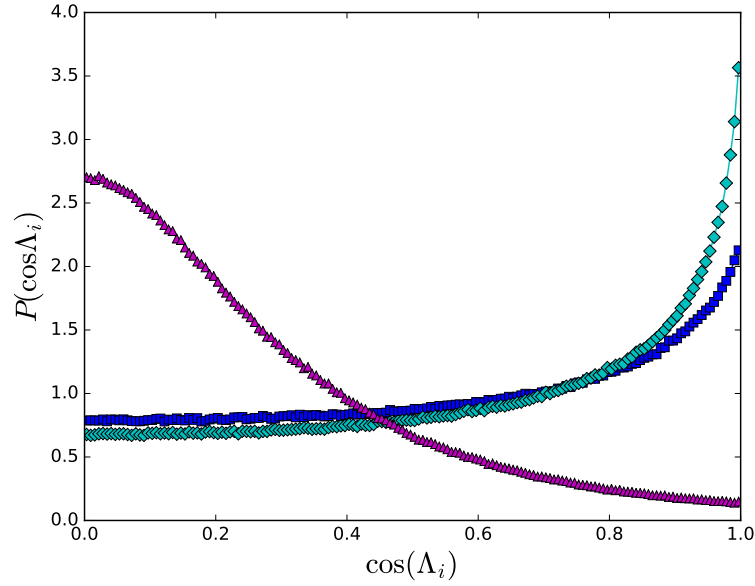
Figure 5.11: PDFs of the cosine of the angles between $\tilde{\omega}_i$ and the eigenvectors of $-\tau_{ij}$. Blue squares: $P(\cos \Lambda_\alpha)$. Cyan diamonds: $P(\cos \Lambda_\beta)$. Medium-orchid triangles: $P(\cos \Lambda_\gamma)$ for 64^3 TDNS-CMT merged velocity field.
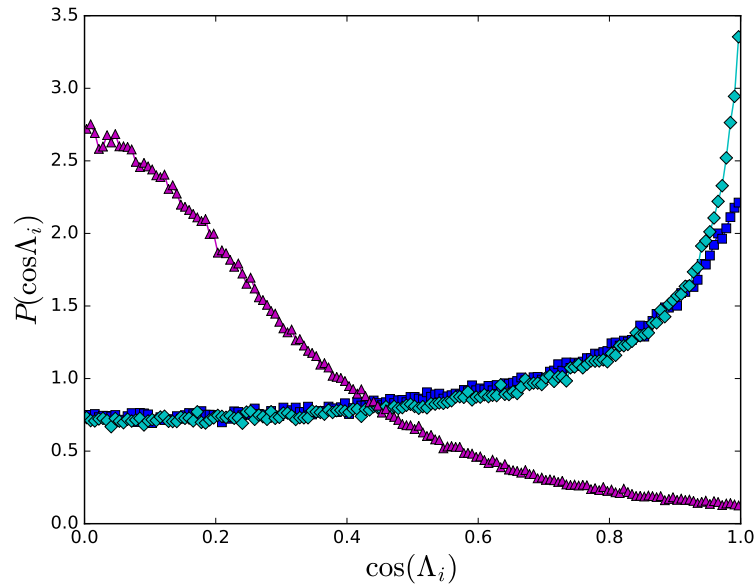
Figure 5.12: PDFs of the cosine of the angles between $\tilde{\omega}_i$ and the eigenvectors of $-\tau_{ij}$. Blue squares: $P(\cos \Lambda_\alpha)$. Cyan diamonds: $P(\cos \Lambda_\beta)$. Medium-orchid triangles: $P(\cos \Lambda_\gamma)$ for 32^3 TDNS-CMT merged velocity field.
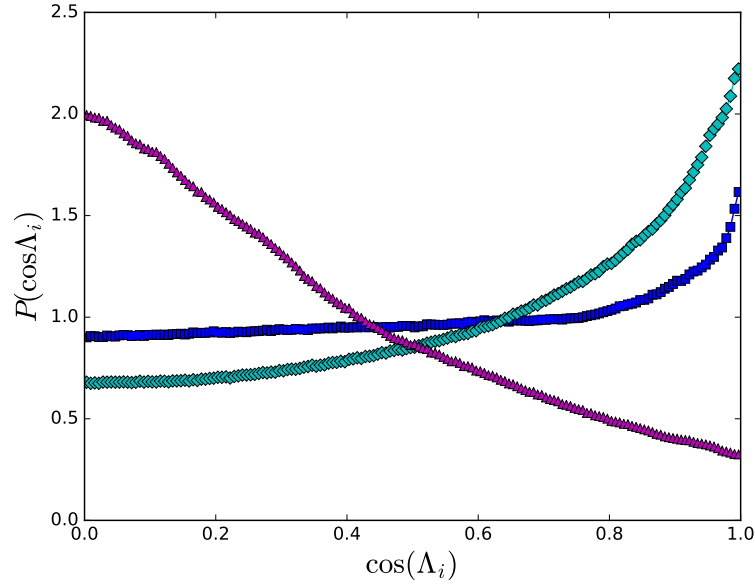
Figure 5.13: PDFs of the cosine of the angles between $\tilde{\omega}_i$ and the eigenvectors of $\tilde{S}_{ij}$. Blue squares: $P(\cos \Lambda_\alpha)$. Cyan diamonds: $P(\cos \Lambda_\beta)$. Medium-orchid triangles: $P(\cos \Lambda_\gamma)$ for 256^3 DNS velocity field.
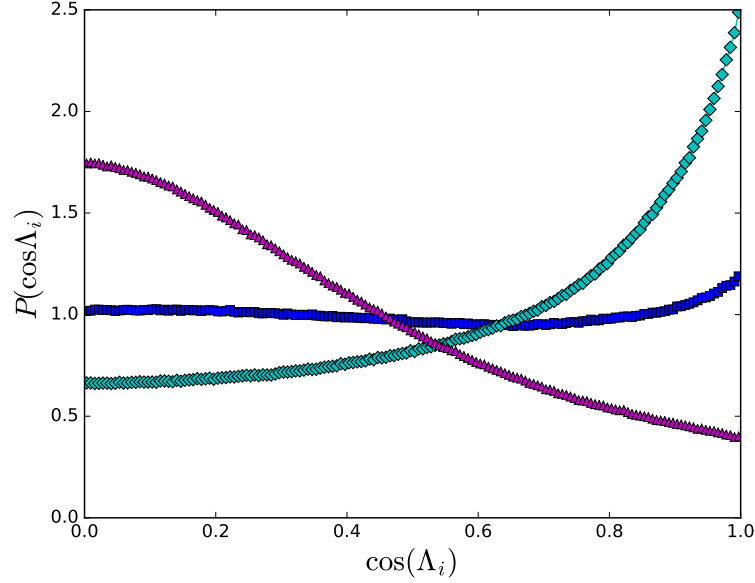
Figure 5.14: PDFs of the cosine of the angles between $\tilde{\omega}_i$ and the eigenvectors of $\tilde{S}_{ij}$. Blue squares: $P(\cos \Lambda_\alpha)$. Cyan diamonds: $P(\cos \Lambda_\beta)$. Medium-orchid triangles: $P(\cos \Lambda_\gamma)$ for 128^3 TDNS-CMT merged velocity field.

The preferential alignments between the filtered vorticity vector $\tilde{\omega}_i$ and the eigenvectors $\boldsymbol{\alpha}_s$, $\boldsymbol{\beta}_s$ and $\boldsymbol{\gamma}_s$ of the filtered strain-rate tensor $\tilde{S}_{ij}$ for 256^3 DNS field are plotted in Fig. 5.13 and for cases A, B and C are presented in Fig. 5.14-5.16, respectively. Also the blue, cyan and medium orchid curves represent the PDFs of the cosines of the angles Λ_α, Λ_β and Λ_γ, respectively. As

112
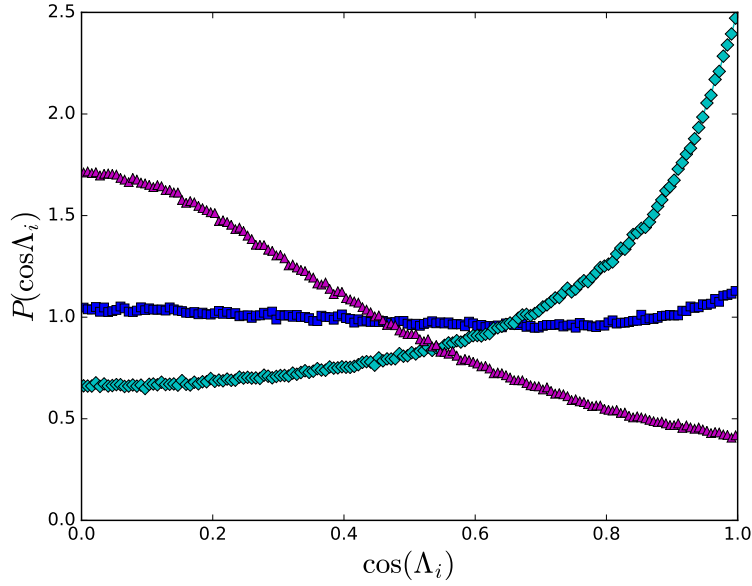
Figure 5.15: PDFs of the cosine of the angles between $\tilde{\omega}_i$ and the eigenvectors of $\tilde{S}_{ij}$. Blue squares: $P(\cos \Lambda_\alpha)$. Cyan diamonds: $P(\cos \Lambda_\beta)$. Medium-orchid triangles: $P(\cos \Lambda_\gamma)$ for 64^3 TDNS-CMT merged velocity field.
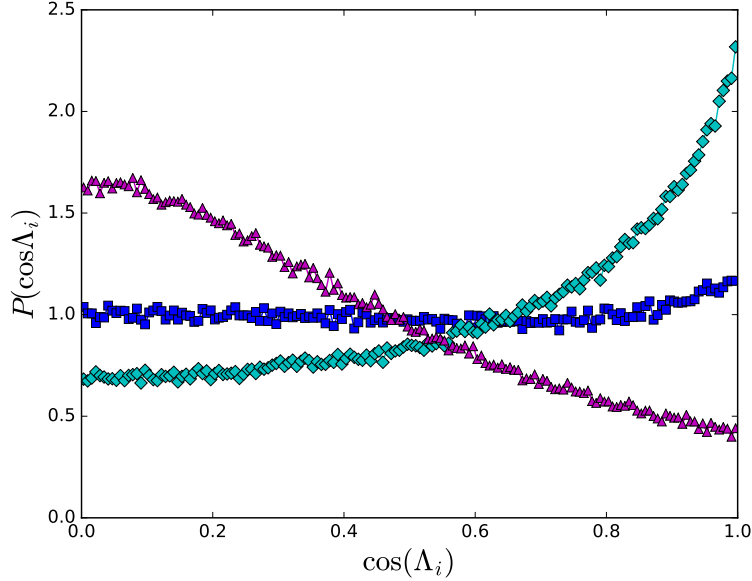
Figure 5.16: PDFs of the cosine of the angles between $\tilde{\omega}_i$ and the eigenvectors of $\tilde{S}_{ij}$. Blue squares: $P(\cos \Lambda_\alpha)$. Cyan diamonds: $P(\cos \Lambda_\beta)$. Medium-orchid triangles: $P(\cos \Lambda_\gamma)$ for 32^3 TDNS-CMT merged velocity field.

in the prior discussion, the same could be concluded about the alignment trends, i.e., all PDFs show the same preferred alignment at $\cos \Lambda_\alpha = 1$, $\cos \Lambda_\beta = 1$, and $\cos \Lambda_\gamma = 0$. In addition, results from merged fields agree very well with the DNS results, even though the statistical fluctuations increase with decreasing resolution in all PDFs.

5.4 Conclusions

The geometrical alignment statistics among the SGS stress τ_{ij} tensor and the the large-scale velocity gradient parameters, for instance, the filtered vorticity $\tilde{\omega}_i$ vector and the filtered strain-rate $\widetilde{S}_{ij}$ tensor dominates the SGS dissipation Π, which grows from the dynamical interaction between resolved and SGS scales. These dynamical interactions should be parametrized in LES. Therefore, in the present chapter we check that the merged fields could capture important statistical trends of three-dimensional SGS interactions.

We investigate the properties of the combination between the DNS and CMTLM data before combining LES and CMTLM data. We performed a priori tests with 128^3, 64^3 and 32^3 grid resolutions for TDNS-CMT velocity fields, in which the respective vector and tensor alignment trends of significant turbulence quantities are described.

The SGS quantities are predicted using TDNS-CMT data, and then compared with the real subgrid-scale quantities which have been computed from DNS field. It can be seen that in all cases predicted SGS quantities display good agreement with the exact ones. The TDNS-CMT model SGS dissipation displays good agreement with the real SGS dissipation (from DNS). The results of geometrical alignment statistics are in very good agreement with the DNS results too. Consequently, we could conclude that the TDNS-CMT model preserves right levels of the SGS dissipation in the actual DNS. For the investigation of the effects of the degree of resolution in resolving the inertial-range statistical geometry orientations, it was found that 128^3 grid resolution more sufficient than the lower ones. However, lower resolution data also provide accurate results, and can be obtained more efficiently. Therefore, using low resolution might be a better approach in practice. In the next step, we will extend this investigation to scalar field, i.e., generalized the TDNS-CMT model to predict the SGS scalar fluxes. Also, a posteriori tests have to be calculated to demonstrate the feasibility of the method in industrial applications.

Chapter 6

Conclusions and Future Works

6.1 Conclusions

This thesis is a study of Multi-Scale Turnover Lagrangian Map applied to synthesize turbulence. The motivations of this research is the major contribution of the turbulence in a wide range of engineering applications due to most flows are turbulence, and its main role in transferring and combining between the matter, momentum, and heat in flows. Synthetic turbulence generates stochastic fields which have features of real hydrodynamic turbulent flows using methods much cheaper in contrast to solving Navier-Stokes equations. The growing interest in synthetic turbulence was motivated by the rising interest for employing Large-Eddy simulation in industrial applications, which requires cost effective and advanced approaches for generating initial and inflow boundary conditions. In addition, different and observable characteristics of real turbulence have been efficiently modelled by synthetic turbulence methods. By doing so, essential aspects of turbulent motion are understood through detecting the lowest set of processes which could capture the fundamental properties of turbulence. Consequently, in recent years advances in the modelling and simulation of turbulent flows and in understanding the dynamics of real hydrodynamic turbulence were made using the synthetic turbulence methods.

In a recently proposed method to generate synthetic three-dimensional turbulent vector fields based on the multiscale turnover Lagrangian (MTLM) map, the advection of fluid particles in a random Gaussian field frequently through a set of increasingly refined grids generates the synthetic field. The MTLM generates a highly non-Gaussian velocity field which has highly realistic statistics of isotropic hydrodynamic turbulence. Also it has been generalized to the synthesis of scalar fields and anisotropic turbulence. From the LES and/or SGS modelling perspective, capturing the nonlinear interactions in real turbulence in an efficient way remains a challenge. The MTLM synthetic fields has been studied in this work using the filtering approach, which has not been pursued so far, in order to understand their ability to model the nonlinear interactions in real turbulence. The multi-scale turnover Lagrangian method is generalized to model scalar fields produced by an imposed linear mean profile. The subgrid-scale stress, SGS scalar flux, SGS scalar variance, SGS energy and scalar variance dissipations, as well as related quantities from the scalar and velocity synthetic fields are calculated.

Comparison with DNSs shows that the synthetic fields reproduce the probability distributions of the SGS energy and scalar dissipation rather well. Related geometrical statistics also display close agreement with DNS results. The synthetic fields slightly under-estimate the mean SGS energy dissipation and slightly over-predict the mean SGS scalar variance dissipation. In general, the synthetic fields tend to slightly under-estimate the probability of large fluctuations for most quantities we have examined. Small scale anisotropy in the scalar field originated from the imposed mean gradient is captured. The sensitivity of the synthetic fields on the input spectra is assessed by using truncated spectra or model spectra as the input. Analyses show that most of the SGS statistics agree well with those from MTLM fields with DNS spectra as the input. Besides, the ability of MTLM to produce the energy flux across the energy spectrum is proved in this work. For the mean SGS energy dissipation, some significant deviation is observed. However, it is shown that the deviation can be parametrized by the input energy spectrum, which demonstrates the robustness of the MTLM procedure. These results shed new light on the potential applications of the synthetic fields in large eddy simulations and SGS modelling. In order to model an anisotropic turbulence that is more applicable, MTLM is formulated as an

optimization problem where the Gaussian random input is taken as a control variable and some specific velocity field is taken as the target field. This new technique is named as CMTLM. As such, CMTLM is a possible method for generation anisotropic synthetic incompressible turbulence with maintaining the realistic small scale statistics in MTLM. Therefore, as a second goal of this work, we modified the CMTLM method to include the effects of solid wall boundaries and to synthesize the turbulent channel flow. The reflectionally symmetric synthetic field is generated using modified CMTLM procedure, in which the symmetric field is a model of the velocity field in a fully developed channel flow. The adjoint optimally system with reflectional symmetry is derived in accordance to the new modified CMTLM map. All of MTLM procedure operators were proved to conserve the reflectional symmetries. Mean statistics of the modified CMTLM synthetic fields were computed and were compared with those of computed and experimental results data. The results show an agreement to some extents in some details in comparison with DNS and experimental results, further work is needed to obtain more reliable results statistics.

In the Constrained MTLM method, the optimality system for the optimization problem is constituted from state equation, adjoint equation, and the optimality condition. It is derived using the adjoint formulation. Solving the adjoint equation and the optimality condition leads to the optimal solution for control variable that reduces the difference between the target function and the synthetic field, measured using cost function. In other words, the goal is to reduce the cost function for all possible control variable, subject to the state equation. In order to quantify the contributions of the adjoint operator in the modelling process, the adjoint fields and the gradients of the cost function were studied, which have not been inspected. Two constrained MTLM Kolmogorov flows were considered, and we synthesized a new flow field using the CMTLM method with the target field taken from the DNS data. Contours of the mean of the gradients of the cost functions and the adjoint fields for the above three cases are computed. It was found that the non-linearity of CMTLM procedure has considerable contributions in the cost function gradient evolution. In addition, the target field has considerable impacts on the adjoint field and the gradient of the cost function.

Finally, we investigated the ability of using the CMTLM synthetics fields as SGS models. As a first step, we combine between truncated DNS of turbulence and CMTLM synthetic fields. To do so, truncated DNS data sets are extracted from 256^3 DNS data. Three CMTLM synthetics

velocity fields are generated using these truncated DNS data as target fields with different resolutions. The large scale truncated DNS data are merged with CMTLM synthetics velocity fields to obtain new merged TDNS-CMT velocity fields. SGS quantities obtained using the merged TDNS-CMT velocity fields displayed high correlations with the exact DNS results in priori tests. In addition, the three-dimensional geometrical alignments between the SGS stress tensors and the filtered velocity gradient tensor, such as the vorticity and the strain-rate, show very good agreement between DNS and TDNS-CMT velocity fields results. Our investigation about the effects of different degrees of resolution in resolving the inertial-range statistical geometry orientations shows that 128^3 grid resolution is more sufficient than the lower ones. However, lower resolution data also provide accurate results, and can be obtained more efficiently. Therefore, using low resolution might be a better approach in practice.

6.2 Future Works

Our work demonstrates that using the MTLM is able to build a synthetic SGS model with a number of good features which many currently SGS models (including those for the scalar flux) do not have. So it supplies a solid basis for its applications in LES and SGS modelling. Future research will focus on technical challenges such as, among others, the modelling of inhomogeneous flows, where no complete information regarding the spectra is available. In such cases, one may have to estimate the spectra from the resolved the scales and make use of the physics of the flows. How to implement such a scheme and assess the performance of MTLM in these flows are some of the challenges among others.

The robustness of the CMTLM technique has already been tested and validated in synthetics anisotropic turbulence. More work, however, is needed in the future to improve the results of synthetics fully developed channel flow using CMTLM method. Further applications could include generalization of the CMTLM procedure to synthetic scalar fields, and it can implement the method with a simulation code to confirm its capabilities a posteriori. Because the process of nonlinear energy is captured by CMTLM, the merged TDNS-CMT velocity fields in our combine technique reproduce a wide range of SGS statistics with very good agreement with DNS. A plan is to use MTLM as a downscaling method to develop localized models for atmospheric boundary layer flows, to use the idea of constrained MTLM to couple the resolved and sub-grid scales. In the next step, we will extend this investigation to scalar field, i.e., generalized the TDNS-CMT model to predict the SGS scalar fluxes. Also, a posterior tests have to be calculated to demonstrate the feasibility of the method in industrial applications.

Appendices

Appendix A

A.1   Transformation property of the MTLM procedure

We let $\varphi_2(\mathbf{x})$ be an odd function of x_2 in order to generate anisotropic synthetic turbulence with the impermeable boundary conditions such that the normal components of the velocity field are zero. Thus we need to show, applying the constraint equation $\mathbf{u}_e = \mathcal{M}\boldsymbol{\varphi}$ where $\boldsymbol{\varphi}(\mathbf{x}) = \frac{1}{2}[\boldsymbol{\psi}(\mathbf{x}) + H\boldsymbol{\psi}(H\mathbf{x})]$, leads to $\mathbf{u}_e(x_1, x_2 = 0, x_3) = 0$. That is, we need to show that the CMTLM procedure preserves the reflectional symmetries. In what follows, we will show separately that each operator of the MTLM procedure maintains this property, such that $\mathbf{u}_e$ has the same symmetries of $\boldsymbol{\varphi}$.

A.1.1   Filtering operator $\mathcal{G}$

Following Eq. 2.12, we can define

$$\mathbf{u}_i^{\mathcal{G}}(\mathbf{x}) = \int G(\mathbf{x} - \mathbf{y})\mathbf{u}_i(\mathbf{y})d^3\mathbf{y}. \tag{A.1}$$

Supposing that

$$u_1(\mathbf{x}) = u_1(\mathbf{x}^*), u_2(\mathbf{x}) = -u_2(\mathbf{x}^*), u_3(\mathbf{x}) = u_3(\mathbf{x}^*), \tag{A.2}$$

where, $\mathbf{x}^* = (x_1, -x_2, x_3)$. We need to prove that $\mathbf{u}^{\mathcal{G}}(\mathbf{x}) = [\mathcal{G}\mathbf{u}](\mathbf{x})$ has the reflectional symmetric property. i.e.,

$$u_1^{\mathcal{G}}(\mathbf{x}) = u_1^{\mathcal{G}}(\mathbf{x}^*), u_2^{\mathcal{G}}(\mathbf{x}) = -u_2^{\mathcal{G}}(\mathbf{x}^*), u_3^{\mathcal{G}}(\mathbf{x}) = u_3^{\mathcal{G}}(\mathbf{x}^*). \tag{A.3}$$

Now we will prove that $u_1^{\mathcal{G}}(\mathbf{x}) = u_1^{\mathcal{G}}(\mathbf{x}^*)$. Firstly,

$$u_1^{\mathcal{G}}(\mathbf{x}) = \int G(\mathbf{x} - \mathbf{y})u_1(\mathbf{y})d^3\mathbf{y} \tag{A.4}$$

$$= \int G[x_1 - y_1, x_2 - y_2, x_3 - y_3]u_1(y_1, y_2, y_3)dy_1 dy_2 dy_3. \tag{A.5}$$

We have

$$u_1^{\mathcal{G}}(\mathbf{x}^*) = \int G(\mathbf{x}^* - \mathbf{y})u_1(\mathbf{y})d^3\mathbf{y} \tag{A.6}$$

$$= \int G[x_1 - y_1, -x_2 - y_2, x_3 - y_3]u_1(y_1, y_2, y_3)dy_1 dy_2 dy_3. \tag{A.7}$$

And we have $G(x_1, -x_2, x_3) = G(x_1, x_2, x_3)$. Thus,

$$u_1^{\mathcal{G}}(\mathbf{x}^*) = \int G[x_1 - y_1, x_2 + y_2, x_3 - y_3] u_1(y_1, y_2, y_3) dy_1 dy_2 dy_3. \tag{A.8}$$

Using variable substitution such that $y_2 \to -y_2$, leads to

$$u_1^{\mathcal{G}}(\mathbf{x}^*) = \int G[x_1 - y_1, x_2 - y_2, x_3 - y_3] u_1(y_1, -y_2, y_3) dy_1 dy_2 dy_3. \tag{A.9}$$

According Eq. A.2, we may write

$$u_1^{\mathcal{G}}(\mathbf{x}^*) = \int G[x_1 - y_1, x_2 - y_2, x_3 - y_3] u_1(y_1, y_2, y_3) dy_1 dy_2 dy_3. \tag{A.10}$$

Comparing between Eqs A.5 and A.10 , we have

$$u_1^{\mathcal{G}}(\mathbf{x}) = u_1^{\mathcal{G}}(\mathbf{x}^*). \tag{A.11}$$

Now we will prove that $u_2^{\mathcal{G}}(\mathbf{x}) = -u_2^{\mathcal{G}}(\mathbf{x}^*)$. We have

$$u_2^{\mathcal{G}}(\mathbf{x}) = \int G(x - \mathbf{y}) u_2(\mathbf{y}) d^3 \mathbf{y} \tag{A.12}$$

$$= \int G[x_1 - y_1, x_2 - y_2, x_3 - y_3] u_2(y_1, y_2, y_3) dy_1 dy_2 dy_3. \tag{A.13}$$

$$-u_2^{\mathcal{G}}(\mathbf{x}^*) = -\int G(\mathbf{x}^* - \mathbf{y}) u_2(\mathbf{y}) d^3 \mathbf{y} \tag{A.14}$$

$$= -\int G[x_1 - y_1, -x_2 - y_2, x_3 - y_3] u_2(y_1, y_2, y_3) dy_1 dy_2 dy_3. \tag{A.15}$$

Again, we have $G(x_1, -x_2, x_3) = G(x_1, x_2, x_3)$. Thus,

$$-u_2^{\mathcal{G}}(\mathbf{x}^*) = -\int G[x_1 - y_1, x_2 + y_2, x_3 - y_3] u_2(y_1, y_2, y_3) dy_1 dy_2 dy_3. \tag{A.16}$$

Using variable substitution such that $y_2 \to -y_2$. Then,

$$-u_2^{\mathcal{G}}(\mathbf{x}^*) = -\int G[x_1 - y_1, x_2 - y_2, x_3 - y_3] u_2(y_1, -y_2, y_3) dy_1 dy_2 dy_3. \tag{A.17}$$

Using Eq. A.2, the last equation becomes

$$-u_2^{\mathcal{G}}(\mathbf{x}^*) = \int G[x_1 - y_1, x_2 - y_2, x_3 - y_3] u_2(y_1, y_2, y_3) dy_1 dy_2 dy_3. \tag{A.18}$$

Comparison between A.13 and A.18 results in

$$u_2^{\mathcal{G}}(\mathbf{x}) = -u_2^{\mathcal{G}}(\mathbf{x}^*). \tag{A.19}$$

For third part, we can prove it as above, so that

$$u_3^{\mathcal{G}}(\mathbf{x}) = u_3^{\mathcal{G}}(\mathbf{x}^*). \tag{A.20}$$

Eqs. A.11 A.19 and A.20 (2.11), Eq. (2.19) and Eq. (2.20) indicates that the $\mathbf{u}^{\mathcal{G}}(\mathbf{x}) = [\mathcal{G}\mathbf{u}](\mathbf{x})$ maintains the reflectional symmetric property.

A.1.2 Advection operator $\mathcal{A}$

Using Eq. 2.11, we have

$$\mathbf{u}_i^{\mathcal{A}}(\mathbf{x}) = \int W(\mathbf{x} - \mathbf{y} - \mathbf{u}_j(\mathbf{y})t)\mathbf{u}_i(\mathbf{y})d^3\mathbf{y}. \tag{A.21}$$

Let us assume that

$$u_1(\mathbf{x}) = u_1(\mathbf{x}^*), u_2(\mathbf{x}) = -u_2(\mathbf{x}^*), u_3(\mathbf{x}) = u_3(\mathbf{x}^*) \tag{A.22}$$

where $\mathbf{x}^* = (x_1, -x_2, x_3)$. In order to show that $\mathbf{u}^{\mathcal{A}}(\mathbf{x}) = [\mathcal{A}\mathbf{u}](\mathbf{x})$ can transfer the reflectional symmetric property, we need to prove

$$u_1^{\mathcal{A}}(\mathbf{x}) = u_1^{\mathcal{A}}(\mathbf{x}^*), u_2^{\mathcal{A}}(\mathbf{x}) = -u_2^{\mathcal{A}}(\mathbf{x}^*), u_3^{\mathcal{A}}(\mathbf{x}) = u_3^{\mathcal{A}}(\mathbf{x}^*) \tag{A.23}$$

Now we first prove that $u_1^{\mathcal{A}}(\mathbf{x}) = u_1^{\mathcal{A}}(\mathbf{x}^*)$. Following A.21, we find

$$u_1^{\mathcal{A}}(\mathbf{x}) = \int W(\mathbf{x} - \mathbf{y} - \mathbf{u}_j(\mathbf{y})t)u_1(\mathbf{y})d^3\mathbf{y} \tag{A.24}$$

$$= \int W[x_1 - y_1 - u_1(\mathbf{y})t, x_2 - y_2 - u_2(\mathbf{y})t, x_3 - y_3 - u_3(\mathbf{y})t]u_1(\mathbf{y})dy_1 dy_2 dy_3. \tag{A.25}$$

$$u_1^{\mathcal{A}}(\mathbf{x}^*) = \int W(\mathbf{x}^* - \mathbf{y} - \mathbf{u}_j(\mathbf{y})t)u_1(\mathbf{y})d^3\mathbf{y} \tag{A.26}$$

$$= \int W[x_1 - y_1 - u_1(\mathbf{y})t, -x_2 - y_2 - u_2(\mathbf{y})t, x_3 - y_3 - u_3(\mathbf{y})t]u_1(\mathbf{y})dy_1 dy_2 dy_3. \tag{A.27}$$

We have $W(\mathbf{x}) = 1/|\mathbf{x}|$. Thus, $W(x_1, -x_2, x_3) = W(x_1, x_2, x_3)$. Hence,

$$u_1^{\mathcal{A}}(\mathbf{x}^*) = \int W[(\mathbf{x}) - (\mathbf{y}^*) - (u_1(\mathbf{y}), -u_2(\mathbf{y}), u_3(\mathbf{y}))\, t]u_1(\mathbf{y})dy_1 dy_2 dy_3, \tag{A.28}$$

where $\mathbf{y}^* = (y_1, -y_2, y_3)$. After applying Eq. A.22, Eq. A.28 becomes,

$$u_1^{\mathcal{A}}(\mathbf{x}^*) = \int W[x_1 - y_1 - u_1(\mathbf{y})t, x_2 + y_2 - u_2(\mathbf{y}^*)t, x_3 - y_3 - u_3(\mathbf{y})t]u_1(\mathbf{y})dy_1 dy_2 dy_3. \tag{A.29}$$

Using variable substitution such that $y_2 \to -y_2$ leads to

$$u_1^{\mathcal{A}}(\mathbf{x}^*) = \int W[x_1 - y_1 - u_1(\mathbf{y}^*)t, x_2 - y_2 - u_2(\mathbf{y})t, x_3 - y_3 - u_3(\mathbf{y}^*)t]u_1(\mathbf{y}^*)dy_1 dy_2 dy_3. \tag{A.30}$$

According to Eq. A.22, last equation would be

$$u_1^{\mathcal{A}}(\mathbf{x}^*) = \int W[x_1 - y_1 - u_1(\mathbf{y})t, x_2 - y_2 - u_2(\mathbf{y})t, x_3 - y_3 - u_3(\mathbf{y})t]u_1(\mathbf{y})dy_1 dy_2 dy_3. \tag{A.31}$$

Comparison between Eqs. A.25 and A.31 shows

$$u_1^{\mathcal{A}}(\mathbf{x}) = u_1^{\mathcal{A}}(\mathbf{x}^*). \tag{A.32}$$

Now we prove $u_2^{\mathcal{A}}(\mathbf{x}) = -u_2^{\mathcal{A}}(\mathbf{x}^*)$.

$$u_2^{\mathcal{A}}(\mathbf{x}) = \int W(\mathbf{x} - \mathbf{y} - \mathbf{u}_j(\mathbf{y})t)u_2(\mathbf{y})d^3\mathbf{y} \tag{A.33}$$

$$= \int W[x_1 - y_1 - u_1(\mathbf{y})t, x_2 - y_2 - u_2(\mathbf{y})t, x_3 - y_3 - u_3(\mathbf{y})t]u_2(\mathbf{y})dy_1dy_2dy_3. \tag{A.34}$$

$$-u_2^{\mathcal{A}}(\mathbf{x}^*) = -\int W(\mathbf{x}^* - \mathbf{y} - \mathbf{u}_j(\mathbf{y})t)u_2(\mathbf{y})d^3\mathbf{y} \tag{A.35}$$

$$= \int W[x_1 - y_1 - u_1(\mathbf{y})t, -x_2 - y_2 - u_2(\mathbf{y})t, x_3 - y_3 - u_3(\mathbf{y})t] - u_2(\mathbf{y})dy_1dy_2dy_3. \tag{A.36}$$

Appling Eq. A.22, last one becomes

$$-u_2^{\mathcal{A}}(\mathbf{x}^*) = \int W[x_1 - y_1 - u_1(\mathbf{y})t, -x_2 - y_2 - u_2(\mathbf{y})t, x_3 - y_3 - u_3(\mathbf{y})t]u_2(\mathbf{y}^*)dy_1dy_2dy_3. \tag{A.37}$$

We have $W(x_1, -x_2, x_3) = W(x_1, x_2, x_3)$. Then,

$$-u_2^{\mathcal{A}}(\mathbf{x}^*) = \int W[x_1 - y_1 - u_1(\mathbf{y})t, x_2 + y_2 + u_2(\mathbf{y})t, x_3 - y_3 - u_3(\mathbf{y})t]u_2(\mathbf{y}^*)dy_1dy_2dy_3. \tag{A.38}$$

Using Eq. A.22, Eq. A.38 would be

$$-u_2^{\mathcal{A}}(\mathbf{x}^*) = \int W[x_1 - y_1 - u_1(\mathbf{y})t, x_2 + y_2 - u_2(\mathbf{y}^*)t, x_3 - y_3 - u_3(\mathbf{y})t]u_2(\mathbf{y}^*)dy_1dy_2dy_3. \tag{A.39}$$

Using variable substitution such that $y_2 \to -y_2$ leads to

$$-u_2^{\mathcal{A}}(\mathbf{x}^*) = \int W[x_1 - y_1 - u_1(\mathbf{y}^*)t, x_2 - y_2 - u_2(\mathbf{y})t, x_3 - y_3 - u_3(\mathbf{y}^*)t]u_2(\mathbf{y})dy_1dy_2dy_3. \tag{A.40}$$

Using Eq. A.22, Eq. A.40 becomes

$$-u_2^{\mathcal{A}}(\mathbf{x}^*) = \int W[x_1 - y_1 - u_1(\mathbf{y})t, x_2 - y_2 - u_2(\mathbf{y})t, x_3 - y_3 - u_3(\mathbf{y})t]u_2(\mathbf{y})dy_1dy_2dy_3. \tag{A.41}$$

Comparing between Eq. A.34 and Eq. A.41 leads to

$$u_2^{\mathcal{A}}(\mathbf{x}) = -u_2^{\mathcal{A}}(\mathbf{x}^*). \tag{A.42}$$

Now we need to prove $u_3^{\mathcal{A}}(\mathbf{x}) = u_3^{\mathcal{A}}(\mathbf{x}^*)$. For this part of proof, we can prove it similarly to the first part. Thus we have

$$u_3^{\mathcal{A}}(\mathbf{x}) = u_3^{\mathcal{A}}(\mathbf{x}^*). \tag{A.43}$$

Eqs. A.32, A.42 and A.43 shows that $\mathbf{u}^{\mathcal{A}}(\mathbf{x}) = [\mathcal{A}\mathbf{u}](\mathbf{x})$ has the reflectional symmetric property.

A.1.3 Projection operator $\mathcal{P}$

According to Eq. 2.13, we can write this projection operator as follows

$$u_i^{\mathcal{P}}(\mathbf{x}) = \frac{1}{(2\pi)^3} \int\!\!\!\int_{-\infty}^{\infty} d^3\mathbf{x}' d^3\mathbf{k} \mathcal{P}_{ij}(\mathbf{k}) \mathbf{u}_j(\mathbf{x}') e^{i\mathbf{k}.\mathbf{x}'} e^{-i\mathbf{k}.\mathbf{x}}, \tag{A.44}$$

where $\mathcal{P}_{ij}(\mathbf{k}) = \delta_{ij} - \frac{k_i k_j}{k^2}$ and $\mathbf{x}' = (x_1', x_2', x_3')$. We want to prove

$$u_1^{\mathcal{P}}(\mathbf{x}) = u_1^{\mathcal{P}}(\mathbf{x}^*), u_2^{\mathcal{P}}(\mathbf{x}) = -u_2^{\mathcal{P}}(\mathbf{x}^*), u_3^{\mathcal{P}}(\mathbf{x}) = u_3^{\mathcal{P}}(\mathbf{x}^*). \tag{A.45}$$

Now we will prove that $u_1^{\mathcal{P}}(\mathbf{x}) = u_1^{\mathcal{P}}(\mathbf{x}^*)$. Using Eq. A.44, we find

$$u_1^{\mathcal{P}}(\mathbf{x}) = \frac{1}{(2\pi)^3} \int\!\!\!\int_{-\infty}^{\infty} d^3\mathbf{x}' d^3\mathbf{k} \mathcal{P}_{1j}(\mathbf{k}) \mathbf{u}_j(\mathbf{x}') e^{i\mathbf{k}.\mathbf{x}'} e^{-i\mathbf{k}.\mathbf{x}} \tag{A.46}$$

$$= \frac{1}{(2\pi)^3} \int\!\!\!\int_{-\infty}^{\infty} d^3\mathbf{x}' d^3\mathbf{k} \mathcal{P}_{1j}(\mathbf{k}) \mathbf{u}_j(\mathbf{x}') e^{i\mathbf{k}.(x_1', x_2', x_3')} e^{-i\mathbf{k}.(x_1, x_2, x_3)}. \tag{A.47}$$

$$u_1^{\mathcal{P}}(\mathbf{x}^*) = \frac{1}{(2\pi)^3} \int\!\!\!\int_{-\infty}^{\infty} d^3\mathbf{x}' d^3\mathbf{k} \mathcal{P}_{1j}(\mathbf{k}) \mathbf{u}_j(\mathbf{x}') e^{i\mathbf{k}.\mathbf{x}'} e^{-i\mathbf{k}.\mathbf{x}^*} \tag{A.48}$$

$$= \frac{1}{(2\pi)^3} \int\!\!\!\int_{-\infty}^{\infty} d^3\mathbf{x}' d^3\mathbf{k} \mathcal{P}_{1j}(\mathbf{k}) \mathbf{u}_j(\mathbf{x}') e^{i\mathbf{k}.(x_1', x_2', x_3')} e^{-i\mathbf{k}.(x_1, -x_2, x_3)} \tag{A.49}$$

$$= \frac{1}{(2\pi)^3} \int\!\!\!\int_{-\infty}^{\infty} d^3\mathbf{x}' d^3\mathbf{k} \left[(\delta_{11} - \frac{k_1 k_1}{k^2}) u_1(\mathbf{x}') + (\delta_{12} - \frac{k_1 k_2}{k^2}) u_2(\mathbf{x}') + (\delta_{13} - \frac{k_1 k_3}{k^2}) u_3(\mathbf{x}') \right]$$
$$e^{i\mathbf{k}.\mathbf{x}'} e^{-i\mathbf{k}.x^*}. \tag{A.50}$$

We use variable substitution $\mathbf{k} \to \mathbf{k}' = (k_1, -k_2, k_3)$, such that $\mathbf{k}.\mathbf{x}^* = \mathbf{k}.(x_1, -x_2, x_3) = k_1 x_1 - k_2 x_2 + k_3 x_3 = k_1' x_1 + k_2' x_2 + k_3' x_3 = \mathbf{k}'.\mathbf{x}$ and $\mathbf{k}.\mathbf{x}' = \mathbf{k}.(x_1', x_2', x_3') = k_1 x_1' + k_2 x_2' + k_3 x_3' = k_1' x_1' - k_2' x_2' + k_3' x_3' = \mathbf{k}'.\mathbf{x}'^*$. Then we find

$$u_1^{\mathcal{P}}(\mathbf{x}^*) = \frac{1}{(2\pi)^3} \int\!\!\!\int_{-\infty}^{\infty} d^3\mathbf{x}' d^3\mathbf{k}' \left[(\delta_{11} - \frac{k_1' k_1'}{k'^2}) u_1(\mathbf{x}') + (\delta_{12} + \frac{k_1' k_2'}{k'^2}) u_2(\mathbf{x}') + (\delta_{13} - \frac{k_1' k_3'}{k'^2}) u_3(\mathbf{x}') \right]$$
$$e^{i\mathbf{k}'.(x_1', -x_2', x_3')} e^{-i\mathbf{k}'.(x_1, x_2, x_3)}. \tag{A.51}$$

We then use variable substitution $\mathbf{x}' \to \mathbf{x}'' = (x_1', -x_2', x_3')$, such that

$$u_1(\mathbf{x}') = u_1(\mathbf{x}''^*) = u_1(\mathbf{x}''), \tag{A.52}$$

$$u_2(\mathbf{x}') = u_2(\mathbf{x}''^*) = -u_2(\mathbf{x}''), \tag{A.53}$$

$$u_3(\mathbf{x}') = u_3(\mathbf{x}''^*) = u_3(\mathbf{x}''), \tag{A.54}$$

where $\mathbf{x}''^* = (x_1'', -x_2'', x_3'')$. Then, we have

$$u_1^{\mathcal{P}}(\mathbf{x}^*) = \frac{1}{(2\pi)^3} \iint\limits_{-\infty}^{\infty} d^3\mathbf{x}'' d^3\mathbf{k}' \Big[(\delta_{11} - \frac{k_1' k_1'}{k'^2}) u_1(x_1'', -x_2'', x_3'') + (-\delta_{12} + \frac{k_1' k_2'}{k'^2}) u_2(x_1'', -x_2'', x_3'')$$

$$+ (\delta_{13} - \frac{k_1' k_3'}{k'^2}) u_3(x_1'', -x_2'', x_3'') \Big] e^{i\mathbf{k}'.(x_1'', x_2'', x_3'')} e^{-i\mathbf{k}'.(x_1, x_2, x_3)} \tag{A.55}$$

$$= \frac{1}{(2\pi)^3} \iint\limits_{-\infty}^{\infty} d^3\mathbf{x}'' d^3\mathbf{k}' \Big[(\delta_{11} - \frac{k_1' k_1'}{k'^2}) u_1(x_1'', x_2'', x_3'') + (\delta_{12} - \frac{k_1' k_2'}{k'^2}) u_2(x_1'', x_2'', x_3'')$$

$$+ (\delta_{13} - \frac{k_1' k_3'}{k'^2}) u_3(x_1'', x_2'', x_3'') \Big] e^{i\mathbf{k}'.(x_1'', x_2'', x_3'')} e^{-i\mathbf{k}'.(x_1, x_2, x_3)} \tag{A.56}$$

$$= \frac{1}{(2\pi)^3} \iint\limits_{-\infty}^{\infty} d^3\mathbf{x}'' d^3\mathbf{k}' \mathcal{P}_{1j}(\mathbf{k}') \mathbf{u}_j(\mathbf{x}'') e^{i\mathbf{k}'.\mathbf{x}''} e^{-i\mathbf{k}'.\mathbf{x}}, \tag{A.57}$$

where $\mathbf{k}'.\mathbf{x}'^* = k_1' x_1' - k_2' x_2' + k_3' x_3' = k_1' x_1'' + k_2' x_2'' + k_3' x_3'' = \mathbf{k}'.\mathbf{x}''$. Comparison between Eqs. A.47 and A.57 shows

$$u_1^{\mathcal{P}}(\mathbf{x}) = u_1^{\mathcal{P}}(\mathbf{x}^*). \tag{A.58}$$

Now we need to prove $u_2^{\mathcal{P}}(\mathbf{x}) = -u_2^{\mathcal{P}}(\mathbf{x}^*)$.

$$u_2^{\mathcal{P}}(\mathbf{x}) = \frac{1}{(2\pi)^3} \iint\limits_{-\infty}^{\infty} d^3\mathbf{x}' d^3\mathbf{k} \mathcal{P}_{2j}(\mathbf{k}) \mathbf{u}_j(\mathbf{x}') e^{i\mathbf{k}.\mathbf{x}'} e^{-i\mathbf{k}.\mathbf{x}} \tag{A.59}$$

$$= \frac{1}{(2\pi)^3} \iint\limits_{-\infty}^{\infty} d^3\mathbf{x}' d^3\mathbf{k} \mathcal{P}_{1j}(\mathbf{k}) \mathbf{u}_j(\mathbf{x}') e^{i\mathbf{k}.(x_1', x_2', x_3')} e^{-i\mathbf{k}.(x_1, x_2, x_3)} \tag{A.60}$$

$$-u_2^{\mathcal{P}}(\mathbf{x}^*) = \frac{-1}{(2\pi)^3} \iint\limits_{-\infty}^{\infty} d^3\mathbf{x}' d^3\mathbf{k} \mathcal{P}_{2j}(\mathbf{k}) \mathbf{u}_j(\mathbf{x}') e^{i\mathbf{k}.\mathbf{x}'} e^{-i\mathbf{k}.\mathbf{x}^*} \tag{A.61}$$

$$= \frac{-1}{(2\pi)^3} \iint\limits_{-\infty}^{\infty} d^3\mathbf{x}' d^3\mathbf{k} \mathcal{P}_{2j}(\mathbf{k}) \mathbf{u}_j(\mathbf{x}') e^{i\mathbf{k}.(x_1', x_2', x_3')} e^{-i\mathbf{k}.(x_1, -x_2, x_3)} \tag{A.62}$$

$$= \frac{-1}{(2\pi)^3} \iint\limits_{-\infty}^{\infty} d^3\mathbf{x}' d^3\mathbf{k} \Big[(\delta_{21} - \frac{k_2 k_1}{k^2}) u_1(\mathbf{x}') + (\delta_{22} - \frac{k_2 k_2}{k^2}) u_2(\mathbf{x}') + (\delta_{23} - \frac{k_2 k_3}{k^2}) u_3(\mathbf{x}') \Big]$$

$$\tag{A.63}$$

$$e^{i\mathbf{k}.\mathbf{x}'} e^{-i\mathbf{k}.\mathbf{x}^*}.$$

Using variable substitution $\mathbf{k} \to \mathbf{k}' = (k_1, -k_2, k_3)$ we have

$$-u_2^{\mathcal{P}}(\mathbf{x}^*) = \frac{-1}{(2\pi)^3} \iint\limits_{-\infty}^{\infty} d^3\mathbf{x}' d^3\mathbf{k}' \Big[(\delta_{21} + \frac{k_2' k_1'}{k'^2}) u_1(\mathbf{x}') + (\delta_{22} - \frac{k_2' k_2'}{k'^2}) u_2(\mathbf{x}') + (\delta_{23} + \frac{k_2' k_3'}{k'^2}) u_3(\mathbf{x}') \Big]$$

$$e^{i\mathbf{k}'.(x_1', -x_2', x_3')} e^{-i\mathbf{k}'.(x_1, x_2, x_3)}. \tag{A.64}$$

Using variable substitution $\mathbf{x}' \to \mathbf{x}'' = (x_1', -x_2', x_3')$ results in

$$-u_2^{\mathcal{P}}(\mathbf{x}^*) = \frac{-1}{(2\pi)^3} \iint\limits_{-\infty}^{\infty} d^3\mathbf{x}'' d^3\mathbf{k}' \Big[(\delta_{21} + \frac{k_2'k_1'}{k'^2}) u_1(\mathbf{x}''^*) + (\delta_{22} - \frac{k_2'k_2'}{k'^2}) u_2(\mathbf{x}''^*)$$

$$+ (\delta_{23} + \frac{k_2'k_3'}{k'^2}) u_3(\mathbf{x}''^*) \Big] e^{i\mathbf{k}'.(x_1'',x_2'',x_3'')} e^{-i\mathbf{k}'.(x_1,x_2,x_3)}. \tag{A.65}$$

According to Eqs. A.52, A.53 and A.54, we find

$$-u_2^{\mathcal{P}}(\mathbf{x}^*) = \frac{-1}{(2\pi)^3} \iint\limits_{-\infty}^{\infty} d^3\mathbf{x}'' d^3\mathbf{k}' \Big[(\delta_{21} + \frac{k_2'k_1'}{k'^2}) u_1(\mathbf{x}'') + (-\delta_{22} + \frac{k_2'k_2'}{k'^2}) u_2(\mathbf{x}'')$$

$$+ (\delta_{23} + \frac{k_2'k_3'}{k'^2}) u_3(\mathbf{x}'') \Big] e^{i\mathbf{k}'.(x_1'',x_2'',x_3'')} e^{-i\mathbf{k}'.(x_1,x_2,x_3)} \tag{A.66}$$

$$= \frac{1}{(2\pi)^3} \iint\limits_{-\infty}^{\infty} d^3\mathbf{x}'' d^3\mathbf{k}' \Big[(-\delta_{21} - \frac{k_2'k_1'}{k'^2}) u_1(\mathbf{x}'') + (\delta_{22} - \frac{k_2'k_2'}{k'^2}) u_2(\mathbf{x}'')$$

$$+ (-\delta_{23} - \frac{k_2'k_3'}{k'^2}) u_3(\mathbf{x}'') \Big] e^{i\mathbf{k}'.(x_1'',x_2'',x_3'')} e^{-i\mathbf{k}'.(x_1,x_2,x_3)} \tag{A.67}$$

$$= \frac{1}{(2\pi)^3} \iint\limits_{-\infty}^{\infty} d^3\mathbf{x}'' d^3\mathbf{k}' \mathcal{P}_{2j}(\mathbf{k}') \mathbf{u}_j(\mathbf{x}'') e^{i\mathbf{k}'.\mathbf{x}''} e^{-i\mathbf{k}'.\mathbf{x}}. \tag{A.68}$$

Comparison between Eqs. A.60 and A.68, shows

$$u_2^{\mathcal{P}}(\mathbf{x}) = -u_2^{\mathcal{P}}(\mathbf{x}^*). \tag{A.69}$$

Now we will prove that $u_3^{\mathcal{P}}(\mathbf{x}) = u_3^{\mathcal{P}}(\mathbf{x}^*)$.

$$u_3^{\mathcal{P}}(\mathbf{x}) = \frac{1}{(2\pi)^3} \iint\limits_{-\infty}^{\infty} d^3\mathbf{x}' d^3\mathbf{k} \mathcal{P}_{3j}(\mathbf{k}) \mathbf{u}_j(\mathbf{x}') e^{i\mathbf{k}.\mathbf{x}'} e^{-i\mathbf{k}.\mathbf{x}} \tag{A.70}$$

$$= \frac{1}{(2\pi)^3} \iint\limits_{-\infty}^{\infty} d^3\mathbf{x}' d^3\mathbf{k} \mathcal{P}_{3j}(\mathbf{k}) \mathbf{u}_j(\mathbf{x}') e^{i\mathbf{k}.(x_1',x_2',x_3')} e^{-i\mathbf{k}.(x_1,x_2,x_3)}. \tag{A.71}$$

$$u_3^{\mathcal{P}}(\mathbf{x}^*) = \frac{1}{(2\pi)^3} \iint\limits_{-\infty}^{\infty} d^3\mathbf{x}' d^3\mathbf{k} \mathcal{P}_{3j}(\mathbf{k}) \mathbf{u}_j(\mathbf{x}') e^{i\mathbf{k}.\mathbf{x}'} e^{-i\mathbf{k}.\mathbf{x}^*} \tag{A.72}$$

$$= \frac{1}{(2\pi)^3} \iint\limits_{-\infty}^{\infty} d^3\mathbf{x}' d^3\mathbf{k} \mathcal{P}_{3j}(\mathbf{k}) \mathbf{u}_j(\mathbf{x}') e^{i\mathbf{k}.(x_1',x_2',x_3')} e^{-i\mathbf{k}.(x_1,-x_2,x_3)} \tag{A.73}$$

$$= \frac{1}{(2\pi)^3} \iint\limits_{-\infty}^{\infty} d^3\mathbf{x}' d^3\mathbf{k} \Big[(\delta_{31} - \frac{k_3 k_1}{k^2}) u_1(\mathbf{x}') + (\delta_{32} - \frac{k_3 k_2}{k^2}) u_2(\mathbf{x}') + (\delta_{33} - \frac{k_3 k_3}{k^2}) u_3(\mathbf{x}') \Big]$$

$$e^{i\mathbf{k}.\mathbf{x}'} e^{-i\mathbf{k}.\mathbf{x}^*}. \tag{A.74}$$

Using variable substitution $\mathbf{k} \to \mathbf{k}' = (k_1, -k_2, k_3)$, we have

$$u_3^{\mathcal{P}}(\mathbf{x}^*) = \frac{1}{(2\pi)^3} \iint_{-\infty}^{\infty} d^3\mathbf{x}' d^3\mathbf{k}' \Big[(\delta_{31} - \frac{k_3' k_1'}{k'^2}) u_1(\mathbf{x}') + (\delta_{32} + \frac{k_3' k_2'}{k'^2}) u_2(\mathbf{x}') + (\delta_{33} - \frac{k_3' k_3'}{k'^2}) u_3(\mathbf{x}') \Big]$$

$$e^{i\mathbf{k}'.(x_1', -x_2', x_3')} e^{-i\mathbf{k}'.(x_1, x_2, x_3)}. \tag{A.75}$$

Using variable substitution such that $\mathbf{x}' \to \mathbf{x}'' = (x_1', -x_2', x_3')$, with Eqs. A.52, A.53 and A.54.

$$u_3^{\mathcal{P}}(\mathbf{x}^*) = \frac{1}{(2\pi)^3} \iint_{-\infty}^{\infty} d^3\mathbf{x}'' d^3\mathbf{k}' \Big[(\delta_{31} - \frac{k_3' k_1'}{k'^2}) u_1(x_1'', -x_2'', x_3'') + (-\delta_{32} + \frac{k_3' k_2'}{k'^2}) u_2(x_1'', -x_2'', x_3'')$$

$$+ (\delta_{33} - \frac{k_3' k_3'}{k'^2}) u_3(x_1'', -x_2'', x_3'') \Big] e^{i\mathbf{k}'.(x_1'', x_2'', x_3'')} e^{-i\mathbf{k}'.(x_1, x_2, x_3)} \tag{A.76}$$

$$= \frac{1}{(2\pi)^3} \iint_{-\infty}^{\infty} d^3\mathbf{x}'' d^3\mathbf{k}' \Big[(\delta_{31} - \frac{k_3' k_1'}{k'^2}) u_1(x_1'', x_2'', x_3'') + (\delta_{32} - \frac{k_3' k_2'}{k'^2}) u_2(x_1'', x_2'', x_3'')$$

$$+ (\delta_{33} - \frac{k_3' k_3'}{k'^2}) u_3(x_1'', x_2'', x_3'') \Big] e^{i\mathbf{k}'.(x_1'', x_2'', x_3'')} e^{-i\mathbf{k}'.(x_1, x_2, x_3)} \tag{A.77}$$

$$= \frac{1}{(2\pi)^3} \iint_{-\infty}^{\infty} d^3\mathbf{x}'' d^3\mathbf{k}' \mathcal{P}_{3j}(\mathbf{k}') \mathbf{u}_j(\mathbf{x}'') e^{i\mathbf{k}'.\mathbf{x}''} e^{-i\mathbf{k}'.\mathbf{x}}. \tag{A.78}$$

Comparison between Eqs. A.71 and A.78 leads to

$$u_3^{\mathcal{P}}(\mathbf{x}) = u_3^{\mathcal{P}}(\mathbf{x}^*). \tag{A.79}$$

Eqs. A.58, A.69 and A.79 showS that $\mathbf{u}^{\mathcal{P}}(\mathbf{x}) = [\mathcal{P}\mathbf{u}](\mathbf{x})$ preserves the reflectional symmetric property.

A.1.4 Rescaling operator $\mathcal{R}$

Eq. 3.11, leads to

$$u_j^{\mathcal{R}}(\mathbf{x}) = \frac{1}{(2\pi)^3} \iint_{-\infty}^{\infty} d^3\mathbf{x}' d^3\mathbf{k} \Big(\frac{E_p(k)}{E_u(k)} \Big)^{1/2} \mathbf{u}_j(\mathbf{x}') e^{i\mathbf{k}.\mathbf{x}'} e^{-i\mathbf{k}.\mathbf{x}} \tag{A.80}$$

Aiming to prove $u_1^{\mathcal{R}}(\mathbf{x}) = u_1^{\mathcal{R}}(\mathbf{x}^*), u_2^{\mathcal{R}}(\mathbf{x}) = -u_2^{\mathcal{R}}(\mathbf{x}^*), u_3^{\mathcal{R}}(\mathbf{x}) = u_3^{\mathcal{R}}(\mathbf{x}^*)$, we first prove that $u_1^{\mathcal{R}}(\mathbf{x}) = u_1^{\mathcal{R}}(\mathbf{x}^*)$. We have

$$u_1^{\mathcal{R}}(\mathbf{x}) = \frac{1}{(2\pi)^3} \iint_{-\infty}^{\infty} d^3\mathbf{x}' d^3\mathbf{k} \Big(\frac{E_p(k)}{E_u(k)} \Big)^{1/2} \mathbf{u}_1(\mathbf{x}') e^{i\mathbf{k}.\mathbf{x}'} e^{-i\mathbf{k}.\mathbf{x}} \tag{A.81}$$

$$= \frac{1}{(2\pi)^3} \iint_{-\infty}^{\infty} d^3\mathbf{x}' d^3\mathbf{k} \Big(\frac{E_p(k)}{E_u(k)} \Big)^{1/2} \mathbf{u}_1(\mathbf{x}') e^{i\mathbf{k}.\mathbf{x}'} e^{-i\mathbf{k}.(x_1, x_2, x_3)} \tag{A.82}$$

$$u_1^{\mathcal{R}}(\mathbf{x}^*) = \frac{1}{(2\pi)^3} \iint\limits_{-\infty}^{\infty} d^3\mathbf{x}' d^3\mathbf{k} \Big(\frac{E_p(k)}{E_u(k)}\Big)^{1/2} \mathbf{u}_1(\mathbf{x}') e^{i\mathbf{k}.\mathbf{x}'} e^{-i\mathbf{k}.(x_1,-x_2,x_3)}. \tag{A.83}$$

Applying variable substitution $\mathbf{k} \to \mathbf{k}' = (k_1, -k_2, k_3)$, we have

$$u_1^{\mathcal{R}}(\mathbf{x}^*) = \frac{1}{(2\pi)^3} \iint\limits_{-\infty}^{\infty} d^3\mathbf{x}' d^3\mathbf{k}' \Big(\frac{E_p(k')}{E_u(k')}\Big)^{1/2} \mathbf{u}_1(\mathbf{x}') e^{i\mathbf{k}'.(x_1',-x_2',x_3')} e^{-i\mathbf{k}'.(x_1,x_2,x_3)}. \tag{A.84}$$

Using variable substitution $\mathbf{x}' \to \mathbf{x}'' = (x_1', -x_2', x_3')$, we find

$$u_1^{\mathcal{R}}(\mathbf{x}^*) = \frac{1}{(2\pi)^3} \iint\limits_{-\infty}^{\infty} d^3\mathbf{x}'' d^3\mathbf{k}' \Big(\frac{E_p(k')}{E_u(k')}\Big)^{1/2} \mathbf{u}_1(x_1'', -x_2'', x_3'') e^{i\mathbf{k}'.(x_1'',x_2'',x_3'')} e^{-i\mathbf{k}'.(x_1,x_2,x_3)}, \tag{A.85}$$

where $k' = |\mathbf{k}'|$. Using Eq. A.52, gives

$$u_1^{\mathcal{R}}(\mathbf{x}^*) = \frac{1}{(2\pi)^3} \iint\limits_{-\infty}^{\infty} d^3\mathbf{x}'' d^3\mathbf{k}' \Big(\frac{E_p(k')}{E_u(k')}\Big)^{1/2} \mathbf{u}_1(x_1'', x_2'', x_3'') e^{i\mathbf{k}'.(x_1'',x_2'',x_3'')} e^{-i\mathbf{k}'.(x_1,x_2,x_3)} \tag{A.86}$$

$$= \frac{1}{(2\pi)^3} \iint\limits_{-\infty}^{\infty} d^3\mathbf{x}'' d^3\mathbf{k}' \Big(\frac{E_p(k')}{E_u(k')}\Big)^{1/2} \mathbf{u}_1(\mathbf{x}'') e^{i\mathbf{k}'.\mathbf{x}''} e^{-i\mathbf{k}'.\mathbf{x}} \tag{A.87}$$

Comparison between Eqs. Eqs. A.82 and A.87 results in

$$u_1^{\mathcal{R}}(\mathbf{x}) = u_1^{\mathcal{R}}(\mathbf{x}^*). \tag{A.88}$$

To prove $u_2^{\mathcal{R}}(\mathbf{x}) = -u_2^{\mathcal{R}}(\mathbf{x}^*)$, we have

$$u_2^{\mathcal{R}}(\mathbf{x}) = \frac{1}{(2\pi)^3} \iint\limits_{-\infty}^{\infty} d^3\mathbf{x}' d^3\mathbf{k} \Big(\frac{E_p(k)}{E_u(k)}\Big)^{1/2} \mathbf{u}_2(\mathbf{x}') e^{i\mathbf{k}.\mathbf{x}'} e^{-i\mathbf{k}.\mathbf{x}} \tag{A.89}$$

$$= \frac{1}{(2\pi)^3} \iint\limits_{-\infty}^{\infty} d^3\mathbf{x}' d^3\mathbf{k} \Big(\frac{E_p(k)}{E_u(k)}\Big)^{1/2} \mathbf{u}_2(\mathbf{x}') e^{i\mathbf{k}.\mathbf{x}'} e^{-i\mathbf{k}.(x_1,x_2,x_3)} \tag{A.90}$$

$$-u_2^{\mathcal{R}}(\mathbf{x}^*) = \frac{-1}{(2\pi)^3} \iint\limits_{-\infty}^{\infty} d^3\mathbf{x}' d^3\mathbf{k} \Big(\frac{E_p(k)}{E_u(k)}\Big)^{1/2} \mathbf{u}_2(\mathbf{x}') e^{i\mathbf{k}.\mathbf{x}'} e^{-i\mathbf{k}.(x_1,-x_2,x_3)}. \tag{A.91}$$

Using variable substitution $\mathbf{k} \to \mathbf{k}' = (k_1, -k_2, k_3)$, we have

$$-u_2^{\mathcal{R}}(\mathbf{x}^*) = \frac{-1}{(2\pi)^3} \iint\limits_{-\infty}^{\infty} d^3\mathbf{x}' d^3\mathbf{k}' \Big(\frac{E_p(k')}{E_u(k')}\Big)^{1/2} \mathbf{u}_2(\mathbf{x}') e^{i\mathbf{k}'.(x_1',-x_2',x_3')} e^{-i\mathbf{k}'.(x_1,x_2,x_3)} \tag{A.92}$$

Applying $\mathbf{x}' \to \mathbf{x}'' = (x_1', -x_2', x_3')$, we find

$$-u_2^{\mathcal{R}}(\mathbf{x}^*) = \frac{-1}{(2\pi)^3} \iint\limits_{-\infty}^{\infty} d^3\mathbf{x}'' d^3\mathbf{k}' \Big(\frac{E_p(k')}{E_u(k')}\Big)^{1/2} \mathbf{u}_2(x_1'', -x_2'', x_3'') e^{i\mathbf{k}'.(x_1'',x_2'',x_3'')} e^{-i\mathbf{k}'.(x_1,x_2,x_3)}. \tag{A.93}$$

Using Eq. A.53, gives

$$u_2^{\mathcal{R}}(\mathbf{x}^*) = \frac{-1}{(2\pi)^3} \int\!\!\!\int_{-\infty}^{\infty} d^3\mathbf{x}'' d^3\mathbf{k}' \left(\frac{E_p(k')}{E_u(k')}\right)^{1/2} - \mathbf{u}_2(x_1'', x_2'', x_3'') e^{i\mathbf{k}'.(x_1'', x_2'', x_3'')} e^{-i\mathbf{k}'.(x_1, x_2, x_3)} \quad (A.94)$$

$$= \frac{1}{(2\pi)^3} \int\!\!\!\int_{-\infty}^{\infty} d^3\mathbf{x}'' d^3\mathbf{k}' \left(\frac{E_p(k')}{E_u(k')}\right)^{1/2} \mathbf{u}_2(\mathbf{x}'') e^{i\mathbf{k}'.\mathbf{x}''} e^{-i\mathbf{k}'.\mathbf{x}} \quad (A.95)$$

Comparing between Eqs. A.90 and A.95, we find

$$u_2^{\mathcal{R}}(\mathbf{x}) = -u_2^{\mathcal{R}}(\mathbf{x}^*). \quad (A.96)$$

The third equation can be proved as before so that

$$u_3^{\mathcal{R}}(\mathbf{x}) = u_3^{\mathcal{R}}(\mathbf{x}^*). \quad (A.97)$$

Eqs.A.88, A.96 and A.97, shows $\mathbf{u}^{\mathcal{R}}(\mathbf{x}) = [\mathcal{R}\mathbf{u}](\mathbf{x})$ is maintaining the reflectional symmetry.

A.2 Derivation of the adjoint system with reflectional symmetry

In order to form the adjoint system with reflectional symmetry, we have assumed that

$$\boldsymbol{\varphi}(\mathbf{x}) = \frac{1}{2}[\boldsymbol{\psi}(\mathbf{x}) + H\boldsymbol{\psi}(H\mathbf{x})],$$

where H is defined as

$$H = \begin{pmatrix} 1 & 0 & 0 \\ 0 & -1 & 0 \\ 0 & 0 & 1 \end{pmatrix},$$

and

$$H\mathbf{x} = \begin{pmatrix} x_1 \\ -x_2 \\ x_3 \end{pmatrix} = \mathbf{x}^*,$$

for arbitrary $\boldsymbol{\psi}$, ensuring the velocity feild $\boldsymbol{\varphi}$ has the reflectional symmetry such that $\varphi_2(\mathbf{x})$ be an odd function of x_2. The optimal solution for $\boldsymbol{\psi}$ can be found as part of the solution of the coupled optimality system, which includes the constraint, the adjoint equation and the optimality condition [107]. Setting the first variation of $\mathcal{L}$ with respect to the Lagrange multiplier $\boldsymbol{\xi}$ equal to zero, following the standard technique [64], we have

$$\lim_{\epsilon \to 0} \left(\frac{\mathcal{L}(\boldsymbol{\xi} + \epsilon\widetilde{\boldsymbol{\xi}}) - \mathcal{L}(\boldsymbol{\xi})}{\epsilon} \right) = \lim_{\epsilon \to 0} \frac{1}{\epsilon} \left[\{J(\mathbf{u}_e) + \int (\boldsymbol{\xi} + \epsilon\widetilde{\boldsymbol{\xi}}).(\mathbf{u}_e - \mathcal{M}\boldsymbol{\varphi})d^3\mathbf{x}\} - \{J(\mathbf{u}_e) \right.$$

$$\left. + \int \boldsymbol{\xi}.(\mathbf{u}_e - \mathcal{M}\boldsymbol{\varphi})d^3\mathbf{x}\} \right] \quad (A.98)$$

$$= \lim_{\epsilon \to 0} \frac{1}{\epsilon} \int \epsilon\widetilde{\boldsymbol{\xi}}.(\mathbf{u}_e - \mathcal{M}\boldsymbol{\varphi})d^3\mathbf{x} \quad (A.99)$$

$$= \int \widetilde{\boldsymbol{\xi}}.(\mathbf{u}_e - \mathcal{M}\boldsymbol{\varphi})d^3\mathbf{x} = 0. \quad (A.100)$$

Since the variation $\widetilde{\boldsymbol{\xi}}$ in the Lagrange multiplier $\boldsymbol{\xi}$ is arbitrary, we obtain the state equation, i.e.,

$$\mathbf{u}_e = \mathcal{M}\boldsymbol{\varphi}. \tag{A.101}$$

The adjoint equation is given by the condition

$$\lim_{\epsilon \to 0}\left(\frac{\mathcal{L}(\mathbf{u}_e + \epsilon\widetilde{\mathbf{u}_e}) - \mathcal{L}(\mathbf{u}_e)}{\epsilon}\right) = \lim_{\epsilon \to 0}\frac{1}{\epsilon}\left[\{J(\mathbf{u}_e + \epsilon\widetilde{\mathbf{u}_e}) + \int \boldsymbol{\xi}.((\mathbf{u}_e + \epsilon\widetilde{\mathbf{u}_e}) - \mathcal{M}\boldsymbol{\varphi})d^3\mathbf{x}\} - \{J(\mathbf{u}_e)\right.$$

$$\left. + \int \boldsymbol{\xi}.(\mathbf{u}_e - \mathcal{M}\boldsymbol{\varphi})d^3\mathbf{x}\}\right] = 0 \tag{A.102}$$

$$= \lim_{\epsilon \to 0}\frac{1}{\epsilon}\left[J(\mathbf{u}_e + \epsilon\widetilde{\mathbf{u}_e}) - J(\mathbf{u}_e) + \int \boldsymbol{\xi}.\epsilon\widetilde{\mathbf{u}_e}d^3\mathbf{x}\right]. \tag{A.103}$$

Using Eq. 3.13, we find

$$\lim_{\epsilon \to 0}\left(\frac{\mathcal{L}(\mathbf{u}_e + \epsilon\widetilde{\mathbf{u}_e}) - \mathcal{L}(\mathbf{u}_e)}{\epsilon}\right) = \lim_{\epsilon \to 0}\frac{1}{\epsilon}\left[\frac{1}{2}\|\mathcal{F}[\mathbf{u}_e + \epsilon\widetilde{\mathbf{u}_e} - \mathbf{w}]\|^2 - \frac{1}{2}\|\mathcal{F}[\mathbf{u}_e - \mathbf{w}]\|^2 + \int \boldsymbol{\xi}.\epsilon\widetilde{\mathbf{u}_e}d^3\mathbf{x}\right] \tag{A.104}$$

$$= \lim_{\epsilon \to 0}\frac{1}{\epsilon}\left[\frac{1}{2}\int \{\mathcal{F}[\mathbf{u}_e + \epsilon\widetilde{\mathbf{u}_e} - \mathbf{w}]\}.\{\mathcal{F}[\mathbf{u}_e + \epsilon\widetilde{\mathbf{u}_e} - \mathbf{w}]\}d^3\mathbf{x}\right.$$

$$\left. - \frac{1}{2}\int \{\mathcal{F}[\mathbf{u}_e - \mathbf{w}]\}.\{\mathcal{F}[\mathbf{u}_e - \mathbf{w}]\}d^3\mathbf{x} + \int \boldsymbol{\xi}.\epsilon\widetilde{\mathbf{u}_e}d^3\mathbf{x}\right]. \tag{A.105}$$

$$\lim_{\epsilon \to 0}\left(\frac{\mathcal{L}(\mathbf{u}_e + \epsilon\widetilde{\mathbf{u}_e}) - \mathcal{L}(\mathbf{u}_e)}{\epsilon}\right) = \lim_{\epsilon \to 0}\frac{1}{\epsilon}\left[\frac{1}{2}\int \{\mathcal{F}[\mathbf{u}_e - \mathbf{w}] + \epsilon\mathcal{F}[\widetilde{\mathbf{u}_e}]\}.\{\mathcal{F}[\mathbf{u}_e - \mathbf{w}] + \epsilon\mathcal{F}[\widetilde{\mathbf{u}_e}]\}d^3\mathbf{x}\right.$$

$$\left. - \frac{1}{2}\int \{\mathcal{F}[\mathbf{u}_e - \mathbf{w}]\}.\{\mathcal{F}[\mathbf{u}_e - \mathbf{w}]\}d^3\mathbf{x} + \int \boldsymbol{\xi}.\epsilon\widetilde{\mathbf{u}_e}d^3\mathbf{x}\right] \tag{A.106}$$

$$= \lim_{\epsilon \to 0}\frac{1}{\epsilon}\left[\frac{1}{2}\int \{\mathcal{F}[\mathbf{u}_e - \mathbf{w}].\mathcal{F}[\mathbf{u}_e - \mathbf{w}] + 2\epsilon(\mathcal{F}[\mathbf{u}_e - \mathbf{w}].\mathcal{F}[\widetilde{\mathbf{u}_e}])\right.$$

$$\left. + O(\epsilon^2)\}d^3\mathbf{x} - \frac{1}{2}\int \{\mathcal{F}[\mathbf{u}_e - \mathbf{w}]\}.\{\mathcal{F}[\mathbf{u}_e - \mathbf{w}]\}d^3\mathbf{x} + \int \boldsymbol{\xi}.\epsilon\widetilde{\mathbf{u}_e}d^3\mathbf{x}\right]. \tag{A.107}$$

$$\lim_{\epsilon \to 0}\left(\frac{\mathcal{L}(\mathbf{u}_e + \epsilon\widetilde{\mathbf{u}_e}) - \mathcal{L}(\mathbf{u}_e)}{\epsilon}\right) = \lim_{\epsilon \to 0}\frac{1}{\epsilon}\left[\frac{1}{2}\int \{\mathcal{F}[\mathbf{u}_e - \mathbf{w}].\mathcal{F}[\mathbf{u}_e - \mathbf{w}] + 2\epsilon\mathcal{F}[\mathbf{u}_e - \mathbf{w}].\mathcal{F}[\widetilde{\mathbf{u}_e}] + O(\epsilon^2)\}d^3\mathbf{x}\right.$$

$$\left. - \frac{1}{2}\int \{\mathcal{F}[\mathbf{u}_e - \mathbf{w}]\}.\{\mathcal{F}[\mathbf{u}_e - \mathbf{w}]\}d^3\mathbf{x} + \int \boldsymbol{\xi}.\epsilon\widetilde{\mathbf{u}_e}d^3\mathbf{x}\right] = 0 \tag{A.108}$$

$$= \int \{\mathcal{F}[\mathbf{u}_e - \mathbf{w}].\mathcal{F}[\widetilde{\mathbf{u}_e}]\}d^3\mathbf{x} + \int \boldsymbol{\xi}.\widetilde{\mathbf{u}_e}d^3\mathbf{x} \tag{A.109}$$

$$= \int \{\mathcal{F}^+\mathcal{F}[\mathbf{u}_e - \mathbf{w}].\widetilde{\mathbf{u}_e}\}d^3\mathbf{x} + \int \boldsymbol{\xi}.\widetilde{\mathbf{u}_e}d^3\mathbf{x} \tag{A.110}$$

$$= \int \{\mathcal{F}^+\mathcal{F}[\mathbf{u}_e - \mathbf{w}].\widetilde{\mathbf{u}_e} + \boldsymbol{\xi}.\widetilde{\mathbf{u}_e}\}d^3\mathbf{x} \tag{A.111}$$

$$= \int \{\mathcal{F}^+\mathcal{F}[\mathbf{u}_e - \mathbf{w}] + \boldsymbol{\xi}\}.\widetilde{\mathbf{u}_e}d^3\mathbf{x}. \tag{A.112}$$

We have used $\mathcal{F}^+\mathcal{F} = \mathcal{F}^+ = \mathcal{F}$, where $\mathcal{F}^+$ is the adjoint operator of the linear operator $\mathcal{F}$. Since the variation $\widetilde{\mathbf{u}_e}$ in the state variable $\mathbf{u}_e$ is arbitrary, we have

$$\boldsymbol{\xi}(\mathbf{x}) = -\mathcal{F}[\mathbf{u}_e(\mathbf{x}) - \mathbf{w}(\mathbf{x})]. \tag{A.113}$$

The optimality condition is achieved by setting the first variation of the $\mathcal{L}$ with respect to the control variable ψ equal to zero, which is equivalent to

$$\lim_{\epsilon \to 0} \left(\frac{\mathcal{L}(\psi + \epsilon \widetilde{\psi}) - \mathcal{L}(\psi)}{\epsilon} \right) = \lim_{\epsilon \to 0} \frac{1}{\epsilon} \left[(J(\mathbf{u}_e(\mathbf{x})) + \int \boldsymbol{\xi}(\mathbf{x}).(\mathbf{u}_e(\mathbf{x}) - \mathcal{M}(\boldsymbol{\varphi}(\mathbf{x}) + \delta\boldsymbol{\varphi}(\mathbf{x}))d^3\mathbf{x} - (J(\mathbf{u}_e(\mathbf{x})) \right.$$

$$\left. + \int \boldsymbol{\xi}(\mathbf{x}).(\mathbf{u}_e(\mathbf{x}) - \mathcal{M}(\boldsymbol{\varphi}(\mathbf{x})))d^3\mathbf{x} \right] = 0. \tag{A.114}$$

where $\delta\boldsymbol{\varphi}$ is the variation corresponding to $\epsilon\widetilde{\psi}$, which is defined by

$$\delta\boldsymbol{\varphi}(\mathbf{x}) = \frac{1}{2}[\psi + \epsilon\widetilde{\psi} + H[\psi(H\mathbf{x}) + \epsilon\widetilde{\psi}(H\mathbf{x})] - \frac{1}{2}[\psi(\mathbf{x}) + H\psi(H\mathbf{x}) = \frac{\epsilon}{2}[\widetilde{\psi} + H\widetilde{\psi}(H\mathbf{x})].$$

Thus

$$\lim_{\epsilon \to 0} \left(\frac{\mathcal{L}(\psi + \epsilon\widetilde{\psi}) - \mathcal{L}(\psi)}{\epsilon} \right) = \lim_{\epsilon \to 0} \frac{1}{\epsilon} \left[\int \boldsymbol{\xi}(\mathbf{x}).[\mathbf{u}_e(\mathbf{x}) - \mathcal{M}(\boldsymbol{\varphi}(\mathbf{x}) + \delta\boldsymbol{\varphi}(\mathbf{x}))]d^3\mathbf{x} - \int \boldsymbol{\xi}(\mathbf{x}) \right.$$

$$\left. .[\mathbf{u}_e - \mathcal{M}(\boldsymbol{\varphi}(\mathbf{x}))]d^3\mathbf{x} \right] \tag{A.115}$$

$$= \lim_{\epsilon \to 0} \frac{-1}{\epsilon} \int \boldsymbol{\xi}(\mathbf{x}).[\mathcal{M}(\boldsymbol{\varphi}(\mathbf{x}) + \delta\boldsymbol{\varphi}(\mathbf{x})) - \mathcal{M}(\boldsymbol{\varphi}(\mathbf{x}))]d^3\mathbf{x}. \tag{A.116}$$

Using Eq. A.101, which is resulting in $\mathbf{u}_e(\mathbf{x}) = \mathcal{M}(\boldsymbol{\varphi}(\mathbf{x}))$. Then,

$$\delta\mathbf{u}_e(\mathbf{x}) = [\mathcal{M}(\boldsymbol{\varphi}(\mathbf{x}) + \delta\boldsymbol{\varphi}(\mathbf{x})) - \mathcal{M}(\boldsymbol{\varphi}(\mathbf{x}))]. \tag{A.117}$$

We have $M+1$ fields after M iteration: $\mathbf{u}_{10}, \mathbf{u}_{20}, ..., \mathbf{u}_{M0}$ and $\mathbf{u}_e$, where the control variable $\boldsymbol{\varphi}(\mathbf{x})$ is projected onto the divergence-free subspace, giving $\mathbf{u}_{10} \equiv \mathcal{P}\boldsymbol{\varphi}(\mathbf{x})$ and $\mathbf{u}_e$ is the final velocity field. $\mathbf{u}_{n0}$ is the output of the $(n-1)th$ iteration and the input of the nth iteration [107], such that

$$\mathbf{u}_{n0}(\mathbf{x}) = \mathbf{u}_{(n-1)3}(\mathbf{x}) + \mathcal{G}^c_{(n-1)}\mathbf{u}_{(n-1)0}(\mathbf{x}). \tag{A.118}$$

Thus, we have

$$\mathbf{u}_{(n+1)0}(\mathbf{x}) = \mathbf{u}_{n3}(\mathbf{x}) + \mathcal{G}^c_n\mathbf{u}_{n0}(\mathbf{x}) \tag{A.119}$$

For $n = 1, 2, ..., M$. Then,

$$\mathbf{u}_e(\mathbf{x}) = \mathcal{R}_M(\mathcal{P}\mathcal{A}_M)^{m_M}(G_M(\mathbf{u}_{M0}(\mathbf{x}))) + \mathcal{G}^c_M\mathbf{u}_{M0}(\mathbf{x}) \tag{A.120}$$

$$= \mathcal{R}_M(\mathcal{P}\mathcal{A}_M)^{m_M}(G_M(\mathbf{u}_{M0}(\mathbf{x}))) + \mathcal{G}^c_M\mathbf{u}_{M0}(\mathbf{x}) \tag{A.121}$$

$$= [\mathcal{R}_M(\mathcal{P}\mathcal{A}_M)^{m_M}\mathcal{G}_M + \mathcal{G}^c_M]\mathbf{u}_{M0}(\mathbf{x}). \tag{A.122}$$

Hence, the final field $\mathbf{u}_e(\mathbf{x})$ is given by

$$\mathbf{u}_{(M+1)0}(\mathbf{x}) = \mathbf{u}_e(\mathbf{x}). \tag{A.123}$$

$$\mathbf{u}_e(\mathbf{x}) = \mathcal{M}\boldsymbol{\varphi}(\mathbf{x}), \tag{A.124}$$

where

$$\mathcal{M} = \prod_{n=1}^{M} [\mathcal{R}_n (\mathcal{P}\mathcal{A}_n)^{m_n} \mathcal{G}_n + \mathcal{G}_n^c]\mathcal{P}. \tag{A.125}$$

According to Eq. A.117, where $\delta\mathbf{u}_e(\mathbf{x})$ represent the variation of $\mathbf{u}_e(\mathbf{x})$ corresponding to $\delta\varphi$. using Eqs. A.122 and A.123, we find

$$\delta\mathbf{u}_e(\mathbf{x}) = \delta\mathbf{u}_{(M+1)0}(\mathbf{x}) \tag{A.126}$$

$$= (\mathcal{D}_M^R \mathcal{D}_M^A \mathcal{G}_M + \mathcal{G}_M^c)\delta\mathbf{u}_{M0}(\mathbf{x}) \tag{A.127}$$

$$= (\mathcal{D}_M^R \mathcal{D}_M^A \mathcal{G}_M + \mathcal{G}_M^c)(\mathcal{D}_{M-1}^R \mathcal{D}_{M-1}^A \mathcal{G}_{M-1} + \mathcal{G}_{M-1}^c)\delta\mathbf{u}_{(M-1)0}(\mathbf{x}) \tag{A.128}$$

$$= \prod_{n=1}^{M} [\mathcal{D}_n^R \mathcal{D}_n^A \mathcal{G}_n + \mathcal{G}_n^c]\delta\mathbf{u}_{10}(\mathbf{x}). \tag{A.129}$$

Where $\mathcal{D}_n^R$ and $\mathcal{D}_n^A$ are the tangent operator of $\mathcal{R}_n$ and $\mathcal{P}\mathcal{A}_n$ operators, respectively. Given

that $\mathbf{u}_{10} \equiv \mathcal{P}\varphi(\mathbf{x})$ with Eq. 3.15. Thus,

$$\mathbf{u}_{10} = \mathcal{P}\left[\frac{1}{2}[\psi(\mathbf{x}) + H\psi(H\mathbf{x})]\right]. \tag{A.130}$$

$$\delta\mathbf{u}_{10} = \frac{\epsilon}{2}\mathcal{P}\left[\widetilde{\psi}(\mathbf{x}) + H\widetilde{\psi}(H\mathbf{x})\right]. \tag{A.131}$$

Eq. A.129 gives the linearization of the $\mathcal{R}_n$ and $\mathcal{P}\mathcal{A}_n$ operators, which are also the tangent operator of the operators. We thus find

$$\delta\mathbf{u}_e(\mathbf{x}) = \{\prod_{n=1}^{M} [\mathcal{D}_n^R \mathcal{D}_n^A \mathcal{G}_n + \mathcal{G}_n^c]\}\frac{\epsilon}{2}\mathcal{P}\left[\widetilde{\psi}(\mathbf{x}) + H\widetilde{\psi}(H\mathbf{x})\right] \tag{A.132}$$

$$= \frac{\epsilon}{2}\{\prod_{n=1}^{M} [\mathcal{D}_n^R \mathcal{D}_n^A \mathcal{G}_n + \mathcal{G}_n^c]\mathcal{P}[\widetilde{\psi}(\mathbf{x})] + \prod_{n=1}^{M} [\mathcal{D}_n^R \mathcal{D}_n^A \mathcal{G}_n + \mathcal{G}_n^c]\mathcal{P}[H\widetilde{\psi}(H\mathbf{x})]\}. \tag{A.133}$$

Following last equation, Eq. A.116 becomes

$$\lim_{\epsilon\to 0}\left(\frac{\mathcal{L}(\psi + \epsilon\widetilde{\psi}) - \mathcal{L}(\psi)}{\epsilon}\right) = \lim_{\epsilon\to 0}\frac{-1}{\epsilon}\int \boldsymbol{\xi}(\mathbf{x}).\left[\frac{\epsilon}{2}\{\prod_{n=1}^{M} [\mathcal{D}_n^R \mathcal{D}_n^A \mathcal{G}_n + \mathcal{G}_n^c]\mathcal{P}[\widetilde{\psi}(\mathbf{x})]\right.$$

$$\left. + \prod_{n=1}^{M} [\mathcal{D}_n^R \mathcal{D}_n^A \mathcal{G}_n + \mathcal{G}_n^c]\mathcal{P}[H\widetilde{\psi}(H\mathbf{x})]d^3\mathbf{x} \right. \tag{A.134}$$

$$= \frac{-1}{2}\left[\int \boldsymbol{\xi}(\mathbf{x}).\prod_{n=1}^{M} [\mathcal{D}_n^R \mathcal{D}_n^A \mathcal{G}_n + \mathcal{G}_n^c]\mathcal{P}[\widetilde{\psi}(\mathbf{x})]d^3\mathbf{x}\right.$$

$$\left. + \int \boldsymbol{\xi}(\mathbf{x}).\prod_{n=1}^{M} [\mathcal{D}_n^R \mathcal{D}_n^A \mathcal{G}_n + \mathcal{G}_n^c]\mathcal{P}[H\widetilde{\psi}(H\mathbf{x})]d^3\mathbf{x}\right] \tag{A.135}$$

$$= \frac{-1}{2}\left[\int \mathcal{P}\prod_{n=1}^{M} [\mathcal{G}_n \mathcal{D}_n^{A+} \mathcal{D}_n^{R+} + \mathcal{G}_n^c]\boldsymbol{\xi}(\mathbf{x}).\widetilde{\psi}(\mathbf{x})d^3\mathbf{x}\right.$$

$$\left. + \int \mathcal{P}\prod_{n=1}^{M} [\mathcal{G}_n \mathcal{D}_n^{A+} \mathcal{D}_n^{R+} + \mathcal{G}_n^c]\boldsymbol{\xi}(\mathbf{x}).H\widetilde{\psi}(H\mathbf{x})d^3\mathbf{x}\right]. \tag{A.136}$$

$\mathcal{D}_n^{R+}$ and $\mathcal{D}_n^{A+}$ are the adjoint operators of the the linearizion of the of $\mathcal{R}_n$ and $(\mathcal{P}\mathcal{A}_n)^{m_n}$, respectively. Which are defined the adjoint operator of the operator $\mathcal{M}$ as follows:

$$\mathcal{M}^+ = \mathcal{P}\prod_{n=1}^M [\mathcal{G}_n \mathcal{D}_n^{A+}\mathcal{D}_n^{R+} + \mathcal{G}_n^c]. \tag{A.137}$$

Therefore

$$\lim_{\epsilon\to 0}\left(\frac{\mathcal{L}(\psi + \epsilon\widetilde{\psi}) - \mathcal{L}(\psi)}{\epsilon}\right) = \frac{-1}{2}\left[\int(\mathcal{M}^+\boldsymbol{\xi})(\mathbf{x}).\widetilde{\psi}(\mathbf{x})d^3\mathbf{x} + \int(\mathcal{M}^+\boldsymbol{\xi})(\mathbf{x}).H\widetilde{\psi}(H\mathbf{x})d^3\mathbf{x}\right]. \tag{A.138}$$

Using variable substitution $H\mathbf{x} = \mathbf{x}'$, such that $H\mathbf{x} = (x_1, -x_2, x_3) = (x'_1, x'_2, x'_3) = \mathbf{x}'$. which is resulting in

$$\lim_{\epsilon\to 0}\left(\frac{\mathcal{L}(\psi + \epsilon\widetilde{\psi}) - \mathcal{L}(\psi)}{\epsilon}\right) = \frac{-1}{2}\left[\int(\mathcal{M}^+\boldsymbol{\xi})(\mathbf{x}).\widetilde{\psi}(\mathbf{x})d^3\mathbf{x} + \int H(\mathcal{M}^+\boldsymbol{\xi})(H\mathbf{x}').\widetilde{\psi}(\mathbf{x}')d^3\mathbf{x}'\right], \tag{A.139}$$

where

$$H\mathbf{x}' = (x'_1, -x'_2, x'_3). \tag{A.140}$$

Then

$$\lim_{\epsilon\to 0}\left(\frac{\mathcal{L}(\psi + \widetilde{\psi}) - \mathcal{L}(\psi)}{\epsilon}\right) = -\int\frac{1}{2}[(\mathcal{M}^+\boldsymbol{\xi})(\mathbf{x}) + H(\mathcal{M}^+\boldsymbol{\xi})(H\mathbf{x})].\widetilde{\psi}(\mathbf{x})d^3\mathbf{x} \tag{A.141}$$

Thus,

$$\frac{\delta\mathcal{L}}{\delta\psi}\Big|_{\mathbf{u}_e,\boldsymbol{\xi}} = \frac{-1}{2}\{(\mathcal{M}^+\boldsymbol{\xi})(\mathbf{x}) + H(\mathcal{M}^+\boldsymbol{\xi})(H\mathbf{x})\}. \tag{A.142}$$

Since the adjoint equation and the state equation are solved exactly [107], we have

$$\frac{DJ}{D\psi} = \frac{\delta\mathcal{L}}{\delta\psi}\Big|_{\mathbf{u}_e,\boldsymbol{\xi}} = \frac{-1}{2}\{(\mathcal{M}^+\boldsymbol{\xi})(\mathbf{x}) + H(\mathcal{M}^+\boldsymbol{\xi})(H\mathbf{x})\}. \tag{A.143}$$

It can be calculated by Knowing the $\boldsymbol{\xi}$ and the operator $\mathcal{M}^+$. Thus following Eq. A.114, we find

$$\frac{\delta\mathcal{L}}{\delta\psi}\Big|_{\mathbf{u}_e,\boldsymbol{\xi}} = \frac{-1}{2}\{(\mathcal{M}^+\boldsymbol{\xi})(\mathbf{x}) + H(\mathcal{M}^+\boldsymbol{\xi})(H\mathbf{x})\} = 0. \tag{A.144}$$

Eqs. A.101, A.113 and A.144, forms the optimality system for the optimization problem.

Appendix B

B.1   The pseudo-code for the numerical implementation of the CMTLM map

In this appendix, the pseudo-code for some key parts of the numerical algorithm is given.

B.1.1   The algorithm for the CMTLM map

It is assumed that a tolerance $e > 0$ and a step size $\lambda > 0$ have been given. The pseodu-code for the outer iteration in the CMTLM map is given below. Those of the inner iterations will be given in the next subsection.

For $k = 0, 1, 2, ...,$ **do:**

1. $\mathcal{M}\boldsymbol{\varphi}^{(k)} \to \mathbf{u}_e^{(k)}$;
2. Find J from Eq. (3.13)

   If $J < e$ **then:** exit;
   Else continue;
3. Find $\boldsymbol{\xi}^{(k)}$ from Eq. (3.18)
4. Find $\mathcal{D}J/\mathcal{D}\boldsymbol{\varphi}^{(k)}$ from Eq. (3.21)
5. Update $\boldsymbol{\varphi}$, i.e.:

$$\boldsymbol{\varphi}^{(k)} - \lambda \frac{\mathcal{D}J}{\mathcal{D}\boldsymbol{\varphi}^{(k)}} \to \boldsymbol{\varphi}^{(k+1)}. \tag{B.1}$$

The iteration exits when the cost function is smaller than the given tolerance e. The last value for $\mathbf{u}_e$ is the CMTLM synthetic velocity field.

B.1.2   The iterations in the MTLM map (inner iterations)

It is assumed that M is given, and we have chosen $L = \pi/2$ so that $\ell_n = 2^{-(n+1)}\pi$ and $k_{c,n} = 2^{n+2}$. The pseudo-code for the MTLM map is as follows:

1. Define a $(N/2) \times N \times N$ three dimensional complex array $\boldsymbol{\varphi}$; initialize $\boldsymbol{\varphi}$ with Gaussian random number.

2. **For:** $n = 1, 2, ..., M$, **do:**

(a) Define a $N_n/2 \times N_n \times N_n$ three dimensional complex array $\mathbf{u}_n$ where $N_n = 2^{n+2}$;

(b) Copy the first $N_n/2 \times N_n \times N_n$ Fourier modes in φ to $\mathbf{u}_n$;

(c) **For:** $i = 1, 2, ..., m_n$, **do:**

    i. Inverse FFT $\mathbf{u}_n$;

    ii. Apply operator $\mathcal{A}_n$ on $\mathbf{u}_n$, i.e.: Define real $N_n \times N_n \times N_n$ arrays F and s and a temporary three dimensional $N_n \times N_n \times N_n$ real array $\mathbf{v}_n$; let $s = 0$, $F = 0$, $\mathbf{v}_n = 0$;

        For $i = 1$ to N_n, $j = 1$ to N_n, $k = 1$ to N_n, **Do:**

        A. Find the location $\mathbf{X}(t_n)$ for the fluid particle on grid point (i, j, k);

        B. For the 8 grid points $\mathbf{x}_p$ $(p = 1, 2, ..., 8)$ around the fluid particle, find the weight $W(\mathbf{x}_p - \mathbf{X}(t_n)) \rightarrow F(\mathbf{x}_p)$;

        C. $\mathbf{v}_n(\mathbf{x}_p) + F(\mathbf{x}_p)\mathbf{u}_n(i, j, k) \rightarrow \mathbf{v}_n(\mathbf{x}_p)$; $s(\mathbf{x}_p) + F(\mathbf{x}_p) \rightarrow s(\mathbf{x}_p)$;

    iii. $\mathbf{v}_n/s \rightarrow \mathbf{u}_n$

    iv. FFT $\mathbf{u}_n$;

    v. Apply operator $\mathcal{P}$ on $\mathbf{u}_n$;

(d) Apply $\mathcal{R}_n$ to $\mathbf{u}_n$;

(e) Copy $\mathbf{u}_n$ back into the first $N_n/2 \times N_n \times N_n$ Fourier modes in φ.

The final result in φ is the MTLM synthetic velocity field.

B.1.3 The algorithm for the calculation of the gradient of the cost function

We consider only a generic cost function $J = ||\mathcal{F}(\mathbf{u}_e - \mathbf{w})||_2^2/2$ where $\mathbf{w}$ is the target function and $\mathbf{u}_e$ is the synthetic field constructed using the MTLM map. When CMTLM is applied to construct a synthetic model for the velocity field in a channel, the pseudo-code for the calculation of the gradient of J with respect to the control ψ (i.e., $\mathcal{D}J/\mathcal{D}\psi$) is given as follows:

1. Define a $(N/2) \times N \times N$ three dimensional complex array $\boldsymbol{\xi}$;

2. Calculate the adjoint, i.e.: $-\mathcal{F}(\mathbf{u}_e - \mathbf{w}) \rightarrow \boldsymbol{\xi}$;

3. **For:** $n = M, M - 1, ..., 2, 1$, **do:**

    (a) Define a $N_n/2 \times N_n \times N_n$ three dimensional complex array $\boldsymbol{\xi}_n$ where $N_n = 2^{n+2}$;

    (b) Copy the first $N_n/2 \times N_n \times N_n$ Fourier modes in $\boldsymbol{\xi}$ to $\boldsymbol{\xi}_n$;

    (c) Apply $\mathcal{D}_n^{R+}$ to $\boldsymbol{\xi}_n$;

    (d) **For:** $i = m_n, m_n - 1, ..., 2, 1$, **Do:**

        i. Apply operator $\mathcal{P}$ on $\boldsymbol{\xi}_n$;

        ii. Apply operator $\mathcal{D}_n^{A+}$ on $\boldsymbol{\xi}_n$;

    (e) Copy $\boldsymbol{\xi}_n$ back into the first $N_n/2 \times N_n \times N_n$ Fourier modes in $\boldsymbol{\xi}$.

4. Find the antisymmetric part of $\boldsymbol{\xi}$ according to Eq. (3.21)

The final result in $\boldsymbol{\xi}$ is $\mathcal{D}J/\mathcal{D}\psi$.

Bibliography

[1] J. L. Aider and A. Danet, "Large-eddy simulation study of upstream boundary conditions influence upon a backward-facing step flow," Comptes Rendus Mcanique **334(7)**, 447-453 (2006).

[2] K. Akselvoll and P. Moin, "Large-eddy simulation of turbulent confined coannular jets," Journal of Fluid Mechanics **315**, 387-411 (1996).

[3] J. C. Alamo, J. Jimnez, P. Zandonade and R.D. Moser , "Scaling of the energy spectra of turbulent channels," Journal of Fluid Mechanics **500**, 135-144 (2004).

[4] A. Arneodo, E. Bacry, and J. F. Muyz, "Random cascades on wavelet dyadic trees," J. Math. Phys. **39**, 4142-1998 (1998).

[5] J. S. Baggett, J. Jimenez and A. G. Kravchenko, "Resolution requirements in large-eddy simulations of shear flows," Annual research briefs, 51-66 (1997).

[6] G. Balarac, H. Pitsch, and V. Raman, "Development of a dynamic model for the subfilter scalar variance using the concept of optimal estimators, " Phys. Fluids **20**, 035114 (2008).

[7] G. Balarac, H. Pitsch, and V. Raman, "Modelling of the subfilter scalar dissipation rate using the concept of optimal estimators, " Phys. Fluids **20**, 091701 (2008).

[8] E. Balaras, C. Benocci and U. Piomelli, " Two-layer approximate boundary conditions for large-eddy simulations," AIAA journal, **34(6)**, 1111-1119 (1996).

[9] J. Barding, J. H. Ferziger and W.C. Reynolds, "Improved subgrid-scale models for large-eddy simulation," In American Institute of Aeronautics and Astronautics, Fluid and Plasma Dynamics Conference, 13th, Snowmass, Colo., July 14-16, (1980).

[10] J. Bardino, J.H. Ferziger, and W.C. Reynolds, "Improved turbulence models based on large eddy simulation of homogeneous, incompressible turbulent flows," (1983).

[11] G. K. Batchelor , "An Introduction to Fluid Dynamics," Cambridge University Press, Cambridge, (1967).

[12] P. Batten, U. Goldberg and S. Chakravarthy, "Interfacing statistical turbulence closures with large-eddy simulation," AIAA J. **42(3)**, 485-492 (2004).

[13] M. J. Beals, J.P. Fugal, R.A. Shaw, J. Lu, S.M. Spuler and J.L. Stith, "Holographic measurements of inhomogeneous cloud mixing at the centimeter scale," Science **350**, 6256 (2015).

[14] R. Benzi, L. Biferale, A. Crisanti, G. Paladin, M. Vergassola and A. Vulpiani, "A random process for the construction of multiaffine fields," Physica D **65**, 352 (1993).

[15] G. A. Blaisdell, E. T. Spyropoulos and J.H. Qin, "The effect of the formulation of nonlinear terms on aliasing errors in spectral methods," Applied Numerical Mathematics, **21(3)**, 207-219 (1996).

[16] C. Bogey and C. Bailly, "Effects of inflow conditions and forcing on subsonic jet flows and noise," AIAA J. **43**, 1000-1007 (2005).

[17] V. Borue and S. A. Orszag, "Numerical study of three-dimensional Kolmogorov flow at high Reynolds numbers," Journal of Fluid Mechanics **306**, 293-323 (1996).

[18] J. Bred berg, "On the Wall Boundary Condition for Turbulence Models," Chalmers University of Technology Goteborg, Sweden (2000).

[19] J. Bull and A. Jameson, "Explicit filtering and exact reconstruction of the sub-filter stresses in large eddy simulation," J. Comput. Phys. **306**, 117-136 (2016).

[20] B. Chaouat and R. Schiestel, "A new partially integrated transport model for subgrid-scale stresses and dissipation rate for turbulent developing flows," Physics of Fluids **17(6)**, 065106 (2005).

[21] D. R. Chapman, "Computational Aerodynamics Development and Outlook," AIAA J. **17(12)** (1979).

[22] S. Chekov, and C.J. Rutland, "Dynamic structure models for scalar flux and dissipation in large eddy simulation," AIAA journal, **42(6)** (2004).

[23] M. Chertov, G. Falkovich, I. Kolokolov, and V. Lebedev, "Normal and anomalous scaling of the fourth-order correlation function of a randomly advected passive scalar," Phys. Rev. E **52**, 4924 (1995).

[24] L. Chevillard, R. Robert and V. Vargas, "A stochastic representation of the local structure of turbulence," Europhys. Lett. **89**, 54002 (2010).

[25] L. Chevillard, E. Leveque, F. Taddia, C. Meneveau, H. Yu and C. Rosales, "Local and nonlocal pressure Hessian effects in real and synthetic fluid turbulence," Phys. Fluids **23**, 095108 (2011).

[26] S. G. Chumakov and C.J. Rutland, "Dynamic structure subgridscale models for large eddy simulation," International journal for numerical methods in fluids **47(89)**, 911-923 (2005).

[27] S. G. Chumakov, "Statistics of subgrid-scale stress states in homogeneous isotropic turbulence," Journal of Fluid Mechanics **562**, 405-414 (2006).

[28] S. G. Chumakov, "A priori study of subgrid-scale flux of a passive scalar in isotropic homogeneous turbulence," Phys. Rev. E **78**, 036313 (2008).

[29] Y. M. Chung and H.J. Sung, "Comparative study of in ow conditions for spatially evolving simulation" AIAA journal **35(2)**, 269274 (1997).

[30] R. A. Clark, J.H. Ferziger and W.C. Reynolds, "Evaluation of subgrid-scale models using an accurately simulated turbulent flow," Journal of Fluid Mechanics **91(1)**, 1-16 (1970).

[31] S. Corrsin, "Limitations of gradient transport models in random walks and in turbulence," Advances in geophysics **18**, 25-60 (1975).

[32] A. S. Cruz, L. David, J. Pcheux, and A. Texier, "Characterization by proper-orthogonal-decomposition of the passive controlled wake flow downstream of a half cylinder," Exp. Fluids **39**, 730 (2005).

[33] J. Dacles-Mariani, G. G. Zilliac, J. S. Chow, and P. Bradshaw, "Numerical/Experimental Study of a Wingtip Vortex in the Near Field," AIAA Journal **33(9)**, 1561-1568 (1995).

[34] J. Dandois, E. Garnier and P. Sagaut, "Numerical simulation of active separation control by a synthetic jet," Journal of Fluid Mechanics **574**, 25-58 (2007).

[35] L. Davidson and M. Billson, "Hybrid RANS-LES using synthetized turbulence for forcing at the interface," In ECCOMAS (2004).

[36] L. Davidson and S. Dahlstrm, "Hybrid LES-RANS: An approach to make LES applicable at high Reynolds number," International journal of computational fluid dynamics **19(6)**, 415-427 (2005).

[37] L. Davidson and M. Billson, "Hybrid LES-RANS using synthesized turbulent fluctuations for forcing in the interface region," Int. J. Heat Fluid Flow **27**, 1028-1042 (2006).

[38] L. Davidson, "Hybrid LES-RANS: inlet boundary conditions for flows including recirculation," In TSFP Digital Library Online. Begel House Inc.(2007).

[39] J. W. Deardorff, "Three-dimensional numerical study of the height and mean structure of a heated planetary boundary layer," Boundary-Layer Meteorology **7**, 81-106 (1974).

[40] P. E. Dimotakis, "Turbulent mixing," Annu. Rev. Fluid Mech. **37**, 329-356 (2005).

[41] J. A. Domaradzki and E.M. Saiki, "A subgrid-scale model based on the estimation of unresolved scales of turbulence," Phys. Fluids **9**, 2148 (1997).

[42] P. Druault, P. Guibert, and F. Alizon, "Use of proper orthogonal decomposition for time interpolation from PIV data. Application to the cycle-to- cycle variation analysis of in-cylinder engine flows," Exp. Fluids **39**, 1009 (2005).

[43] P. A. Durbin, "Near-wall turbulence closure modeling without damping functions," Theoretical and Computational Fluid Dynamics **3(1)**, 1-13 (1991).

[44] P. A. Durbin, "On the k-epsilon Stagnation Point Anomaly," International Journal of Heat and Fluid Flow **17**, 89-90 (1996).

[45] H. Eckemann, "The structure of the viscous sublayer and the adjacent wall region in a turbulent channel flow," J . Fluid Mech. **65**, 439 (1974).

[46] J. Eggers and S. Grossmann, "Effect of dissipation fluctuations on anomalous velocity scaling in turbulence," Physical Review A **45(4)**, 2360-2369 (1992).

[47] T. Esch and F. R. Menter, "Heat transfer predictions based on two-equation turbulence models with advanced wall treatment," Turbulence Heat Mass Transfer **4**, 6333-6640 (2003).

[48] A. Ferrante and S. E. Elghobashi, " A robust method for generating inflow conditions for direct simulation of spatially developing turbulent boundary layers," Journal of Computational Physics **198**, 372-387 (2004).

[49] P. Flohr and J.C. Vassilicos, "A scalar subgrid model with flow structure for large-eddy simulations of scalar variances," J. Fluid Mech. **407**, 315–349 (2000).

[50] R. Friedrich and M. Arnal, "Analysing turbulent backward-facing step flow with the lowpass-filtered Navier-Stokes equation," Journal of Wind Engineering and its Applications **35**, 101-128 (1990).

[51] U. Frisch, A. Mazzino, and M. Vergassola, "Intermittency in passive scalar advection," Phys. Rev. Lett. **80**, 5532 (1998).

[52] U. Frisch and J. Bec, "Burgulence," in New trends in turbulence Turbulence: nouveaux aspects by M. Lesieur, A. Yaglom and F. David (Ed.), 341–383 (2003).

[53] J. C. H. Fung, J. C. Hunt, N. A. Malik and R. J. Perkins, "Kinematic simulation of homogeneous turbulence by unsteady random Fourier modes," Journal of Fluid Mechanics, **236**, 281-318(1992).

[54] J. C. H. Fung and J. C. Vassilicos,"Two-particle dispersion in turbulent like flows," Phys. Rev. E **57(2)**, 1677-1690 (1998).

[55] B. Galperina and S. A. eds. Orszag, "Large eddy simulation of complex engineering and geophysical flows," Cambridge University Press, Cambridge (1993).

[56] Y. Gao, N. Chabraborty, and N. Swaminathan, "Dynamic closure of scalar dissipation rate for large eddy simulations of turbulent premixed combustion: a direct numerical simulations analysis," Flow Turbulence Combust **95**, 775–802 (2015).

[57] K. Gawedzki and A. Kupiainen, "Anomalous scaling of the passive scalar," Phys. Rev. Lett. **75**, 3834 (1995).

[58] M. Germano, U. Piomelli, P. Moin and W. H. Cabot , "A dynamic subgrid-scale eddy viscosity model," Phys. Fluids A. **3**(7), 1760-1765 (1991).

[59] S. Ghosal, T. S. Lund, P. Moin and K. Akselvoll , "A dynamic localization model for large-eddy simulation of turbulent flows," J. Fluid Mech. **286**, 229-255 (1995).

[60] D. J. Glaze and S. H. Frankel, "Stochastic inlet conditions for large-eddy simulation of a fully turbulent jet," AIAA journal, **41(6)**, 1064-1073 (2003).

[61] G. Glushko, "Turbulent boundary layer on a flat plate in an incompressible fluid," Izvestia Akademiya Nauk SSSR, Mekh, No 4, 13 (1965).

[62] T. Gotoh and T. Watanabe, "Scalar flux in a uniform mean scalar gradient in homogeneous isotropic steady turbulence," Physica D **241**, 141-148 (2012).

[63] T. Gotoh and T. Watanabe, "Power and nonpower laws of passive scalar moments convected by isotropic turbulence," Phys. Rev. Lett. **115**, 114502 (2015).

[64] M. D. Gunzburger," Perspectives in Flow Control and Optimization," (SIAM, 2003).

[65] R. A. Handler, E. Levich and L. Sirovich, "Drag reduction in turbulent channel flow by phase randomization," Physics of Fluids A: Fluid Dynamics **5(3)**, 686-694 (1993).

[66] K. Hanjalic, "Will RANS survive LES? A view of perspectives," Journal of fluids engineering **127(5)**, 831-839 (2005).

[67] T. J. Hanratty, L. G. Chorn and D. T. Hatziavramidis, "Turbulent fluctuations in the viscous wall region for Newtonian and drag reducing fluids," Phys. Fluids **20**, S112 (1977).

[68] C. W. Higgins, M. B. Parlance, and C. Meneveau, "The heat flux and the temperature gradient in the lower atmosphere," Geophysical research letters, **31(22)** (2004).

[69] M. Holzer and D. Siggia, "Turbulent mixing of a passive scalar," Phys. Fluids **6**, 1820 (1994).

[70] K. Horiuti, "Roles of non-aligned eigenvectors of strain-rate and subgrid-scale stress tensors in turbulence generation," Journal of Fluid Mechanics **491**, 65-100 (2003).

[71] N. Jarrin, S. Benhamadouche, D. Laurence, and R. Prosser, "A synthetic-eddy-method for generating inflow conditions for large-eddy simulations," Int. J. Heat Fluid Flow **27**, 585593 (2006).

[72] N. Jarrin, "Synthetic inflow boundary conditions for the numerical simulation of turbulence," Ph.D. Thesis University of Manchester (2008).

[73] N. Jarrin, R. Prosser, J.C. Uribe, S. Benhamadouche, and D. Laurence, "Reconstruction of turbulent fluctuations for hybrid RANS/LES simulations using a synthetic-eddy Method," Int. J. Heat Fluid Flow **30**, 435442 (2009).

[74] P. S. Johansen and H. I. Andersson, " Generation of inflow data for inhomogeneous turbulence," Theoretical and Computational Fluid Dynamics **18(5)**, 371-389 (2004).

[75] W. P. Jones and B. E. Launder, "The prediction of laminarization with a two-equation model of turbulence," International Journal of Heat Mass Transfer **15**, 301-314 (1972).

[76] A. Juneja, D. P. Lathrop, K.R.Sreenivasan and G. Stolovitzky, "Synthetic turbulence," Phys. Rev. E **49**, 5179-5194 (1994).

[77] H. J. Kaltenbach, M. Fatica, R. Mittal, T. S. Lund, and P. Moin, " Study of flow in a planar asymmetric diffuser using large eddy simulation," Journal of Fluid Mechanics **390**, 151-185 (1999).

[78] J. Kaltenbach and G. Janke,"Direct numerical simulation of flow separation behind a swept, rearward-facing step at $Re_H = 3000H$," Phys. Fluids **12(9)**, 2320-2337 (2000).

[79] H. S. Kang and C. Meneveau, "Universality of large eddy simulation model parameters across a turbulent wake behind a heated cylinder," Journal of Turbulence **3**, 26-26 (2002).

[80] H. S. Kang, S. Chester and C. Meneveau, "Decaying turbulence in an active-grid-generated flow and comparisons with large-eddy simulation," J. Fluid Mech. **480**, 129 (2003).

[81] H. S. Kang and C. Meneveau, "Effect of large-scale coherent structures on subgrid-scale stress and strain-rate eigenvector alignments in turbulent shear flow," Phys. Fluids **17**, 055103 (2005).

[82] T. von Karman, "Mechanische ahnlichkeit und turbulenz," In Proc. Third Int. Congr. Applied Mechanics, 85-105 (1930).

[83] X. WU and K. Squires, "Numerical investigation of the turbulent boundary layer over a bump," J. Fluid Mech. **362**, 229-271 (1998).

[84] A. Keating U. Piomelli, E. Balaras and H-J Kaltenbach, " A priori and and a posteriori tests of inflow conditions for large-eddy simulation," Phys Fluids **16(12)**, 4696-712 (2004).

[85] A. Keating, and U. Piomelli, "A dynamic stochastic forcing method as a wall-layer model for large-eddy simulation," Journal of Turbulence **(7)**, N12 (2006).

[86] A. Kempf, M. Klein and J. Janicka, "Efficient Generation of Initial- and Inflow-Conditions for Transient Turbulent Flows in Arbitrary Geometries," Flow Turbulence Combust **74**, 67-84 (2005).

[87] J. Kim , P. Moin, and R. Mose , "Turbulence statistics in fully developed channel flow at low Reynolds number," Journal of fluid mechanics **177**, 133-166 (1987).

[88] Y. Kim, I.P. Castro and Z.T. Xie,"Divergence-free turbulence inflow conditions for large-eddy simulations with incompressible flow solvers," Computers and Fluids **84**, 56-68 (2013).

[89] M. Klein, A. Sadiki and J. Janicka, "A digital filter based generation of inflow data for spatially developing direct numerical or large eddy simulations," Journal of computational Physics **186(2)**, 652-665 (2003).

[90] E. Knudsen, E. S. Richardson, E. M. Doran, H. Pitsch, and J. H. Chen, "Modelling scalar dissipation and scalar variance in large eddy simulation: Algebraic and transport equation closures," Phys. Fluids **24**, 055103 (2012).

[91] J. Komminaho, A. Lundblah, and V. Johansson, "Very large structures in plane turbulent Couette flow," J. Fluid Mech. **320**, 259-285 (1996).

[92] K. Kondo, S. Nakamura and A. Mochida, "Generation of velocity fluctuations for inflow boundary condition of LES. Journal of Wind Engineering and Industrial Aerodynamics," **67**, 51-64 (1997).

[93] L. S. G. Kovasznay, "Spectrum of locally isotropic turbulence, " Journal of the Aeronautical Sciences **15**, 745-753 (1948).

[94] R. H. Kraichnan, " Diffusion by a random velocity field. The physics of fluids," **13(1)**, 22-31 (1969).

[95] R.H. Kraichnan, "Anomalous scaling of a randomly advected passive scalar," Phys. Rev. Lett. **72**, 1016 (1994).

[96] B. de Laage de Meux, B. Audebert, R. Manceau, and R. Perrin, "Anisotropic linear forcing for synthetic turbulence generation in large eddy simulation and hybrid RANS/LES modelling," Phys. Fluids **27**, 035115 (2015).

[97] E. Labourasse, and P. Sagaut, "Reconstruction of turbulent fluctuations using a hybrid RANS/LES approach," Journal of Computational Physics **182(1)**, 301-336 (2002).

[98] B. E. Launder and B.I. Sharma, "Application of the energy-dissipation model of turbulence to the calculation of flow near a spinning disc," Letters in heat and mass transfer **1(2)**, 131-137 (1974).

[99] B. E. Launder, G.J. Reece and W. Rodi, " Progress in the development of a Reynolds-stress turbulence closure," Journal of fluid mechanics **68(3)**, 537-566 (1975).

[100] H. Le, P. Moin and J. Kim, "Direct numerical simulation of turbulent flow over a backward-facing step," Journal of fluid mechanics **330**, 349-374 (1997).

[101] S. Lee, S. K. Lele, and P. Moin, " Simulation of spatially evolving turbulence and the applicability of Taylors hypothesis in compressible flow," Physics of Fluids A: Fluid Dynamics **4(7)**, 1521-1530 (1992).

[102] A. Leonard, "Large-eddy simulation of chaotic convection and beyond," AIAA paper **97**, 0204 (1997).

[103] M. Lesieur and O. Metais, " New trends in large-eddy simulations of turbulence," Annual Review of Fluid Mechanics **28(1)**, 45-82 (1996).

[104] M. Lesieur, "Turbulence in Fluids," third revised and enlarged edition (1997).

[105] C. W. Li and J. H. Wang,"Large eddy simulation of free surface shallow-water flow," Int. J. Numer. Methods Fluids **34**, 31-46 (2000).

[106] N. Li, E. Balaras and U. Piomelli, "Inflow conditions for large-eddy simulations of mixing layers," Physics of Fluids **12(4)**, 935-938 (2000).

[107] Y. Li and C. Rosales, "Constrained multi-scale turnover Lagrangian map for anisotropic synthetic turbulence: A priori tests," Phys. Fluids **26**, 075102 (2014).

[108] Y. Li, "The evolution towards the rod-like axisymmetric structure for turbulent stress tensor," Phys. Fluids **27**, 085104 (2015).

[109] D. K. Lilly, "The representation of small-scale turbulence in numerical simulation experiments Proc," IBM Scientific Computing Symp. on Environmental Sciences (Yorktown Heights, New York) ed H H Goldstine, IBM form no. 320-1951, p 195, (1967).

[110] D. K. Lilly, "A proposed modification of the Germano subgridscale closure method, " Physics of Fluids A: Fluid Dynamics **4(3)**, 633-635 (1992).

[111] S. Liu, C. Meneveau, and J. Katz, "On the properties of similarity subgrid-scale models as deduced from measurements in a turbulent jet," Journal of Fluid Mechanics **275**, 83-119 (1994).

[112] T. S. Lund, X. Wu and K. D. Squires, "Generation of turbulent inflow data for spatially-developing boundary layer simulations," Journal of Computational Physics **140(2)**, 233-258 (1998).

[113] L. di Mare, M. Klein, W. P. Jones and J. Janicka,"Synthetic turbulence inflow conditions for large-eddy simulation," Phys. Fluids **18**, 025107 (2006).

[114] W. D. McComb, "The Physics of Fluid Turbulence," Oxford: Oxford

[115] C. Meneveau, T. S. Lund and W.H. Cabot, "A Lagrangian dynamic subgrid-scale model of turbulence," Journal of Fluid Mechanics **319**, 353-385 (1996).

[116] C. Meneveau and J. Katz, " Scale-invariance and turbulence models for large-eddy simulation," Annual Review of Fluid Mechanics **32(1)**, 1-32 (2000).

[117] C. Meneveau and J. Katz, "Scale-invariance and turbulence models for large-eddy simulation," Annu. Rev. Fluid Mech. **32**, 1 (2000).

[118] F. R. Menter and Y. Egorov, "Turbulence models based on the length-scale equation," In TSFP DIGITAL LIBRARY ONLINE. Begel House Inc (2005).

[119] F. R. Menter and Y. Egorov, "A scale adaptive simulation model using two-equation models," In: AIAA Paper 2005-1095 (2006).

[120] F. R. Menter, R. B. Langtry, S. R. Likki, and Y. B. Suzen, "A correlation-based transition model using local variables," Part I: model formulation. Journal of Turbomachinery, **128**, 413 (2006).

[121] K. E. Meyer, J. M. Pedersen, and O. zcan, "A turbulent jet in crossflow analysed with proper orthogonal decomposition," J. Fluid Mech. **583**, 199 (2007).

[122] H. H. Minh, and A. Kourta, "Semi-deterministic turbulence modelling for flows dominated by strong organised structures," In 9th Symposium On Turbulent Shear Flow, 10-5 (1993).

[123] P. Moin and J. Kim , " Numerical investigation of turbulent channel flow," Journal of fluid mechanics **118**, 341-377 (1982).

[124] P. Moin, K. Squires, W. Cabot and S. Lee, "A dynamic subgridscale model for compressible turbulence and scalar transport," Physics of Fluids A: Fluid Dynamics **3(11)**, 2746-2757 (1991).

[125] P. Moin, "Progress in large eddy simulation of turbulent flows," AIAA paper, 970749 (1997).

[126] P. Moin and K. Mahesh, "Direct numerical simulation: a tool in turbulence research," Annual review of fluid mechanics **30(1)**, 539-578 (1998).

[127] L. Mydlarski and Z. Warhaft, "Passive scalar statistics in high-Peclet-number grid turbulence," J. Fluid Mech. **358**, 135 (1998).

[128] Y. Na and P. Moin, "Direct numerical simulation of a separated turbulent boundary layer," Journal of Fluid Mechanics **374**, 379405 (1998).

[129] F. Nicolleau and A. ElMaihy, "Effect of the Reynolds number on three and four-particle diffusion in three-dimensional turbulence using kinematic simulation," Phys. Rev. E **74**, 046302 (2006).

[130] N. V. Nikitin, F. Nicoud, B. Wasistho, K. D. Squires and P. R. Spalart, "An approach to wall modeling in large-eddy simulations," Physics of fluids **12(7)**, 1629-1632 (2000).

[131] C. Nilsen and H. I. Andersson, "Mechanisms of particle clustering in Gaussian and non-Gaussian synthetic turbulence," Phys. Rev. E **90**, 043005 (2014).

[132] J. O. H. N. O'Neil and C. Menelaus, "Subgrid-scale stresses and their modelling in a turbulent plane wake," Journal of Fluid Mechanics **349**, 253-293 (1997).

[133] D. R. Osborne, J.C. Vassilicos and J.D. Haigh, "One-particle two-time diffusion in three-dimensional homogeneous isotropic turbulence," Phys. Fluids **17**, 035104 (2005).

[134] S. Panchev, "Kovasznay's spectral theory of turbulence," Phys. Fluids **12**, 935 (1969).

[135] R. L. Panton, "Incompressible flow," New York: Wiley (1984).

[136] C. Peniguel, M. Sakiz, S. Benhamadouche, J.M. Stephan and C. Vindeirinho, " Presentation of a numerical 3D approach to tackle thermal striping in a PWR nuclear T-junction," In ASME 2003 Pressure Vessels and Piping Conference (pp. 125-132). American Society of Mechanical Engineers.

[137] R.M. Pereira, C. Garban and L. Chevillard, "A dissipative random velocity field for fully developed fluid turbulence," J. Fluid Mech. **794**, 369 (2016).

[138] N. Peters, "Turbulent combustion," Cambridge University Press (2000).

[139] C. D. Pierce and P. Moin, "Progress-variable approach for large-eddy simulation of non-premixed turbulent combustion," Journal of Fluid Mechanics **504**, 73-97 (2004).

[140] U. Piomelli, W. H. Cabot, P. Moin and S. Lee, "Subgridscale backscatter in turbulent and transitional flows," Physics of Fluids A: Fluid Dynamics **3(7)**, 1766-1771 (1991).

[141] U. Piomelli and J. Liu, "Large-eddy simulation of rotating channel flows using a localized dynamic model," Physics of fluids **7(4)**, 839-848 (1995).

[142] U. Piomelli, "Large-eddy simulation: achievements and challenges," Progress in Aerospace Sciences **35(4)**, 335-362 (1999).

[143] U. Piomelli, E. Balaras, H. Pasinato, K.D. Squires and P.R., Spalart, "The inner-outer layer interface in large-eddy simulations with wall-layer models," International Journal of heat and fluid flow **24(4)**, 538-550 (2003).

[144] H. Pitsch, "Large-eddy simulation of turbulent combustion," Ann. Rev. Fluid Mech. **38**, 453-82 (2006).

[145] S. B. Pope, "Turbulent Flows," (Cambridge University Press, Cambridge, 2000).

[146] S. B. Pope, "Ten questions concerning the large eddy simulation of turbulent flows," New J. Phys. **6**, 1-4 (2004).

[147] M. Popovac and K. Hanjalic, "Compound wall treatment for RANS computation of complex turbulent flows and heat transfer," Journal of Flow Turbulence and Combustion **78(2)**, 177-202 (2007).

[148] L. Prandtl, "Bericht uber Untersuchungen zur ausgebildeten Turbulenz," Zeitschrift fur angew Math. u. Mechanik. **5(2)**, 136-9 (1925).

[149] A. Pumir, "A numerical study of the mixing of a passive scalar in three dimensions in the presence of a mean gradient," Phys. Fluids **6**, 2118 (1994).

[150] A. Rasam, G. Brethouwer, and A. Johansson, "An explicit algebraic model for the sub grid-scale passive scalar flux," J. Fluid Mech. **721**, 541 (2013).

[151] O. Reynolds, "An experimental investigation of the circumstances which determine whether the motion of water shall be direct or sinuous, and of the law of resistance in parallel channels," Proceedings of the royal society of London, **35**. (224-226), 84-99 (1883).

[152] O. Reynolds, "On the dynamical theory of incompressible viscous fluids and the determination of the criterion," Proceedings of the Royal Society of London, **56(336-339)**, 40-45 (1894).

[153] W. C. Reynolds, "The potential and limitations of direct and large eddy simulations," In Whither turbulence? Turbulence at the crossroads (pp. 313-343). Springer, Berlin, Heidelberg (1990).

[154] L. F. Richardson, "Weather prediction by numerical process," Cambridge University Press (1922).

[155] R. S. Rogallo and P. Moin , "Numerical simulation of turbulent flows," Annual review of fluid mechanics **16(1)**, 99-137 (1984).

[156] C. Rosales and C. Meneveau, "A minimal multiscale Lagrangian map approach to synthesize non-Gaussian turbulent vector fields," Phys. Fluids **18**, 075104 (2006).

[157] C. Rosales and C. Meneveau, "Anomalous scaling and intermittency in three-dimensional synthetic turbulence," Phys. Rev. E **78**, 016313 (2008).

[158] C. Rosales, "Synthetic three-dimensional turbulent passive scalar fields via the minimal Lagrangian map," Phys. Fluids **23**, 075106 (2011).

[159] P. Sagaut, "Simulations of separated flows with subgrid models," La Recherche Aerospatiale **(1)**, 51-63 (1996).

[160] P. Sagaut, "Large eddy simulation for incompressible flows: an introduction," Springer Berlin Heidelberg (1998).

[161] P. Sagaut, E. Garnier, E. Tromeur, L. Larcheveque, and E. Labourasse, " Turbulent inflow conditions for LES of compressible wall bounded flows," AIAA Journal **42(3)**, (2004).

[162] N. D. Sandham, Y.F. Yao and A. A. Lawal, "Large-eddy simulation of transonic turbulent flow over a bump," International Journal of Heat and Fluid Flow **24(4)**, pp.584-595 (2003).

[163] U. Schumann "Subgrid scale model for finite difference simulations of turbulent flows in plane channels and annuli," Journal of Computational Physics Phys. **18(4)**, 376-404 (1975).

[164] J. U. Schuster, H. Pitsch and P. Moin, "Large eddy simulation inflow conditions for coupling with Reynolds-averaged flow solvers," AIAA journal **42(3)**, 478-484 (2004).

[165] A. Scotti and C. Meneveau, "Fractal model for coarse-grained nonlinear partial differential equation," Phys. Rev. Lett. **78**, 867 (1997).

[166] A. Scotti and C. Meneveau, "A fractal model for large eddy simulation of turbulent flow," Phys. D **127**, 198-232 (1999).

[167] E. Sergent, "Vers une Methodologie de Couplage entre la Simulation des Grandes Echelles et les Modeles Statistiques," PhD Thesis. Ecole Centrale de Lyon, Lyon, France, (2002).

[168] B. I. Shraiman and E.D. Siggia, "Scalar turbulence," Nature **405**, 639 (2000).

[169] J. Smagorinsky, "General circulation experiments with the primitive equations: I. The basic experiment," Monthly weather review **91(3)**, 99-164 (1963).

[170] A. Smirnov, S. Shi and I. Celik, "Random flow generation technique for large eddy simulations and particle-dynamics modeling," Transactions of the ASME-I-Journal of Fluids Engineering, **123(2)**, 359-371 (2001).

[171] R. Spalart, "Numerical simulations of boundary layers," 88220-88222(1985).

[172] P. R. Spalart, W. H. Jou, M. Strelets, M and S. R. Allmaras, " Comments on the feasibility of LES for wings, and on a hybrid RANS/LES approach," Advances in DNS/LES, **1**, 4-8 (1997).

[173] P. R. Spalart, "Topics in detached-eddy simulation," Computational Fluid Dynamics 3-12 (2004).

[174] P. R. Spalart, "Detached-eddy simulation," Annu. Rev. Fluid Mech. **41**, 181-202 (2009).

[175] C. G. Speziale, "Analytical methods for the development of Reynolds-stress closures in turbulence," Annual Review of Fluid Mechanics **23(1)**, 107-157 (1991).

[176] C. G. Speziale, "Turbulence modeling for time-dependent RANS and VLES a review," AIAA journal **36(2)**, 173-184 (1998).

[177] A. Spille and H-J. Kaltenbach, "Generation of turbulent inflow data with a prescribed shear-stress profile," In C. Liu, L Sakell, and T. Beutner, editors, Thrid AFSOR Conference on DNS and LES, Arlington TX, 5-9 August (2001).

[178] K. R. Sreenivasan and R. A. Antonia, "The phenomenology of small-scale turbulence," Annu. Rev. Fluid Mech. **29**, 435 (1997).

[179] R. Stoll and F. Port-Agel, "Dynamic subgrid-scale models for momentum and scalar fluxes in large-eddy simulations of neutrally stratified atmospheric boundary layers over heterogeneous terrain," Water Resour. Res. **42(1)** (2005).

[180] S. Strolz and N.A. Adams , "An approximate deconvolution procedure for large-eddy simulation," Physics of Fluids **11(7)**, 1699-1701 (1999).

[181] P. Subedi, R. Chhiber, J. A. Tessein, M. Wan, and W. H. Matthaeus, "Generating synthetic magnetic field intermittency using a minimal multiscale Lagrangian mapping approach," The Astrophysical Journal **796**, 97 (2014).

[182] G. Tabor, MH. Baba-Ahmadi, E. de Villiers and HG. Weller, "Construction of inlet conditions for LES of turbulent channel flow," In: Proceedings of the ECCOMAS congress, Jyvskyl, Finland, (2004).

[183] G. R. Tabor and M.H. Baba-Ahmadi, "Inlet conditions for large eddy simulation: A review," Computers and Fluids **39** , 553-567 (2010).

[184] B. Tao, Katz, J. and C. Meneveau, "Application of HPIV data of turbulent duct flow for turbulence modeling," In Proceedings of 3rd ASME/JSME Joint Fluids Engineering Conference (pp. 18-22) (1999).

[185] B. Tao, J. Katz and C. Meneveau, "Geometry and scale relationships in high Reynolds number turbulence determined from three-dimensional holographic velocimetry," Physics of Fluids **12(5)**, 941-944 (2000).

[186] B. Tao, J. Katz, and C. Meneveau, "Statistical geometry of sub-grid-scale stresses determined from holographic particle image velocimetry measurements," Journal of Fluid Mechanics **457**, 35-78 (2002).

[187] H. Tennekes and J.L. Lumley, "A First course in turbulence," MIT Press.

[188] M. Terracol, "Airframe noise prediction by mean of a zonal RANS/LES approach," In TSFP DIGITAL LIBRARY ONLINE. Begel House Inc. (2005).

[189] C. Tong and Z. Warhaft, "On passive scalar derivative statistics in grid turbulence," Phys. Fluids **6**, 2165 (1994).

[190] D. J. Tritton, "Physical fluid dynamics," Oxford: Oxford University Press (1988).

[191] A. Tsinober, E. Kit and T. Dracos, "Experimental investigation of the field of velocity gradients in turbulent flows," Journal of Fluid Mechanics **242**, 169-192 (1992).

[192] J. C. Uribe, N. Jarrin, R. Prosser and D. Laurence, "Two-Velocities Hybrid RANS-LES of a Trailing Edge Flow," In IUTAM Symposium on Unsteady Separated Flows and their Control (pp. 63-76). Springer, Dordrecht (2009).

[193] E. R. Van Driest, " On turbulent flow near a wall," J. Aeronaut. Sci, **23(11)**, 1007-1011 (1956).

[194] I. Veloudis, Z. Yang, J. J. McGuirk and G.J. Page , "Assessment of the Digital Filter Approach for Generating Large-eddy Simulation Inlet Conditions," In: Rodi, W (ed.) Engineering Turbulence Modelling and Experiments 6. Elsevier Science, pp. 307-316. ISBN 9780080445441(2005).

[195] I. Veloudis, Z. Yang , J. J. McGuirK, G. J. Page and A. Spencer, " Novel implementation and accessment of a digtial filter based approach for the generation of LES inlet conditions," Flow Turbul.Combust. **79(1)**, 1-24 (2007).

[196] T. Vicsek and A. Barabasi, "Multi-affine model for the velocity distribution in fully turbulent flows," J. Phys. A **24**, L845 (1991).

[197] A. Vincent, and M. Meneguzzi, "The dynamics of vorticity tubes in homogeneous turbulence," Journal of Fluid Mechanics **258**, 245-254 (1994).

[198] M. Wang and P. Moin, "Computation of trailing-edge flow and noise using large-eddy simulation," AIAA journal **38(12)**, 2201-2209 (2000).

[199] Z. Warhaft, "Passive scalars in turbulent flows,"Annu. Rev. Fluid Mech. **32**, 203 (2000).

[200] T. Watanabe and T. Gotoh, "Statistics of a passive scalar in homogeneous turbulence," New J. Phys. **6**, 40 (2004).

[201] D. C. Wilcox, "Turbulence Modeling for CFD, DCW Industries," Inc. La Canada, California.

[202] D. C. Wilcox, C. David, "Turbulence Modeling for CFD," Second edition. Anaheim: DCW Industries, 174 (1998).

[203] D. C. Wilcox, " Turbulence Modeling for CFD," ISBN 1-928729-10-X, 2nd Ed., DCW Industries, Inc. (2004).

[204] D. C. Wilcox, "Formulation of the ko turbulence model revisited," In: 45th AIAA Aerospace Sciences Meeting. Reno, NV, USA. AIAA Paper 2007-1408 (2007) .

[205] X. Wu, "Inflow Turbulence Generation Methods," Annu. Rev. Fluid Mech. (2017). **49**, 23-49 (2017).

[206] Z. -T. Xie and I. P. Castro, "LES and RANS for turbulent flow over arrays of wall-mounted cubes," Flow Turbul. Combust. **76(3)**, 291-312 (2006).

[207] Z.T. Xie, and I. P. Castro,"Efficient generation of inflow conditions for large eddy simulation of street-scale flows," Flow, turbulence and combustion **81(3)**, 449-470 (2008).

[208] P. K. Yeung, and S. B. Pope, "Lagrangian statistics from direct numerical simulations of isotropic turbulence," Journal of Fluid Mechanics **207**, 531-586(1989).

[209] A. Yoshiwara, "Statistical theory for compressible turbulent shear flows, with the application to subgrid modeling," Physics of fluids **29(7)**, 2152-2164 (1986).

[210] T. A. Zang, "On the rotation and skew-symmetric forms for incompressible flow simulations," Applied Numerical Mathematics **7(1)**, 27-40 (1991).